centralizers were placed on every 2 joints of casing. After all the casing was run, 40 kℓ mud, 5 kℓ lignate water mixture and 2.5 kℓ water were sequentially pumped in order to cool and clean the hole. For the first stage of the cement job, two different ratios of retarder were used. A slurry with 1.5% was used as a lead slurry and 1% retarder as a tail slurry. Both slurrys contained 40% silica flour and 2% bentonite based upon weight percent of cement. A total 31,047 ℓ of cement slurry with density 1.80 sg (specific gravity) was pumped as a first stage, then displaced with 54,400 ℓ of mud. During this displacement, mud circulation to the surface was obtained in about 11 minutes at the middle of operation. After displacement, a metal plug was dropped to open the ports of stage cementer (placed at 775.84 m) and 24 kℓ of mud was pumped to clean the cement slurry placed above it. As a second stage, 3 kℓ water, 34,258 ℓ cement slurry (1.80 sg), and 29,600 ℓ mud were pumped in sequence. Materials used for this second stage slurry were same weight ratios as used for the lead slurry of the first stage. To close the ports of stage cementer, a plug was released into the hole just before pumping mud. Circulation was not returned to the surface for this second stage operation. Judging from the pumping pressure, the top of the cement in the annulus appeared to be below the shoe of 13⅜" c.p., so another cement slurry was pumped into the annulus. A total of 9,060 ℓ of 1.76 to 1.80 sg slurry was pumped and filled up the annulus to the surface. This amount of slurry corresponds to about a 270 m length of annulus volume between the 13⅜" c.p. and 9⅝" c.p.

The cement was drilled out and reached 1,445 m with an 8½" bit size on Jan. 29th. A cement bond log (CBL) was run on Jan. 27th and its was determined that the cement was good enough to continue drilling. Twelve days were spent drilling from 1,445 m to 2,006.80 m. Two cores were cut from 1,500 m to 1,503 m and from 2,003.40 m to 2,006.40 m. The core recoveries for the first and the second core runs were 100% and 85% respectively. Lost circulation of drilling fluid started at 1,486 m after 9⅝" c.p. was set, so drilling was conducted with partial or total lost circulation to the total depth. Sections with more than 40 kℓ/h of lost circulation were encountered while drilling from 1,486 m to 1,489 m, from 1,873 m to 1,877 m, and from 1,885 to 1,886 m. When the drilling was terminated at 2,006.80 m, the amount of lost circulation was 13 kℓ/h.

Temperature and pressure logs were run 4, 8, and 12 hours after pumping was stopped. Maximum temperature recorded was 235.06°C at the bottom of the well and water level was 370 m deep from the ground level. Then water injection tests were conducted.

After logs and test were finished, 7" slotted pipe was run from 1,353.75 to 1,999.52 m, then well was washed with water. While injecting water to clean the well total lost circulation occured. Well head stacks were changed from drilling to production, then rig was released.

Drilling history, the rig layout, and rig inventory are shown Fig. II.3-8, Fig. II.3-9 and Table II.3-8.

3.2.3 Bit record

Bit record and detail rate of penetration are shown in Fig. II.3-10 and Table II.3-9.

3.2.4 Lost circulation

Fig. II.3-11 shows the depths of lost circulation and the depths of lost circulation

treatments. The severity and treatment methods of lost circulations are as follows.

(1) From spud in to Setting 20" Casing

While drilling the pilot hole with a 12¼" bit, first lost circulation occured at 64 m. After drilling to 72 m without circulation two cement plugs were set, but could not cure lost circulation. Hole was drilled to 91 m and seven cement plugs were set, but while drilling out cement lost circulation occured again. So well was drilled to 112 m with 12¼" bit and then opened to 20" and finally 26" without circulation.

(2) After setting 20" casing to setting 13⅜" casing

After 20" casing was set and drilled with 12¼" bit, lost circulation occured at 117 m. Total 24 cement plugs were set to reach 612 m for 12¼" hole and 42 cement plugs were set for 17½" hole.

(3) After setting 13⅜" casing to setting 9⅝" casing

In this section, there were not so many lost circulation zones compared as shallower depth. Total lost circulation was noticed from 1,220 m to 1,240 m. Twentysix cement plugs were set in this section.

(4) After setting 9⅝" casing to total depth

Total lost circulation were noticed following three zones; that is from 1,486 m to 1,489 m, from 1,873 m to 1,877 m, and from 1,885 m to 1,886 m. Since this section is for production zone, no lost circulation treatments were made and drilled with losses. When the total depth was reached, 13 kℓ/h lost circulation was noticed. But after setting 7" slotted liner, well was washed with water and finally more than 105 kℓ/h lost circulation was measured.

(5) Cement slurry

Total eightyone cement plugs were tried for this well. The Cement slurry was made of 100% cement, 40% silicaflour and 2% NaCl and specific gravity was 1.80 for almost all the slurry.

3.2.5 Run casing and cementing

(1) 20" Casing

After 26" hole was drilled to 108 m, 20" casing (H-40, 94 lb/ft) was run to 106.4 m and cemented. The planned cement slurry volume was 42.3 kℓ, but while pumping slurry pump pressure was increased and could not be pumped further. Total of 16.5 kℓ slurry was pumped. After waited on cement, top annular cementing job was made three times (total slurry volume was 17.8 kℓ) and slurry was filled to the surface.

100% cement, 40% silicaflour and 2% bentonite with specific gravity 1.85 was used for this cementing job. (Table II.3-10)

(2) 13⅜" Casing

After 17½" hole was drilled to 612 m, 13⅜" casing (K-55, 54.5 lb/ft) was run to 609.34 m and cemented. Total 48 joints of casing, casing shoe, casing collar and 26 centralizers were used (Table II.3-11). Cementing was performed with two plug method, first, mud was pumped to cool the well and total 63.7 kℓ cement slurry (40% silicaflour, 2% bentonite and 0.3% retarder with 1.80 S.G) was pumped, then displaced with mud. Slurry was not returned to the surface and top annular cementing job was made three times and 17 kℓ slurry was pumped to fill the annulus.

(3) 9⅝" Casing

After hole was washed to the bottom of casing point with the true gauge assembly, 9⅝" casing was run in the hole on Jan. 22nd. But mud circulation was not obtained at 937.24 m and all the casing was pulled out of the hole. Mud was circulated and conditioned with 2 kℓ/h lost circulation and gauging assembly was run again. The 9⅝" casing was rerun and cemented on Jan. 24th and 25th. The two stage cementing method was employed for the job. The casing was run to 1,407.24 m. A casing shoe, float collar and stage cementer were placed at the bottom, 2 joints above the shoe and at 775.84 m respectively. (Table II.3-12) Also centralizers were placed on every 2 joints of casing. After all the casing was run, 40 kℓ mud, 5 kℓ lignate water mixture and 2.5 kℓ water were sequentially pumped in order to cool and clean the hole. For the first stage of the cement job, two different ratios of retarder were used. A slurry with 1.5% was used as a lead slurry and 1% retarder as a tail slurry. Both slurrys contained 40% silica flour and 2% bentonite based upon weight percent of cement. A total 31,047 ℓ of cement slurry with density 1.80 sg (specific gravity) was pumped as a first stage, then displaced with 54,400 ℓ of mud. During this displacement, mud circulation to the surface was obtained in 11 minutes at the middle of operation. After dispalcement, a metal plug was dropped to open the ports of stage cementer (placed at 775.84 m) and 24 kℓ of mud was pumped to clean the cement slurry placed above it. As a second stage, 3 kℓ water, 34,258 ℓ cement slurry (1.80 sg), and 29,600 ℓ mud were pumped in sequence. Materials used for this second stage slurry were same weight ratios as used for the lead slurry of the first stage. To close the ports of stage cementer, a plug was released into the hole just before pumping mud. Circulation was not returned to the surface for this second stage operation. Judging from the pumping pressure, the top of the cement in the annulus appeared to be below the shoe of 13⅜" c.p., so another cement slurry was pumped into the annulus. A total of 9,060 ℓ of 1.76 to 1.80 sg slurry was pumped and filled up the annulus to the surface. This amount of slurry corresponds to about a 270 m length of annulus volume between the 13⅜" c.p. and 9⅝" c.p.

(4) 7" slotted Pipe

After 8½" hole was drilled to 2,006.4 m, 7" casing and slotted pipes (L-80, 29 lb/ft, HYDRIL SEU) were set with liner hanger from 1,353.75 m to 1,995.52 m.

List of strings are shown in Table II.3-13 and Figure of 7" Slotted pipe are shown in Fig. II.3-12.

3.2.6 Blowout preventer stacks

Blowout Preventer Stacks for each drilling stage are shown in Fig. II.3-13 (1) ~ (5).

3.2.7 Bottom hole assembly

Since PR-13 was planned as a straight hole, packed hole assembly (bit, stabilizer, short drill collar, stabilizer for the bottom part of BHA) was mainly used, from surface to total depth. When well was drilled under total lost circulation and well condition was not good for the packed hole assembly stabilizers were eliminated from BHA (Bottom Hole Assembly). Size of drill collars, and heavy weight drill pipe (HWDP) used was 8", 6½" drill collars and 4½" 42 lb/ft HWDP.

3.2.8 Stuck pipe and fishing

Three accidents (stuck pipe) had occured while drilling at 404 m, 416 m and 1,415.20 m. Followings are the procedures how to get fish out of hole.

(1) The first stuck pipe

After hole was opened with 17½" HOP (Holeopener) to 411 m and pulled up to 404 m first stuck pipe occured. So, lignite water and diesel with 2% chemical was pumped from both DP and annulus. Then, fish was pulled and out of the hole.

(2) The second stuck pipe

While drilling with 17½" HOP at 416 m without mud return the second stuck pipe occured. About a month had spent to free the pipe.

The procedure to free pipe were as follows.

① Nov. 8th

Stuck pipe occured at 416 m

② Nov. 8th ~ 9th

Oil spots were tried four times but could not free the pipe.

③ Nov. 10th

Could not pump mud through drill pipe (DP).

④ Nov. 11th ~ 12th

(i) Left hand torque was applied with 27 ton tension and could free pipe between the first HWDP and the second HWDP (Fig. II.3-14 (1)).

(ii) 4½" DP was connected with the fish and pulled 42 tons, then rotated to the left and could free one joint DP and three joint DC (Drill Collar). (Fig. II.3-14 (2))

⑤ Nov. 12th ~ 24th: Washover work

(i) 14" Washover shoe was run and washed over just above the 17½" HOP but could not get the fish (Fig. II.3-15 (1)

(ii) Hole was reamed with 17½" bit and 17½" HOP to the top of fish. Then, fish was washed over with 17½" washover shoe and jarred with bumper safty joint but could not get the fish (Fig. II.3-14 (3)).

⑥ Nov. 25th ~ Dec. 6th

Hole was opened to 18¼" with holeopener above fish and fish was washed over

with 18¼" washover shoe just below the fish and finally could get all the fish out of hole (Fig. II.3-15 (2)).

(3) The third stuck pipe

While pulling the BHA out of hole, the pipe was stucked at 711 m. The pipe was rotated to the right but while releasing the torque, pipe was rotated to the left with reaction torque and strings were disconnected from 138.38 m above the bit. Fish was connected with guid shoe and two oil spots were made to get the fish out of hole.

3.2.9 Used materials

Table II.3-14 shows amount of mud additive, lost circulation materials and cement used for PR-13.

3.2.10 Surveys and logs

(1) Well inclination surveys

Well inclination surveys were performed every 100 m from surface to 1,400 m, and every 50 m from 1,400 m to total depth and found all inclination survey results were less than 3 degrees from vertical (Fig. II.3-8).

(2) Temperature and pressure logs at 1,400 m

Temperatrure and pressure logs were run 6, 10 and 14 hours after pumping was stopped. All the logs were done inside the drill pipe with Kuster meter. Maximum temperature recorded was 186.90°C at 1,406 m. Using those data it was calculated that the temperature would go up to 201°C at static condition at 1,406m. From the pressure logs water level was 180 m deep from ground level (Fig. II.3-16).

(3) Temperature and pressure logs at 2,000 m

Temperature and pressure logs were run 4, 8 and 12 hours after pumping was stopped at total depth (Fig. II.3-17). Maximum temperature recorded was 235.06°C at the bottom of the well and water level was 370 m deep from the ground level.

(4) Water Injection Test

After finishing logs at total depth, 1,000 ℓ/min of water was pumped from wellhead 2" valve and pressure was measured at 1,400 m deep from GL with Kuster meter. Fig. II.3-18 shows the results of the injection test.

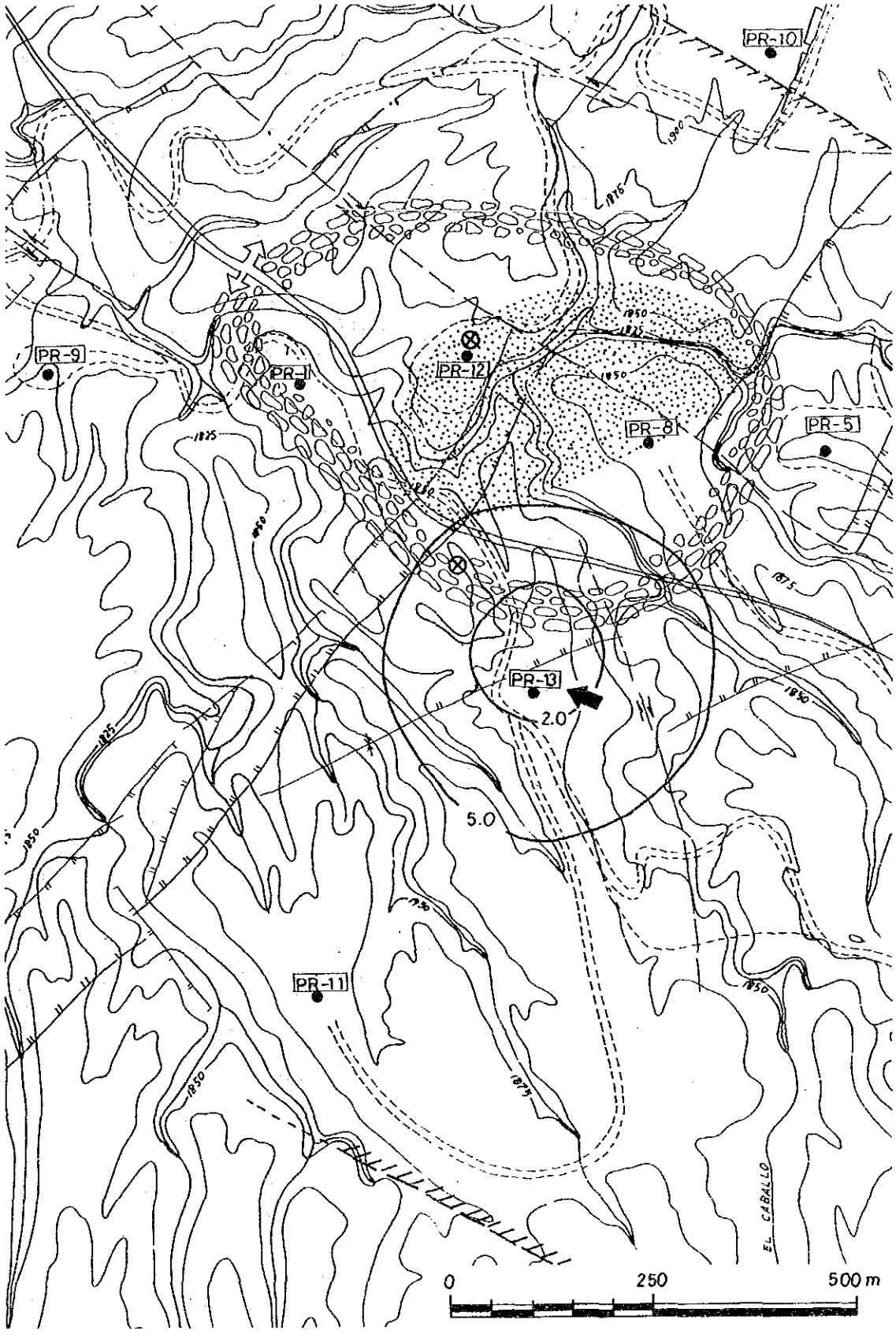

Fig. II. 3-6 Location of PR-13

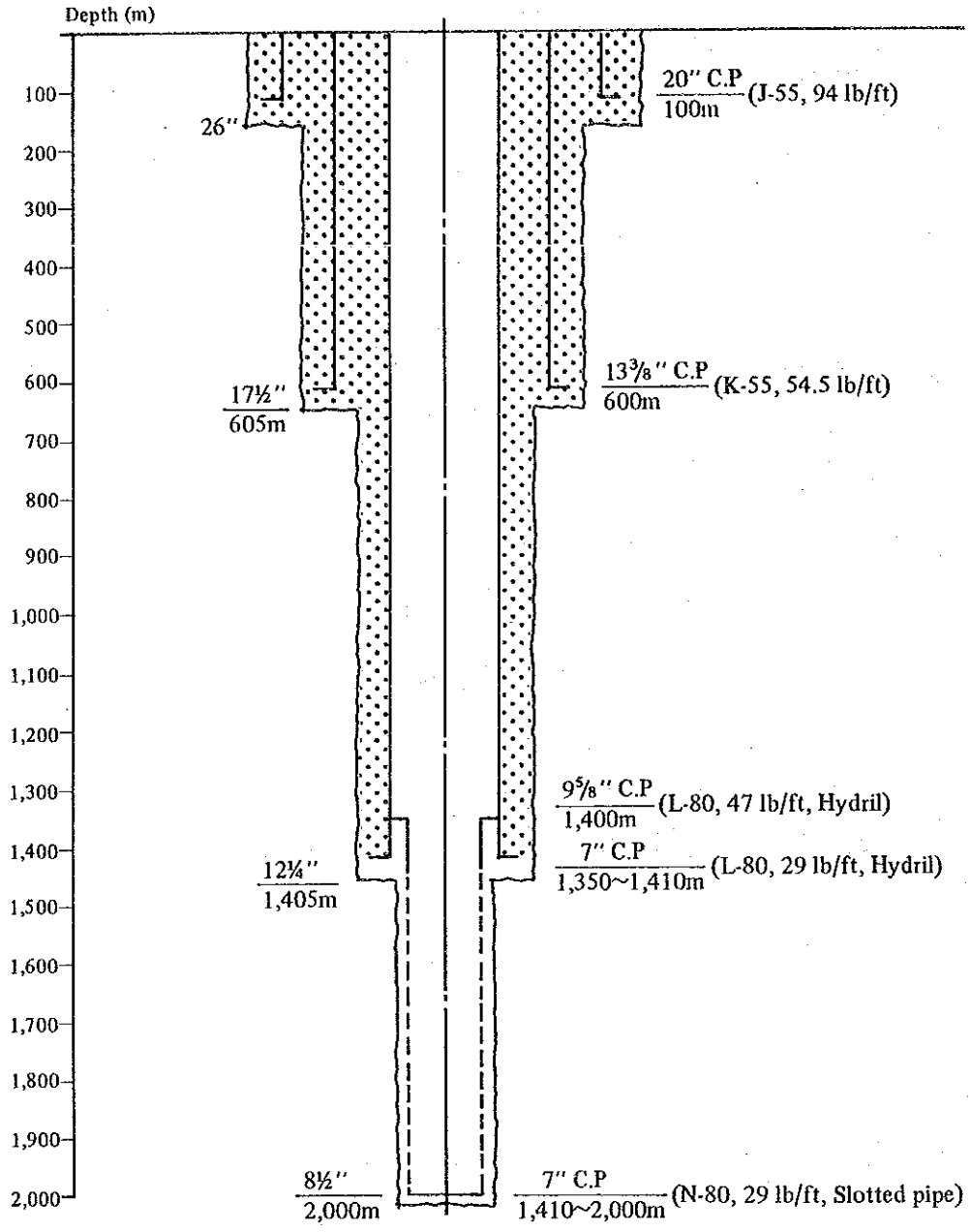

Fig. II. 3-7 Casing Program of PR-13

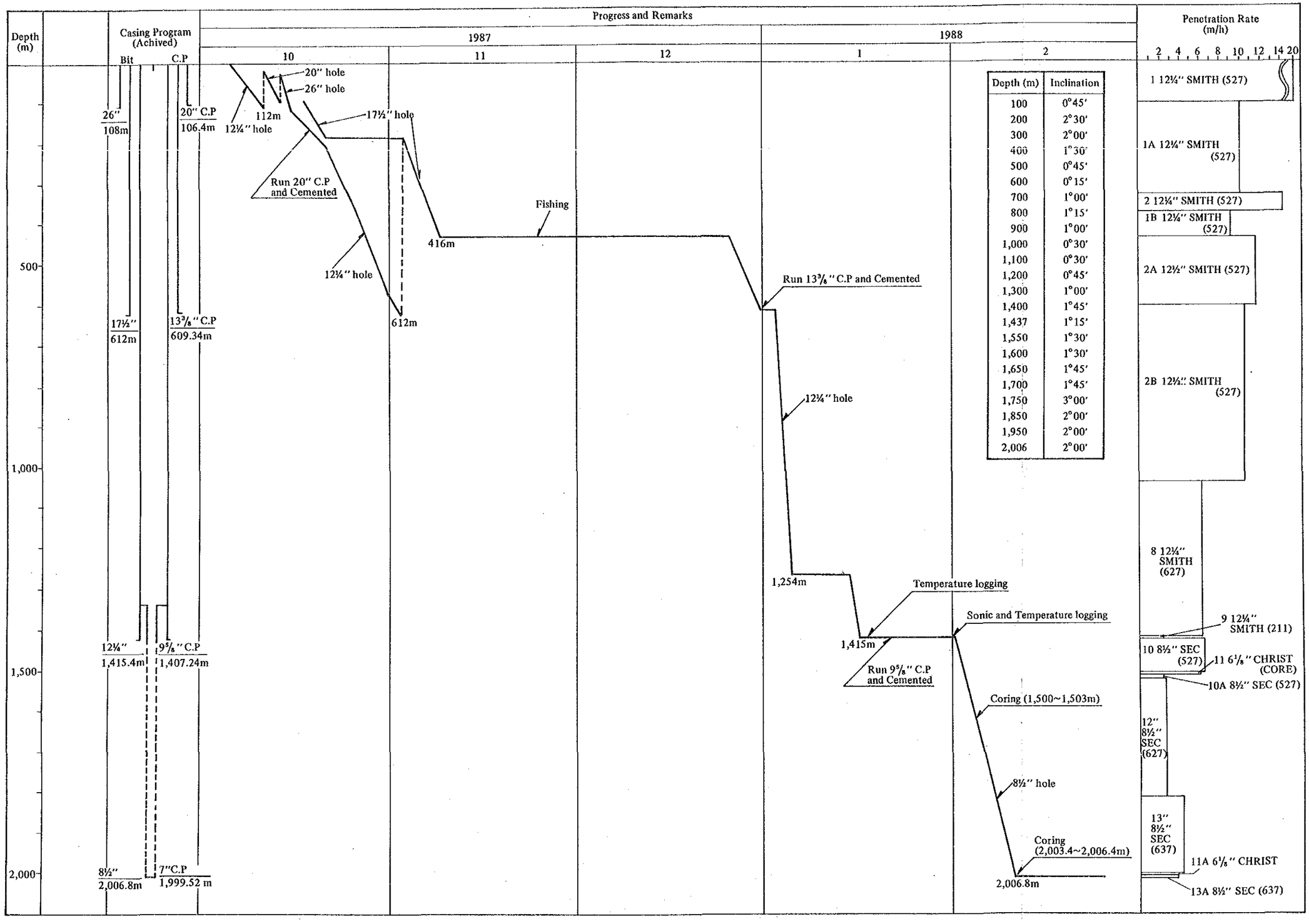

Fig. II. 3-8 Drilling History of PR-13

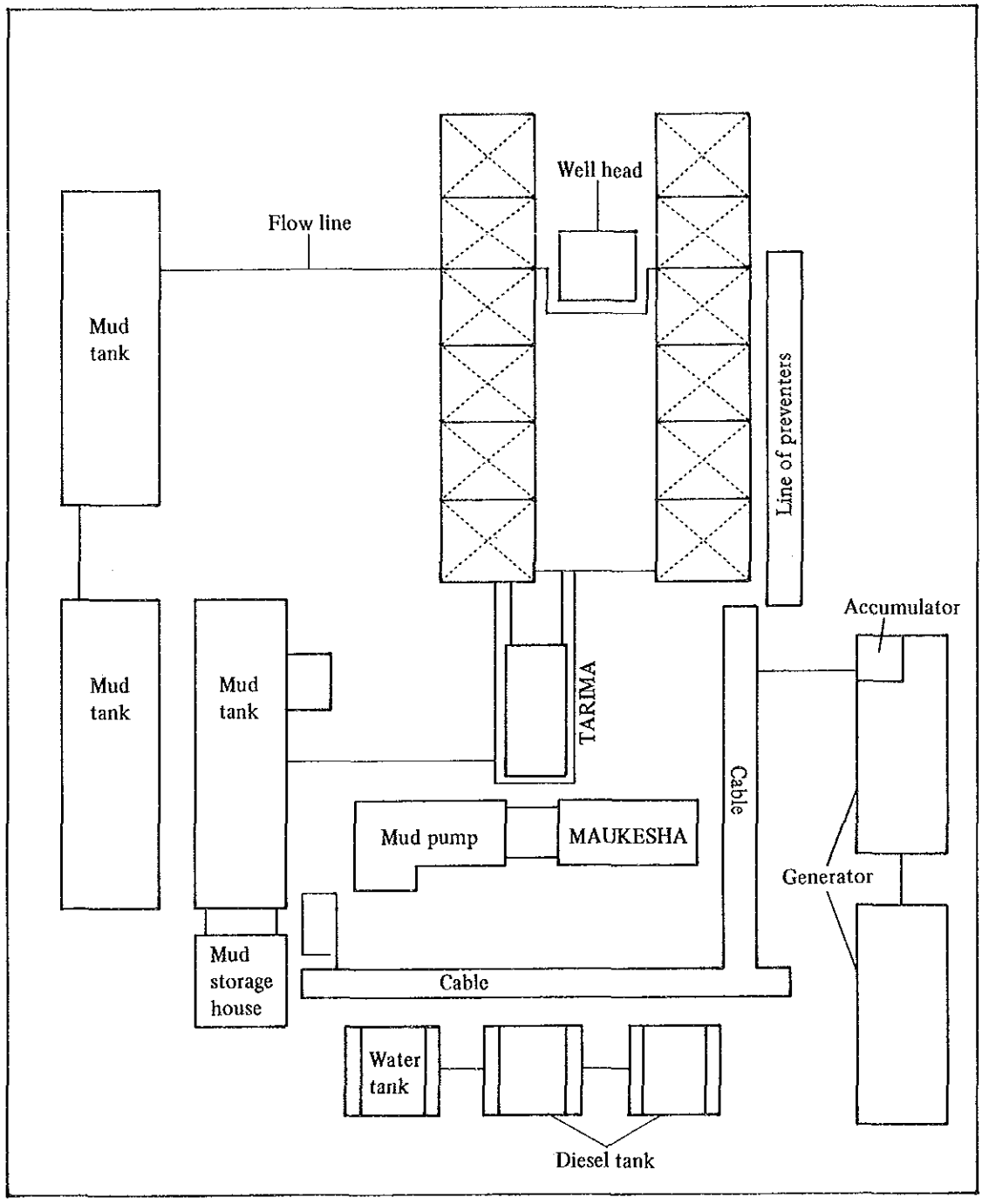

Fig. II. 3-9 Layout of Drilling Site of PR-13

Table II. 3-8 List of Major Drilling Materials of PR-13

Machine Item	*Sepecification*	*Quantity*
Draw Works	IDECO H-1200	1
Derick	IDECO 143-650, Max. hook load 750,000 lbs	1
Crown Block	IDECO 143-FV, Max. hook load 570 t	1
Rotary Table	IDECO 275-K 27½", Max. hook load 570t	1
Swivel	IDECO TL-400, 400t	1
Traveling Block	IDECO UTE-360-5-50, 350t	1
Engine	Draw Works ~ WAUKESHA L-5792-DU 1,023 HP Mud Pump ~ WAUKESHA L-5792-DU 1,023 HP	1 2
Mud Pump	IDECO T-800, TRIPLEX	
Accumulator	KOOMEY 090-11-S SN-1264	
Generator	CATERPILLAR T-3406 P.C 300 H.P. Motor Generator ~ SR-4 48 BH 200 kW	
Compressor	INGERSOLL RAND 71T2 30T 474687 INGERSOLL RAND 40-B	1 1
Tank	Mud Tank 60 kℓ Water 40 kℓ	3 2
Centrifugal Pump	Mission 3" x 4" 25HP SENTINEL C-380 Mission 5" x 6" 50HP Mission 5" x 6" 60HP	2 2 1 1
Shale Shaker Desander Desilter	SWACO SUPER SCREEN SWACO 212-455 SWACO 8T425	1 1 1
Agitator	LIGNTNIN LM-616/80	5
B.O.P	CAMERON DOUBLE 13⅜" -5,000 psi "U" CAMERON SINGLE 13⅜" -5,000 psi "D" Hydril M.S.P Bug type 21¼" -2,000 psi	1 1 1
Kelly	VARCO HEXAGONAL 5¼" x 40'	1
Drill Collar	8" OD – $2^{13}/_{16}$"ϕ ID 30' 8" OD – $2^{13}/_{16}$"ϕ ID 10' 6½" OD – $2^{13}/_{16}$"ϕ ID 30' 6½" OD – $2^{13}/_{16}$"ϕ ID 10'	15 1 24 1
HWDP Drill Pipe	4½" OD 4½" x H GRADO "E" "S"	6

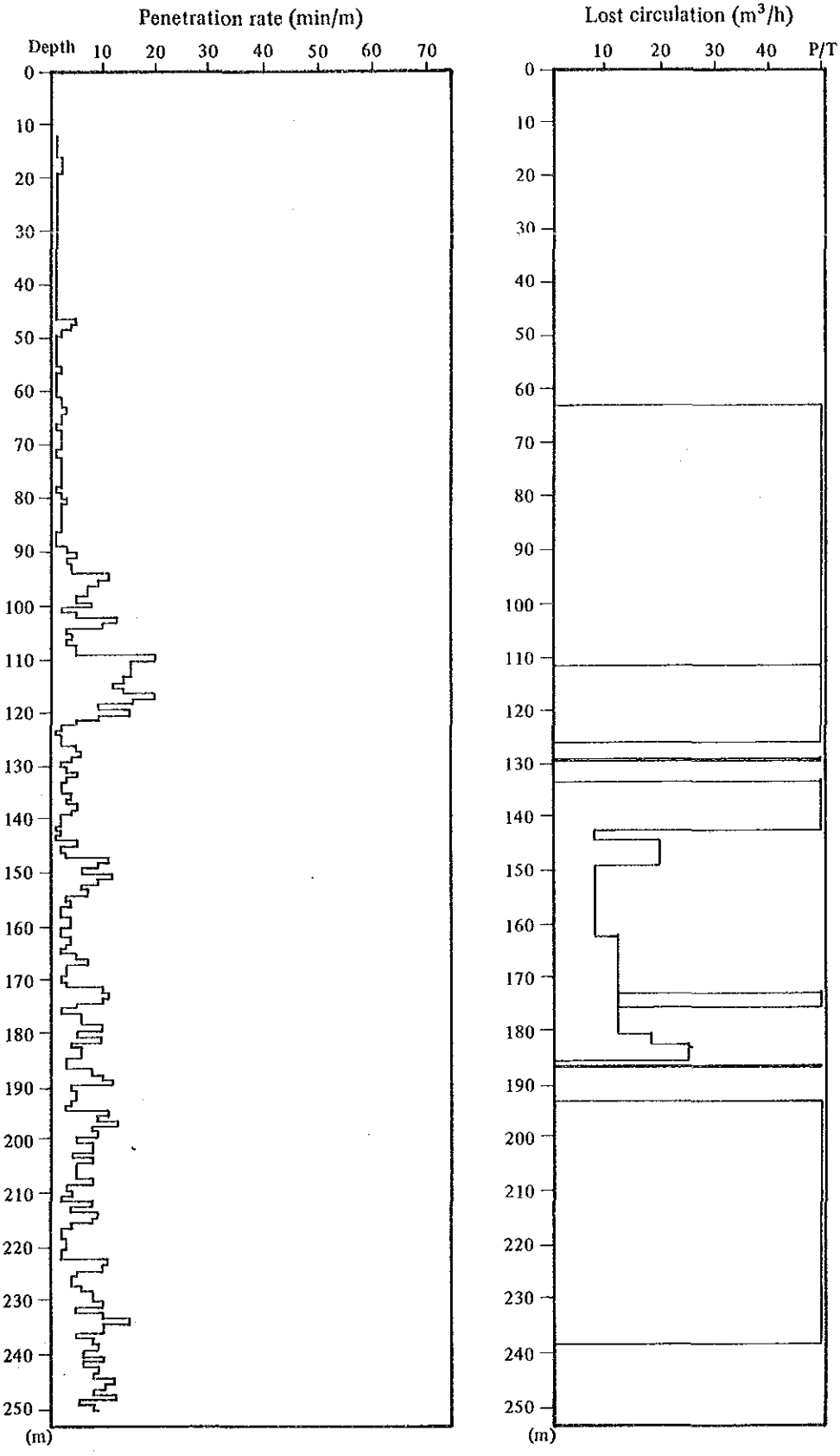

Fig. II. 3-10 Record of Penetration Rate and Lost Circulation of PR-13 (1)

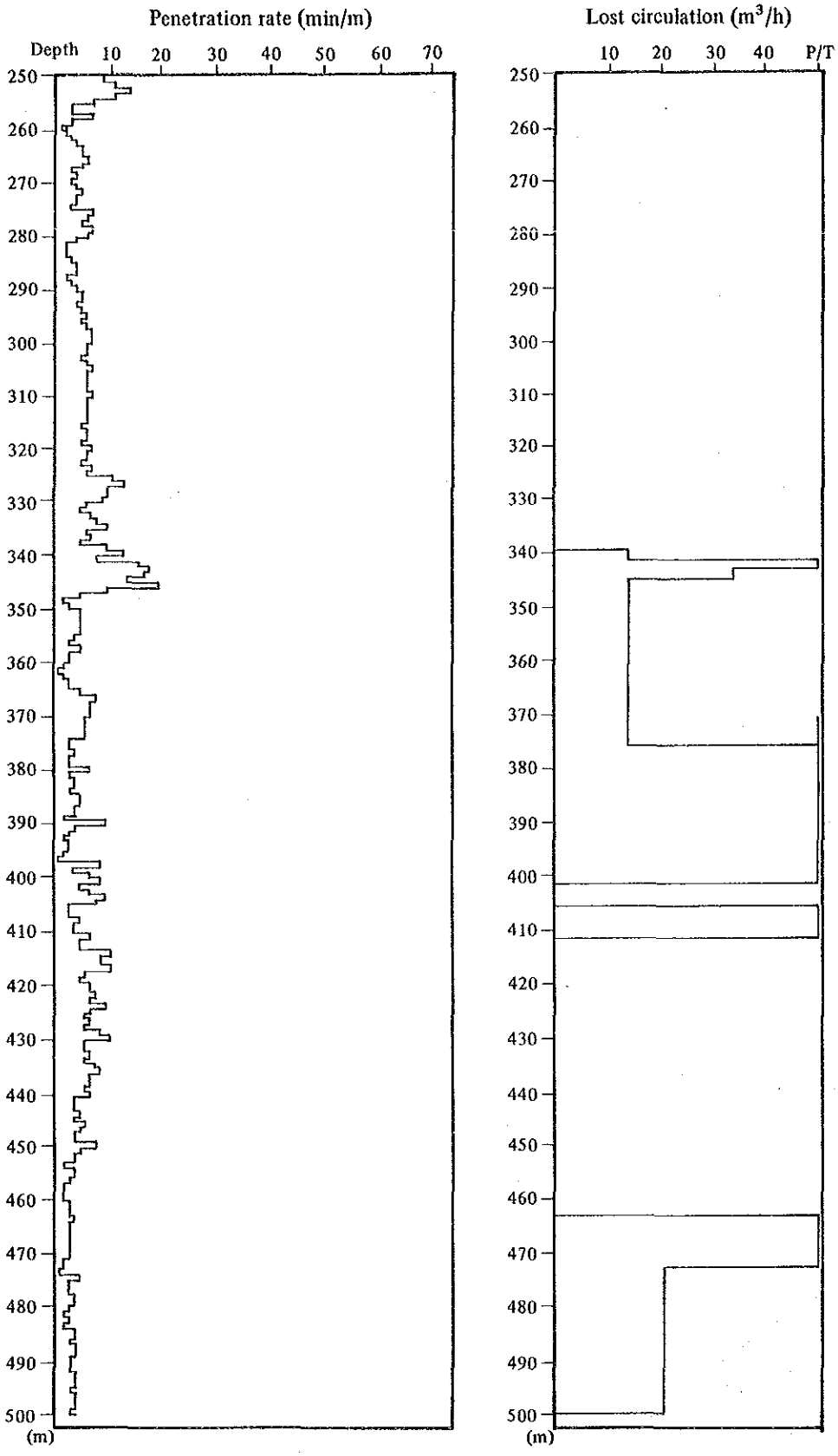

Fig. II. 3-10 Record of Penetration Rate and Lost Circulation of PR-13 (2)

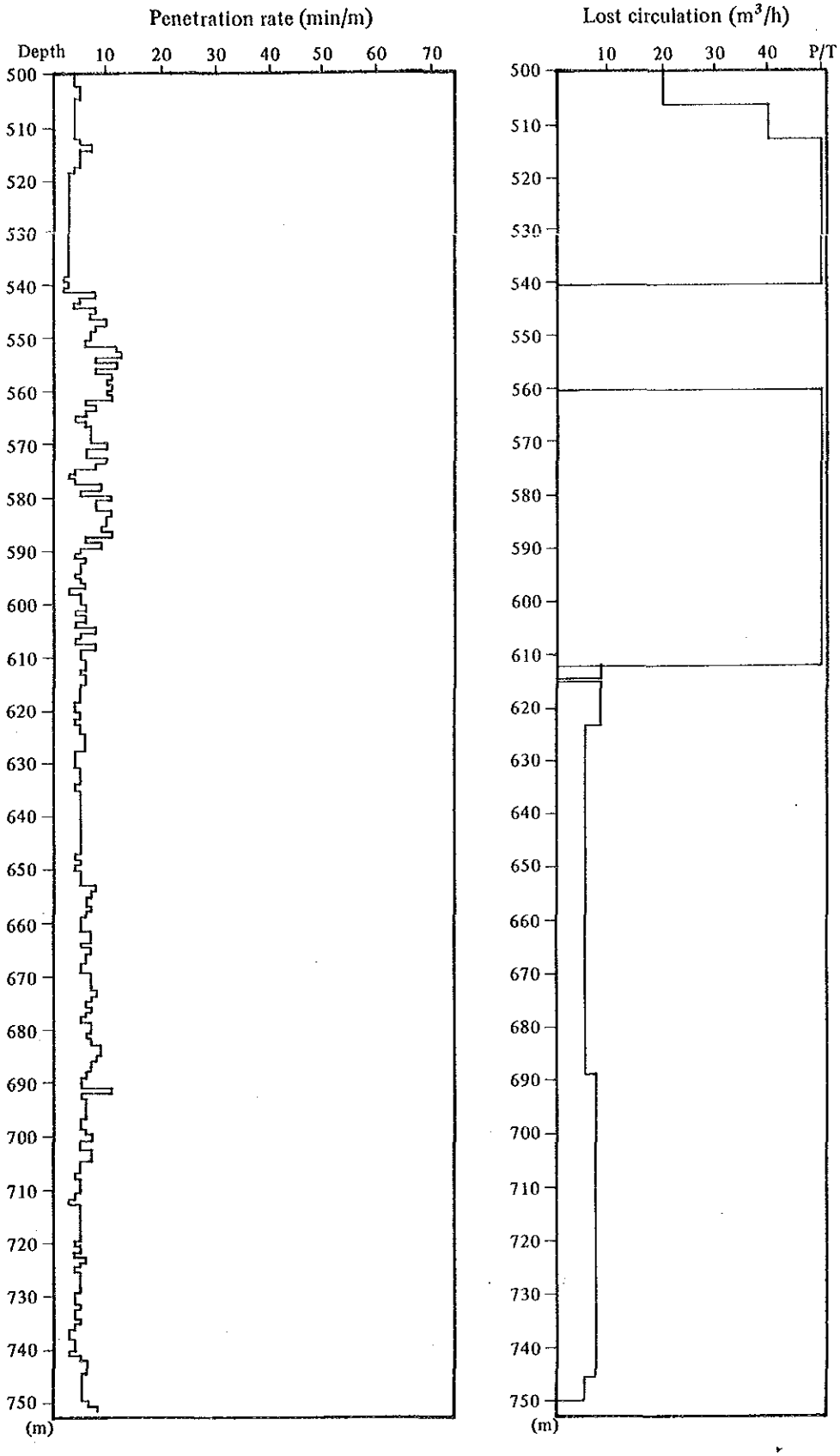

Fig. II. 3-10 Record of Penetration Rate and Lost Circulation of PR-13 (3)

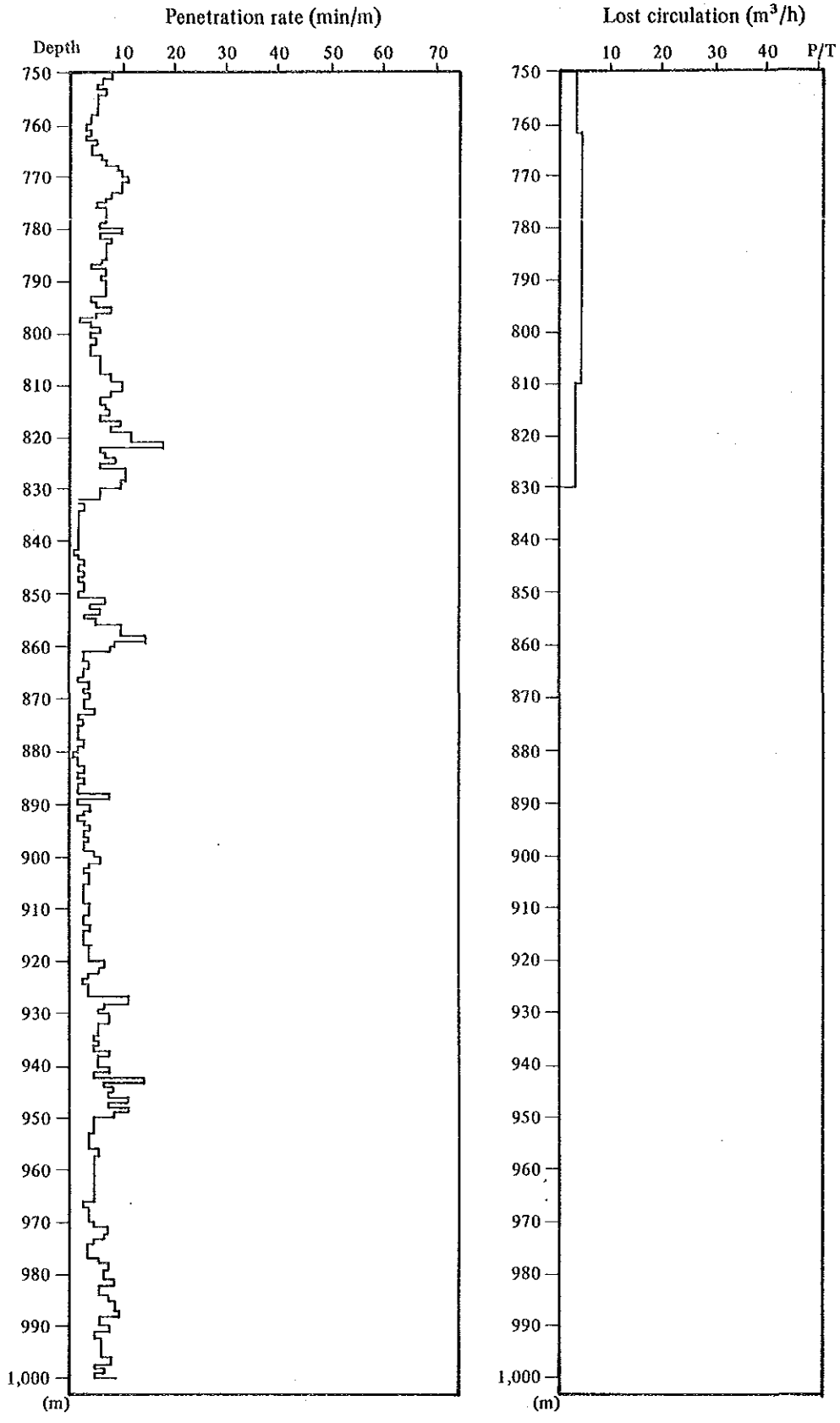

Fig. II. 3-10 Record of Penetration Rate and Lost Circulation of PR-13 (4)

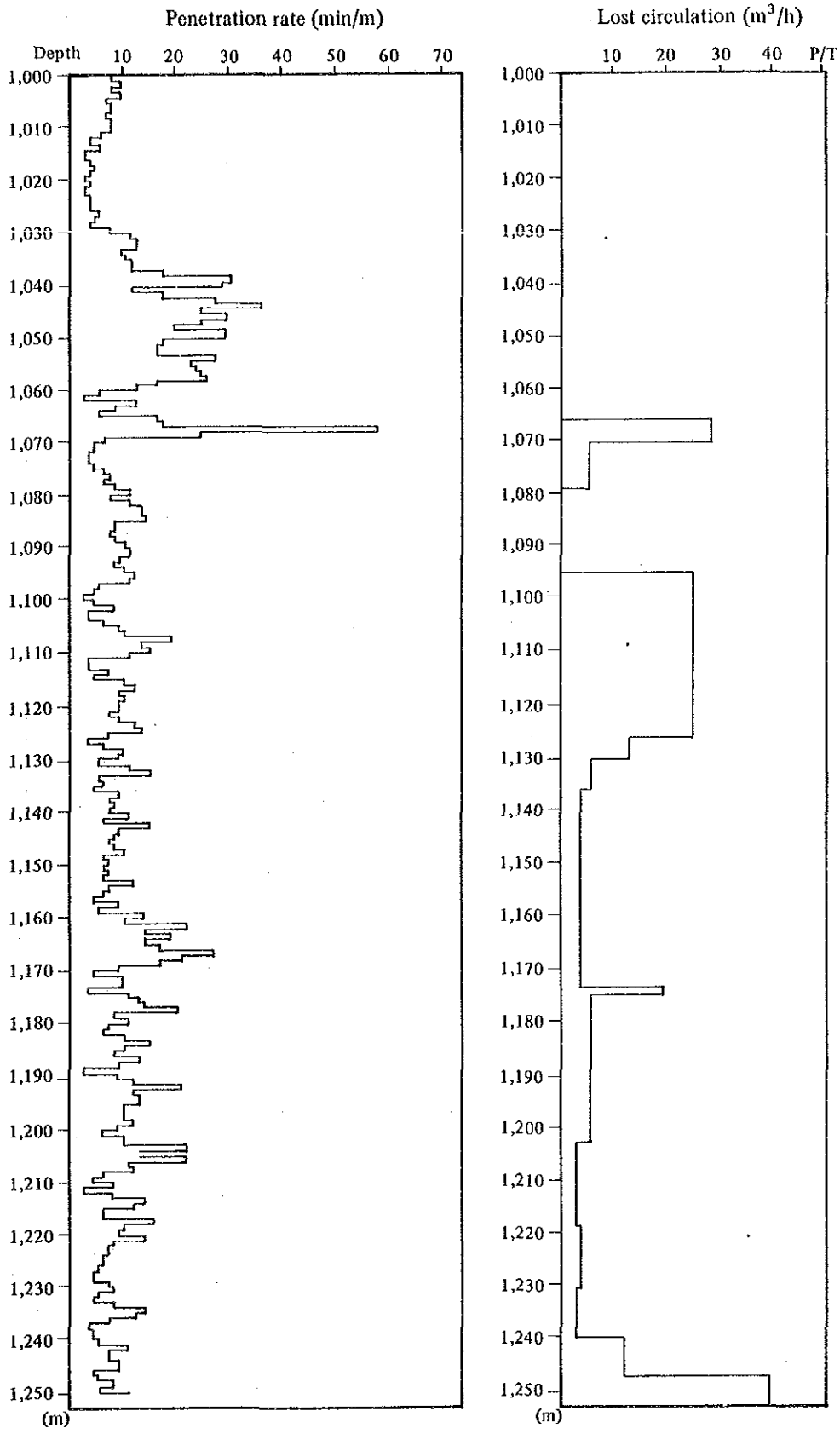

Fig. II. 3-10 Record of Penetration Rate and Lost Circulation of PR-13 (5)

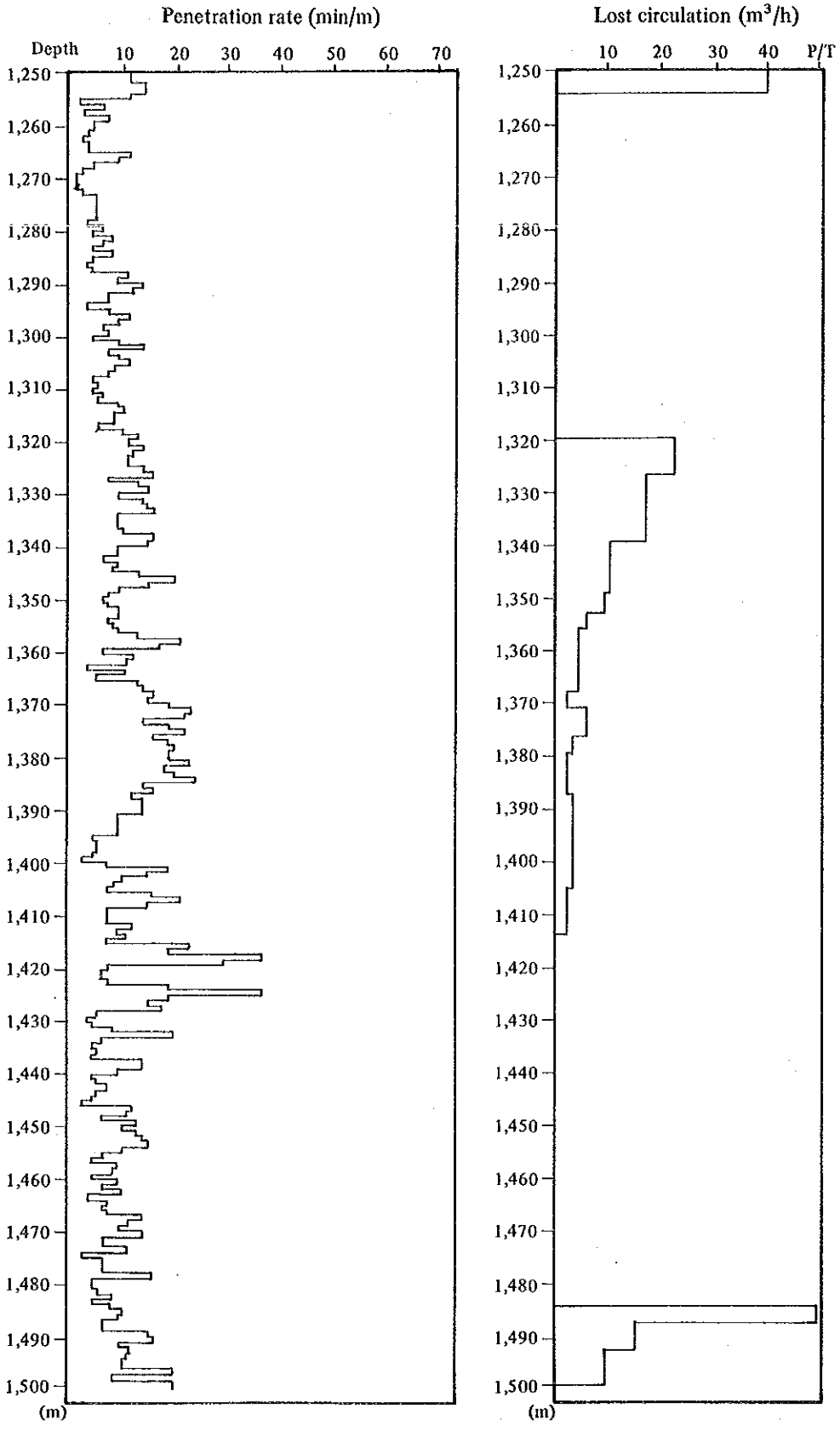

Fig. II. 3-10 Record of Penetration Rate and Lost Circulation of PR-13 (6)

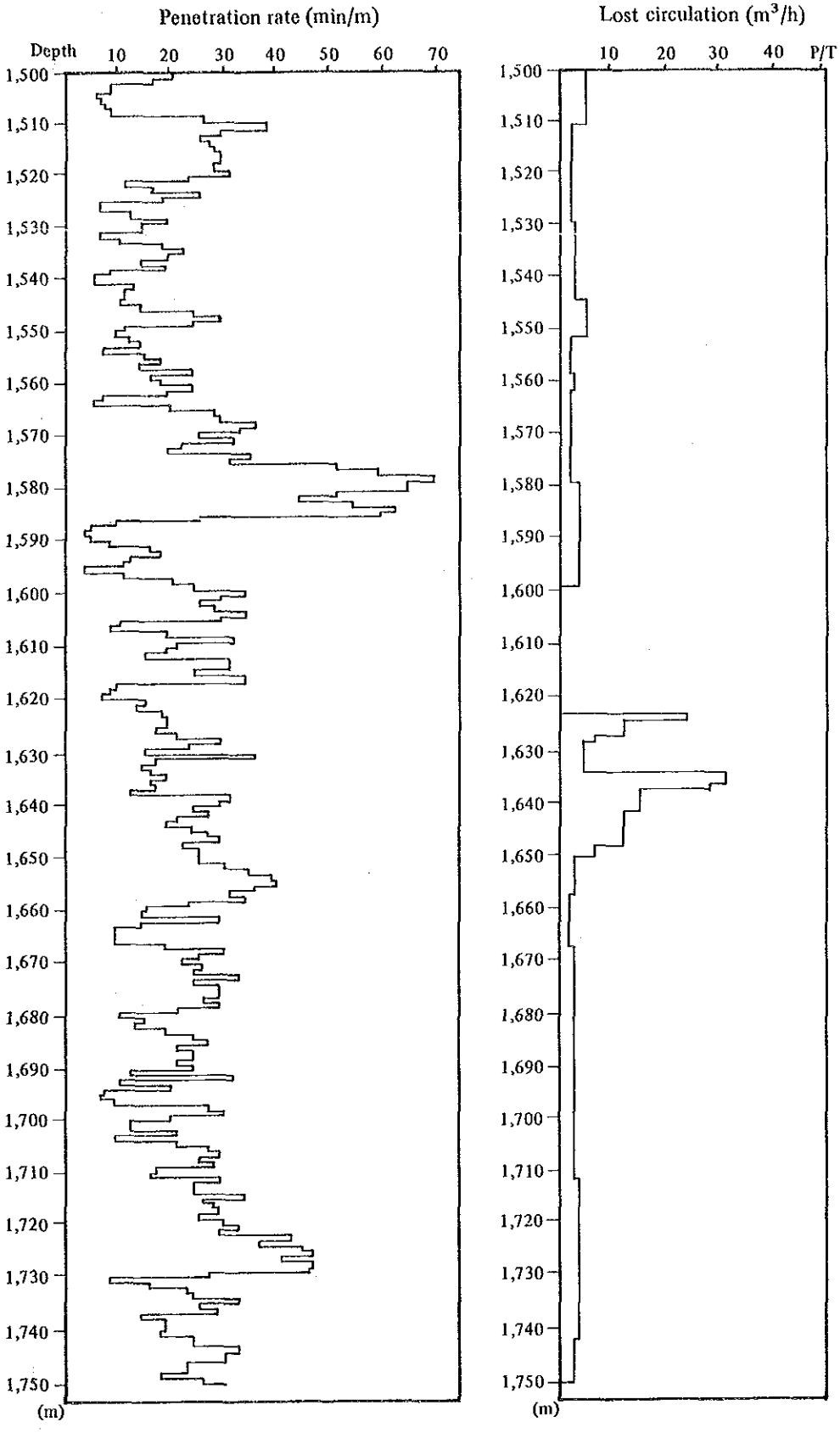

Fig. II. 3-10 Record of Penetration Rate and Lost Circulation of PR-13 (7)

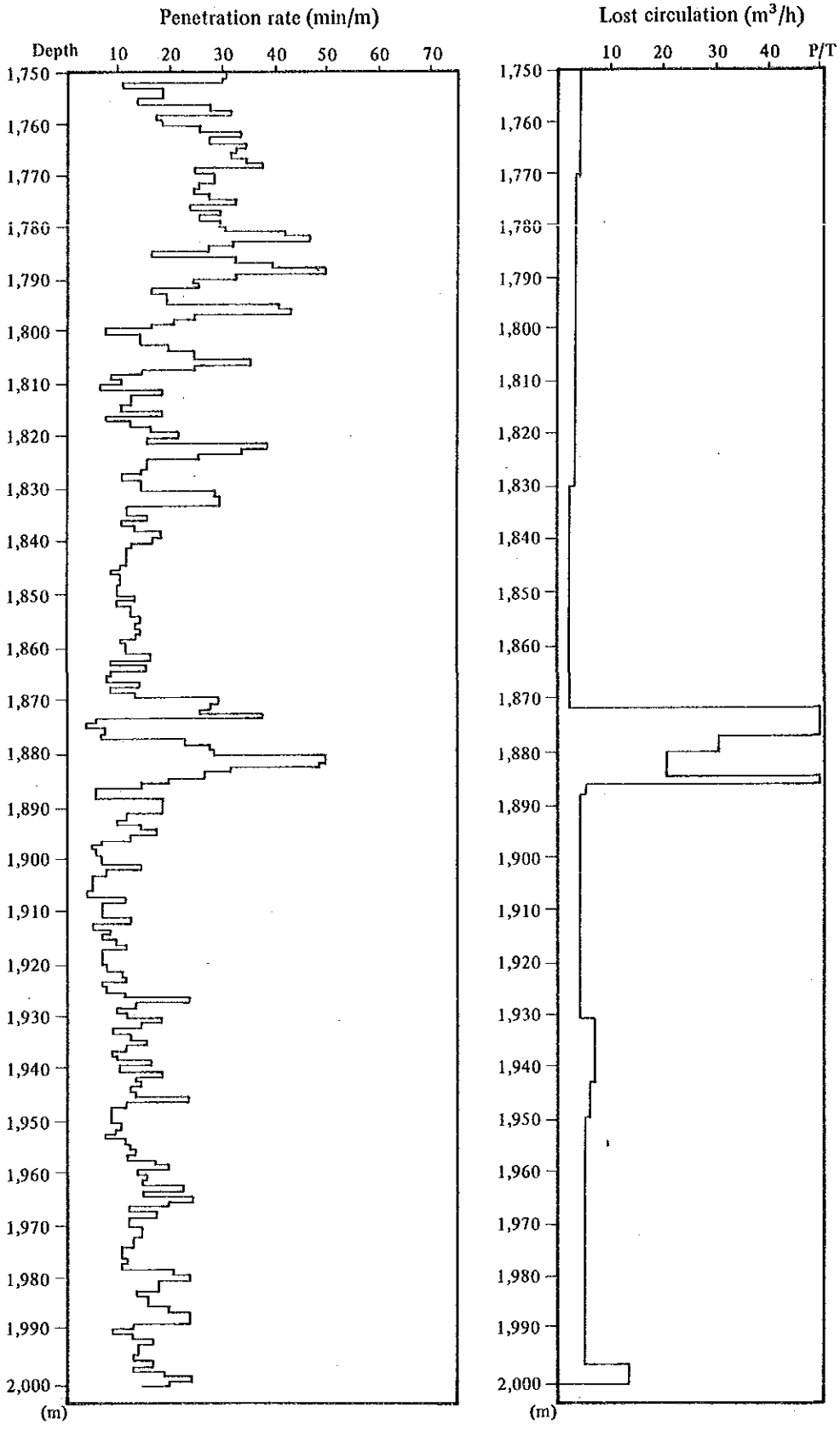

Fig. II. 3-10 Record of Penetration Rate and Lost Circulation of PR-13 (8)

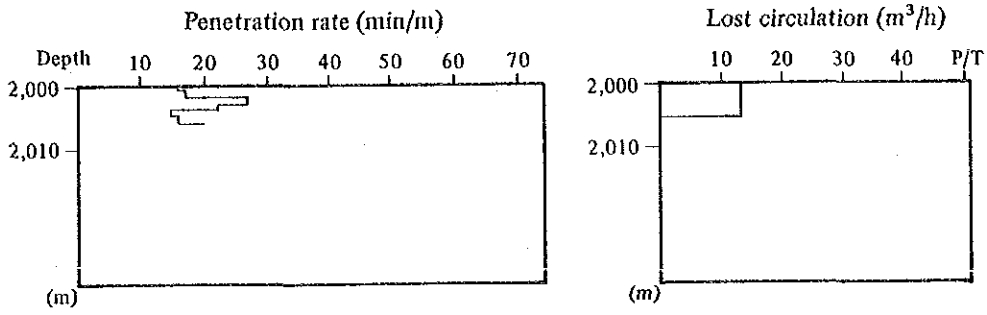

Fig. II. 3-10 Record of Penetration Rate and Lost Circulation of PR-13 (9)

Table II. 3-9 Records of Bits and Lost Circulation of PR-13

No.	Size	Drilling depth (m)	Drilling length (m)	Drilling time (h)	Penetration rate (m/h)	Bit weight (t)	Revolutions/min (RPM)	Pump			Mud water			Remarks
								LS	Pressure (kg/cm²G)	L/M	SG	P.V	Sand	
1	12¼"	12 ~ 112	100	4.51	20.6	6	60		17.5		1	Water		
	20"	12 ~ 109	97	8.30	11.4	5	60			1,174	1	Water		
	26"	12 ~ 108	96	9.57	9.6	5	60			1,174	1	Water		
1A	12¼"	112 ~ 345	233	24.37	9.4	6/8	60	6½" x 126	35	1,850	1.09	47	38/42	
	17½"	Drilling out cement									1	Water		
	17½"	109 ~ 416	307	27.47	11.0	4/5				1,175	1	Water		
2	12¼"	345 ~ 388	43	3.08	13.7	12	60	6½"x 803 PM	35	1,174	1.07	42		
1B		388 ~ 439	51	5.45	8.9	7	65	126	42	1,174	1.08	46	48/52	
2A		439 ~ 612	173	14.27	11.9	7	65	126	42.5	1,174	1.08	40	59/60	
	17½"	416 ~ 612									1.05	43		
3	17½"	Drilling out cement												
4	17½"													
5	17½"													
6	17½"													
7	12¼"													
2B	12¼"	612 ~ 1,043	431	42.11	10.21	10	60	6½" x 130	63	1,908	1.09	45	46/58	
8	12¼"	1,043 ~ 1,415	372	69.32	5.35	10/15	60	6½" x 126	77	1,849	1.08	44	45/55	
9	8½"	1,415 ~ 1,418	3	1.22	2.19	5	60	6½" x 90	14	1,321	1.07	42	45/63	
10	8½"	1,418 ~ 1,500	82	14.48	5.54	6/7	65	6½" x 85	70	1,247	1.08	47	44/56	
11	6⅛"	1,500 ~ 1,503	3	0.35	5.14	4	60	6½" x 80	28	1,174	1.07	40	44/56	Core recovery 100%
10A	8½ "	1,503 ~ 1,519	16	6.48	2.35	6/8	65	5½" x 110	14	1,153	1.07	40	44/56	
12	8½ "	1,519 ~ 1,795	276	113.11	2.44	5/10	65	6½" x 80	38	1,174	1.09	45	46/60	
13	8½ "	1,795~2,003.40	208.40	52.18	3.98	6/7	65	6½" x 80	24	1,174			59/65	
11A	6⅛"	2,003.40~2,006.40	3	0.51	3.53	4	60	6½" x 80	24	1,174			59/65	Core recovery 85%
13A	8½ "	2,003.40~2,006.80	3.40	0.35	1.98		65	6½" x 80	38	1,174			59/65	

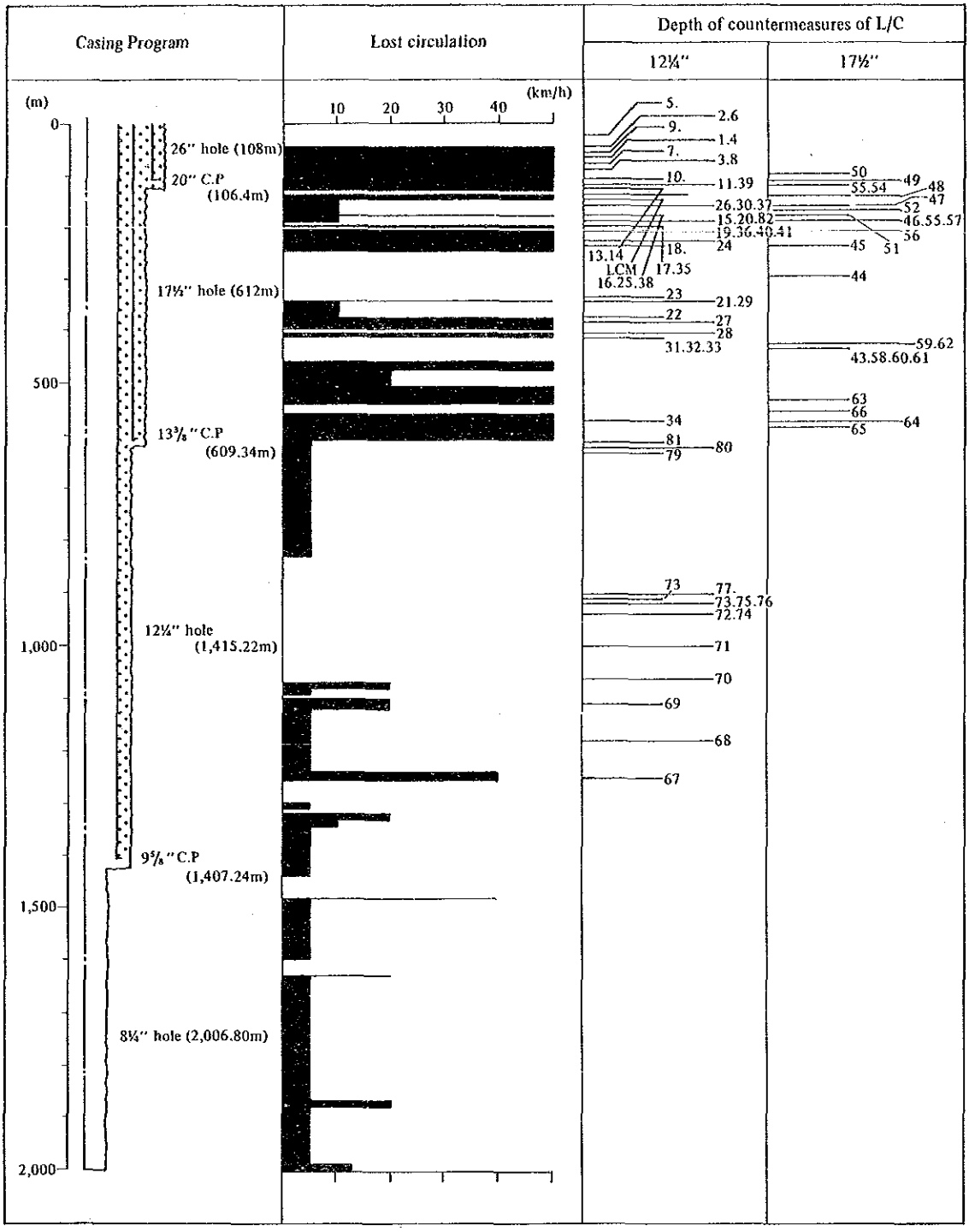

Fig. II. 3-11 Depth of Lost Circulation and Treatments of L/C for PR-13

Table II. 3-10 Measuring of 20" Casing Pipe of PR-13

No.	Length	Total length	Depth*	Remark
			106.40	94 lb/ft. H-40
C/S	1.20	1.20	105.20	94 lb/ft. H-40
1	12.82	14.02	92.38	94 lb/ft. H-40
2	12.22	26.24	80.16	94 lb/ft. H-40
3	12.17	38.41	67.99	94 lb/ft. H-40
4	12.18	50.59	55.81	94 lb/ft. H-40
5	11.80	62.39	44.01	94 lb/ft. H-40
6	11.43	73.82	32.58	94 lb/ft. H-40
7	12.28	86.10	20.30	94 lb/ft. H-40
8	12.73	98.83	7.57	94 lb/ft. H-40
9	12.20	111.03	- 4.63	94 lb/ft. H-40

* Depth of Casing is from Rotary table. G.L from Rotary table is 6.4 m.

Table II. 3-11 Measuring of 13 3/8" Casing Pipe of PR-13

(Pipe 54.5 lb/ft, K-55)

No.	Length (m)	Total length (m)	Depth* (m)	Centra lizer	No.	Length (m)	Total length (m)	Depth* (m)	Centra lizer
			609.94		24	13.24	299.26	310.68	1
C/S	0.43	0.43	609.51		25	12.77	312.03	297.91	
1	12.02	12.45	597.49	2	26	13.81	325.84	284.10	1
2	10.60	23.05	586.89	1	27	11.88	337.72	272.22	
C/C	0.55	23.60	586.34		28	13.06	350.78	259.16	1
3	11.56	35.16	574.78		29	14.28	365.06	244.88	
4	11.88	47.04	562.90	1	30	13.25	378.31	231.63	1
5	11.75	58.79	551.15		31	11.30	389.61	220.33	
6	12.05	70.84	539.10	1	32	12.93	402.54	207.40	1
7	13.44	84.28	525.66		33	11.48	414.02	195.92	
8	12.08	96.36	513.58	1	34	11.03	425.05	184.89	1
9	11.75	108.11	501.83		35	13.50	438.55	171.39	
10	13.81	121.92	488.02	1	36	13.78	452.33	157.61	1
11	11.86	133.78	476.16		37	12.20	464.53	145.41	
12	12.78	146.56	463.38	1	38	12.03	476.56	133.38	1
13	12.05	158.61	451.33		39	13.21	489.77	120.17	
14	12.17	170.78	439.16	1	40	12.51	502.28	107.66	1
15	14.11	184.89	425.05		41	11.04	513.32	96.62	
16	12.08	196.97	412.97	1	42	11.38	524.70	85.24	1
17	13.09	210.06	399.98		43	12.22	536.92	73.02	
18	13.32	223.38	386.56	1	44	12.09	549.01	60.93	1
19	13.21	236.59	373.35		45	13.31	562.32	47.62	
20	11.03	247.62	362.32	1	46	12.48	574.80	35.14	1
21	12.76	260.38	349.56		47	13.28	588.08	21.86	
22	13.15	273.53	336.41	1	48	14.46	602.54	7.40	1
23	12.49	286.02	323.92			7.40	609.94	0.00	

* Depth is from Rotary table. Depth from surface is substract 6.4 m from it.

Table II. 3-12 Measuring of 9 5/8" Casing Pipe of PR-13

(47 pd/ft, L-80 Hydril, SEU)

No.	Length (m)	Total length (m)	*Depth from rotary table (m)	Centra lizer	No.	Length (m)	Total length (m)	*Depth from rotary table (m)	Centra lizer
			1,407.24		24	12.34	291.68	1,115.56	1
C/S	0.35	0.35	1,406.89		25	11.81	303.49	1,103.75	
1	11.34	11.69	1,395.55	2	26	10.99	314.48	1,092.76	1
2	12.25	23.94	1,383.30	1	27	12.14	326.62	1,080.62	
C/C	0.47	24.41	1,382.83		28	12.23	333.85	1,068.39	1
3	12.77	37.18	1,370.06		29	9.30	348.15	1,059.09	
4	13.39	50.57	1,356.67	1	30	11.05	359.20	1,048.04	1
5	11.28	61.85	1,345.39		31	12.47	371.67	1,035.57	
6	11.02	72.87	1,334.37	1	32	11.07	382.74	1,024.50	1
7	13.09	85.96	1,321.28		33	12.78	395.52	1,011.72	
8	12.65	98.61	1,308.63	1	34	12.44	407.96	999.28	1
9	12.26	110.87	1,296.37		35	13.52	421.48	985.76	
10	12.34	123.21	1,284.03	1	36	12.32	433.80	973.44	1
11	13.49	136.70	1,270.54		37	13.10	446.90	960.34	
12	11.29	147.99	1,259.25	1	38	12.36	459.26	947.98	1
13	11.42	159.41	1,247.83		39	13.13	472.39	934.85	
14	12.32	171.73	1,235.51	1	40	13.06	485.45	921.79	1
15	11.94	183.67	1,223.57		41	12.67	498.12	909.12	
16	12.56	196.23	1,211.01	1	42	13.41	511.53	895.71	1
17	12.85	209.08	1,198.16		43	11.47	523.00	884.24	
18	10.85	219.93	1,187.31	1	44	12.69	535.69	871.55	1
19	11.82	231.75	1,175.49		45	12.83	548.52	858.72	
20	12.40	244.15	1,163.09	1	46	11.67	560.19	847.05	1
21	12.75	256.90	1,150.34		47	12.13	572.32	834.92	
22	10.33	267.33	1,140.01	1	48	11.60	583.92	823.32	1
23	12.11	279.34	1,127.90		49	12.48	596.40	810.84	

* It's 6.4 m from Rotary table to surface.

No.	Length (m)	Total length (m)	*Depth from rotary table (m)	Centra lizer	No.	Length (m)	Total length (m)	*Depth from rotary table (m)	Centra lizer
50	12.82	609.22	798.02	1	75	13.10	913.38	493.86	
51	9.15	618.37	788.87		76	11.55	924.93	482.31	1
52	12.19	630.56	776.68	1	77	12.31	937.24	470.00	
C/M	0.84	631.40	775.84		78	9.57	946.81	460.43	1
53	13.10	644.50	762.74		79	12.04	958.85	448.39	
54	12.60	657.10	750.14	1	80	11.93	970.78	436.46	1
55	12.23	669.33	737.91		81	13.43	984.21	423.03	
56	12.01	681.34	725.90	1	82	12.44	996.65	410.59	1
57	11.75	693.09	714.15		83	10.92	1,007.57	399.67	
58	12.26	705.35	701.89	1	84	13.30	1,020.87	386.37	1
59	12.96	718.31	688.93		85	12.67	1,033.54	373.70	
60	12.00	730.31	676.93	1	86	10.91	1,044.45	362.79	1
61	11.80	742.11	665.13		87	13.42	1,057.87	349.37	
62	12.21	754.32	652.92	1	88	12.68	1,070.55	336.69	1
63	12.62	766.94	640.30		89	12.92	1,083.47	323.77	
64	12.06	779.00	628.24	1	90	11.46	1,094.93	312.31	1
65	12.35	791.35	615.89		91	12.12	1,107.05	300.19	
66	11.42	802.77	604.47	1	92	12.99	1,120.04	287.20	1
67	11.76	814.53	592.71		93	11.84	1,131.88	275.36	
68	12.65	827.18	580.06	1	94	12.26	1,144.14	263.10	1
69	10.24	837.42	569.82		95	13.24	1,157.38	249.86	
70	12.51	849.93	557.31	1	96	12.51	1,169.89	237.35	1
71	12.26	862.19	545.05		97	13.02	1,182.91	224.33	
72	11.75	873.94	533.30	1	98	9.17	1,192.08	215.16	1
73	13.00	886.94	520.30		99	12.72	1,204.80	202.44	
74	13.34	900.28	506.96	1	100	11.64	1,216.44	190.80	1

No.	Length (m)	Total length (m)	*Depth from rotary table (m)	Centra lizer	No.	Length (m)	Total length (m)	*Depth from rotary table (m)	Centra lizer
101	12.60	1,229.04	178.20						
102	11.97	1,241.01	166.23	1					
103	10.43	1,251.44	155.80						
104	11.44	1,262.88	144.36	1					
105	12.67	1,275.55	131.69						
106	12.38	1,287.93	119.31	1					
107	12.80	1,300.73	106.51						
108	12.41	1,313.14	94.10	1					
109	12.50	1,325.64	81.60						
110	12.74	1,338.38	68.86	1					
111	12.97	1,351.35	55.89						
112	11.25	1,362.60	44.64	1					
113	13.05	1,375.65	31.59						
114	12.28	1,387.93	19.31	1					
115	12.91	1,400.84	6.40						
Rotory table	6.40 (11.50)	1,407.24	0.00						

Table II. 3-13 Measuring of 7" Casing pipe of PR-13

(Pipe: 29 lb/ft, L-80
Hydril, SEU)

No.	Length (m)	Total length (m)	Depth (m)	Centra lizer	No.	Length (m)	Total length (m)	Depth (m)	Centra lizer
			1,999.52		25	12.80	320.47	1,679.05	
C/S	0.34	0.34	1,999.18		26	12.86	333.33	1,666.19	
1	12.47	12.81	1,986.71		27	12.67	346.00	1,653.52	
2	12.79	25.60	1,973.92		28	12.91	358.91	1,640.61	
3	12.95	38.55	1,960.97		29	12.97	371.88	1,627.64	
4	12.85	51.40	1,948.12		30	12.89	384.77	1,614.75	
5	12.54	63.94	1,935.58		31	12.78	397.55	1,601.97	
6	12.88	76.82	1,922.70		32	13.32	410.87	1,588.65	
7	12.94	89.76	1,909.76		33	12.60	423.47	1,576.05	
8	12.66	102.42	1,897.10		34	12.78	436.25	1,563.27	
9	12.84	115.26	1,884.26		35	12.79	449.04	1,550.48	
10	12.72	127.98	1,871.54		36	13.47	462.51	1,537.01	
11	12.97	140.95	1,858.57		37	12.73	475.24	1,524.28	
12	12.94	153.89	1,845.63		38	12.79	488.03	1,511.49	
13	13.24	167.13	1,832.39		39	12.77	500.80	1,498.72	
14	13.11	180.24	1,819.28		40	13.10	513.90	1,485.62	
15	12.96	193.20	1,806.32		41	13.36	527.26	1,472.26	
16	13.10	206.30	1,793.22		42	12.58	539.84	1,459.68	
17	12.61	218.91	1,780.61		43	13.16	553.00	1,446.52	
18	12.86	231.77	1,767.75		44	12.47	565.47	1,434.05	
19	13.03	244.80	1,754.72		45	12.74	578.21	1,421.31	
20	12.67	257.47	1,742.05		46	12.59	590.80	1,408,72	
21	12.01	269.48	1,730.04		47	12.96	603.76	1,395.76	
22	12.98	282.46	1,717.06		48	12.98	616.74	1,382.78	
23	12.61	295.07	1,704.45		49	13.00	629.74	1,369.78	
24	12.60	307.67	1,691.85		50	12.62	642.36	1,357.16	
					Liner hanger	3.41	645.77	1,353.75	

(Note) No. 1 ~ 42 Slotted pipe
No. 43 ~ 50 Casing

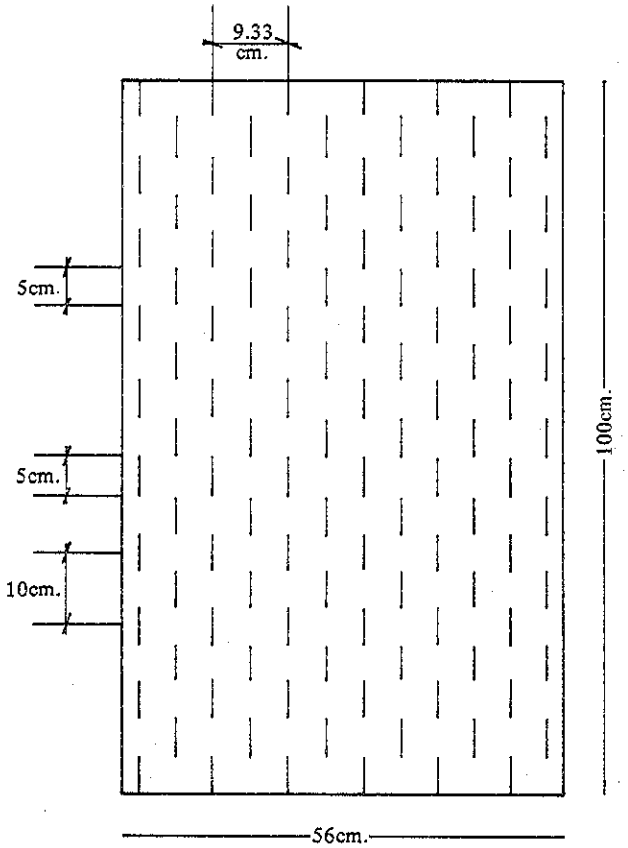

Largo de la ranura 2.0" (5cm.)
Ancho de la ranura 0.250" (0.635cm.)
10 Ranuras por metro longitudinal
12 Linoas de ranuras an al diametro de tubo de 7" a 9.3cm. c/u.
Número de ranuras por metro 114
Area de infiltración por metro de tubo
A = L x A
= 2" x 0.250" = 5 x 0.635 = 3.1cm.
= 3.1cm. x 114 ranuras = 353cm.^{2}
353cm.^{2} = 6%

Fig. II. 3-12 7" Slotted Pipe

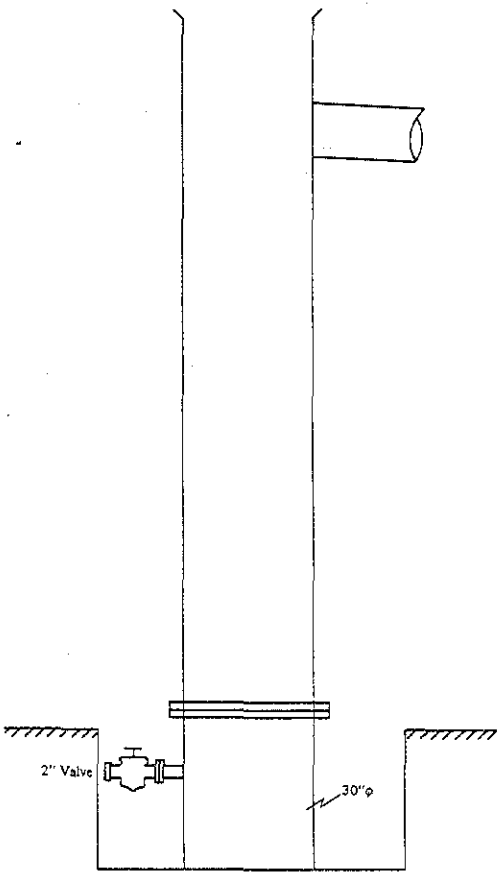

Fig. II. 3-13 Well head Stacks of PR-13 (1)

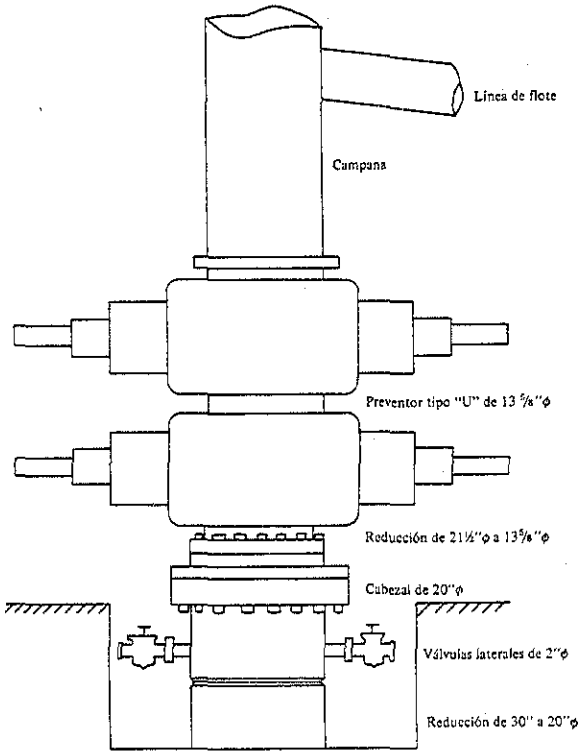

1. – Instalaciones superficiales para la 1ra. etapa (con barrena de 12¼"φ.)

Fig. II. 3-13 Well head Stacks of PR-13 (2)

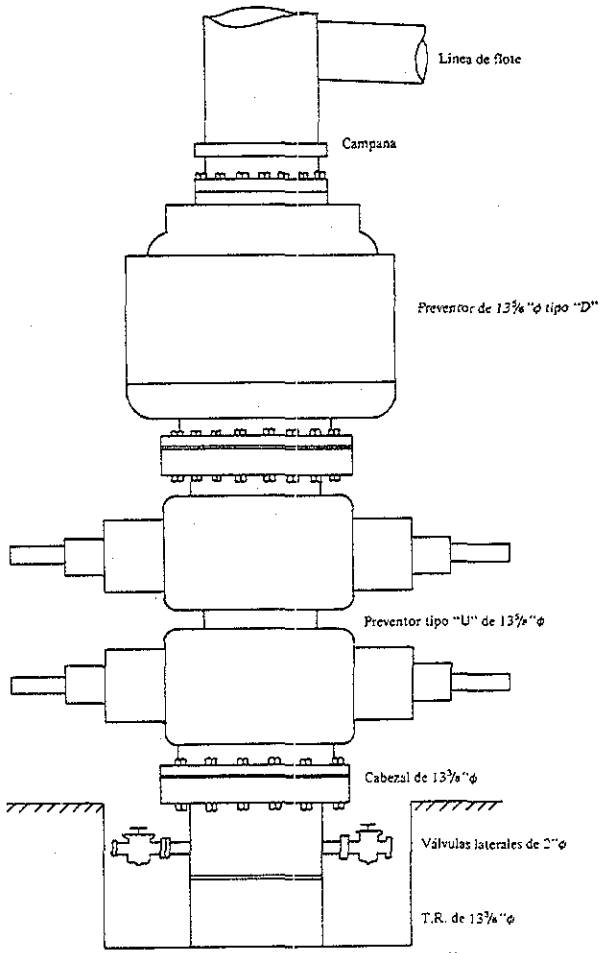

3. – Instalaciones superficiales para la 3ra. etapa. (con barrena de 12¼"φ.)

Fig. II. 3-13 Well head Stacks of PR-13 (3)

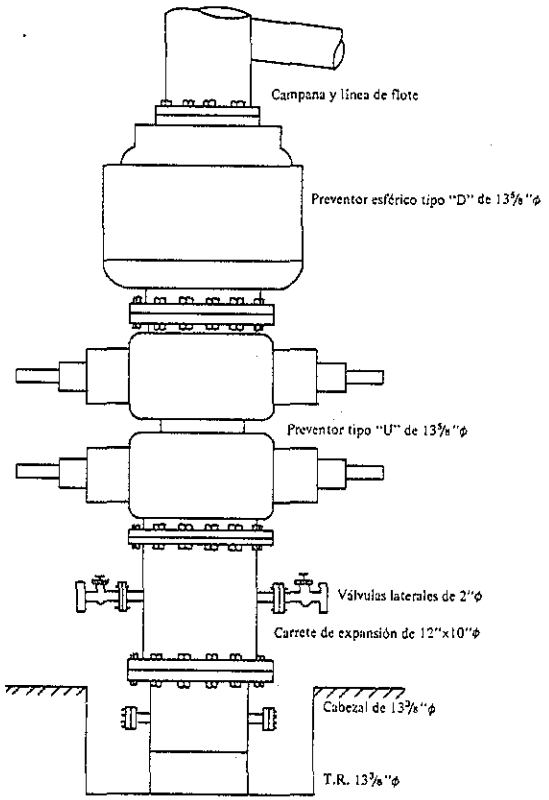

4. – Instalaciones superficiales para la 4a. etapa (con barrena de 8½"ϕ.)

Fig. II. 3-13 Well head Stacks of PR-13 (4)

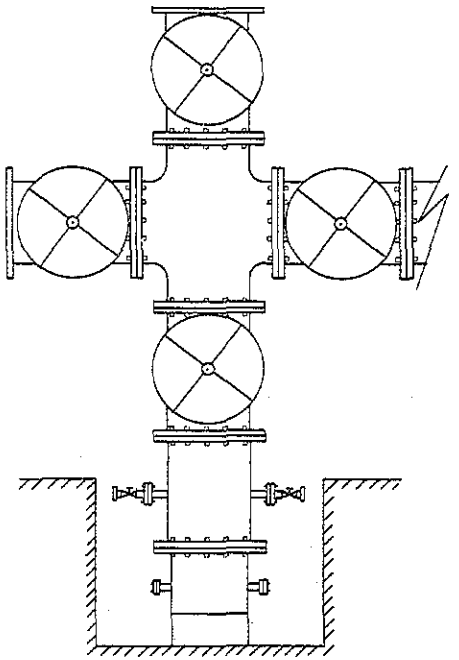

Fig. II. 3-13 Well head Stacks of PR-13 (5)

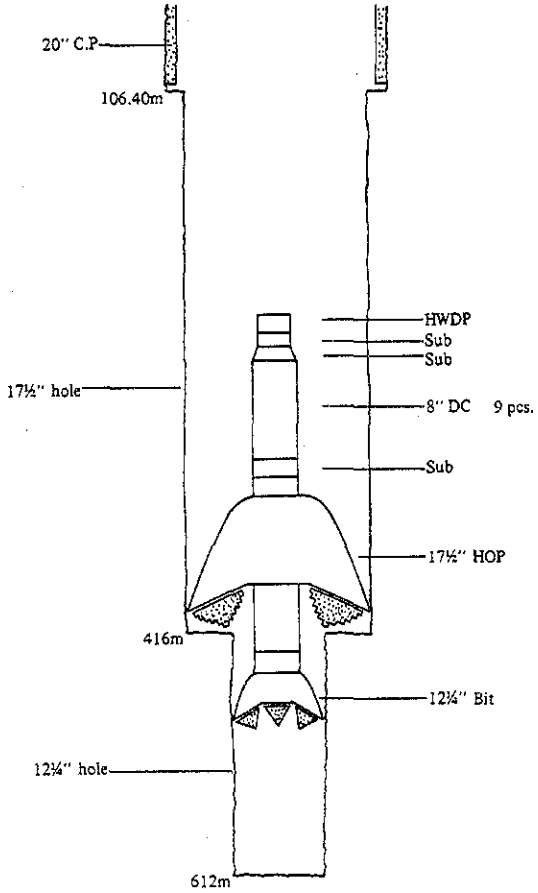

Fig. II. 3-14 Status of Fish for PR-13 (1)

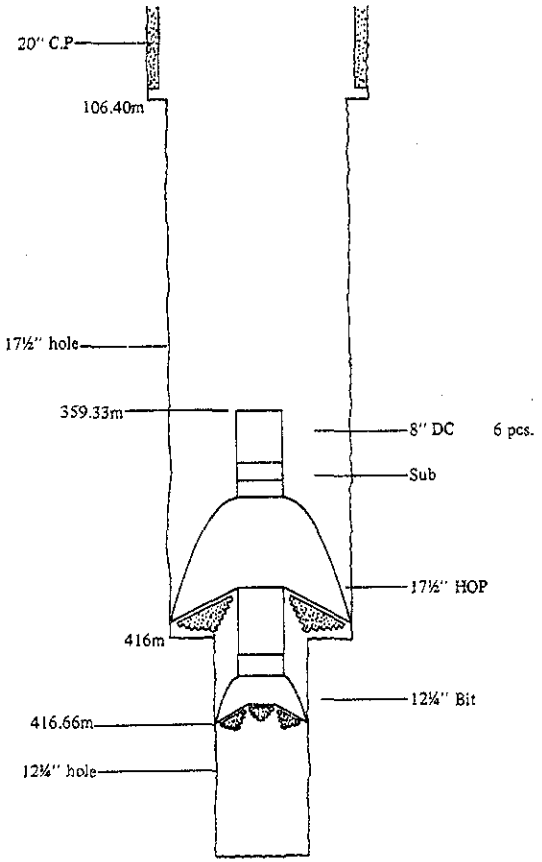

Fig. II. 3-14 Status of Fish for PR-13 (2)

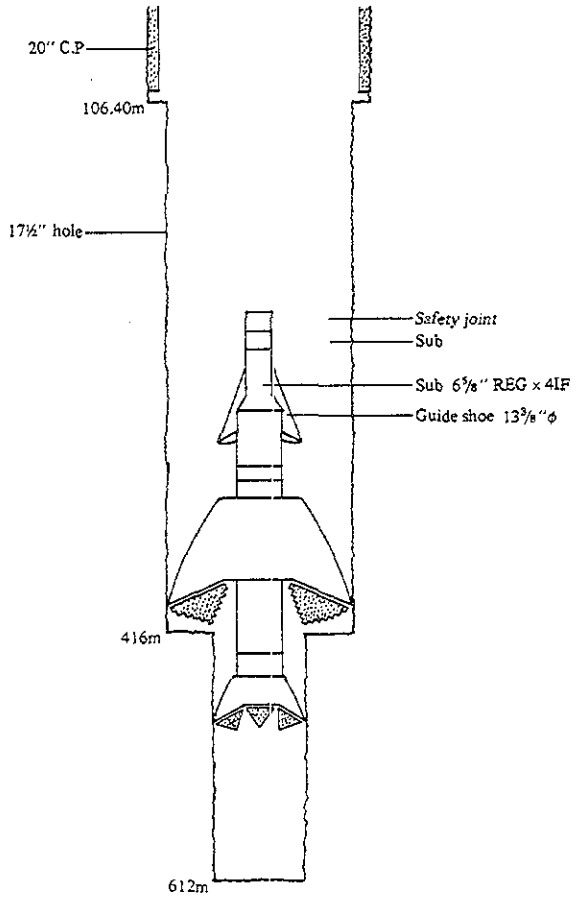

Fig. II. 3-14 Status of Fish for PR-13 (3)

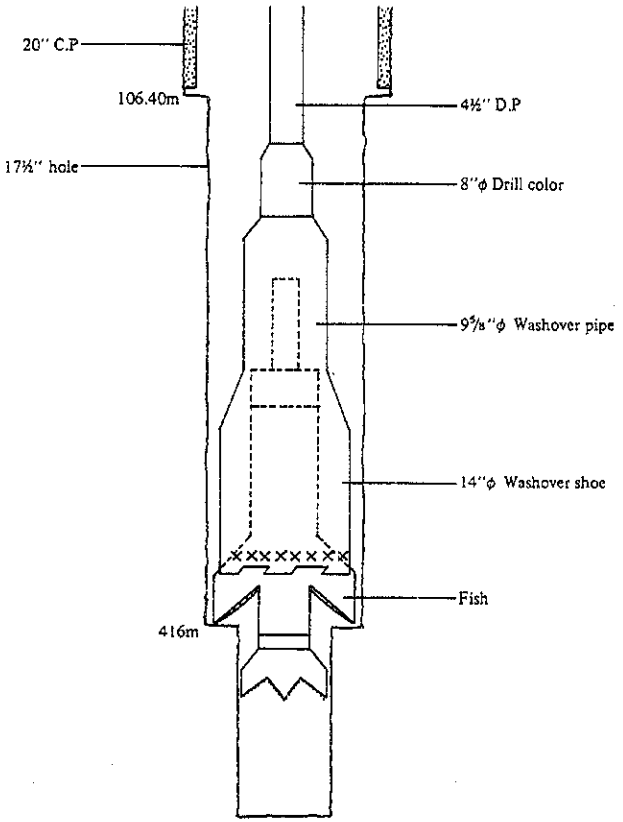

Fig. II. 3-15 Status of Washover for PR-13 (1)

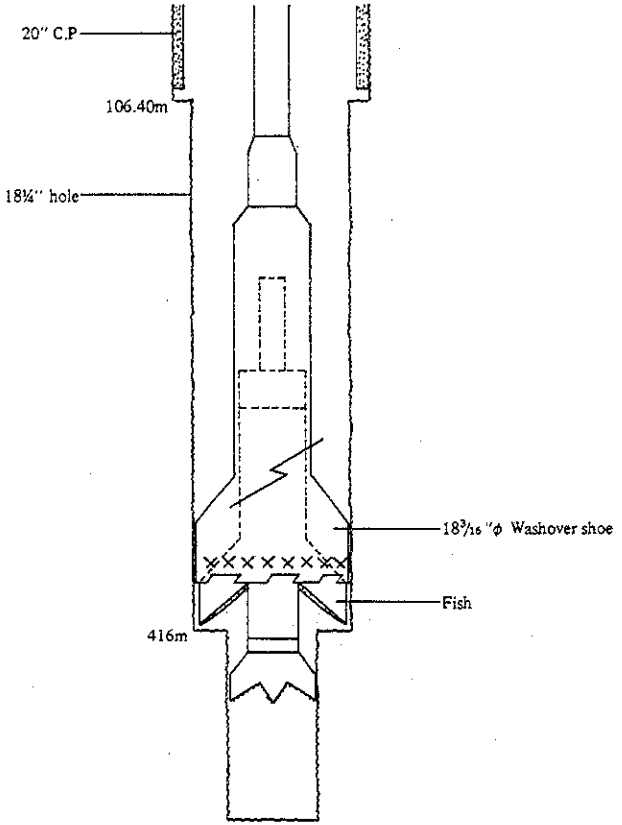

Fig. II. 3-15 Status of Washover for PR-13 (2)

Table II. 3-14 List of Major Drilling Materials of PR-13

			20" C.P	13 3/8" C.P	9 5/8" C.P	Final depth	Total
Mud Additives	Bentnite	50 kg/SX	1,039 SX	19,984 SX	3,114 SX	2,231 SX	26,368 SX
	Lignite	25	0	44 SX	211 SX	150 SX	405 SX
	Supercaltex	25	0	55 SX	225 SX	120 SX	400 SX
	Bicromat Sodico	50	0	0	23 SX	6 SX	29 SX
	Corstic Soda		0	20 kg	420 kg	880 kg	1,320 kg
	Bicarbonate	40	19 SX	102 SX	83 SX	1 SX	205 SX
Lost Circu-lation Materials	Cero Automatico	10	0	8 SX	0	0	0 SX
	LCM (Fine)	25 kg	23 SX	58 SX	0	0	81 SX
	LCM (Medium)	25 kg	38 SX	87 SX	204 SX	0	329 SX
Cement	Cement	50	1,245 SX	5,759 SX	1,225 SX	0	8,229 SX
	SiO_2	40	50 SX	1,560 SX	542 SX	0	2,152 SX
	NaCl		23 SX	107 SX	17 SX	0	147 SX
Fishing	Free Well		0	755 ℓ	480 ℓ	100 ℓ	1,335 ℓ
	Oil		0	64 kℓ	45 kℓ	26 kℓ	133 kℓ

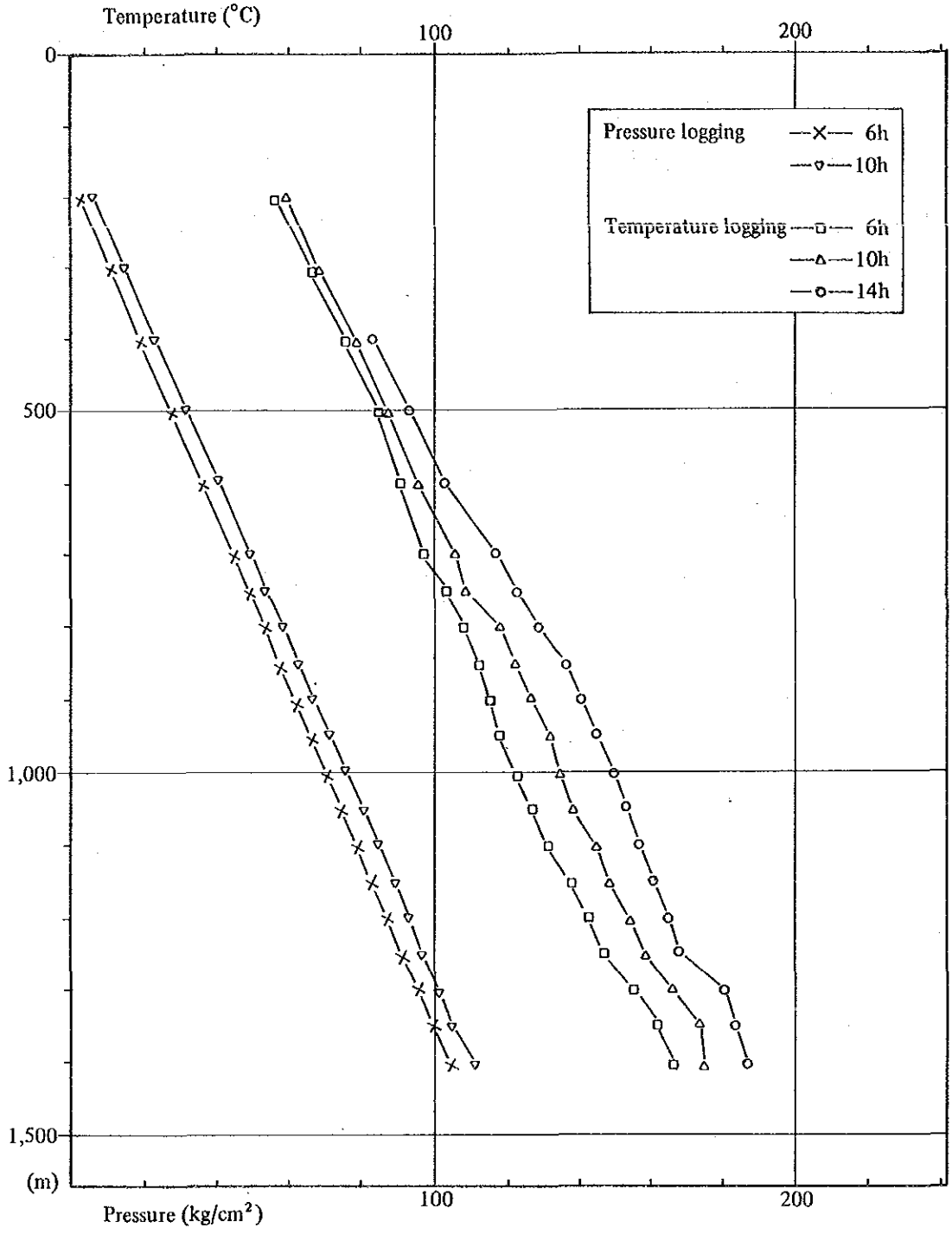

Fig. II. 3-16 Temperature and Pressure Logging Chart of PR-13 (1,400m)

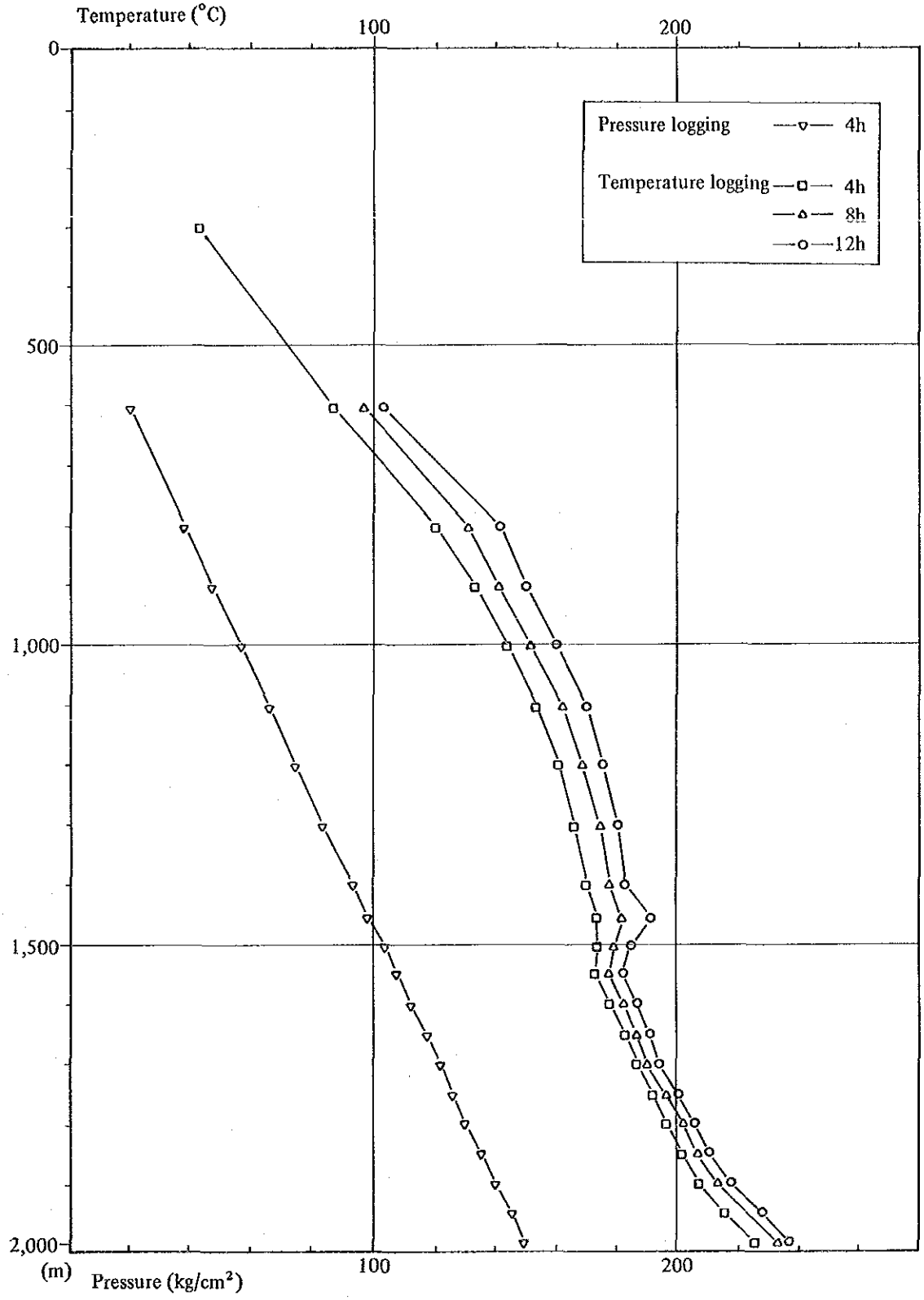

Fig. II. 3-17 Temperature and Pressure Logging Chart of PR-13 (2,000m)

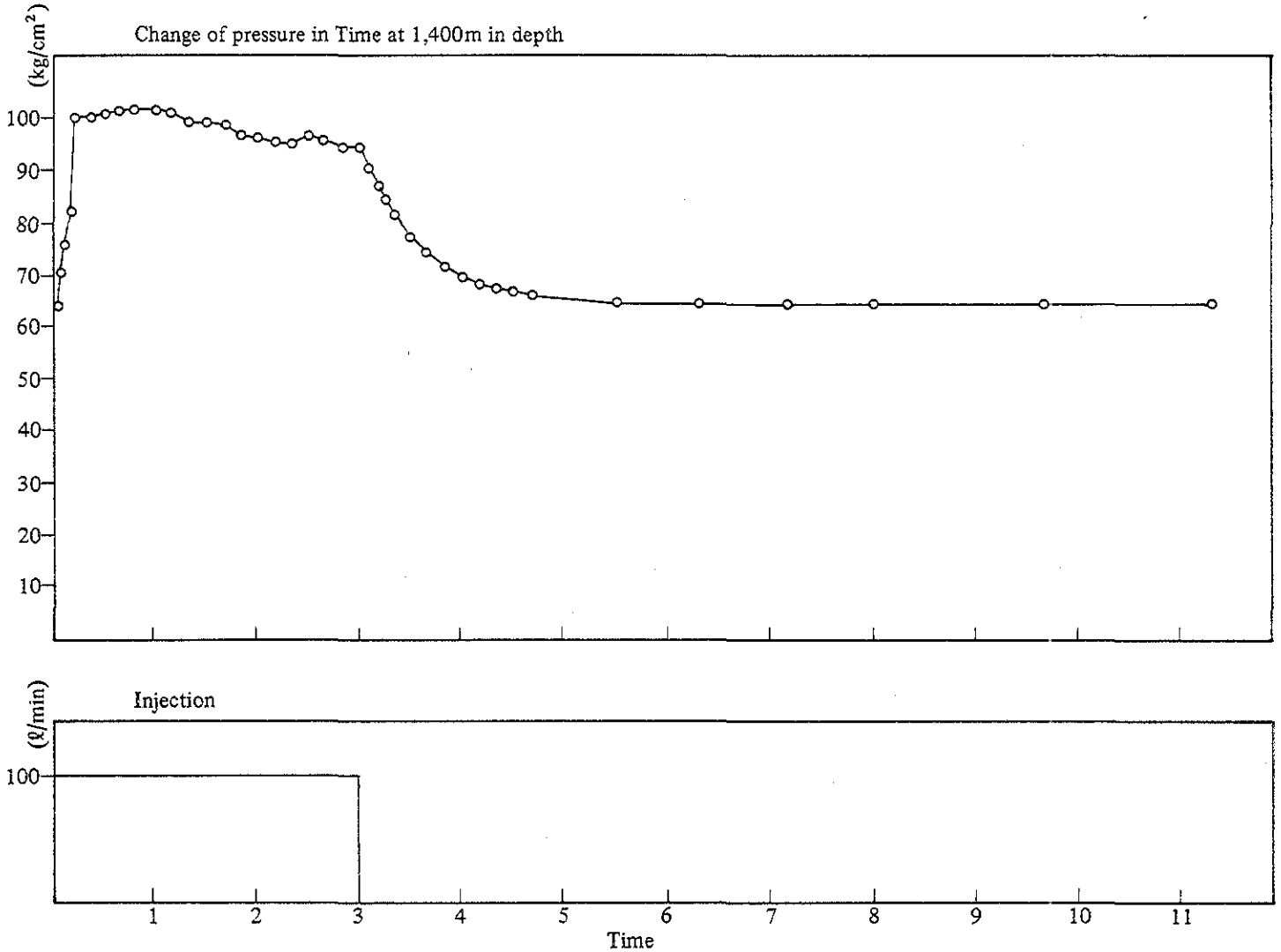

Fig. II. 3-18 Injection Test Chart of PR-13

3.3 Result of survey of PR-13

3.3.1 Core and cuttings survey of PR-13

Various geological characteristics were identified by using cores and cuttings taken from PR-13. Fig. II.3-19 shows the integrated result of drilling and survey of PR-13. Fourty-one cutting samples were collected from 1,200 m to 2,000 m in depth. The result of core measurement will be shown in Chapter III, 2.1.3.

(1) Chemical analysis of Hg and As

Hg concentration is the lowest value among all wells, namely lower than 0.02 ppm. Peaks in As observed at 1,500 ~ 1,640 m in depth correspond to the lost circulation at the same depth. As concentrations suggest that fracture is distributed near the bottom deeper than 1,900 m in depth, where is the main feed point.

(2) X-ray diffraction analysis

Detected alteration minerals are montmorillonite, chlorite-montmorillonite mixed-layer mineral, chlorite, sericite, quartz, calcite and pyrite.

Montmorillonite, which has a low temperature stability field as mentioned above, is widely distributed from 1,200 to 2,000 m. Considering that the static borehole temperature, measured 2,160 hours after drilling, ranges from 281 to 289°C at the depth, the geothermal reservoir is estimated to have increased about over 120°C from the past alteration stage up to the present.

(3) *Homogenization temperature of fluid inclusion*

The homogenization temperatures were measured in vein minerals from cutting samples. These are five samples of vein quartz from 870 m, 1,260 m, 1,440 m, 2,000 m and one of vein calcite from 1,820 m in depth.

The minimum homogenization temperature has a tendency to increase abruptly from 228°C at a depth of 870 m to 290°C at a depth of 1,440 m, to be about constant value of 286 ~ 290°C from 1,440 to 1,820 m in depth, and to decrease about 20°C from 1,820 m in depth to the bottom.

From the result that most homogenization temperatures are distributed in a narrow range of 8 ~ 24°C at three depths of 1,440 m, 1,820 m and 2,000 m, it is considered that fluid inclusion formed simultaneously at the mineralization stage.

3.3.2 Chemical analysis of wellbore fluids from PR-13

(1) Collecting and analytical methods

Sampling of wellbore fluids from PR-13 was carried out on the 12th, August in 1988. Collecting and analytical methods are all the same as the methods of PR-12.

(2) Result and discussion of chemical composition

The results of chemical and isotopic composition are listed in Table II. 3-15. Total gaseous concentration in steam is 1.76 vol% under the condition of 2.5 kg/cm^{2}G at separator pressure. CO_2 gas reaches 99 vol% and CH_4 gas is rich in the rest of gas. He, Ar and N_2 concentrations in

steam are the same values as those of PR-8 and PR-12.

Hot water from PR-13 is rich in Na and Cl, and is richer in SO_4 (112 mg/ℓ) than that of PR-1 and PR-12 (19 ~ 45 mg/ℓ). SiO_2, SO_4 and B concentrations in hot water are the same value as those of PR-8. The ratio of B/Cl has not made a difference among PR-1, PR-8, PR-12 and PR-13. This means the same origin of hot water.

In the isotopic composition diagram, δD is −66.7‰, and $\delta^{18}O$ is −1.7‰. The δD value is lighter than that of PR-1, PR-8 and PR-12, while the $\delta^{18}D$ is nearly equal to that of PR-8. The tritium concentration is lower than 0.25 TR, showing few infiltration of the surface water.

Table II.3-2 shows the chemical thermometers of PR-13. The estimated temperature ranges from 236°C to 278°C. The SiO_2 and Na/K thermometers indicate 278°C and 269°C respectively. Downhole temperature value under the producing condition records 276°C at a maximum. Therefore, the reservoir temperature around PR-13 is estimated to be approximately 280°C. This value is the same degree as that of PR-8, and is not so good as that of PR-1 and PR-12 in thermal degree.

3.3.3 Well tests of PR-13

(1) Method and process of measurement

The well test conducted on PR-13 is the same method as that of PR-12, but the process is slightly different. That is to say, measurements were carried out under two stages (Table II.3-16) at 17.0 kg/cm²G and 21.8 kg/cm²G in wellhead pressure respectively. The test was a simultaneous measurement of temperature and pressure under the flow adjustment by 3″ϕ orifice and full opening of 2nd valve. The equipment could not go down beyond 1,985 m in spite of 2,006.4 m in total depth.

Table II. 3-16 Conditions of Well Test of PR-13

Stage	I	II
Date	19. Aug. 1988	23. Aug. 1988
Measurement	Temperature & pressure	Temperature & pressure
Well head condition	3″ϕ orifice 2nd valve: full open	2½″ϕ orifice 2nd valve: full open
Well head pressure (kg/cm²G)	17.0	21.8
Flow rate (t/h)	Gs = 24.8 Gw = 65.0 G = 89.8 at separator (2.4 kg/cm²G)	Gs = 15.1 Gw = 49.3 G = 64.4 at separator (4.08 kg/cm²G)
Quality at separator	0.276	0.234

(2) Result of measurement

Table II.3-17 and Fig. II.3-20 show the results of downhole temperature and pressure. Based on these results, the condition inside of PR-13 hole is as follows:

① The flow condition in the wellbore the two-phase flash flow exept for near the bottom. However, the liquid phase is dominant near the bottom, because the difference between the static temperature (280°C) and the fluid temperature is small and the pressure gradient is small.

② The main feed point is situated near the bottom.

③ A burried layer of about 10 or more meters might be expected near the bottom.

(3) Calculation of the value of permeability-thickness

The fluids of PR-13 flow into the wellbore from near the bottom. An exact observation makes clear that the fluids flash in the formation at the first test, but flash in the wellbore at the second test. Therefore, to calculate the permeability-thickness (kh), we can use an equation of two-phase flow for the first test and an equation of liquid phase flow for the second test.

An equation of radial flow of two-phase can be expressed by the following formula:

$$G = \frac{2\pi\bar{\bar{k}}h\,(P_e - P_w)}{\ell_n\,(r_e/r_w)} \left(\frac{\gamma_s}{\mu_s} k_{rs} + \frac{\gamma_w}{\mu_w} k_{rw}\right) \qquad (4)$$

where,

G	: Steam flow rate	kg/s
P_e	: Reservoir pressure at inflow depth	kg/m^2
P_w	: Pressure in wellbore at inflow depth	kg/m^2
$\bar{\bar{k}}$	: Absolute permeability	m^2
k_r	: Relative permeability	
h	: Effective thickness	m
γ	: Specific weight of fluid	kg/m^3
μ	: Fluid viscosity	kgs/m^2
r_e	: Radius of influence area	m
r_w	: Wellbore radius	m

Suffix s : Steam, w : Hot water

Using krs + krw = 1 and quality x, the equation (4) can be converted into as follows:

$$G = \frac{2\pi\bar{\bar{k}}h\,(P_e - P_w)}{\ell_n\,(r_e/r_w)} \cdot \frac{1}{\frac{\mu_s}{\gamma_s} x + \frac{\mu_w}{\gamma_w}(1-x)} \qquad (5)$$

Therefore, the value of kh under the two-phase flow can be calculated from the following equation.

$$\bar{\bar{k}}h = \frac{G\ell_n\,(r_e/r_w)}{2\pi\,(P_e - P_w)} \left\{ \frac{\mu_s}{\gamma_s} x + \frac{\mu_w}{\gamma_w}(1-x) \right\} \qquad (6)$$

On the other hand, the value of kh under the liquid phase flow can be easily calculated from an equation (7).

$$kh = \frac{G\,\mu_w\,\ell_n\,(r_e/r_w)}{2\pi\gamma_w\,(P_e - P_w)} \qquad (7)$$

Tables II.3-18 and II.3-19 show the parameter used for calculation and the result respectively. For the calculation, we use an equation (6) for the first test and an equation (7) for the second test. Reservoir pressure at inflow depth is estimated to be 143 kg/cm²A which is the measuring value by CFE. Quality x in an equation (6) is decided by the temperature value (280°C) at the feed point.

The value of kh is approximately 0.3 darcy·m, showing the same value of PR-12.

Table II. 3-15 Chemical Composition of Well Discharge Sample from PR-13

(1) Gas composition of steam

		PR-13	PR-8	PR-12
Well-head pressure (psi)		190	155	120
Liquid-vapor separate pressure (psi)		35	17	47
Total gas in steam (vol. %)		1.76	2.11	1.92
Gas Composition	H_2S (Vol. %)	0.3	0.3	0.9
	CO_2 (vol. %)	99.0	99.0	98.5
	H_2 (ppm)	140	56.9	478
	N_2 (ppm)	2340	2790	2510
	CH_4 (ppm)	4470	4100	2960
	He (ppm)	12.8	13.5	15.5
	Ar (ppm)	39.4	43.2	40.3

(2) Chemical composition of steam condensate

Component	Unit	PR-13
Electrical conductivity	μS/cm	333
pH	–	6.99
Cl	mg/ℓ	0.31
NH_4	mg/ℓ	51.1
As	mg/ℓ	
Hg	mg/ℓ	0.0011

(3) Chemical composition of hot water

Component	Unit	PR-13
Electrical conductivity	μS/m	4,010
Total dissolved solids	mg/ℓ	3,690
pH	–	8.53
Cl	mg/ℓ	870
SO_4	mg/ℓ	112
H_2CO_3	mg/ℓ	3.3
HCO_3	mg/ℓ	475
CO_3	mg/ℓ	12.2
Na	mg/ℓ	767
K	mg/ℓ	132
Ca	mg/ℓ	1.26
Mg	mg/ℓ	0.35
Fe	mg/ℓ	0.68
Al	mg/ℓ	2.04
SiO_2	mg/ℓ	964
Li	mg/ℓ	8.39
B	mg/ℓ	109
F	mg/ℓ	6.3
NH_4	mg/ℓ	3.7
As	mg/ℓ	12.9
Hg	mg/ℓ	<0.0005
D/H	‰ (SMOW)	-66.7
$^{18}O/^{16}O$	‰ (SMOW)	- 1.7
Tritium	TR	<0.25

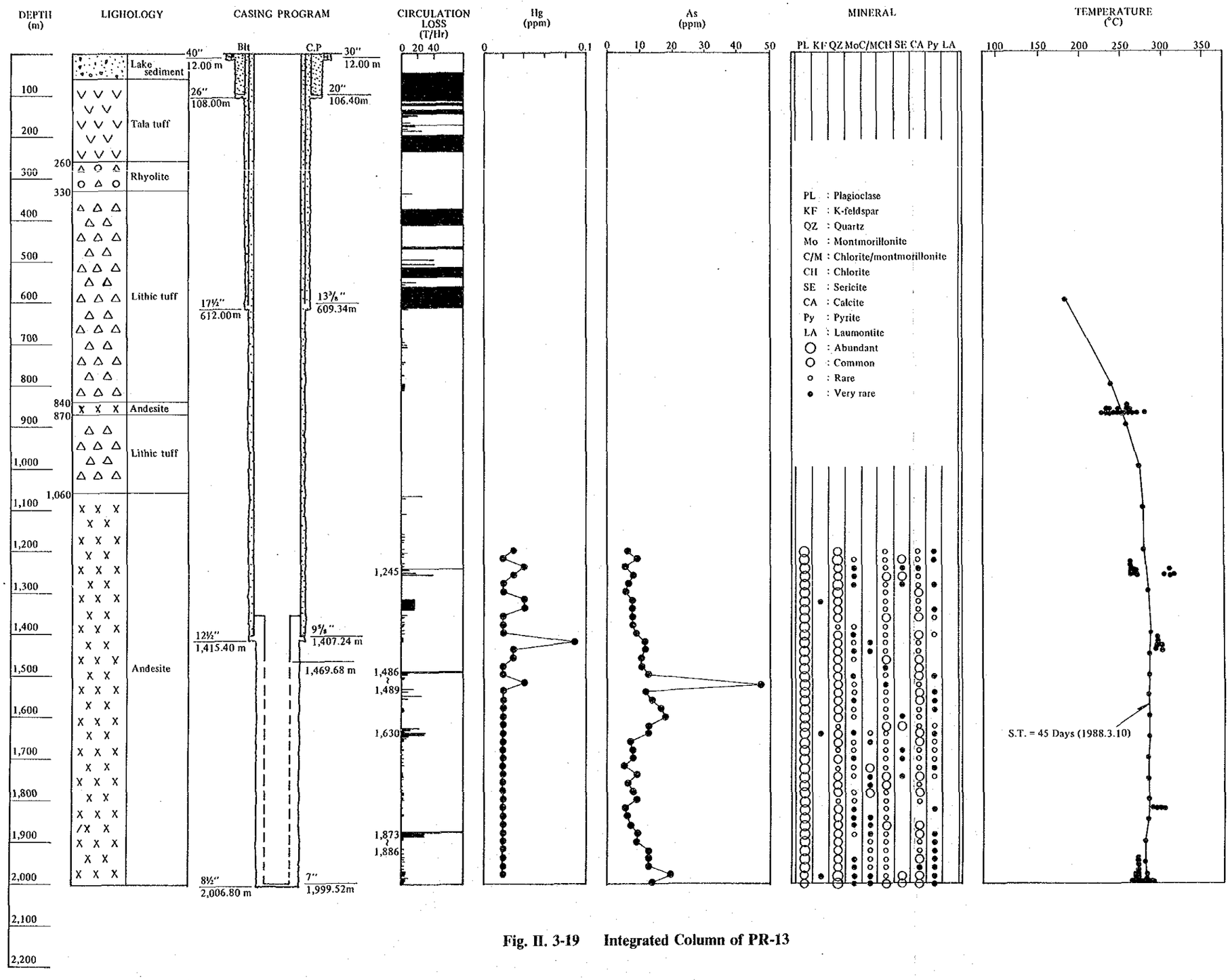

Fig. II. 3-19 Integrated Column of PR-13

Table II. 3-17 Results of Measurement of PR-13

Stage	I		II	
Date	19. Aug. 1988		23. Aug. 1988	
Well head condition	3"ϕ orifice		2½"ϕ orifice	
Well head pressure	17.0 kg/cm^{2}G		21.8 kg/cm^{2}G	
Depth (m)	Temperature (°C)	Pressure (kg/cm^2·abs)	Temperature (°C)	Pressure (kg/cm^2·abs)
100	212	18.7	224	23.7
200	216	19.8	227	25.2
300	218	20.7	230	26.8
400	221	22.3	233	27.9
500	224	23.5	235	29.4
600	227	25.1	238	30.7
700	229	25.9	240	32.3
800	232	27.6	243	33.9
900	235	28.9	245	35.6
1000	237	30.0	248	37.1
1100	240	31.5	251	39.1
1200	242	33.3	253	41.0
1300	245	34.8	256	43.2
1400	248	36.4	259	45.2
1500	251	38.8	261	48.1
1600	253	41.1	264	51.3
1700	256	43.9	266	55.1
1800	260	47.9	270	59.9
1900	267	54.0	276	66.9
1980	270	59.5	276	72.8

Table II. 3-18 List of Paramerters used in Calculation of kh in case of PR-13

Stage	Static (10 May, 1988)	I	II
Well head pressure (kg/cm^{2}G)	–	17.0	21.8
Total flow rate (t/h)	–	89.8	64.4
Pressure at feed point Pw (kg/cm^2 abs)	143	59.5	72.8
Specific weight of fluid at feed point γ (kg/m^3)	–	γ_W = 761 γ_S = 30	γ_W = 739
Viscosity coefficient of fluid at feed point μ (kgs/m^2)	–	$\mu_W = 9.77 \times 10^{-6}$ $\mu_S = 1.89 \times 10^{-6}$	$\mu_W = 9.26 \times 10^{-6}$
Quality at feed point	–	0.02	0.0

Table II. 3-19 Results of Calculation of kh in case of PR-13

Stage	kh (m^3)
I	3.3×10^{-13}
II	2.6×10^{-13}

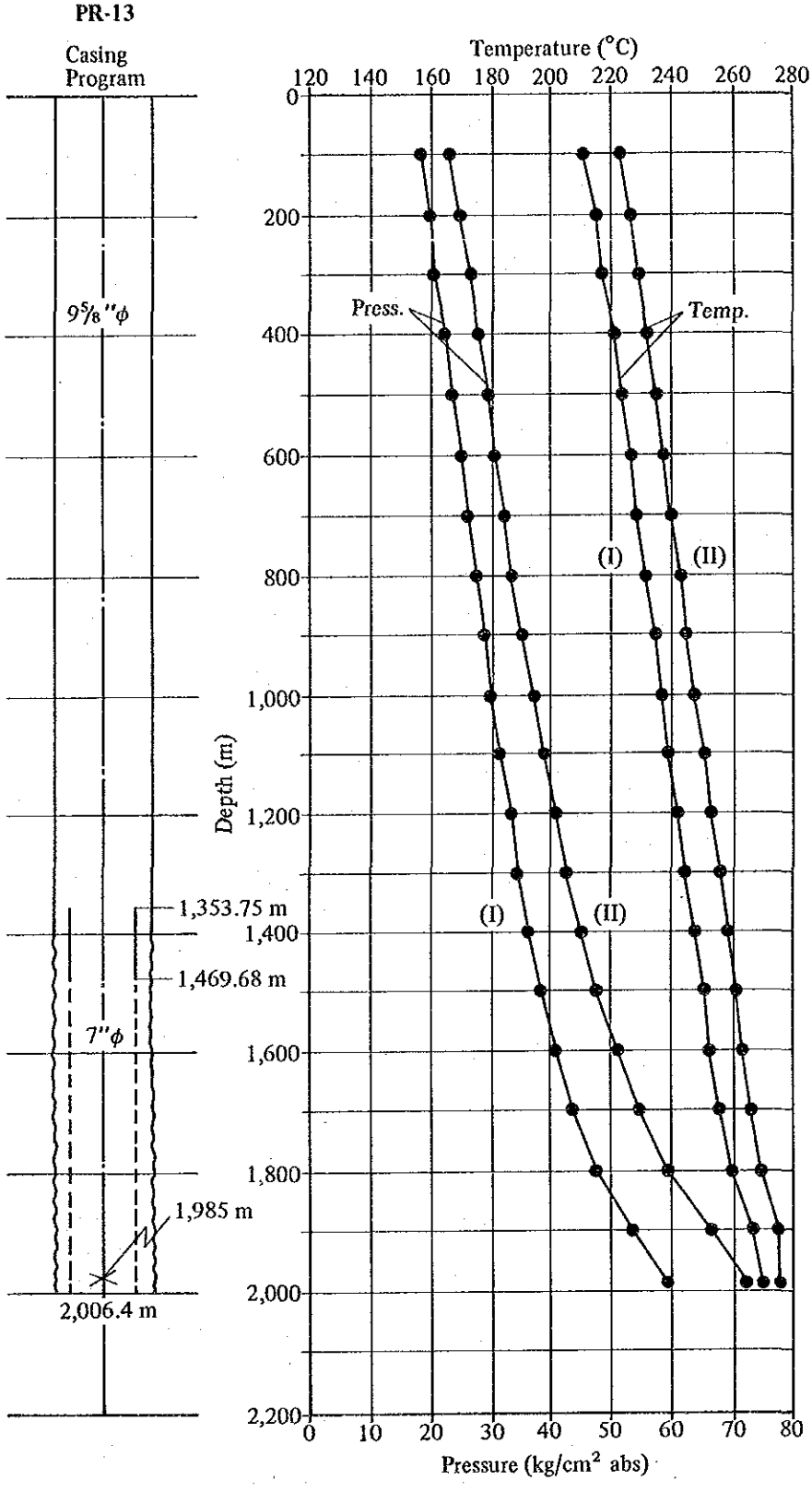

Fig. II. 3-20 Downhole Temperature and Pressure Curves of PR-13 in the Producing Condition

3.3.4 Comprehensive evaluation of PR-13

(1) Evaluation of fracture

Many lost circulations were observed at a depth of shallower than 600 m in depth. Moreover, the remarkable decrease of static borehole temperature, of which recovery time is from 1,080 to 2,160 hours after drilling, was observed at a depth of shallower than about 900 m in depth. From the result, it is concluded that Tala Tuff and the upper lithic tuff play a role of a remarkable infiltration zone of the surface water (Fig. II.3-21).

The temperature of mud water increases abruptly near the depth of 1,880 m, where total lost circulations occurred. We can see the deep seated high temperature geothermal fluid flows into the borehole through the fractures at the depth. However, production test by JICA in 1988 indicates that the permeability of the fractures is no good. Analysis of this test shows that the fractures with partial lost circulation at the bottom is a feed point, and that transmissibility of the fracture at PR-13, which is 2.6-3.3 × 10^{-13} m^3, is about equal to that of PR-12.

Complete lost circulation occurs at 1,878 ~ 1,886 m which is the main feed point. Besides this point, the following lost circulations correspond to fractures:

① Complete lost circulation at a depth of 1,486 ~ 1,489 m: This is due to peameable fracture because Hg and As concentrations in cuttings have high peaks near the depth and the recovery temperature shows high anomaly (Fig. II.3-17).

② Partial lost circulation near 1,630 m in depth: Hg concentration in cuttins is high near the depth.

③ Partial lost circulation (13 kℓ/h) near 2,000 m in depth: This is the same characteristics as fracture of 1,630 m. The pressure pivot analysis shows that the main feed point is near 1,760 m. However, the anomalies of temperature, Hg and As and lost circulation are recognized near the depth. The pivot analysis is available for the case of high permeability, liquid phase in the borehole and high accuracy of pressure measurement. In case of PR-13, poor permeability leads to noticeable error. According to Fig. III.1-11, PR-13 is located at a synclinal axis in the folding structure of Horizon 3 (the upper boundary of rhyolite in the lower Cordilleran Volcanics). Therefore, fractures at depths of 1,486 ~ 1,489 m, near 1,630 m, 1,873 ~ 1,886 m and near 2,000 m are ascribed to vertical fractures developing at a synclinal axis.

(2) Evaluation of temperature

As mentioned above, the minimum homogenization temperature is equal to the static borehole temperature at depths of 870 m, 1,440 m, 1,820 m, but is 17 ~ 22°C lower than the static temperature at 1,260 m and 2,000 m. These indicates that the reservoir temperature has been constant, or increased from the inclusion trapping stage up to the present. On the other hand, it was estimated that the reservoir temperature has increased over about 120°C from the past temperature is probably in equalibrium with the formation temperature.

As mentioned above, the minimum homogenization temperature is equal to the static borehole temperature at depths of 870 m, 1,440 m, and 1,820 m, but is 17 ~ 22°C lower than the static temperature at 1,260 m and 2,000 m. These indicates that the reservoir temperature has been constant, or increased from the inclusion trapping stage up to the present. On the other hand, it was estimated that the reservoir temperature has increased over about 120°C from the

past alteration stage to the present, on the basis of the distribution of montmorillonite and laumontite in the well.

These provide us with the conclusion that the reservoir temperature has been constant, or increased at the successive process: alteration stage, inclusion trapping stage, present.

(3) Comparison the reasons for selection of target with the result after drilling

PR-13 was drilled out by a Mexican drilling company under financial and technical supports of JICA. It is necessary to compare the reasons for selection of target with the results after drilling as well as PR-12.

The following four points are the reasons for selection of target:

① Necessary point to detect the extent of geothermal reservoir
② Located on an up-flow zone
③ Located on possible deep-seated fractures
④ Located on the low resistivity anomaly of MT method

Besides these, the reasons for selection included an anticlinal bending axis and a maximum upheaval zone of giant pumice at the beginning. However, these reasons were excluded because of a steep slope of the location.

For the above reasons, the actual results of the drilling of PR-13 are as follows:

① PR-13 is located within the geothermal reservoir because the well enconters good fractures and high temperature zone.
② The temperature by downhole measurement and fluid inclusion indicates approximately 280°C below 1,400 m in depth.
③ Main fractures are recognized at depths of 1,486 ~ 1,489 m and 1,873 ~ 1,886 m, and small scale fractures are found about 1,630 m and about 200 m in depth.
④ The low resistivity anomaly is not confirmed because an electrical logging has not carried out after drilling.

(4) Well efficiency of PR-13

The well test shows a good efficiency of PR-13 in spite of no confirmation of low resistivity anomaly. Fig. II.3-22 gives a wellhead versus flow rate curve based on Table II.3-16. However, the efficiency under the condition of 7 kg/cm²G at wellhead pressure is unknown, and the estimate by two measuring values is insufficient to evalute the efficiency of this well. Therefore, an attempt was made to complete the wellhead versus frow rate curve using a wellbore flow model.

The following values are set for the calculation:

Fluid temperature	: 276°C at the feed point
Feed point	: below 1,985 m
kh	: $3 \sim 6 \times 10^{-13}$ (m^3)

When a match to Fig. II.3-22 is excuted on the basis of these values, the calculated formation pressure at the feed point is 168 ata. Subsequently, using these values we can complete the wellhead, flow rate curve as shown in Fig. II.3-23. Fig. II.3-23 shows that we can obtain the steam of about 40 t/h under the condition of 7 kg/cm²G at the wellhead pressure.

If the values in Fig. II.3-22 are extended at a straight line, the steam flow rate is about 28

ton/hour. The difference between 40 t/h and 28 t/h is due to the following reasons:

① Fig. II.3-20 indicates the liquid phase near 1,985 m and the increase of temperature as an elapsed production time. This means that the measurement is under temperature recovery and the temperature would arise by the continuous production.

② Fig. II.3-20 shows that the fluids flow into the wellbore from a fracture about 2,000m in depth among fractures of 1,486 ~ 1,489 m, 1,630 m, 1,873 ~ 1,886 m and 2,000 m in depth. Because the formation temperature is more than 280°C below 1,300 m in depth, the fluids must increase by the joinning of flows from the above fractures as a production time elapses, resulting in the increase of steam.

If PR-3 would continue to drill more 500 m, it could cross the shear fracture as shown in Fig. III.1-11, resulting in the increase of steam.

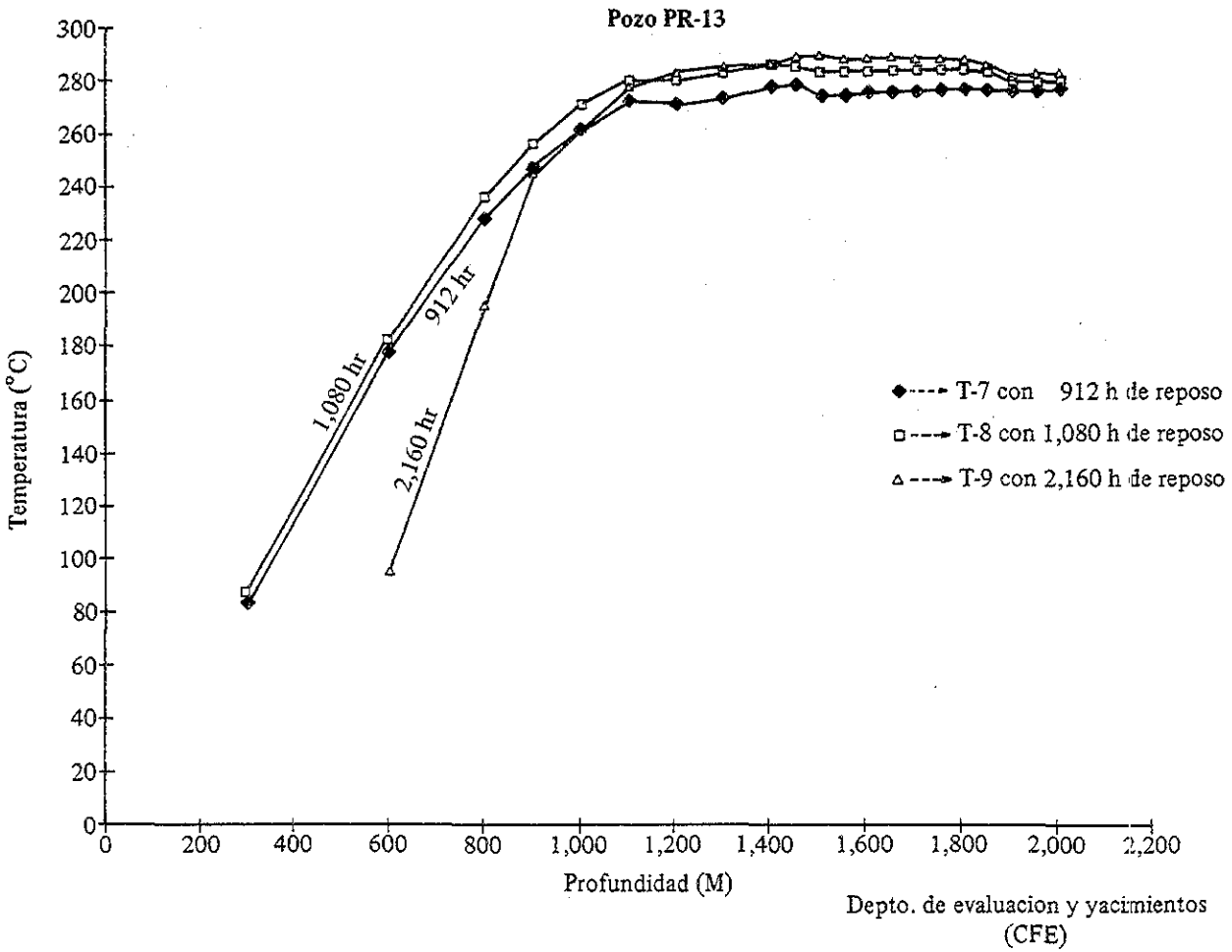

Fig. II. 3-21 Recovery of Temperature of PR-13

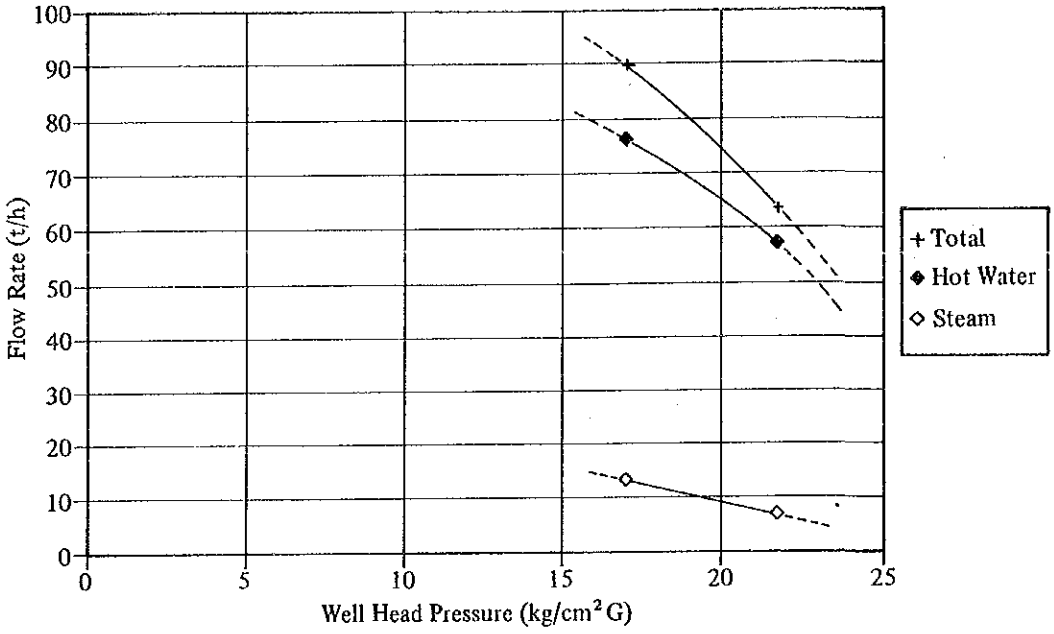

Fig. II. 3-22 Characteristics of Well head Pressure VS. Flow Rate of PR-13

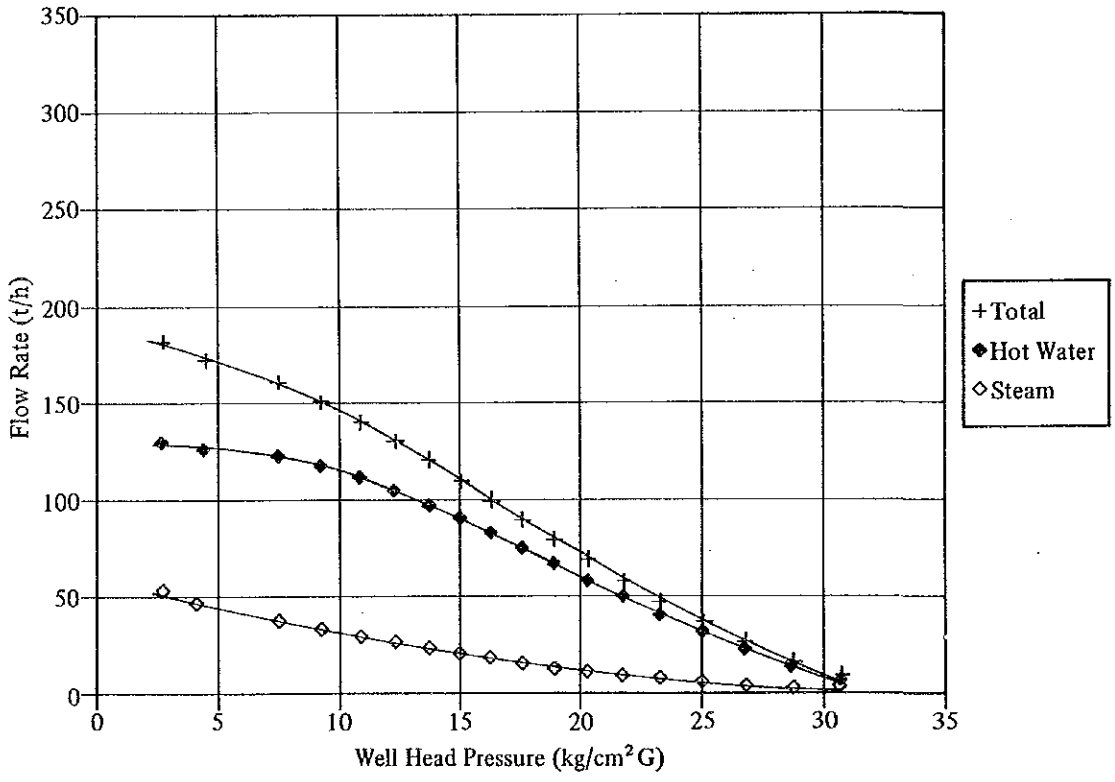

Fig. II. 3-23 Prediction Curve of Well head Pressure VS. Flow Rate of PR-13

III. GEOTHERMAL RESERVOIR EVALUATION

1. Geothermal Reservoir Structure

1.1 Preparation of integrated columnar section and profile

An attempt was made on the improvement of the geothermal reservoir structure in accuracy by the integration of drilling and exploration data available. The data are obtained from CFE in addition to the explorations at first and second stages by JICA. Preparation of integrated columnar section of each well precedes a drawing of reservoir structure. The integrated columnar section includes stratigraphy, lost circulation, various analyses of cuttings and value of temperature which are important to know the efficiency of each well. Figs. III,1-1～7 show the integrated columnar sections except for PR-12 and PR-13.

Subsequently, subsurface profiles, shown in Figs. III.1-8～9 are drawn along NW-SE and NE-SW directions respectively on the basis of the integrated columnar section.

Finally, subsurface fracture system and temperature pattern are considered by the columnar section and the profiles. Moreover, the behavior of fluid flow is also inferred from a chemical analysis of geothermal fluids from the wells.

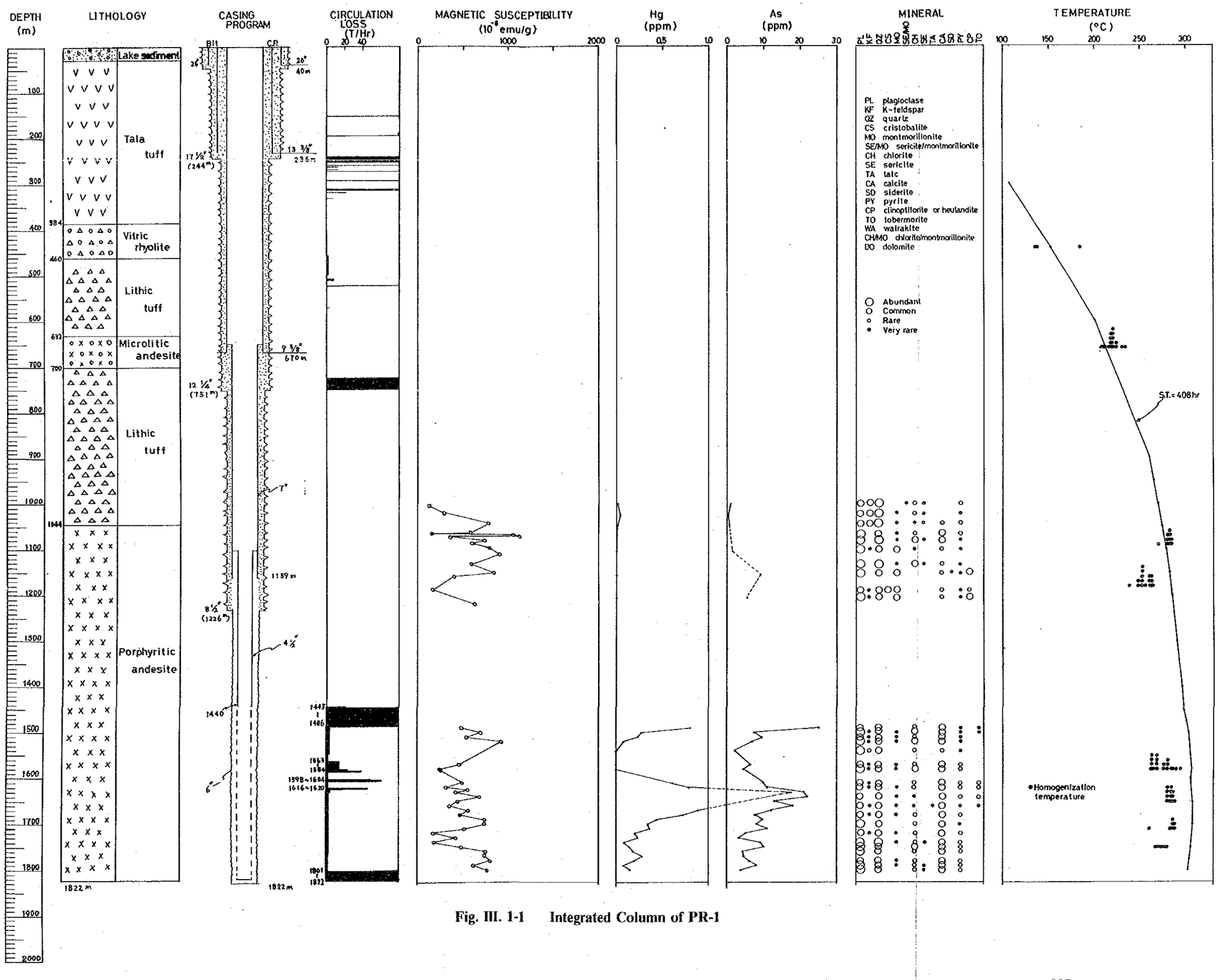

Fig. III. 1-1 Integrated Column of PR-1

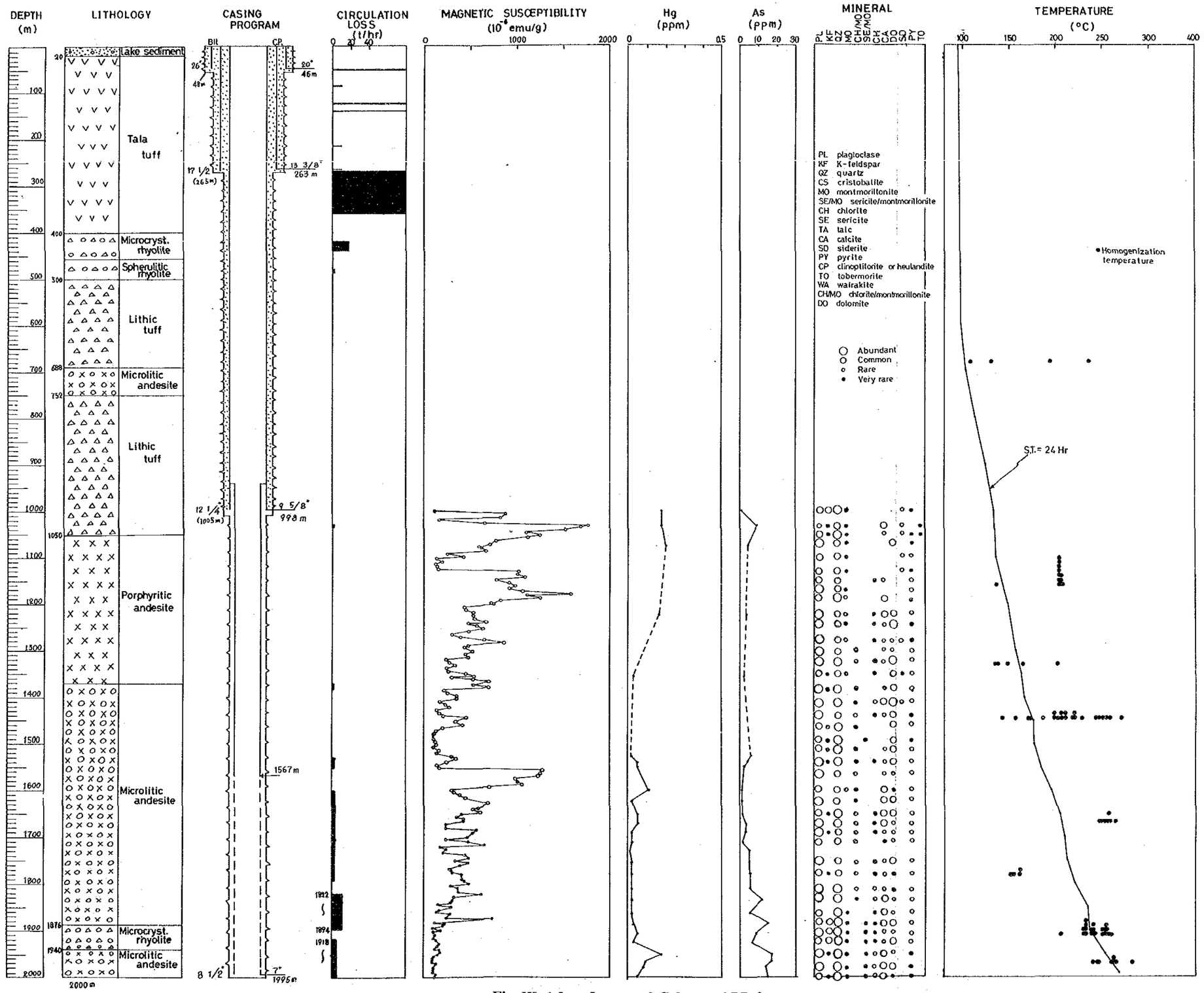

Fig. III. 1-2 Integrated Column of PR-2

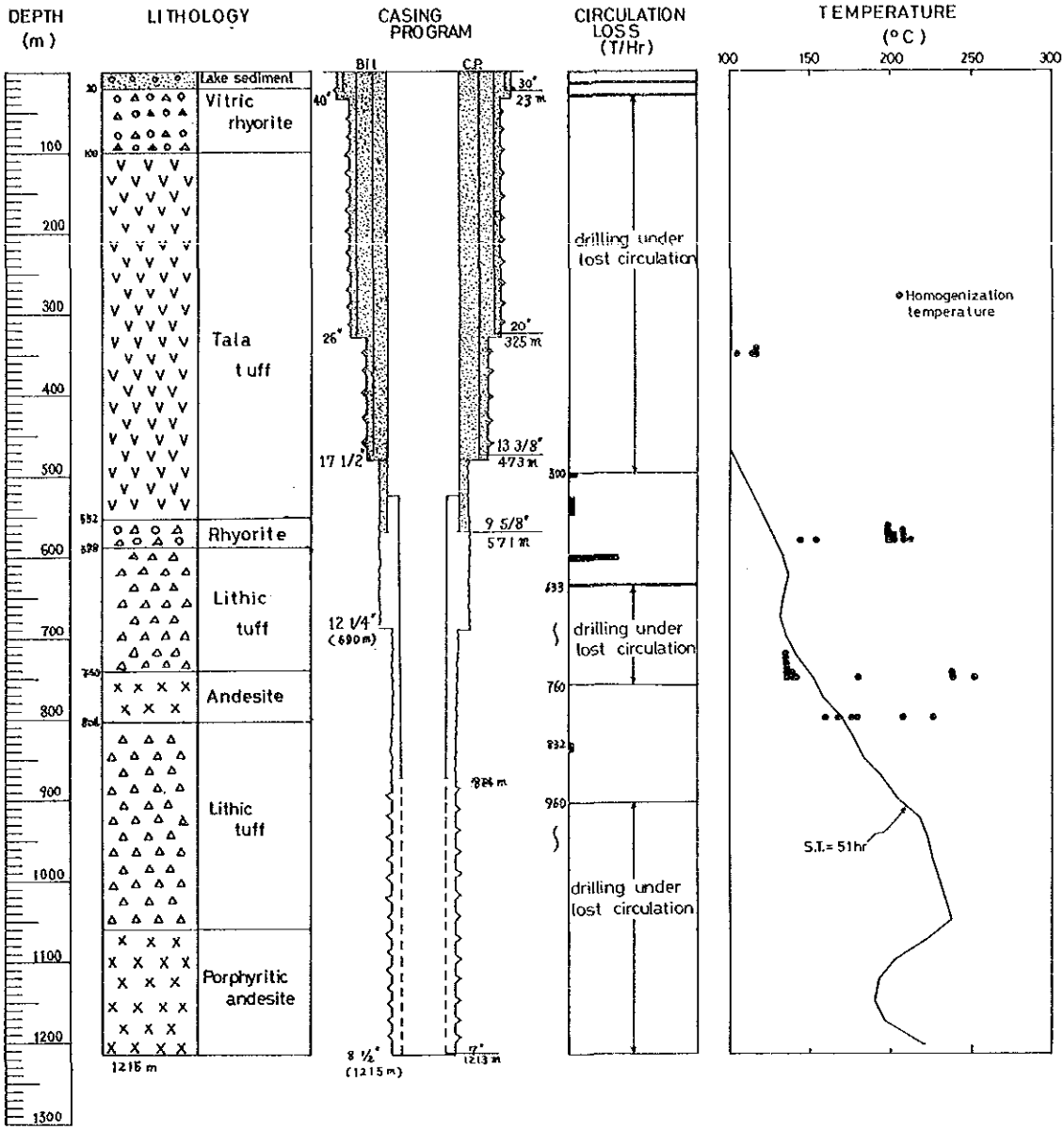

Fig. III. 1-3 Integrated Column of PR-5

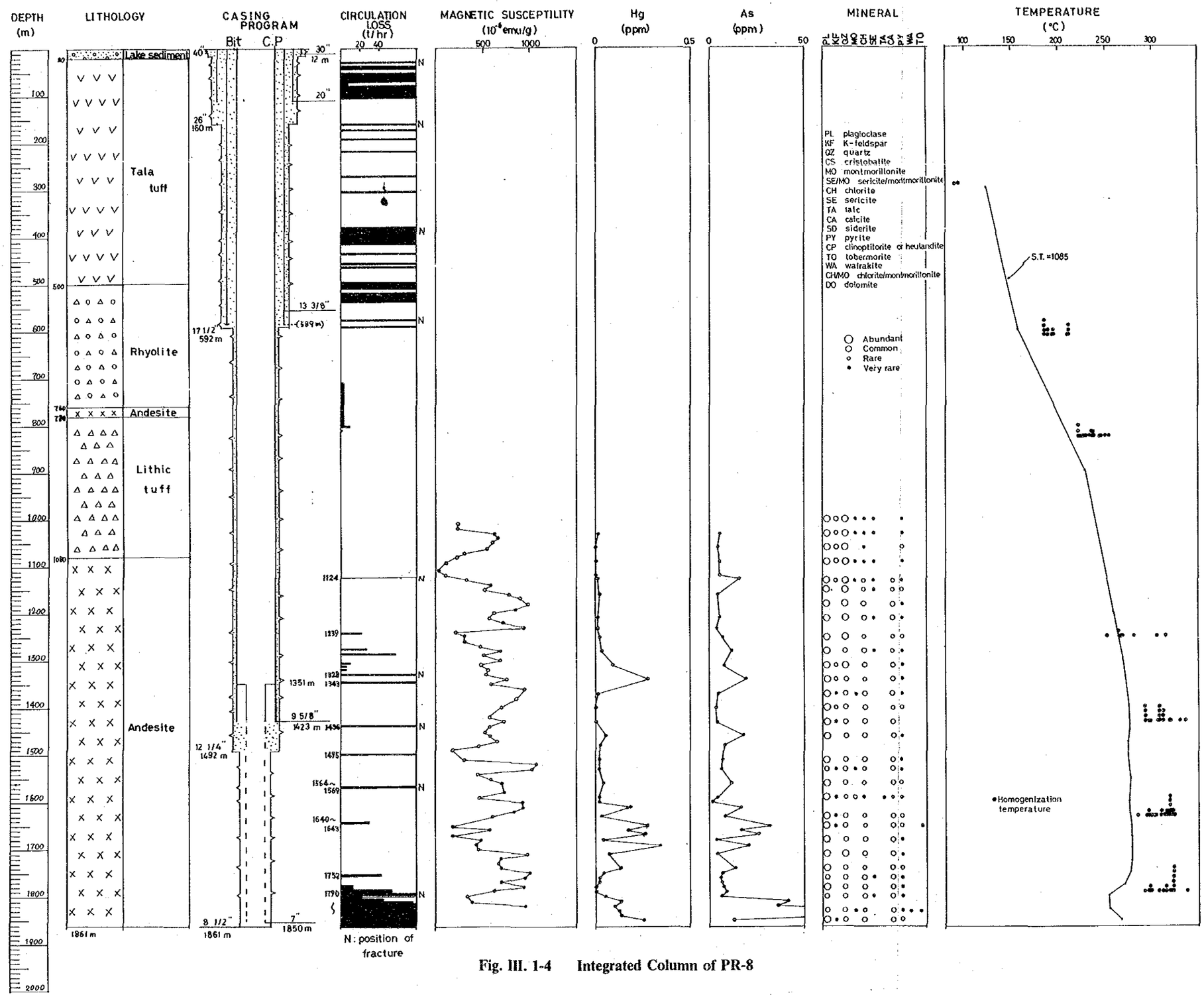

Fig. III. 1-4 Integrated Column of PR-8

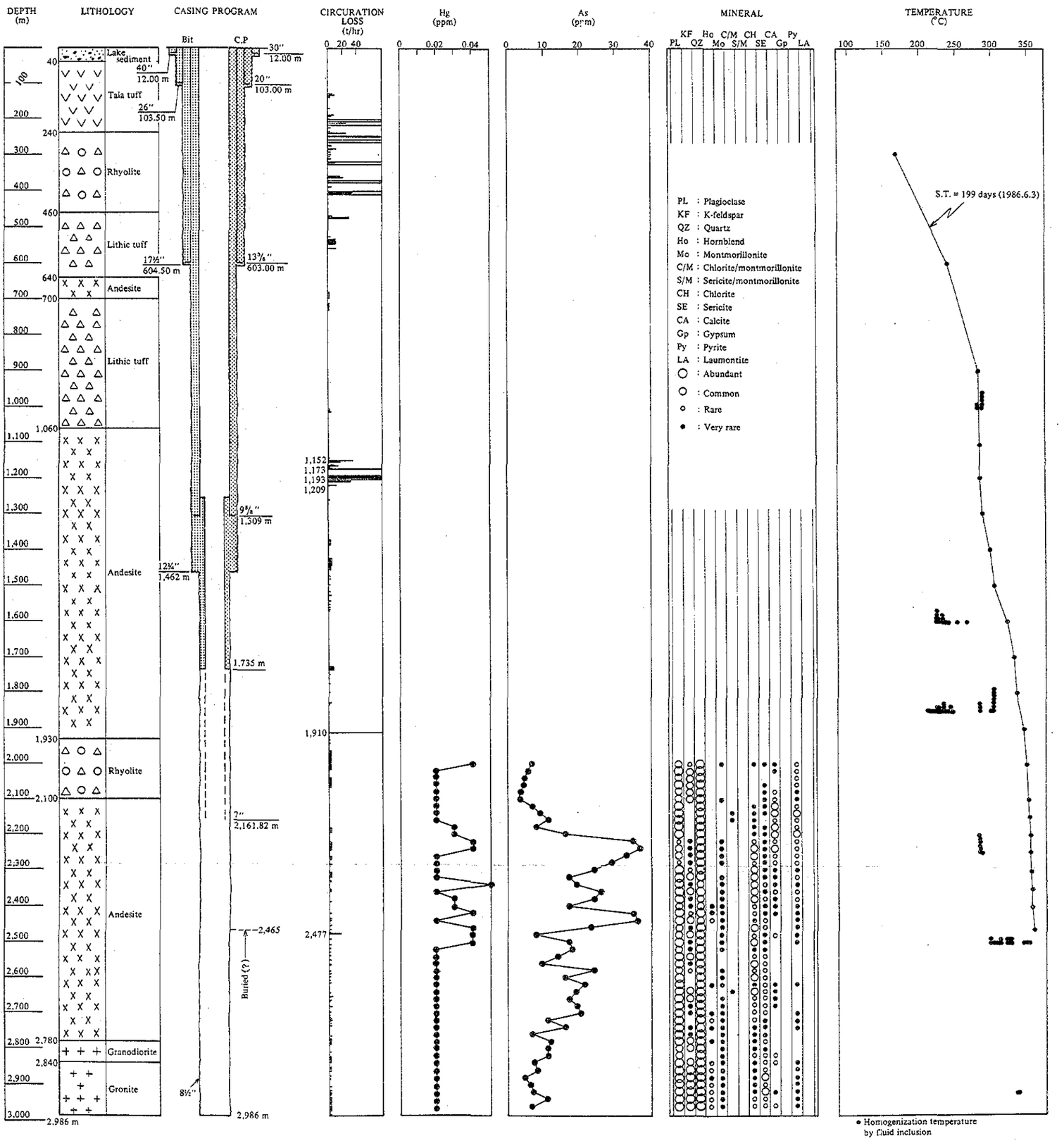

Fig. III. 1-5 Integrated Column of PR-9

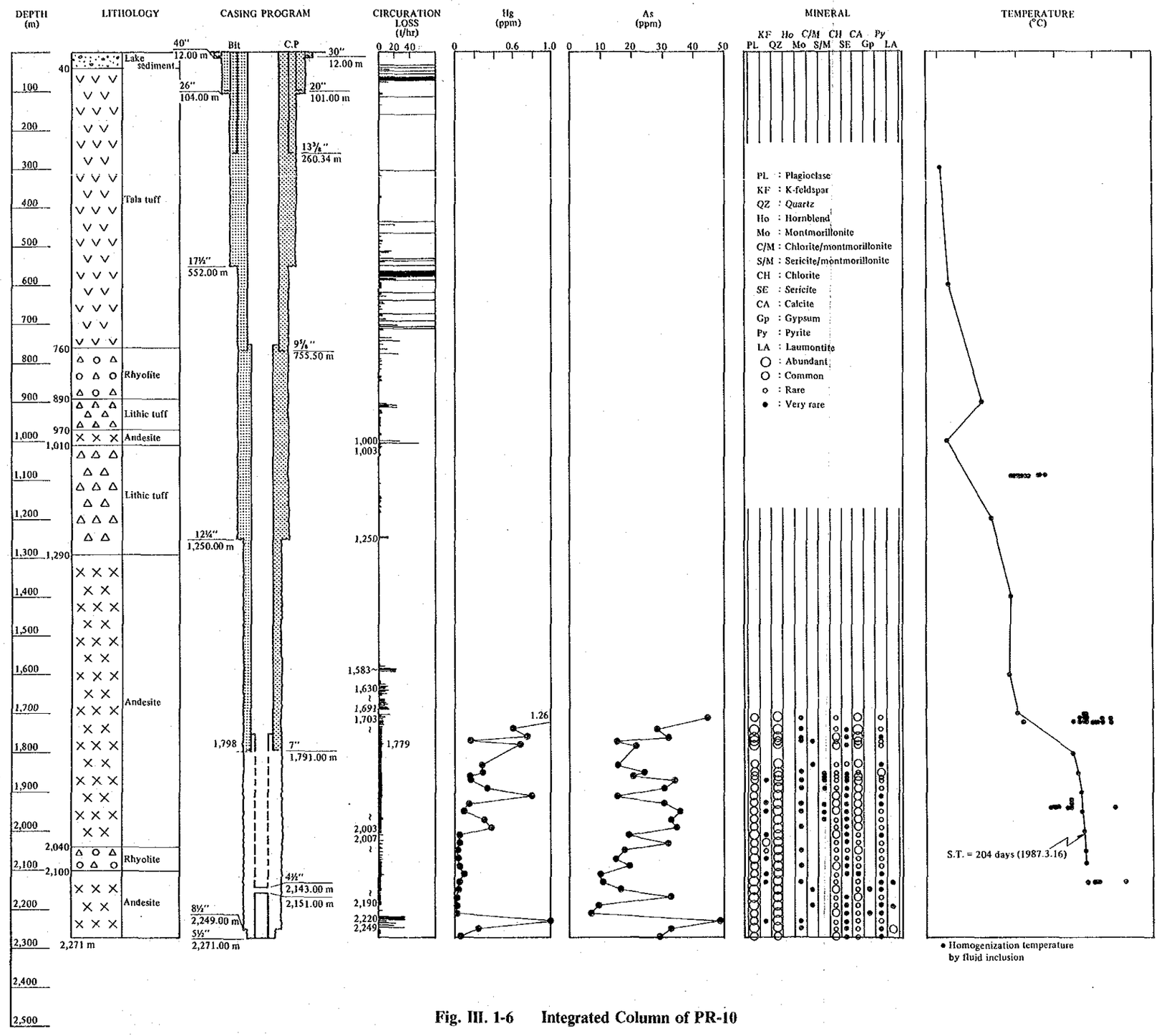

Fig. III. 1-6 Integrated Column of PR-10

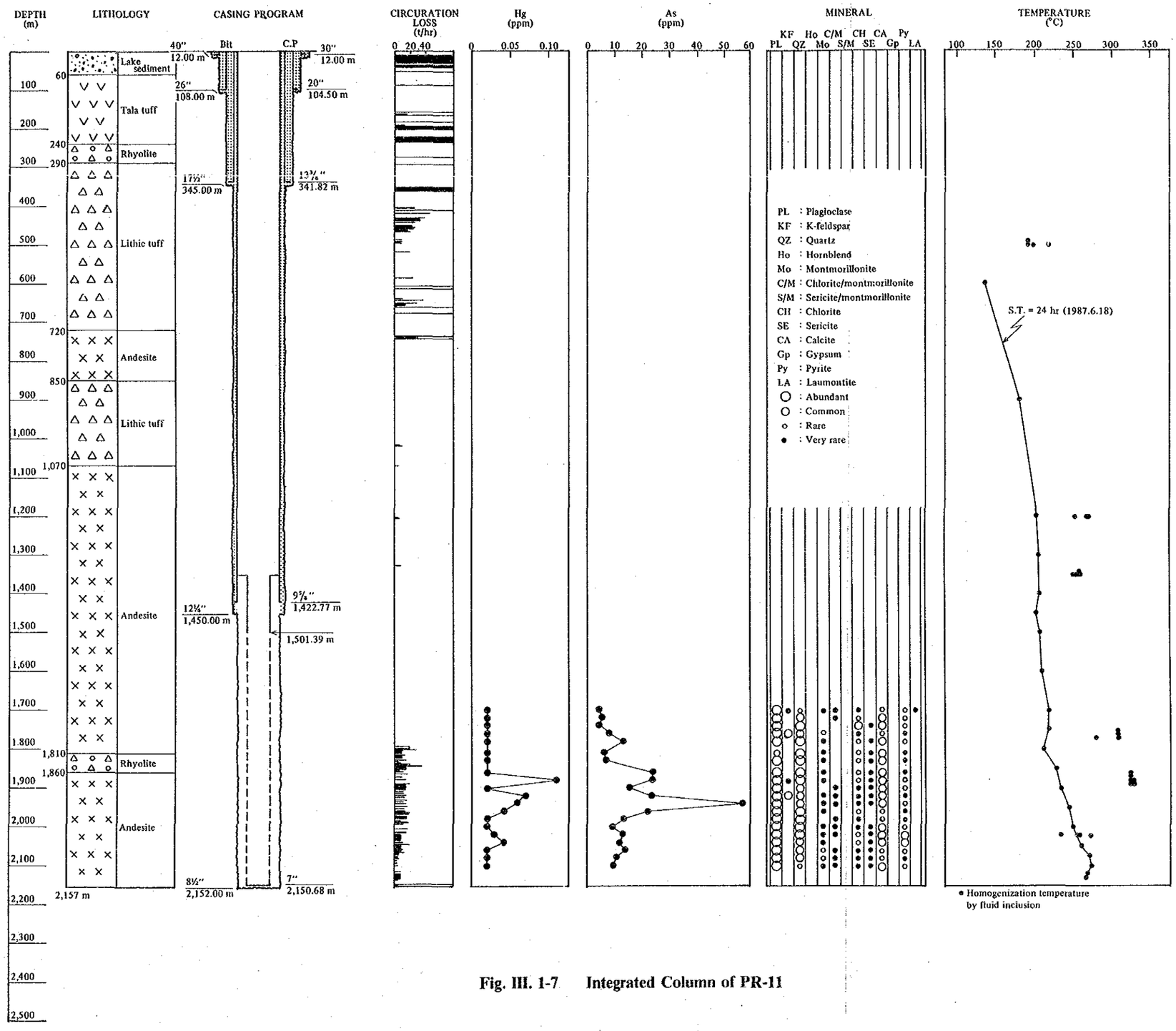

Fig. III. 1-7 Integrated Column of PR-11

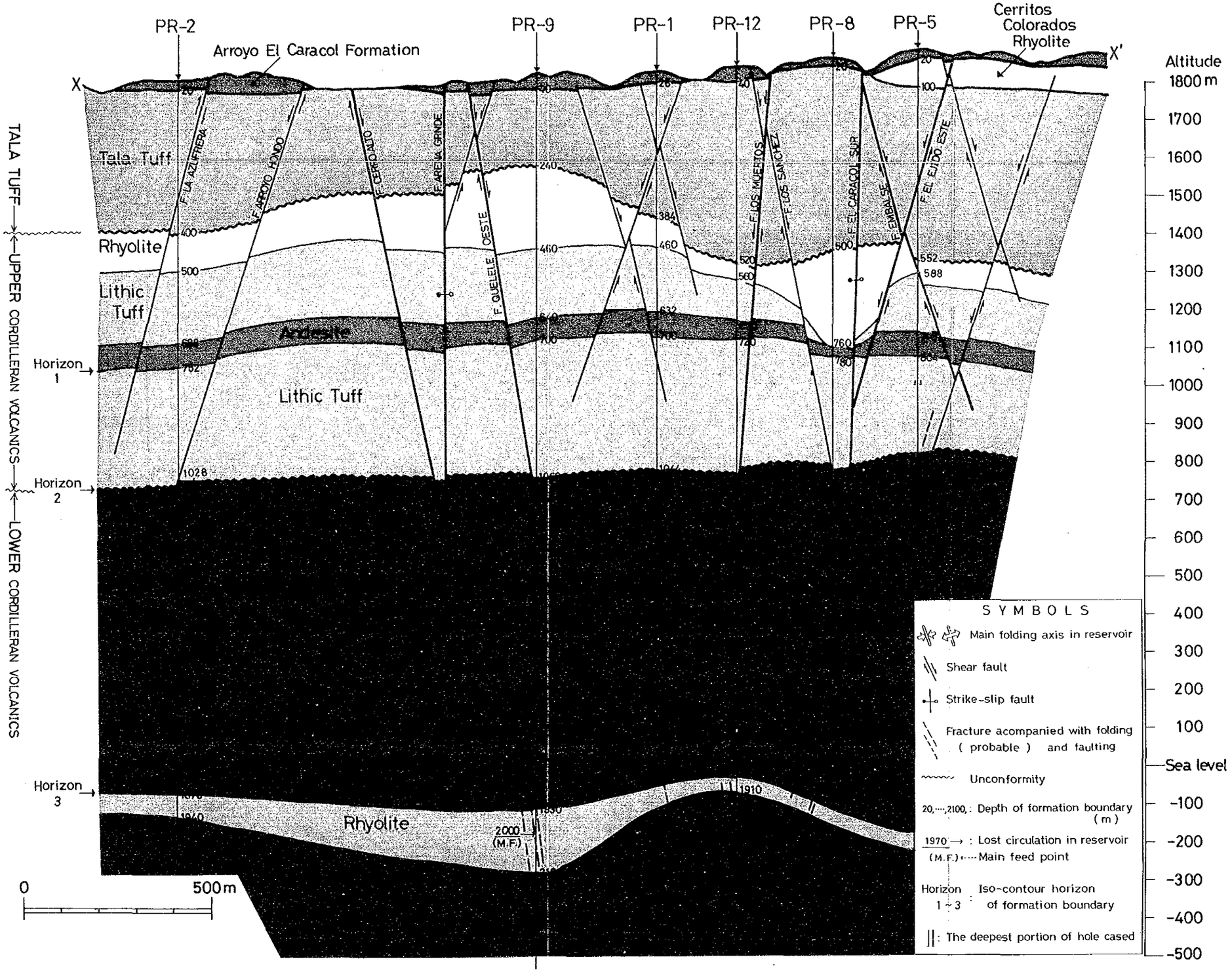

Fig. III. 1-8 Profile of Subsurface Structure in NW-SE Direction

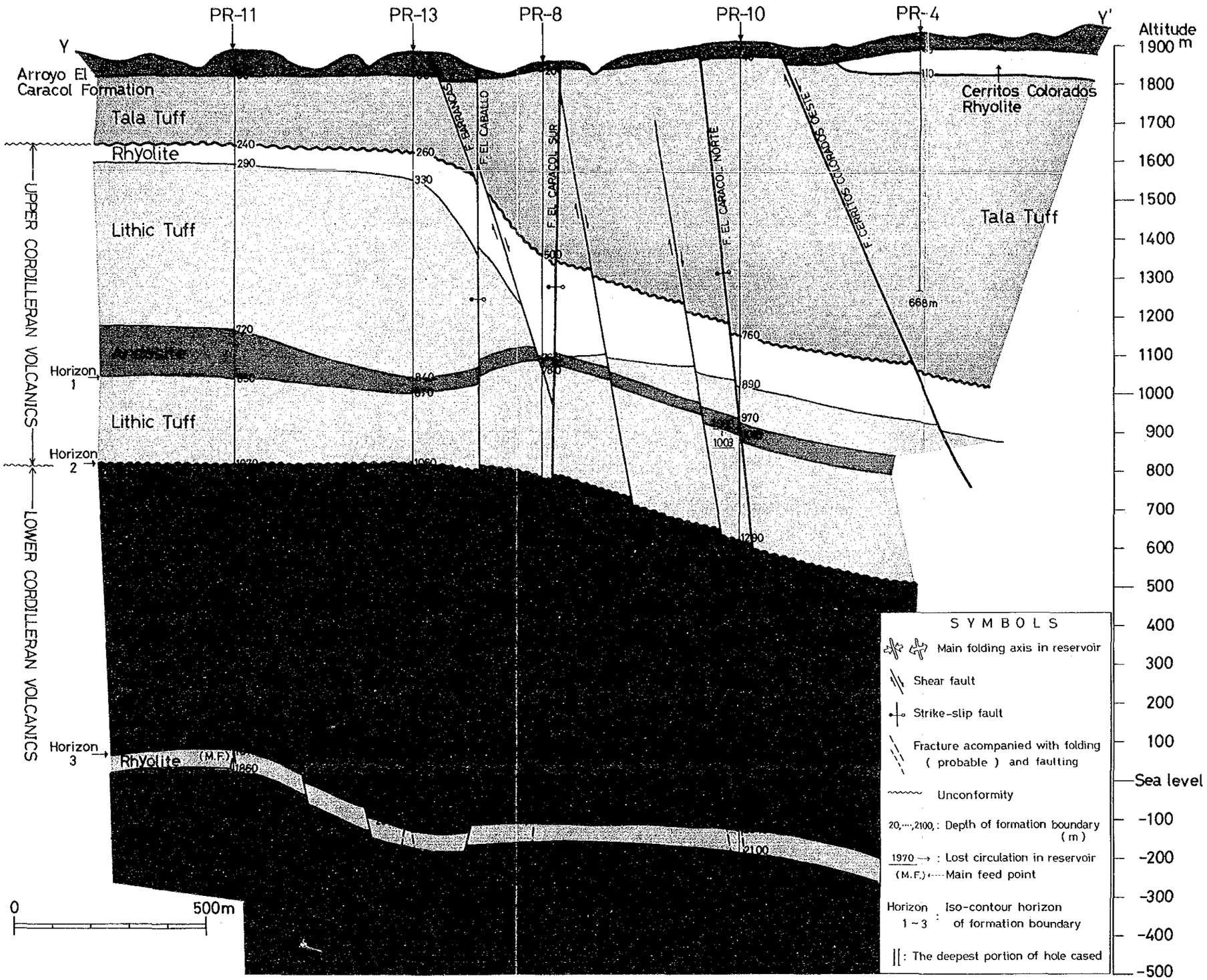

Fig. III. 1-9 Profile of Subsurface Structure in NE-SW Direction

1.2 Subsurface fracture system

As shown in Figs. III.1-8~9, shallow fracture system above about 1,000 m in depth is different from fracture system below about 1,000 m consisting of the main reservoir. Characteristics of both fracture system are described as follows, looking at them from the reason of differences.

1.2.1 Shallow fracture system

(1) The shallow fracture system is composed mainly of faults which are found in the surface and extended to the shallow part. NE-SW trending faults are dominant in the surface as previously mentioned.
The reason of the domination is as follows:
① The σ_1 (maximum principal stress axis) is approximately vertical and the σ_3 is nearly horizontal NW-SE. This restored stress field is considered to be formed by the collapse or the uplift of Sierra La Primavera Caldera, and to be developed in the shallow formation.
② The above mentioned stress field is also provided by the high gravity anomaly which exhibits an ellipse or a rectangle having the apse line of NE-SW trend. The anomaly was formed with the upheave existing in the shallow formation.

(2) The behavior of subsurface fractures is given by the results of tri-axial rock fracture tests in the presence of pressurized water at elevated temperatures as shown in Fig. III.1-10. In general, a type of failure in Fig. III.1-10 is decided by the dependence on brittle or ductile behavior of rocks. The brittle behavior depends upon the following factors:

i) compact and hard rocks
ii) less confining pressure
iii) large differential stress
iv) less pore or less pore pressure
v) low temperature

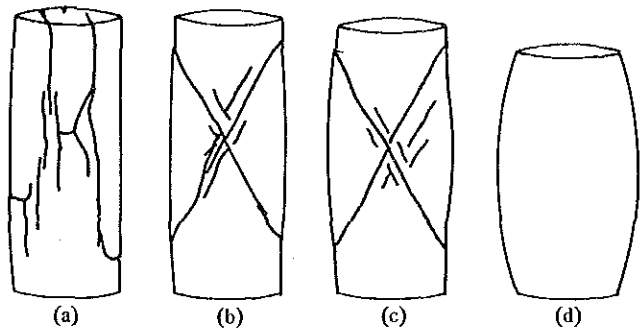

(a) extension fractures (0.1 MPa)
(b) brittle shear fractures (3.5 MPa)
(c) semibrittle shear fractures (30 MPa)
(d) ductile failure (100 MPa)

Fig. III. 1-10 Types of Failure in Experimentally Deformed Limestone at Varying Confining Pressure

When the subsurface formation is homogenous, the rock becomes generally ductile as the depth increases because of the factors of high confining pressure and high temperature. However, in case of La Primevera area, the deep-seated formation is mainly composed of andesite which is compact, hard and not porous. Therefore, the rock becomes brittle as the depth increases. The brittle behavoir in the deep-seated formation is also supported by the high density rock in the lower part of the Cordilleran Volcanics as shown in Fig. II.1-25. The density value varies remarkably between the upper and the lower of the Cordilleran Volcanics.

Moreover, the strata deformation and the fracture forming are mainly caused by the uplift subjected to vertical force. Thus, the depth increases, the more differential stress occurs.

From the above facts, it may be inferred that fractures of (b) and (c) types in Fig. III.1-10, namely shear fractures, can develop easily in the shallow part of this area. It is unreasonable to extend the shear fractures from the surface to the deeper formations, because the fracture behavior of the deeper formations is different from that of the shallow formations. The stress field above about 1,000 m, which is restored from the measurements of the remnant magnetization and the fracture orientation, is harmonized with the surface stress field (Fig. II.1-8) as mentioned Chapter II. It should be emphasized that the fracture system observed in the surface has the same system above the upper part of the Cordilleran Volcanics, and that another fracture system is dominant below the formation. The conclusions are leaded by the following discussions:

i) The restoration of stress field
ii) The results of rock fracture test
iii) The difference of rock density

(3) NW-SE trending strike-slip faults are also recognized in the shallow fracture system. These faults often cannot observe at the surface outcrop because of the difficulty in finding slip plane. From this reason, CFE did not drawn these faults in his map. However, the following evidence suggest that the NW-SE trending faults are present in this area.

① Fault planes of N80°W, 80°S and N83°W, 83°N are found in the tributaries of El Caracol near PR-12 and Hondo respectively as shown in a route map of 1 : 2,000 in scale (see Appendix I).

② The NE-SW trending faults shift their positions in the geological map (Fig. II.1-1). For example, the Quelele Oeste Fault shifts to the La Cuesta Fault, and the Los Muertos Fault continues to the El Ejido Este Fault with horizontal movement.

③ If the NW-SE trending fault does not exist, the topography surrounded by the NE-SW trending faults exhibits unnatural upheave and collapse. That is to say, if the strike-slip fault does not exist in Fig. III.1-11 (a), the faults ① and ② make separate collapses as shown in Fig. III.1-11 (b). However, when these faults are accompanied by the strike-slip fault, the topography around these faults is more natural as given in Fig. III.1-11 (c). This figure resembles the transform fault in Fig. III.1-11 (d). Many investigators point out the importance of strike-slip fault in geothermal areas. Therefore, characteristics of the NW-SE trending fault will be mentioned later from the viewpoint of regional tectonics.

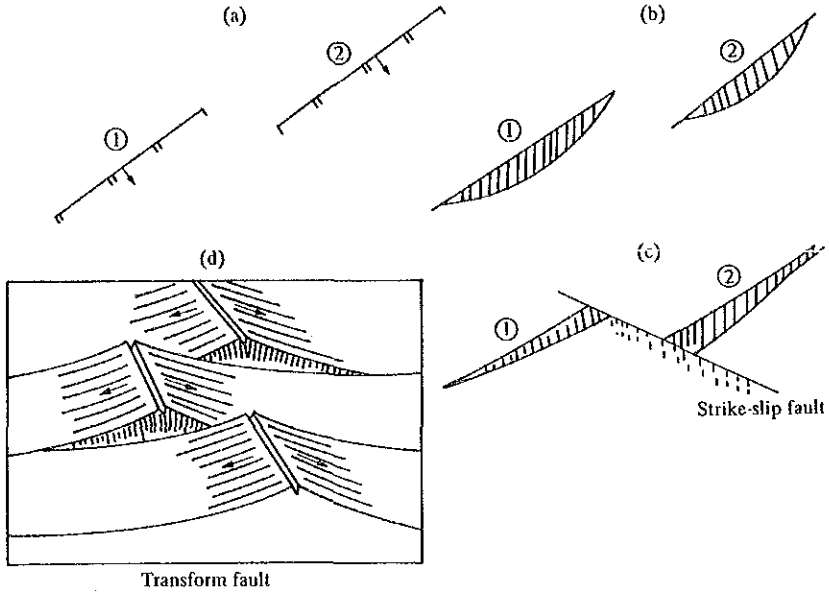

Fig. III. 1-11 Transcurrent and Transform Faults

(4) The shallow fracture system includes joint and tensional fractures in Tala Tuff. Various geothermal manifestations along the NE-SW trending faults are present in this area. They were already mentioned in detail in Chapter II.1.1.4.

1.2.2 Deep fracture system

(1) The deep fracture system is inferred to be characterized by extension fractures in Fig. III.1-10 (a) which is different from the shallow fracture system. The resistivity structure and the regional Bouguer anomaly have a NW-SE direction which is also different from a main direction of shallow fractures. However, because these facts are not direct evidence by observation or measurement, some have still considered the fracture system connecting the deep fractures with the shallow ones.

(2) Accordingly, an attempt was made on the construction of iso-contour map of specified formation boundaries based on the geological columnar sections as shown in Figs. III.1-1 ~ 7. The specified formation boundaries are the following three horizons:

Horizon 1: the boundary between the bottom of andesite and lithic tuff of the upper Cordilleran Volcanics
(This horizon belongs to the shallow formation and ranges from 800 m to 1,000 m in depth).

Horizon 2: the boundary between the upper part and the lower part of the Cordilleran Volcanics
(This boundary is nearly consistent with the boundary between the shallow formation and the deep formation and ranges from 1,100 m to 1,300 m in depth)

Horizon 3: the boundary between the bottom of andesite and rhyolite of the lower Cordilleran Volcanics

(This horizon belongs to the deep formation and ranges from 1800^{m} to 2000^{m} in depth). Iso-contours of three horizons were drawn by the proportional three-point method using computor. The following results are obtained from the iso-contour maps as shown in Figs. III.1-12～14.

Horizon 1: it is shallower to the west of PR-9 but deeper toward the northeastern and the southeastern parts as a whole. The fact shows an anticline of east-west direction from PR-9 to PR-5. The contour dips 15° to 20° generally, but dips 34° at a maximum between PR-8 and PR-10. This indicates the presence of NW-SE trending (NE dipping) faults because the strata distributes approximately horizontal in this area. Therefore, two normal-separation faults are drawn in Fig. III.1-9. The NW-SE trending normal-separation fault is not common in the shallow fracture system. The fault is, however, strike-slip with small normal component or is due to the repeated activity of pre-existing fault having a NW-SE trend and developing in the upper Cordilleran Volcanics.

Horizon 2: it is shallowest near PR-1 but deeper toward the northeastern part. Intervals of iso-contour are broad (dip gently) compared with those of Horizon 1 in spite of having the same trend of Horizon 1. The Horizon 2 shows a WNW-ESE trending structure.

Horizon 3: it shows different pattern from Horizon 1 and 2. Horizon 3 has a dome structure near PR-12 and exhibits the most upheaval structure having N-S a trend from PR-11 to PR-12. The contour dips 30° at a maximum between PR-13 and PR-11 southeast of the dome. The fact indicates the presence of NW-SE trending (NE dipping) faults. Therefore, two normal-separation faults are drawn in Fig. III.1-9.

As mentioned above, the deep fracture system is not accordance with the shallow fracture system. Thus, it is evident that the NW-SE trending faults exist in the deep formation.

(3) Regional geological survey was carried out at first stage to estimate the deep fracture system. The main reservoir in this area consists of fractures which constitute the lower part of the Cordilleran Volcanics. Therefore, it is most important to know the characteristics of those fractures. However, the Cordilleran Volcanics are not distributed in this area. Analyses have been, therefore, made to interpolate the characteristics and the structure of the Volcanics located around the Sierra La Primavera Caldera. The Volcanics contain many fractures with NW-SE, NNE-SSW and ENE-WSW trends which are observed along Santiago River to the northeast of the Caldera. While, fractures with NW-SE trend are dominant near Santa Rosa Dam in the northwest of this area. On the other hand, fractures with NW-SE, N-S and E-W trends are frequently found to the south and the southwest of the Caldera. Consequently, fractures which are dominant over the entire area have a NW-SE trend. In addition, the orientation of Mesozoic formations located in the west of La Vega is N65-70W and 50°N, and the arrangement of the Quaternary volcanoes including Tequila, Tepetiltic and Sierra La Primavera Caldera is in NW-SE direction. Therefore, volcanism in this area is assumed to be provided through fractures with a NW-SE trend in deep subsurface.

Considering the reason why the NW-SE trending fracture tends to develop in Tertiary formation around this area, the following conclusions are reached:

Many geologists pointed out that the location of the Sierra La Primavera seems to have

been controlled by regional tectonics on a large scale. The Sierra La Primavera can be thought of as the "hub of a wheel", with the NW-SE and the E-W trending portions of the Mexican Volcanic Belt and the N-S trending Cordilleran-Colima graben. The Colima graben is a failed and/or forming rift, and the Mexican Volcanic Belt is a failed transform fault. In this geological circumstance, the NE-SW or the N-S trending fractures would be open.

However, since the NW trending subduction zone is present along the Pacific coast of Mexico, the σ_1 (maximum compressive stress axis) direction is the NW-SE and the σ_3 (extensional axis) has the NE-SW direction. This area has a tendency to be occupied by the same stress field because of locating in the vicinity of the Pacific coast. (Fig. III.1-15). That is to say, the failed transform fault is so open that the NW-SE trending fault can develop easily.

(4) Taking all facts of (1) to (3) into consideration, the deep fracture system is illustrated in Figs. III.1-8~9. The basic conception of the fracture system is as follows:

① The deep fracture system has a NW-SE trend except for a part (The downflow of the surface water cools a part of PR-5 and PR-8 which is clarified by downhole temperature survey. Therefore, the shallow fractures extend to this part). This trend shows that the pre-existing fractures with a NW-SE direction acted repeatedly when the collapse or the uplift of the Caldera occurred.

② The deep fracture system is characterized by extensional fracture as given in Fig. III.1-10 (a). The shear normal faults are also expected to be present in some places as shown in the iso-contour maps (Figs III.1-14).

③ The deep fractures are appear to be restricted to the following four areas in substance:

i) the hinge area of folding with deformation of strata (ie. an axis of anticline or syncline) — provides the deep fractures of PR-9, PR-12 and PR-13 which correspond to (b) type in Fig. III.1-16.

ii) the limb area of folding — provides the deep fractures of PR-1 and PR-8 which correspond to (a) type in Fig. III.1-16.

iii) the fault zone — is developed in PR-10 and PR-11 and corresponds to (c) type in Fig. III.1-16.

iv) the extended area of the shallow fracture system — is observed in a part of PR-5 and PR-8.

Therefore, it is necessary to pay attention to the above four areas when it will select a well target for the deep fracture system.

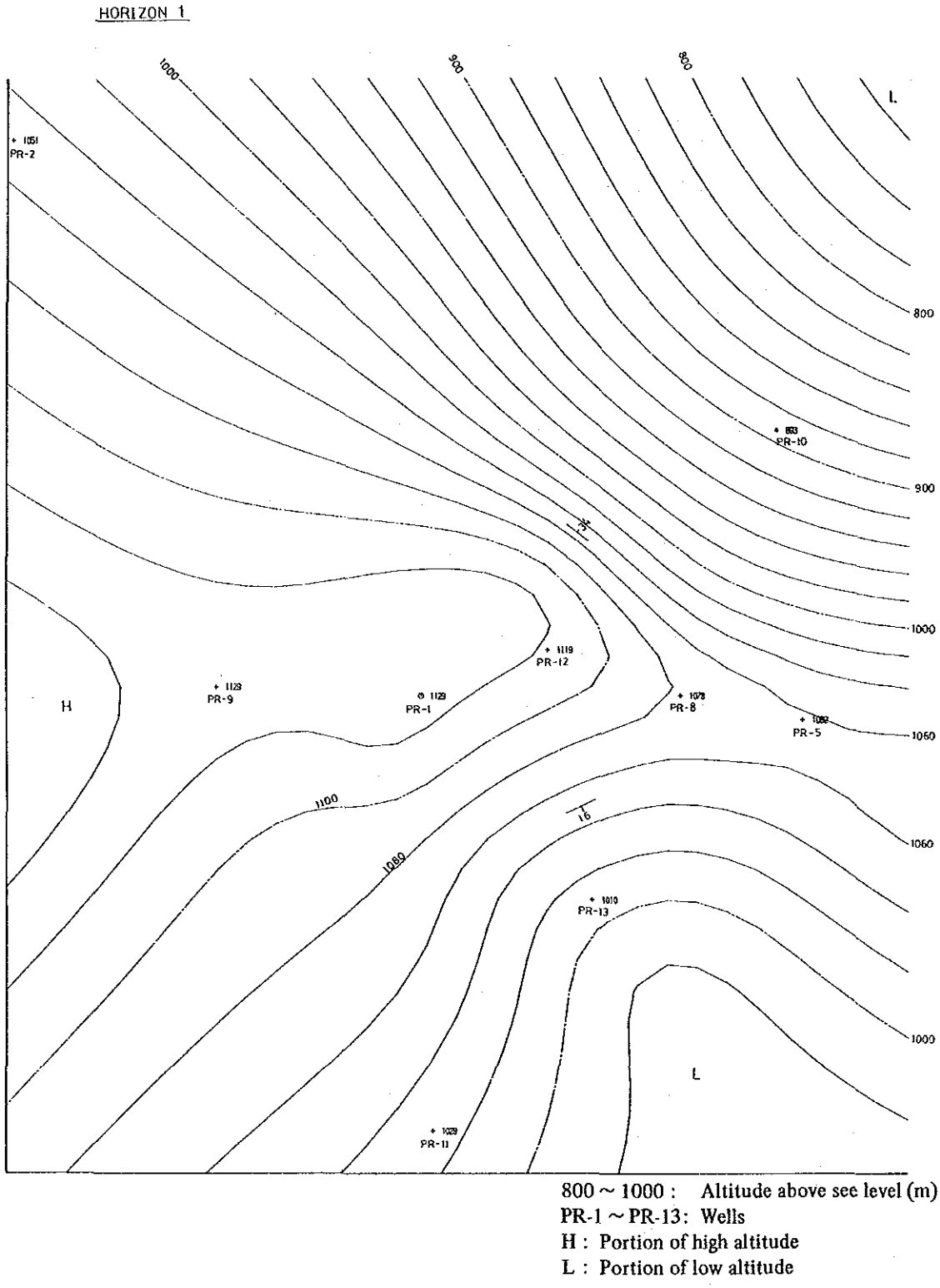

Fig. III. 1-12 ***Iso-Structural Contour of Horizon 1 (Boundary between andesite and lithic tuff of the upper Cordilleran Volcanics)***

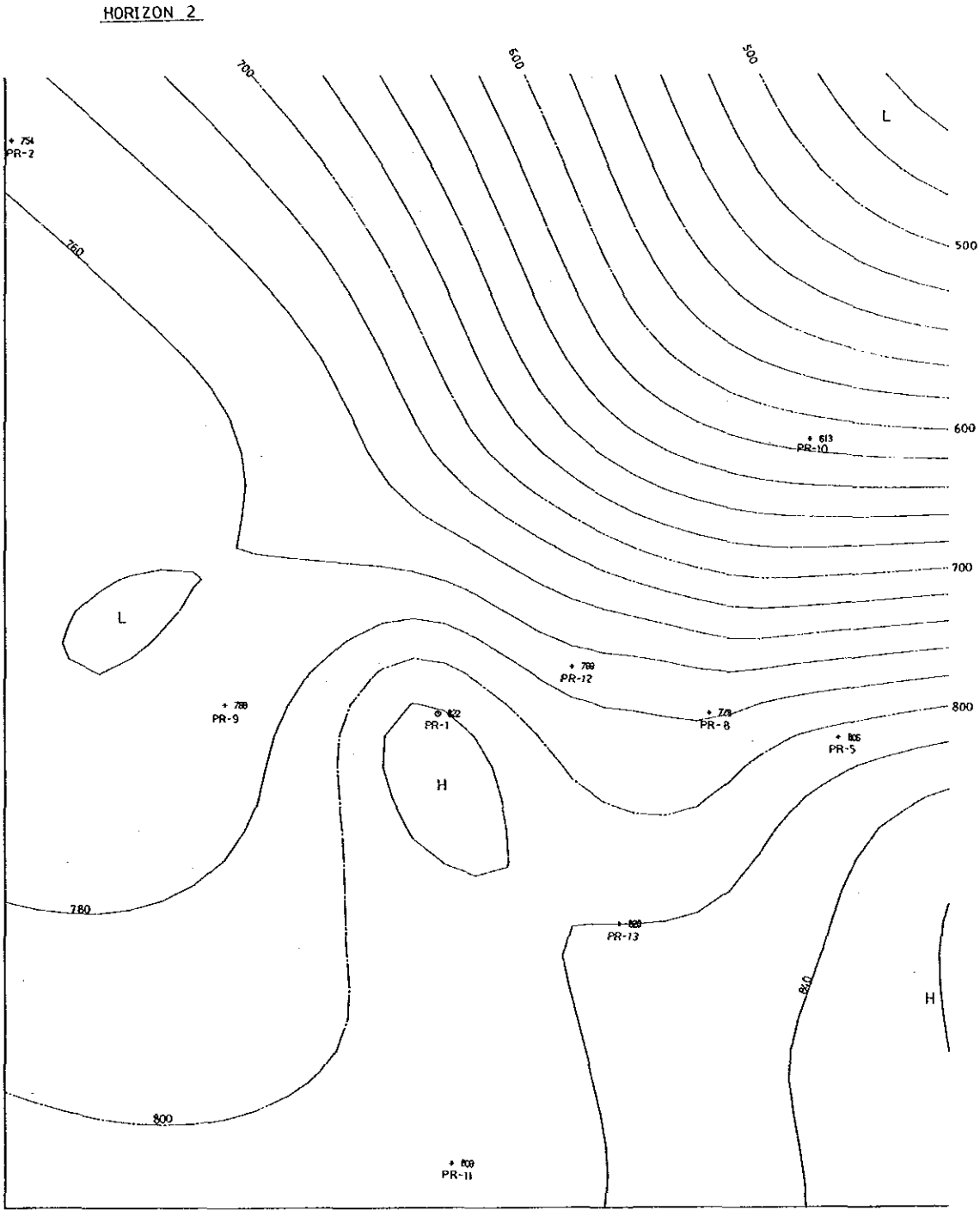

Fig. III. 1-13 Iso-Structural Contour of Horizon 2 (Boundary between lithic tuff and andesite)

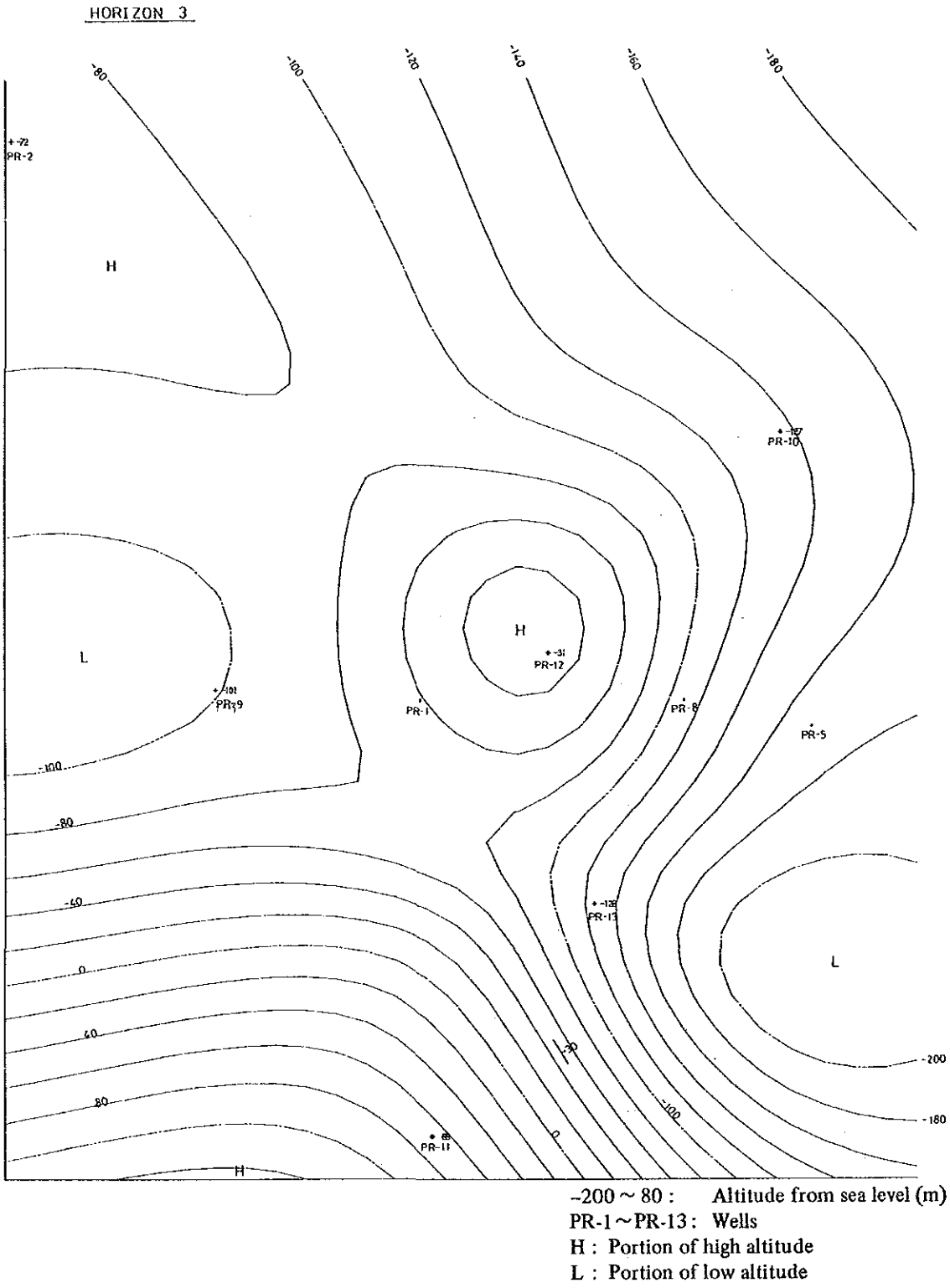

Fig. III. 1-14 Iso-Structural Contour of Horizon 3 (Boundary between andesite and rhyolite of the lower Cordilleran Volcanics)

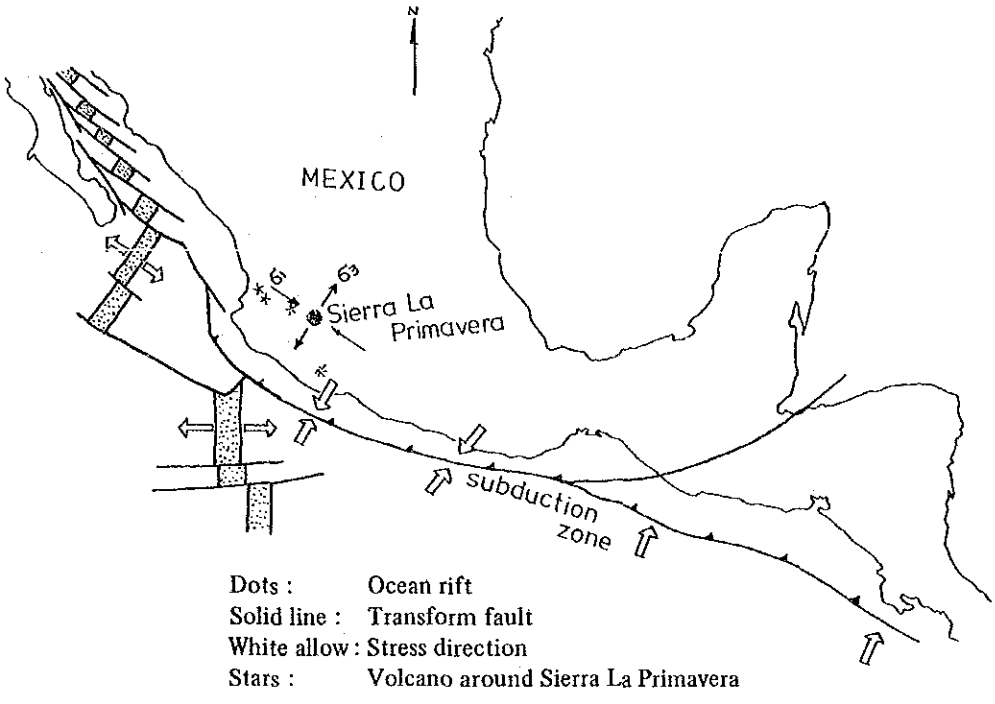

Fig. III. 1-15 Regional Stress Distribution along Pacific Coastal Area of Mexico

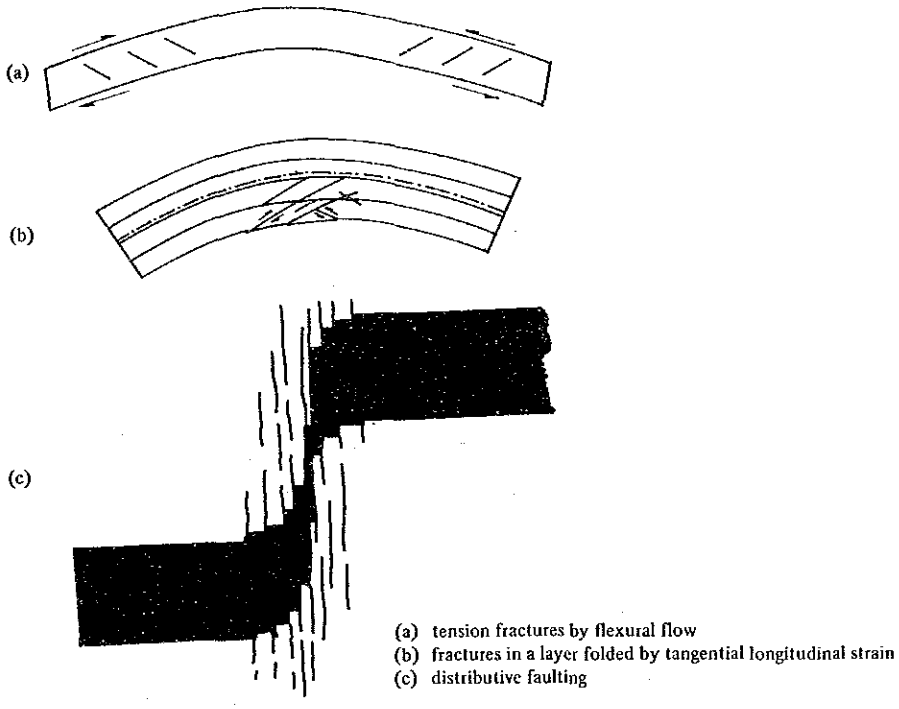

Fig. III. 1-16 Relation between Folding and Fractures

1.3 Subsurface temperature profile

(1) Temperature profile by downhole temperature measurement

Subsurface temperature has to be considered in three dimensional structure. It is difficult to draw horizontal profiles in case of a few measuring data. Therefore, vertical temperature profiles are only made in this Chapter. The horizontal profiles will be drawn in the results of simulation (Figs. III.2-41～45).

We made a recent temperature profile based on the results of static temperature measurements which were carried out after enough temperature recovery. (Fig. III.1-17) The static temperature values are shown in Figs. III.1～7 (integrated columnar sections). An upflow zone of high temperature of more than 300°C is recognized in the vicinity of PR-1, PR-9 and PR-12. Geothermal fluids in this area, therefore, are ascending from the deeper part of this vicinity along vertical fractures recently.

The result of exploration in the first stage indicates that the center of the upflow was considered to be located in the deeper part of PR-1 and PR-8, and be consistent with the uplift zone. On the contrary, the exploration in the second stage and the downhole measurements of each well show that two high temperature anomalies are found near both PR-9 and PR-12 in the main reservoir ranging from 1,000 m to 2,000 m in depth. As compared Fig. III.1-8 with Fig. III.1-17, PR-9 is situated at an axis of syncline and PR-12 is located at an axis of anticline. Vertical fractures related to the folding axes cause a shape of two separate upflow zones.

However, the upflow zones seem to unite below the part of more than 340°C and the center of the upflow appears to be located beneath PR-1. Because the temperature profile is drawn by the interpolation of measuring values, the profile is obscure in its shape. For preference, chemical analysis of fluids reveals that the center of high temperature fluids exists in the deeper part of PR-12.

(2) Temperature profile by minimum homogenization temperature of fluid inclusion.

Subsurface temperature profile is also made by the data of minimum homogenization temperature of fluid inclusion. The data are measured by using cuttings obtained from each well. The profile in Fig. III.1-18 is the same position as that in Fig. III.1-17 through RC-1, PR-2, PR-9, PR-1, PR-12, PR-8 and PR-5. Fig. III.1-18 shows that the upflow zone of high temperature of more than 280°C is recognized in the vicinity of PR-1, PR-12 and PR-8. On the contrary, the temperature at 2,000 m deep in PR-2 records 200 to 240°C showing low grade.

Geothermal fluids were also ascending from the deeper part of near PR-1, PR-12 and PR-8 along vertical fractures in an epoch of trapping of fluid inclusion.

Moreover, it has been made clear that geothermal fluids almost flash in the formation surrounding the well, forming two-phase flash flow entirely in the wellbore. The phenomenon is clarified by the dounhole temperature and pressure measurements under the condition of producing fluids.

(3) Thermal history in this area

Subsurface temperature in this area rises in a steady curve (or in constant) in a period from rock alteration stage up to the present. That is to say, at an epoch of the alteration, altered

minerals including Montmorillonite and Laumontite were formed under the low temperature of less than 250°C. At an epoch of trapping of fluid inclusion, temperature seems to be a little lower than recent temperature.

As compared Fig. III.1-17 (recent temperature) with Fig. III.1-18 (temperature at trapping of fluid inclusion), it has been made clear that the zone of high temperature has spread out toward the western part of this area. This fact suggests that the geothermal development should progress toward the west, considering the NW or WNW trending fractures.

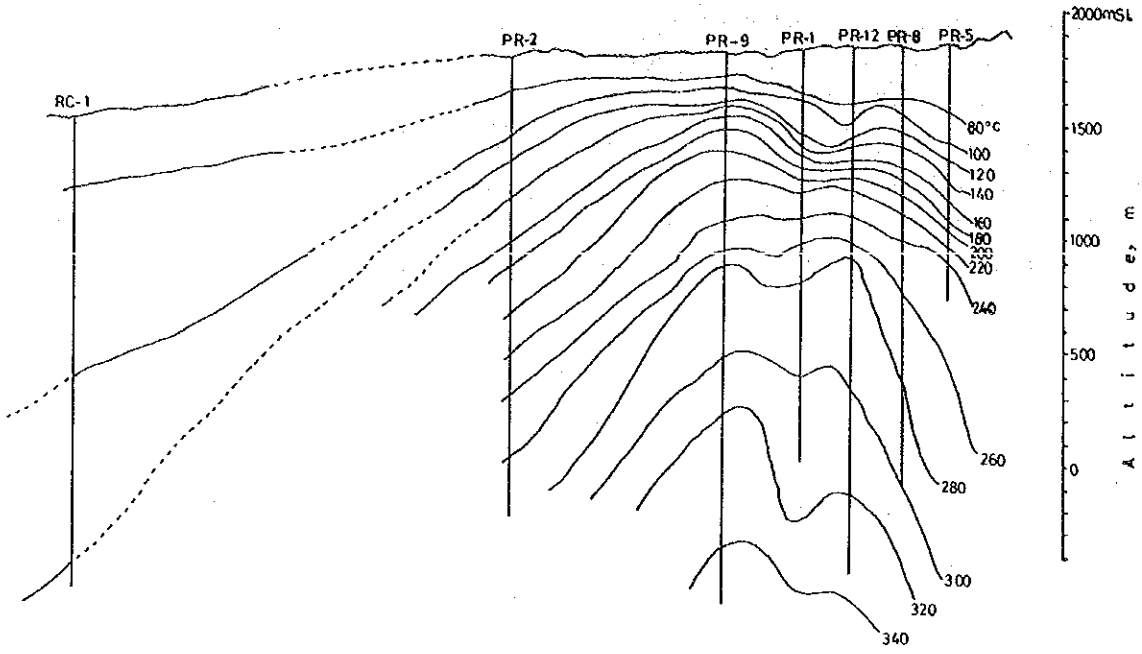

Fig. III. 1-17 Cross-Section of Downhole Temperature Profile

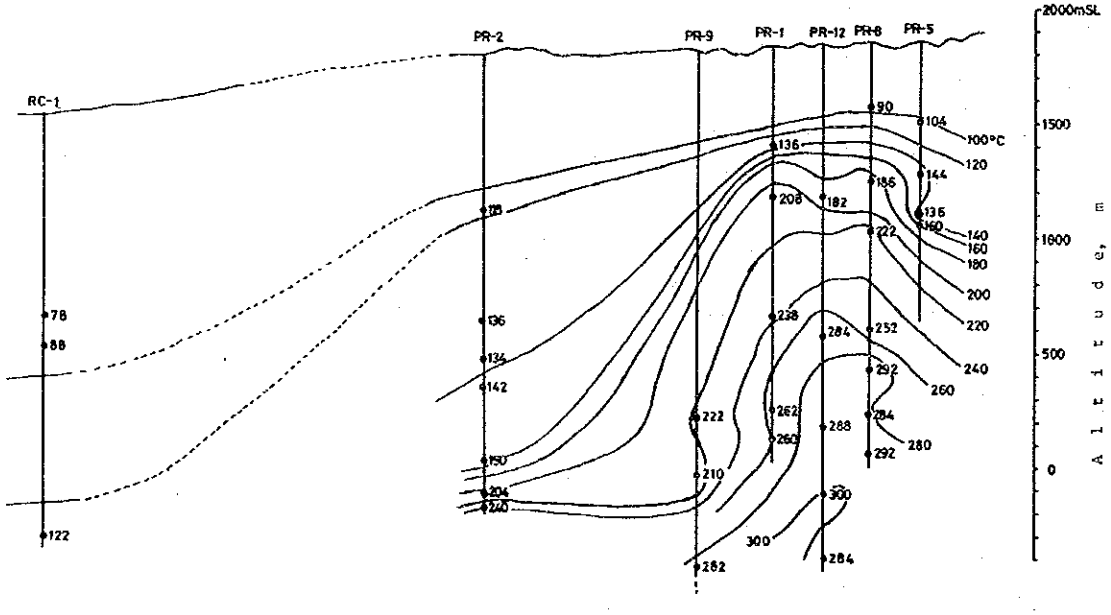

Fig. III. 1-18 Cross-Section of Minimum Homogenization Temperature Profile

1.4 Chemical analysis of wellbore fluids

A flow mechanism of geothermal fluids is investigated by chemical analysis of steam, condensed water and hot water from PR-1, 2, 4, 5, 8, 9, 12 and 13. The analysis of exploration at first stage excepted PR-9, PR-12 and PR-13 from the above mentioned wells. The result of the analysis concluded that the deep-seated geothermal water originates in the deep formation near PR-1 and flows toward PR-8, PR-5 and PR-4 being influenced by mixing with surface water. Chemical characteristics of hot water in PR-2 are different from those in other wells. That is to say, an independent separate reservoir exists around PR-2.

(1) Analysis by gaseous component in steam

Total gaseous concentration in steam of La primavera area ranges from 1.76 to 3.46 vol%, indicating high concentration in comparison with the average of Cerro Prieto and Japanese geothermal areas. CO_2 gas is rich in gaseous component and reaches approximately 99 vol% in concentration. CH_4 gas is extremely rich (14,400 ppm) in gas of PR-11 which emits only gas without steam and H_2S gas.

Fig. III.1-19 shows the ratios of He/Ar and N_2/Ar in gas. High value of the ratio of [(He/Ar) steam/(He/Ar)] air means that steam is derived from the deep gas. The values of wells in this area are close to the mixing line with the deep gas and the dissolved air in water at 10°C.

When the small-sized separator is used for gas analysis, hot water flows into the seperator with steam and flashs again on the inside of the separator. In this case, we obtain the steam containing poor gas in concentration. Therefore, we compare with the value of gas ratio using the large-sized separator.

The ratio of [(He/Ar) steam/(He/Ar) air] is of PR-12 followed in order of its high ratio by PR-13, PR-8 and Hervores de la Vega (a hot spring). Therefore, the deep gas consisting of high *ratio of [(He/Ar) steam/(He/Ar) air] is ascending from near* PR-12, *and is mixing with the* surface water during flow toward PR-8 and PR-13.

(2) Analysis by chemical components of hot water

Chemical composition of hot water in La Primavera is rich in Na and Cl which show neutral or weak alkali. Cl-concentration ranges from 800 to 1,300 mg/l.

① The molar ratio of B/Cl is 0.4 to 0.5 in hot water and spring water. This means chemically homogeneous characteristics of reservoir over a wide area. The concentrations of B and Cl are controlled by a mixing with the high salinity hot water and the surface water *containing low dissolved component because of uniform ratio of B/Cl. That is to say,* the separation of steam and liquid has not generate in the formation, resulting in the uniform ratio of B/Cl. From the above mentioned fact, the vapor dominated reservoir does not exist although high temperature of more than 300°C recognized in this area.

② An isotopic composition diagram is prepared to study on the origin of water and its fluid flow mechanim as shown in Fig. III.1-20. The values of hot spring distributed in this area put on the straight line expressed by an equation $\delta D = 8 \times \delta^{18}O + 10$, whereas both δD and $\delta^{18}O$ values of hot water shift to heavier position in the diagram. The fact

is caused by a mixing mechanism of the surface water with the hot water of high $\delta^{18}O$ value due to an oxygen isotope exchange with rock in the subsurface reservoir.

③ Fig. III.1-21 shows the relation between enthalpy and chloride concentration of hot water before flashing in the reservoir. The data measured recently are adopted in this figure to avoid the error by unstable production in the early stage. That is to say, we use the data of PR-1, 8, 9 and 12 by CFE measuring in 1987 to 1988 and of PR-1, 8, 12 and 13 by JICA. An adequate correlation is estimated from the relation between enthalpy and Cl-concentration. A coefficient of correlation is 0.83 and a regression equation is $h = 56.9 + 0.397 \times Cl$ (where h means enthalpy and Cl means Cl-concentration).

The fact shows a mixing mechanism of high temperature hot water with low temperature surface water in the reservoir. The following are the descending order of high temperature and high Cl-concentration.

PR-12 > PR-1 > PR-9, PR-13 > PR-8

Therefore, the PR-12 well is located in the portion of the highest temperature, the highest Cl-concentration and the highest ratio of He/Ar, namely the center of the upflow. The surface water influences strongly from PR-1 to PR-8 through PR-9 and PR-13.

④ The SO_4 concentration tends to be high in the well influenced by the surface water. The product of Ca and SO_4 is $6.9 \sim 8.3 \times 10^{-9}$ in PR-1 and PR-12, and is $1.2 \sim 1.5 \times 10^{-8}$ in PR-8 and PR-13. High value of the product signifies the high solubility of anhydrite which is strongly influenced by the surface water. From this fact, PR-1 and PR-12 are situated near the up-flow zone.

The result of the exploration at first stage concluded that the up-flow zone is located near PR-1 and PR-8. More detailed investigation at second stage reveals that the hot water of high temperature of more than 330°C is ascending from the deeper part of PR-12, and flowing in and around the reservoir.

The NW-SE and NE-SW trending fractures have an important role as pathways of the flow.

⑤ The values of chemical thermometer as to the wells of this area are given in Table II.1-1. The exploration at first stage concluded that the Na-K-Ca geothermometer seems to be adequate. However, the Na-K thermometer in PR-12 and PR-13 shows the reservoir temperature. The detail of chemical thermometer will treat in separate section (Chapter III.2-4.(2)b).

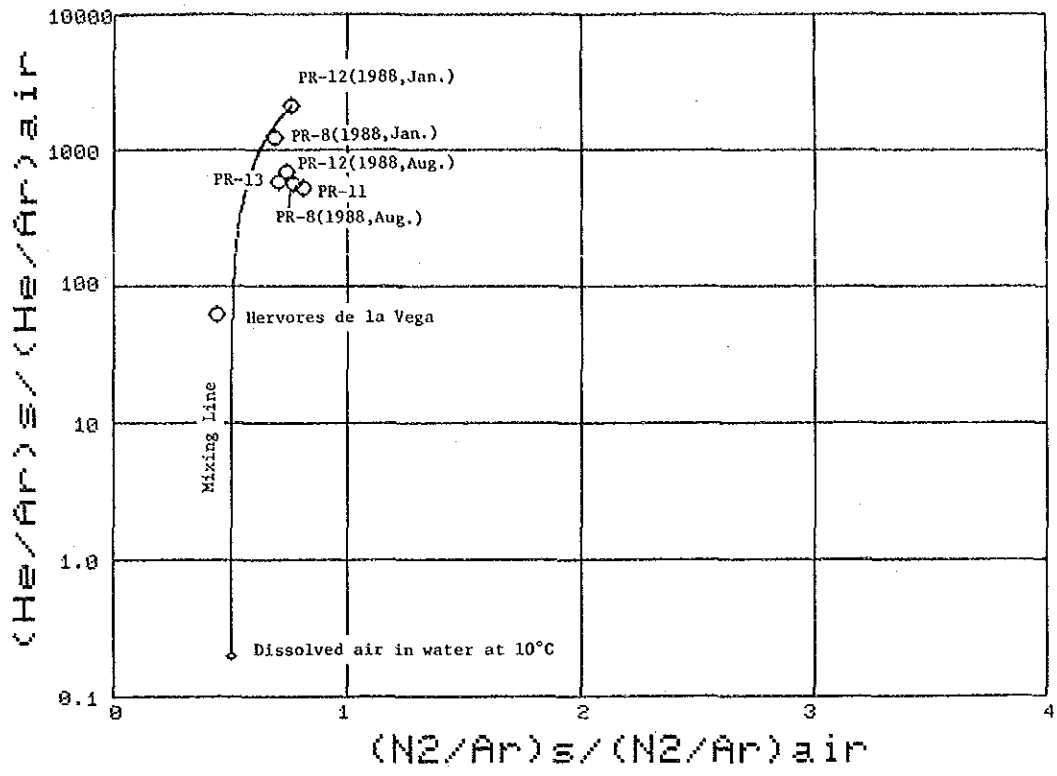

Fig. III. 1-19 **Relationship between He/Ar and H_2/Ar Ratios of Geothermal Gaseous Discharge**

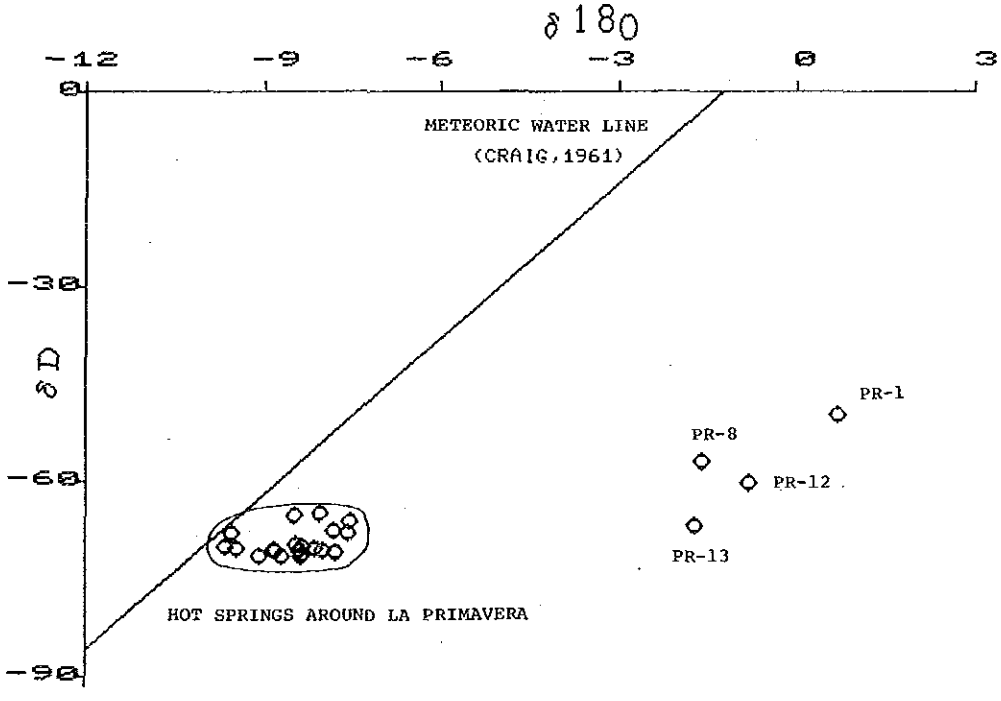

Fig. III. 1-20 **Isotopic Composition of Geothermal Water**

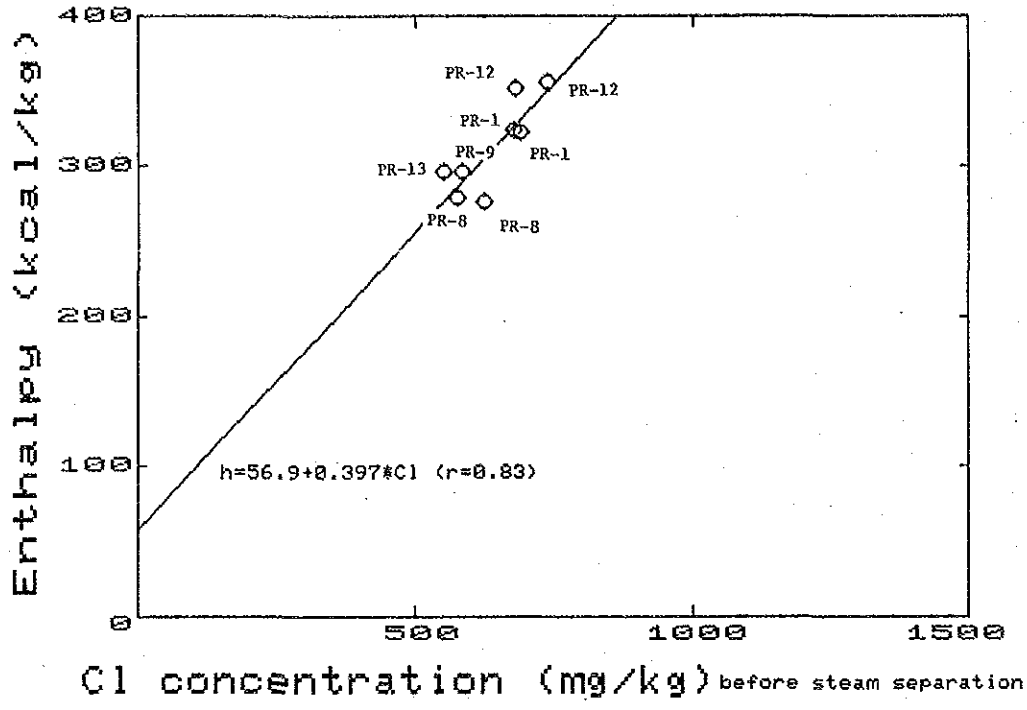

Fig. III. 1-21 Relationship between Cl Concentration and Enthalpy of Hot Water

1.5 Summary of geothermal reservoir structure

The integrated analysis on geothermal reservoir has already been carried out by the exploration in the first stage (Chapter II,2-1). The basic conception of geothermal reservoir does not change, although the data was added by the exploration in the second stage and the survey of CFE. However, the following differences in detail arose from both stages:

(1) Reservoir structure by exploration at first stage

① The main reservoir consists of fractures in the Cordilleran Volcanics occupying below about 1,000 m in depth. The fractures have a NW-SE trend estimated by MT and gravity surveys.

② The NW-SE trending fractures were re-activated by the uplift of the Caldera. The center of the uplift is inferred to be located near PR-1 and PR-8.

③ The portion of high temperature is also situated near PR-1 and PR-8. The fact is estimated by the chemical thermometer, the fluid inclusion survey and the downhole temperature measurements. This geothermal area is underlain by the reservoir consisting of vertical fractures where the upflow is consistent with the uplift.

④ The extent of geothermal reservoir is estimated to be about 2 km in the NW-SE direction and about 1.5 km in the NE-SW direction, showing a rectangle whose main direction is NW-SE. Northern, southern, eastern and western margins of the reservoir are near PR-10, about 1 km south of PR-8, about 1 km east of PR-1 and near PR-2 respectively.

⑤ The fluids of high temperature are ascending from the deeper formation near PR-1 and are flowing toward PR-4 through PR-8 and PR-5 along the NE-SW trending shallow faults. The mechanism is considered by the chemical analysis of hot water from the wells. Hot water of PR-2 is ascribed to a independent separate reservoir which is formed by the different mechanism.

(2) Added and confirmed results by exploration at second stage and CFE's investigation

① According to the iso-contour map based on geological columns of each well, the lower Cordilleran Volcanics, which is the main reservoir in this area, exhibits the most upheaved shape near PR-12 and the presence of the NW-SE trending faults (dips NE) between PR-11 and PR-13. The fact indicates that the main trend of shallow faults is different from that of deeper faults.

② The NW-SE trending deeper fractures originated in the Tertiary and basement system and acted repeatedly by the collapse and the uplift of the caldera forming, resulting in the formation of extensional fissure. The fractures are appear to be restricted to the hinge of folding, the limb of folding and the fault zone which are accompanied with the deformation of strata in substance.

③ The reconsideration of downhole temperature curves of PR-5 and PR-8 makes clear the downflow of the surface water by the recognition of local low temperature in high temperature area. The NE-SW trending faults existing in the shallow formation extend down to the portion of low temperature.

④ Downhole temperature measurements and minimum homogenization temperature of fluid inclusion show that the up-flow zone of high temperature is recognized in the vicinity of PR-1, PR-9 and PR-12.

However, the recent temperature profile indicates that two high temperature anomalies are found near both PR-9 and PR-12. This is due to two vertical fracture zones related to the folding axes. Moreover, subsurface temperature rises from an epoch of rock alteration up to the present through an epock of trapping of fluid inclusion. The zone of high temperature has spread out toward the western part of this area.

⑤ Chemical analysis of wellbore fluids reveals a mixing mechanism of the surface water with hot water of more than 330°C. The hot water of high temperature originates in the deeper formation near PR-12 and spreads from PR-12 to the surroundings through PR-1, PR-9, PR-13 and PR-8.

The above mentioned facts indicate that the center of both the uplift and the up-flow is located in the deeper formation of PR-12, and the location of the center becomes more precise than that by exploration at first stage.

(3) Structural development of geothermal reservoir

A conceptual reservoir model drawn in Fig. II.2-1 is acceptable at the second stage. Detailed structure is shown in Figs. III.1-8 and 9. Table III.1-1 shows the structural development of reservoir and geologic history.

It is the most important point for the structural development to consider by what mechanism and when the fractures formed. It is evident by the geological and paleo-stress survey that the fractures are related to the formation of the Caldera. However, it cannot be decided that the fractures are formed whether by the uplift or the collapse.

The following reasons reveal that the fractures are mainly formed by the uplift:

① If the collapse of the Caldera occurred at a stroke, the σ_1 is vertical, resulting in the formation of fractures shown in Fig. III.1-10 (a) to (c). However, the results of geological survey and well drilling show that the Tala Tuff, provided from the eruption of the Caldera, ranges in thickness from 200 m to 700 m and is subdivided into more than eleven flow units. The facts indicate that the Caldera was not formed at a stroke, but the collapse and the eruption proceeded simultaneously.

Therefore, the stress concentration was too small not to form fractures newly by the collapse. For preference, the collapse has facilitated the movement or the opening of the pre-existing fractures in the Cordilleran Volcanics.

② The uplift of the Caldera occured about 60 to 75 thousand years ago (MAHOOD, 1980). We can regard as appropriate that, rather than resurgence, the uplift appears to have been related to insurgence of the magma provided from wide areas, as has been pointed out by MAHOOD. This fact is also supported by the rise of subsurface temperature from an epoch of trapping of fluid inclusion.

When the uplift happened, the strata itself was under the condition of tensional stress. Thus, the NE-SW trending normal faults was developed in the shallow formation, while the pre-existing fractures with a NW-SE trend acted repeatedly and re-opened in the deep formation.

Thermal history is not given in Table III.1-1. This is because of no evidence of age determination for the alteration and the trapping of fluid inclusion. Although the age determination is required, the following estimate is possible:

① Neutral to weak alkali altered minerals including Montmorillonite, Sericite, Zeolite are not controlled by the fractures on the surface. They were made before the uplift of the Caldera.

② On the contrary, acidic altered minerals including Kaolinite, Alunite are controlled by the NE-SW trending fractures. They are related to the uplift.

③ The minimum homogenization temperature of fluid inclusion is comparatively harmonized with downhole temperature. Therefore, the inclusion was trapped about the present time.

Table III. 1-1 Summary of Geothermal and Geological Histories of the Sierra La Primareva Geothermal Area

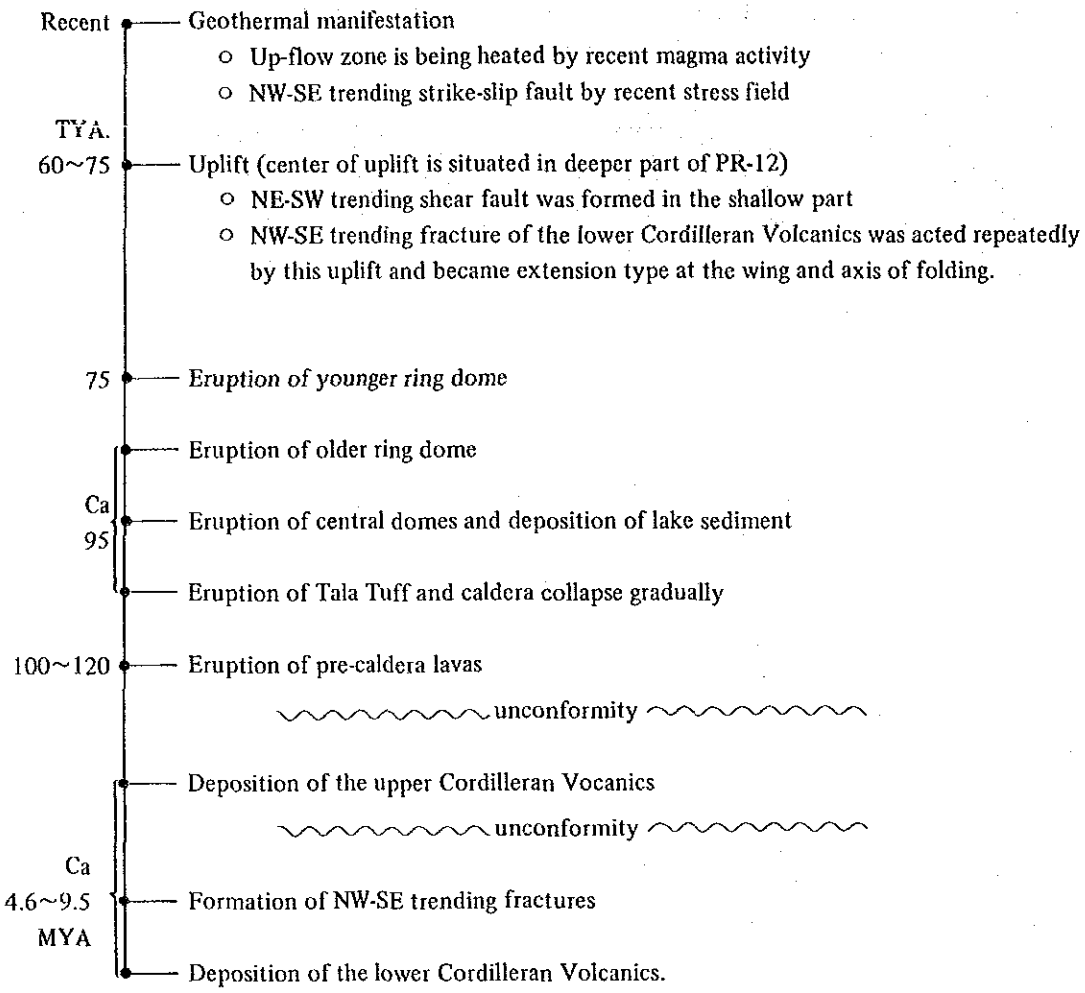

Remarks TYA: thousand years ago.
MYA: million years ago.

2. Reservoir Evaluation by simulation method

2.1 Summary of simulation method

Geothermal reservoir is evaluated by various methods including a lumped-parameter (tank) model, a distributed-parameter (grid) model and a volumetric method. The grid model is adequate to use for heterogeneous and anisotropical reservoir having a long production history. The following description is an approach to predicting the behavior of La Primavera field.

① Mathematical modeling of geothermal reservoir
② History match to the measured value
③ Future prediction of reservoir behavior

(1) Mathematical modeling

Geological systems (geothermal reservoir) require that numerious parameters are defined in order to adequately model the reservoir. These parameters involve reservoir shape, permeability distribution, heat capacity, boundary conditions, initial conditions (pressure and temperature), specification of production and injection and so on. Reservoir evaluation by the grid model should begin making a conceptual model at the initial stage using these parameters.

(2) History match

By using the mathematical model and a simulator, we can obtain output data such as pressure, temperature and water saturation in each grid at an optional time. The match is to compare the output data (calculated data) with the pressure drawdown and temperatures measured in selected wells. The mathematical values of parameters in the primary data are subject to adjust during the iteration process untill the calculated values fit into the measured values. That is to say, the history match simulation proceeds in trial- and error fashion. The calculation finishes when the match between the observed and calculated values is reasonable.

(3) Future prediction

From the history match, we can obtain the best model that can be used to predict the response of the reservoir and individual wells to various exploitation schemes. The purpose of future prediction is ultimately to estimate a capacity of power production with future wells. Although additional new wells for the prediction are tentative, the predictions for different cases can determine the lower limit of pressure, temperature and water saturation changes by the long performance production. A wellbore flow simulator is required to predict the production history with high accuracy in addition to the reservoir simulator.

A conception of the above three stages is illustrated in Fig. III.2-1.

(a)

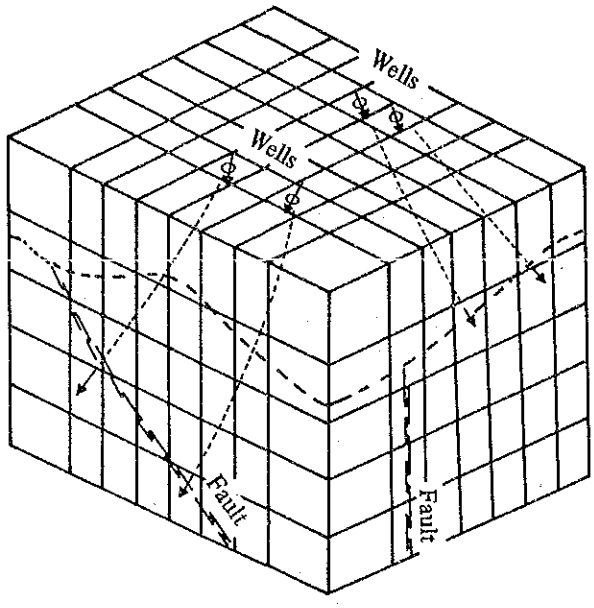

(b)

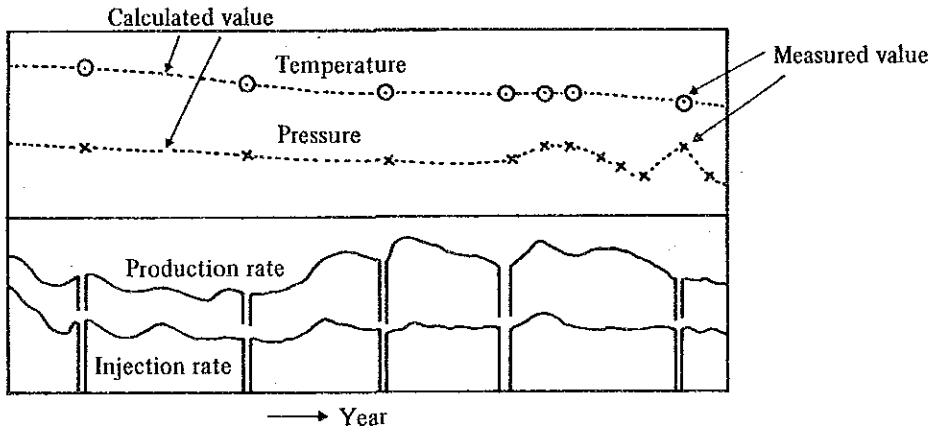

(c)

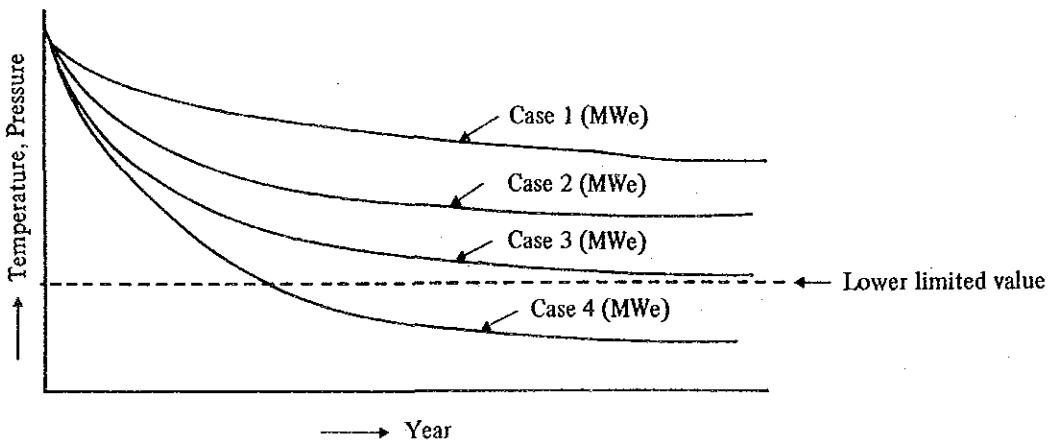

(a) Mathematical grid modeling of reservoir
(b) History matching against measured values
(c) Prediction based on best matched model Case 3 (MWe) is adequate capacity in this figure.

Fig. III. 2-1 Conception of Reservoir Simulation

2.2 Summary of simulator

The geothermal reservoir simulator used for the reservoir evaluation in La Primavera area is a three-dimensional double-porosity grid program which is capable of the two-phase multi-component flow. In this simulator, the laws of conservation of mass and energy are expressed by difference equations by the fully implecite method that are converted into a linear form by the Newton-Raphson method. The coefficient of correction in this method is soived by the successive over-relaxation method of one-line.

The basic form of the laws of conservation of mass and energy used for the simulator is given below.

- The law of conservation of energy

$$-\nabla\cdot(h_w\rho_w u_w + h_g\rho_g u_g) - \nabla\cdot U_c + q_{vw}h_w + q_{vg}h_g + q_{LV}$$
$$= \frac{\partial}{\partial t}(\phi\rho_w S_w u_w + \phi\rho_g S_g u_g) + \frac{\partial}{\partial t}[(\rho c)_f(1-\phi)T] \quad \text{(3.2.1)}$$

- The law of conservation of mass

$$-\nabla\cdot(\rho_w u_w + \rho_g u_g) + q_{vw} + q_{vg} = \frac{\partial}{\partial t}(\phi\rho_w S_w + \phi\rho_g S_g) \quad \text{(3.2.2)}$$

where,

∇ : Hamiltonian operator

$$\nabla\cdot F = \frac{\partial F}{\partial x} + \frac{\partial F}{\partial y} + \frac{\partial F}{\partial z}$$

ρ : fluid density
u : convective velocity
U_c : conduction rate
h : specific enthalpy
T : temperature
S : water saturation
ϕ : porosity
t : time
q_v : source or sink
q_{LV} : heat loss or gain
$(\rho c)_f$: formation specific heat

suffix

w : liquid phase
g : vapour phase
v : per unit volume

The characteristics of the simulator are as follows:

① It can use both porous and double-porosity models.
② It is capable of various phases such as liquid, two-phase and vapour.
③ It can use a great number of grid, and is possible to approximately 20,000 grids.
④ The solution converges to a particular state for various problems because of the fully implecite method. Therefore, the calculation speed is high.
⑤ It can use over a wide range from 1°C to 374.5°C and from 0.001 bar to 1,000 bar.

2.3 Preparation of mathematical grid model

In anticipation of a partial two-phase flow in the formation in La Primavera area, the double-porisity grid model was adopted in the simulation. We treated the fluids of source, sink and flowing formation as pure water which does not contain disolved chemicals.

(1) Division of grid and layer

At first, the areal division of grid model is based on the following consideration:

① The areal grid model covers an area of 3 km^2 (about 2 km in the NW-SE direction and about 1.5 km in the NE-SW direction) which is estimated in Chapter II.2.1.(3).

② The grid model also covers an area of 2.73 × 1.545 km^2 estimated by CFE (J. Rosas E., 1988).

③ The existing wells are superimposed on a each computation grid. A grid does not involve two or more wells.

④ The grids divided into squares every 100 meters exist over the wells that have the good efficiency and are drilled in the center of the reservoir. While, the surrounding grids are larger in area.

⑤ The areal grid model includes the main geological structures and the low resistivity zone of MT method.

The areal extent is a total of 20.16 km^2 (4.8 km in the NW-SE direction and 4.2 km in the NE-SW direction), divided by 20 × 18 grids shown in Fig. III.2-2

Secondly, the vertical section is divided into five layers.

Layer 1 (1,800 ~ 1,300 m above sea level, 500 m in thickness)

: This layer is good permeable because complete lost circulations occur in the encounter joints and tensional fractures of the Tala Tuff and of a part of the upper Cordilleran Volcanics.

Layer 2 (1,300 ~ 500 m above sea level, 800 m in thickness)

: This layer is impermeable. Lost circulation does not occur except for fault zones. This layer includes mainly the upper Cordilleran Volcanics and partially the lower Cordilleran Volcanics. The fault system recognized in the surface can extend to this "shallow" layer.

Layer 3 (500 m above ~ 100 m below sea level, 600 m in thickness)

: This layer is the main reservoir consisting of vertical fractures, and is correlated to andesite of the lower Cordilleran Volcanics. This layer includes the main feed points ranging from 1,400 m to 2,000 m in total depth.

Layer 4 (100 ~ 900 m below sea level, 800 m in thickness)

: This layer corresponds to the lower Cordilleran Volcanics underlain by basement granite. Because PR-9 only penetrates this layer, the physical property is hardly known. It is considered to be less permeable layer.

Layer 5 (900 ~ 1,500m below sea level, 600 m in thickness)

: This layer consists of basement granite.

The division of layer and the sketch of stereogram are shown in Figs. III.2-3 and III.2-4 respectively.

(2) Boundary condition

To compute using the grid model, the buffer zone is required at the outside of an extent of the grids (20 × 18 × 5 = 1,800 grids). The length or the thickness of the buffer zone is boundless. The boundary condition between the grid and the buffer zone is given below.

① All boundaries are open system. The fluids can pass easily through the boundaries maintaining the initial temperature and pressure.

② The physical parameters (initial temperature, initial pressure, permeabilities) of the boundary planes is the same values as those of their neighbour grids (blocks).

③ In the best matched model, the permeabilities of the boundary plane are 0.12×10^{-15} (m^2) at horizontal four boundaries, 360×10^{-15} (m^2) at the upper boundary and 120×10^{-15} (m^2) at the lower boundary.

The actual number of grids for calculation is 2,640 grids (22 × 20 × 6 = 2,640 grids).

(3) Location and flow ratio of feed points of each well.

The best method for detection of feed points is a spinner logging under the producing condition. However, this method was not carried out yet in this area. So, we decide the feed points by the data of lost circulation, Hg and As analyses of cuttings, temperature and pressure loggings and pivot method as listed in Table III.2-1.

(4) Initial temperature distribution

Initial condition in this simulation is defined as before the starting day of continuous production of steam, that is on the 20th, May in 1981. Initial temperature distribution is ambiguous because of insufficient data of temperature logging at that time.

However, an iso-temperature map is prepared using the results of the longest temperature recovery of each well, though the measuring day is different each other. As for the wells in which the static logging have not carried out and the recovery time is not enough such as PR-5 and PR-9, we adopt the temperature estimated from the fluid inclusion. Both initial temperatures of fracture and matrix are treated to be equivalent.

Figs. III.2-5 to III.2-9 show maps of initial temperature distribution on the 20th, May in 1981 (at 0.0 day). In these figures, Z means layer, for example, Z = 1 corresponds to layer 1.

(5) Initial pressure distribution

The static pressure logging was only carried out in PR-2 on the 6th, May in 1981. The measuring data indicate 135 ata at a block of (12, 18, 3) including the main feed point of PR-2 in the initial condition.

The initial pressure distribution was reemerged from the natural state simulation of no-flow condition. The simulation was to calculate to make the initial pressure become 135 ata at that block in the initial state. Both initial pressures of fracture and matrix are treated to be equivalent.

Figs. III.2-10 to III.2-14 show the initial pressure distribution.

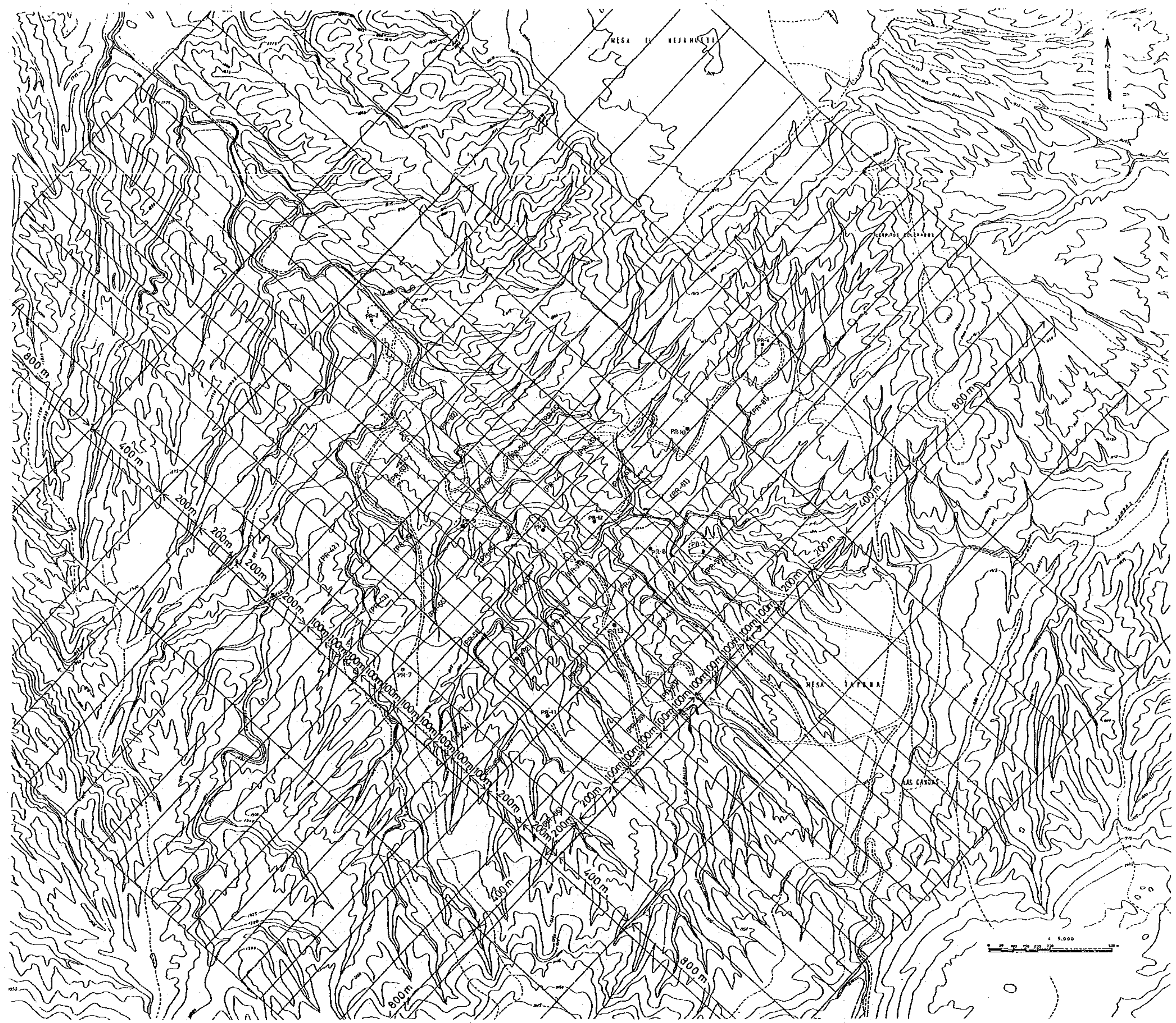

Fig. III. 2-2 Areal Computation Grid used to Simulate the La Primavera Field

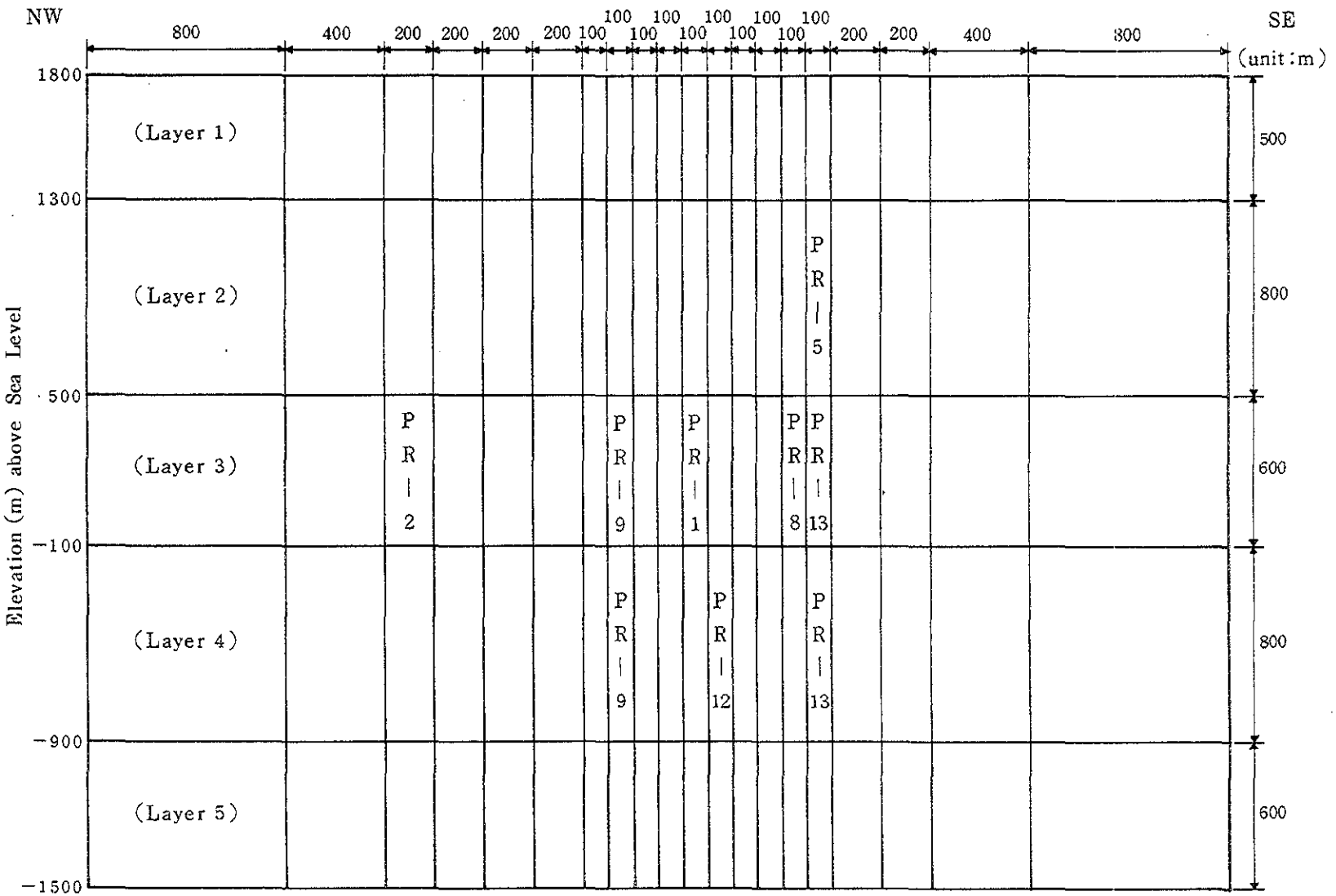

Fig. III. 2-3 Cross Section of Model used for the Simulation

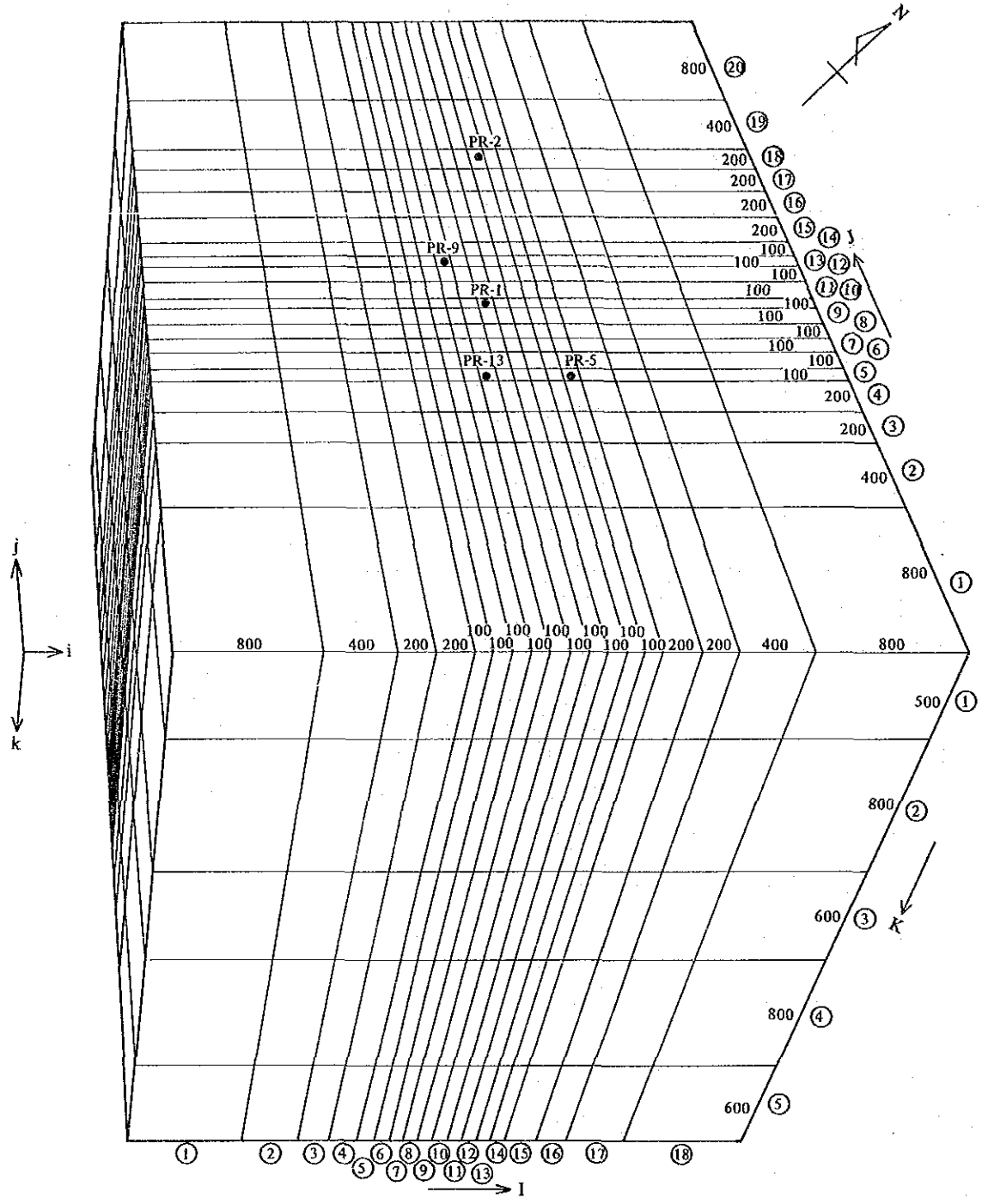

Fig. III. 2-4 Three Dimensional Model of the La Primavera Field

Table III. 2-1 Location of Feed Points and Flow Ratio

Well	Location			Flow Ratio (%)	Remarks
	I	J	K		
PR-1	10	10	3	–	
PR-2	12	18	3	–	
PR-5	14	5	2	–	
PR-8	13	6	3	–	
PR-9	8	13	3	10	
	8	13	4	90	
PR-12	12	9	4	–	
PR-13	9	5	3	95	Do not produce during the period of history match simulation
	9	5	4	5	

Table III. 2-2 Ranks of Initial Fracture Permeability

Rank	permeable					impermeable	
	I	II	III	IV	V	VI	VII
layer 1	complete lost circulation	encounter fault	permeable	less permeable			
layer 2			good fracture in geology	average permeability of fault	poor permeability of fault	high resistivity in MT	impermeable
layer 3	good fracture and less than 5Ω-m in MT	good fracture or less than 5Ω-m in MT	fracture and less than 10Ω-m in MT	average fracture or less than 10Ω-m in MT	less fracture and 10Ω-m$<\rho<$50Ω-m in MT	less fracture or 10Ω-m$<\rho<$50Ω-m in MT	poor fracture
layer 4		good fracture and less than 5Ω-m in MT	good fracture and more than 5Ω-m in MT	average fracture and 5Ω-m$<\rho<$10Ω-m in MT	average fracture and high resistivity in MT	less fracture and high resistivity	impermeable
layer 5		upflow zone	low resistivity in MT				

(6) Initial permeability distribution

① Fracture permeability

Initial permeabilities at each block before simulation are ranked by the results of MT method and geological situation such as faults and fractures (Table III.2-2). Because vertical fractures are dominant in this area, vertical permeabilities are higher than horizontal permeabilities. Absolute values of initial permeabilities are determined with reference to the values of kh by the well tests. The initial permeabilities are amended gradually while the history match progresses. Finally, we can obtain the best permeability model as shown in Figs. III.2-52 to III.2-61.

② Matrix permeability

Matrix permeability is determined by the core permeability test in laboratory about cores taken from PR-7, 9, 11, 12 and 13. The method of the test is given below.

- Cores are formed into a cylindrical shape of 5 cm in diameter and 10 cm in height, and are inserted into a cylindrical pipe with a bonding agent.
- We use the apparatus as shown in Fig. III. 2-15, and measure water volume, pressure and temperature at a elapsed time.
- Matrix permeability is calculated from the following equation.

$$K_{15} = \frac{\mu_T \cdot L \cdot Q}{A \cdot P \cdot t} \cdot \frac{\mu_T}{\mu_{15}} \qquad (3.2.3)$$

where,

K_{15} : Permeability at 15°C (darcy)
μ_T : Fluid viscosity at T°C
μ_{15} : Fluid viscosity at 15°C
L : Height of sample
Q : Water volume
A : Sectional area
P : Water pressure
t : Elapsed time

The result of measurement is shown in Table III. 2-3 base on the above mentioned procedure. We give the average value (0.0126 mD≒0.0126 × 10^{-15} m^2) to all blocks in this simulation.

Table III. 2-3 Matrix Permeability in each Well

Sample No.	Well	Depth (m)	Matrix Permeability (Darcy)
1	PR-7	276.0 ~ 276.5	7.30×10^{-7}
2	PR-9	2,985.0 ~ 2,986.0	6.17×10^{-5}
3	PR-11	1,719.0 ~ 1,719.2	3.87×10^{-6}
4	PR-12	2,302.5 ~ 2,302.7	7.45×10^{-7}
5	PR-13	1,500.6 ~ 1,500.8	7.25×10^{-6}
6	PR-13	2,004.0 ~ 2,004.2	1.20×10^{-6}

(7) Porosity, density, thermal conductivity and specific heat

Physical properties for the simulation is based upon core test as well as the core permeability test with the exception of specific heat. The method and the result of core test have already been shown in Chapter II.1.1.6 (1). Moreover, additional six cores given in Table III.2-3 are measured.

① Porosity: Matrix porosity for each layer is decided by the average of core measurement. The result is listed in Table III.2-4. Fracture porosity is treated as 1% uniformly because a change on pressure standing is unknown. If the change in pressure is known, we can estimate fracture porosity through history match.

Table III. 2-4 Matrix Porosity in each Layer

Layer	Matrix Porosity (%)
Layer 1	7.8
Layer 2	17.3
Layer 3	12.5
Layer 4	6.7
Layer 5	4.5

② Density: Fig. III.2-16 makes clear an adequate correlation between core density and collecting depth of core. The relation is expressed by the following regression equation.

$$\rho = 2.13 + 1.91 \times 10^{-4} \times D \qquad (3.2.4)$$

where,

ρ : density

D : collecting depth of core

The density value for each layer is calculated using the equation (3.2.4) as shown in Table III.2-5.

Table III. 2-5 Density in each Layer

Layer	Density (g/cm^3)
Layer 1	2.19
Layer 2	2.31
Layer 3	2.45
Layer 4	2.58
Layer 5	2.71

③ Thermal conductivity: Thermal conductivity is also correlated to the density as given in Fig. III.2-17. Therefore, the thermal conductivity for each layer is decided by the following equation.

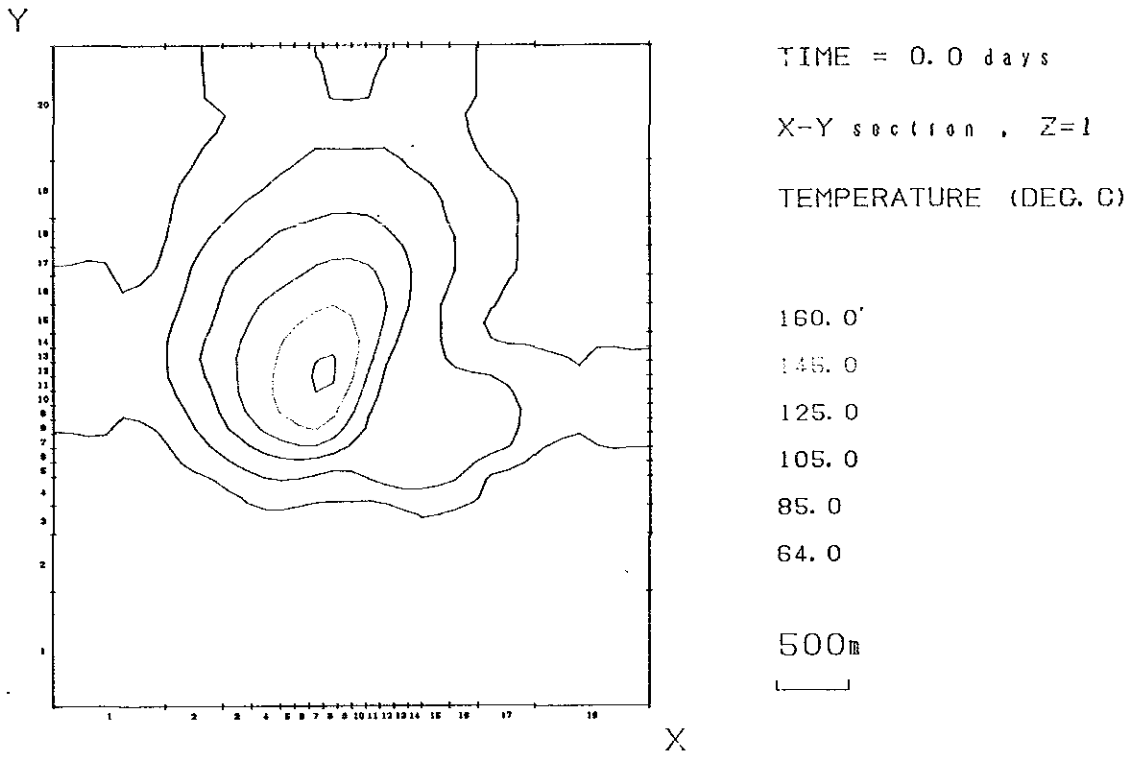

Fig. III. 2-5 Temperature in the Initial Condition (Layer 1)

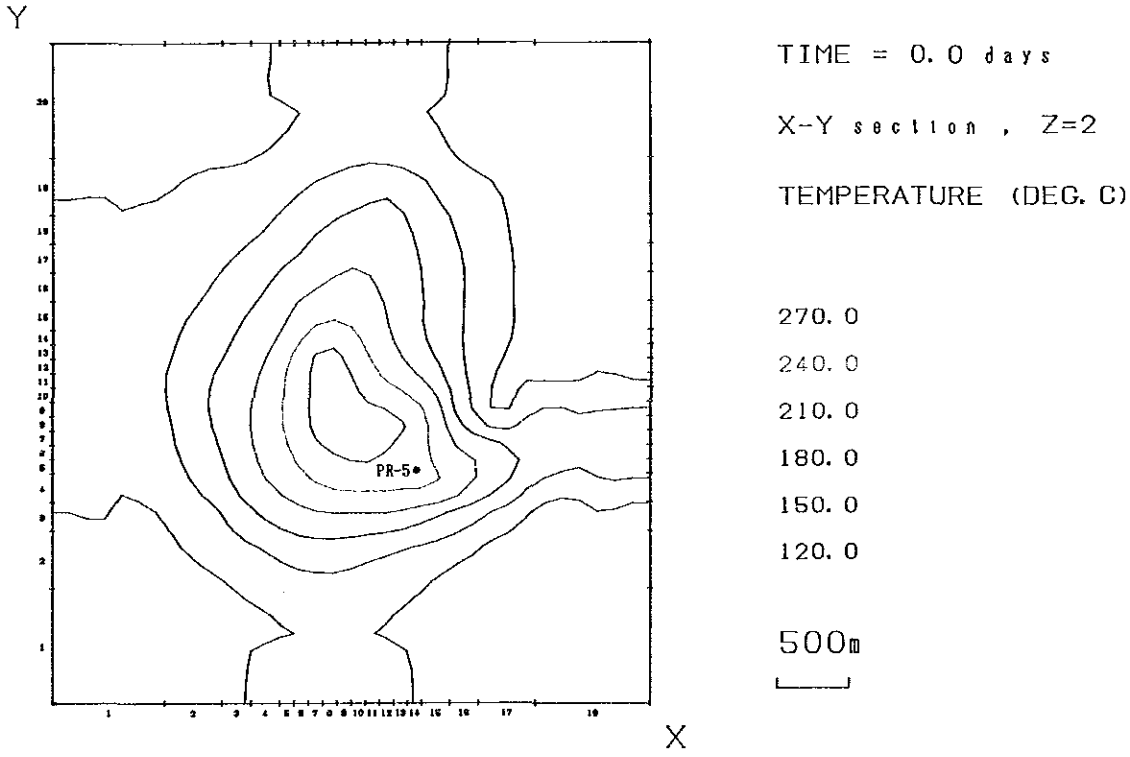

Fig. III. 2-6 Temperature in the Initial Condition (Layer 2)

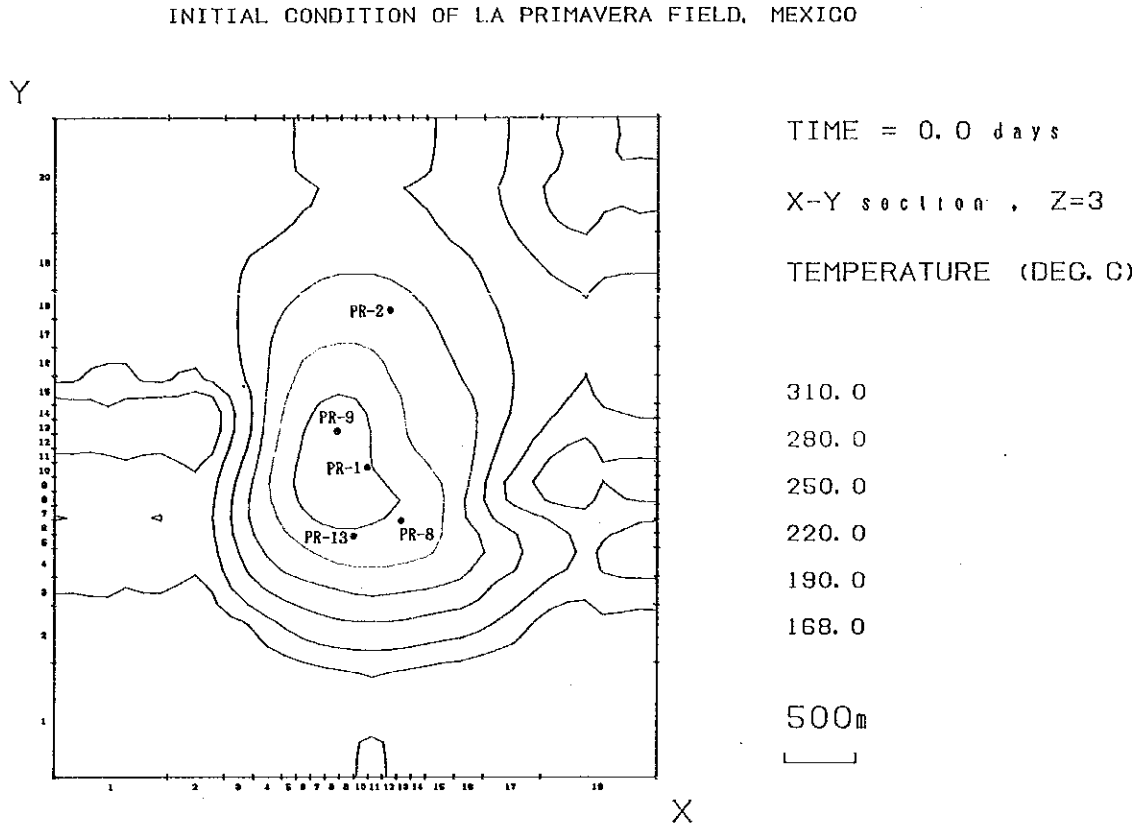

Fig. III. 2-7 Temperature in the Initial Condition (Layer 3)

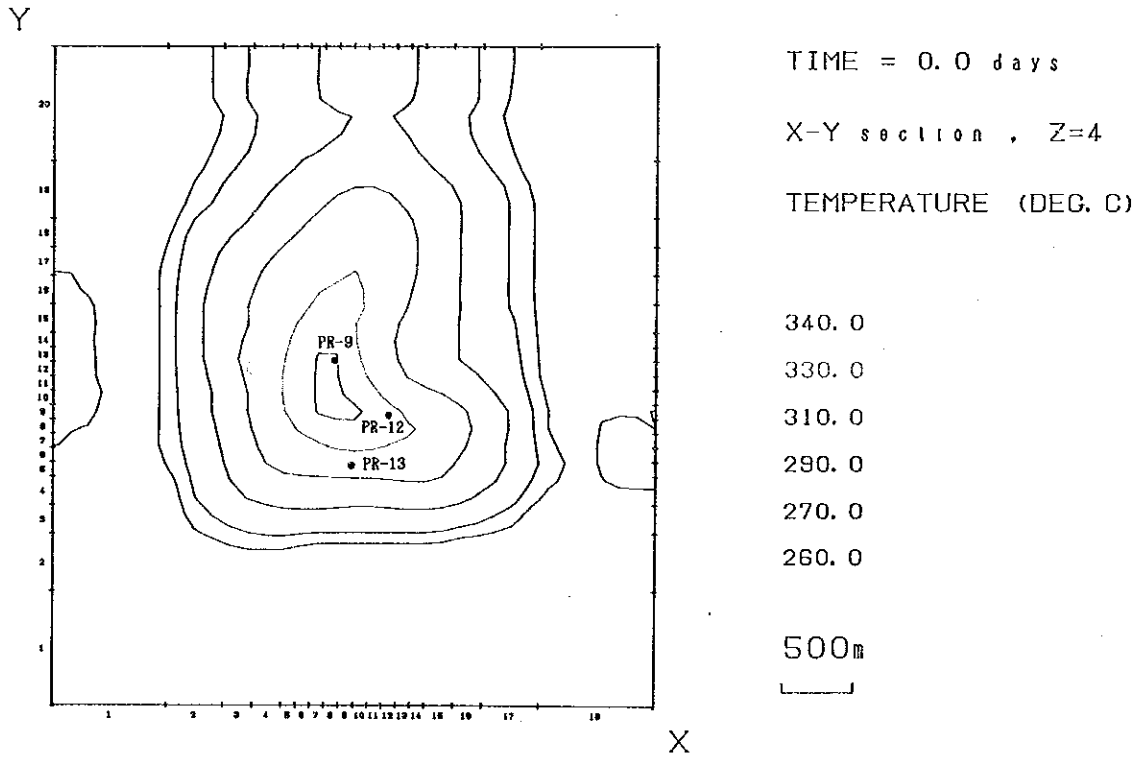

Fig. III. 2-8 Temperature in the Initial Condition (Layer 4)

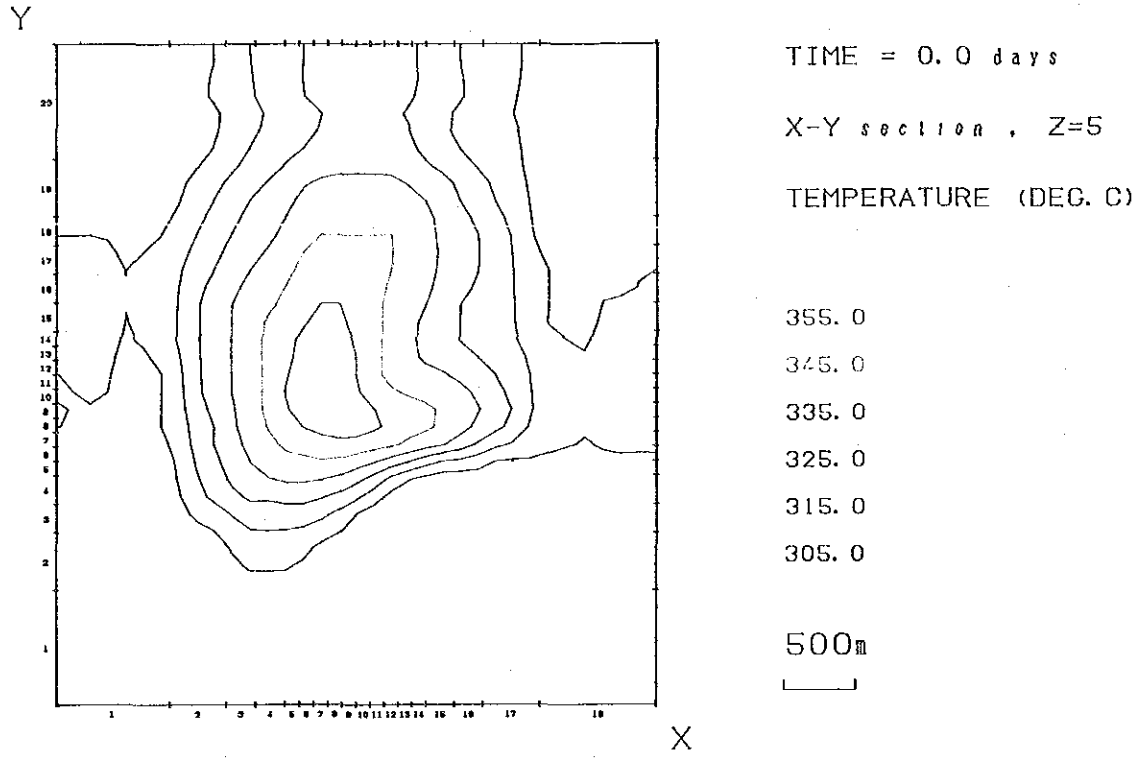

Fig. III. 2-9 Temperature in the Initial Condition (Layer 5)

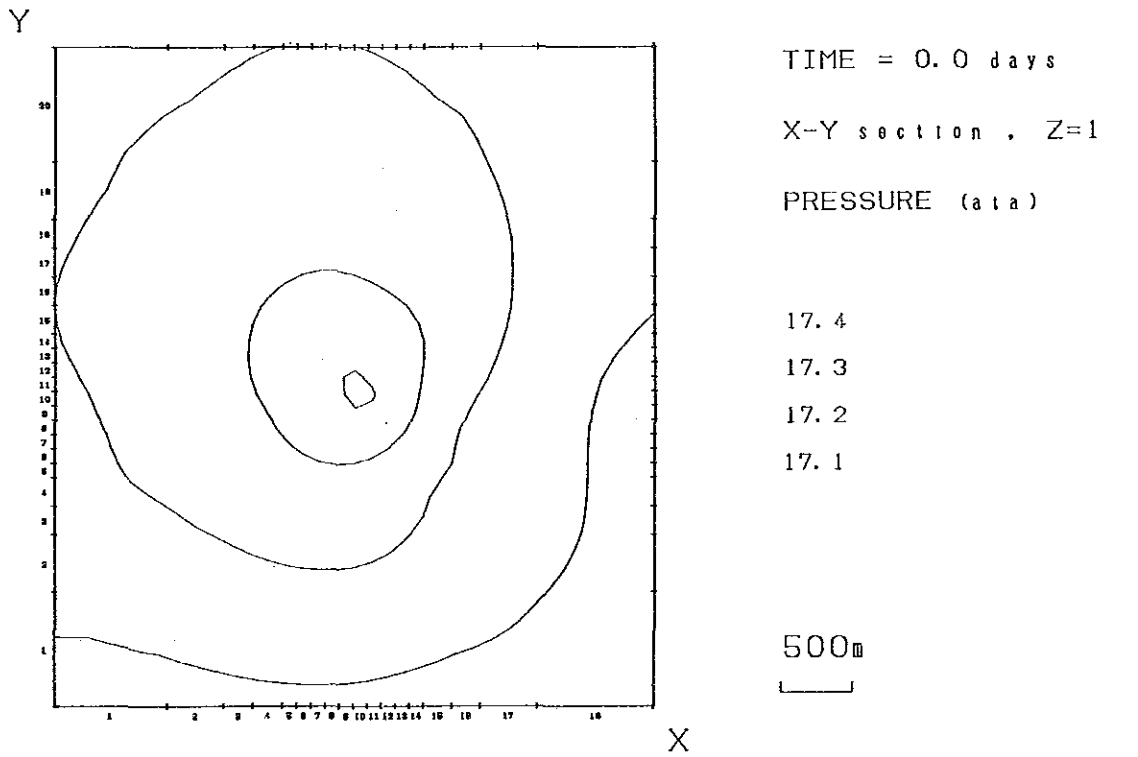

Fig. III. 2-10 Pressure in the Initial Condition (Layer 1)

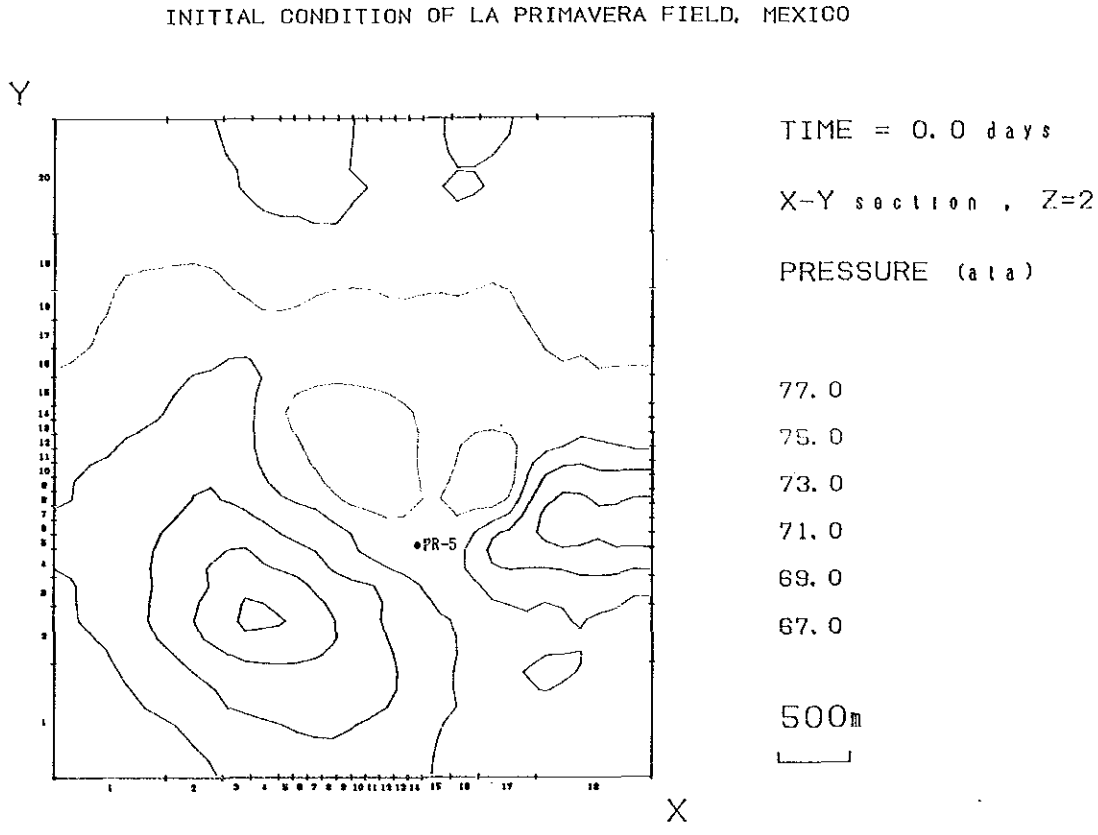

Fig. III. 2-11 Pressure in the Initial Condition (Layer 2)

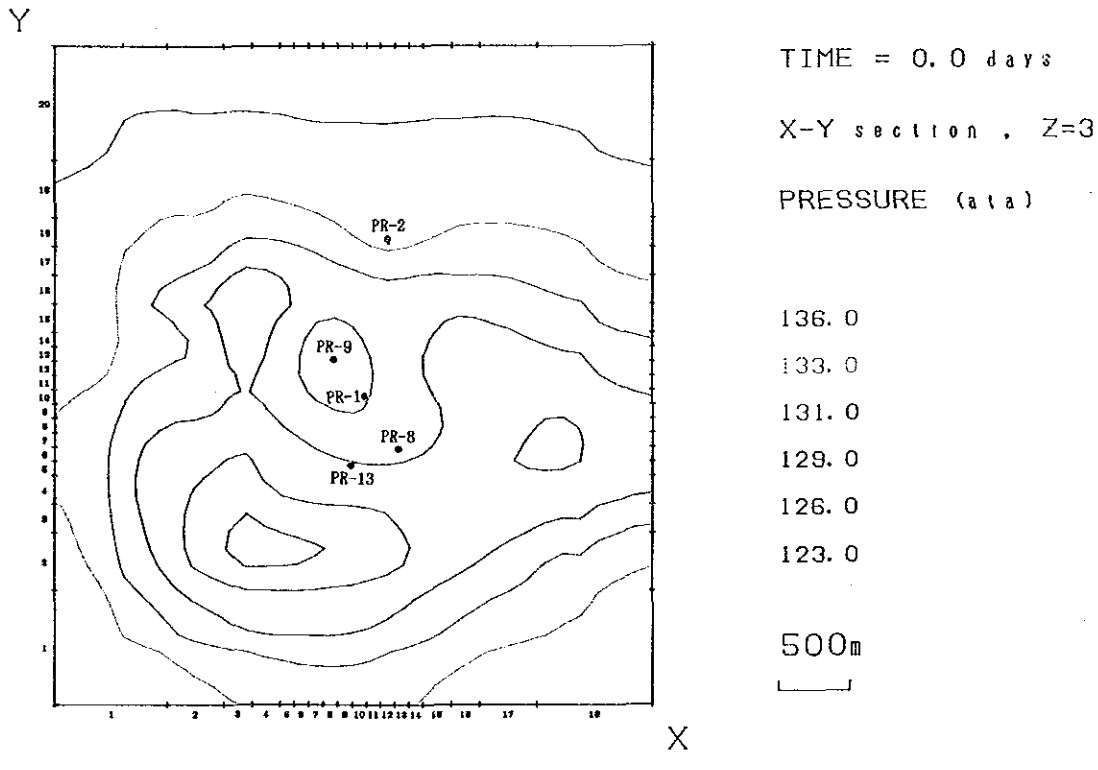

Fig. III. 2-12 Pressure in the Initial Condition (Layer 3)

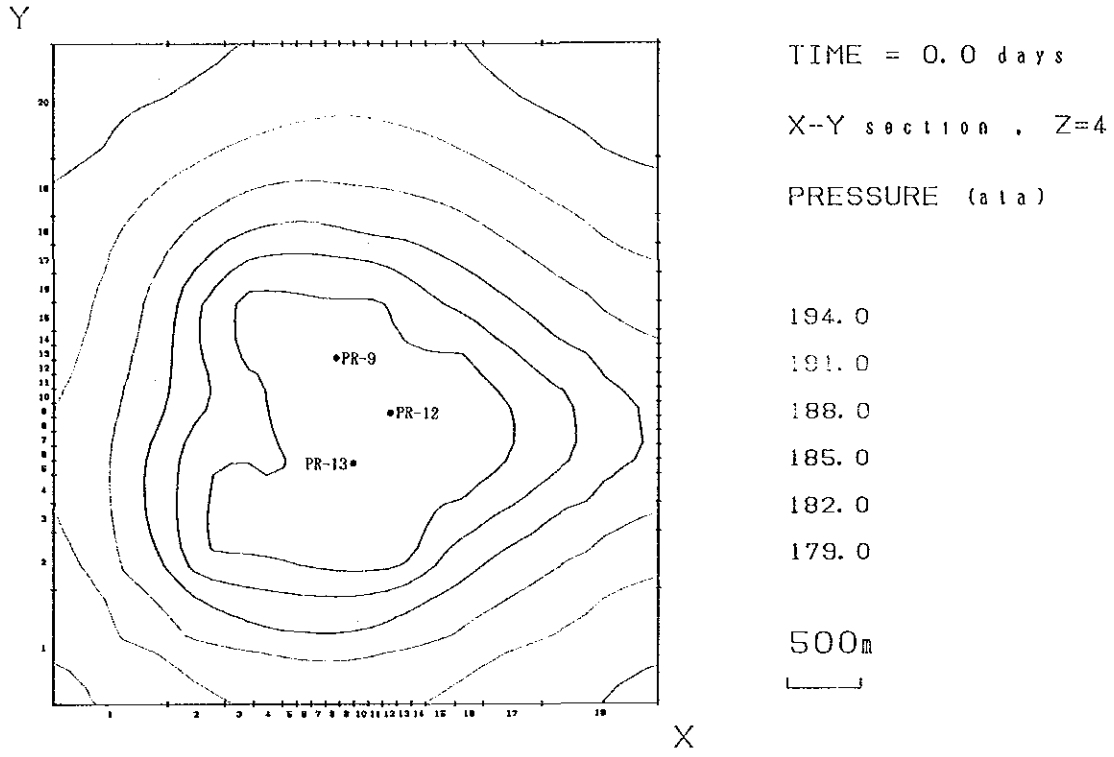

Fig. III. 2-13 Pressure in the Initial Condition (Layer 4)

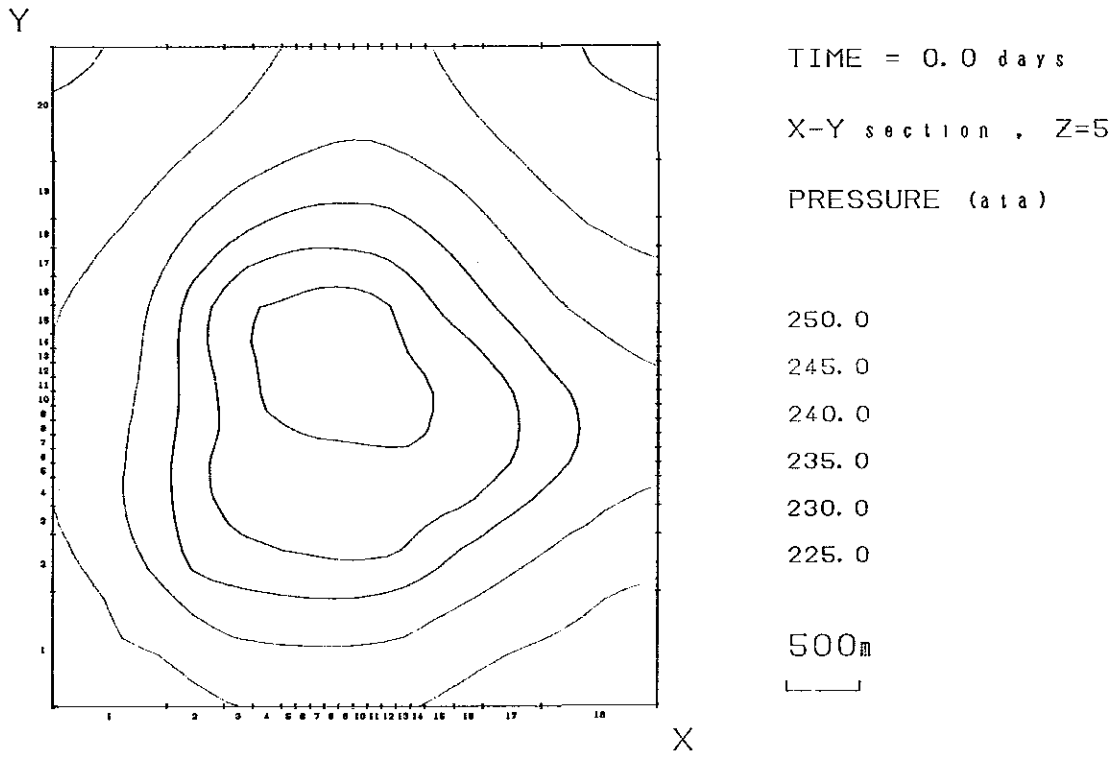

Fig. III. 2-14 Pressure in the Initial Condition (Layer 5)

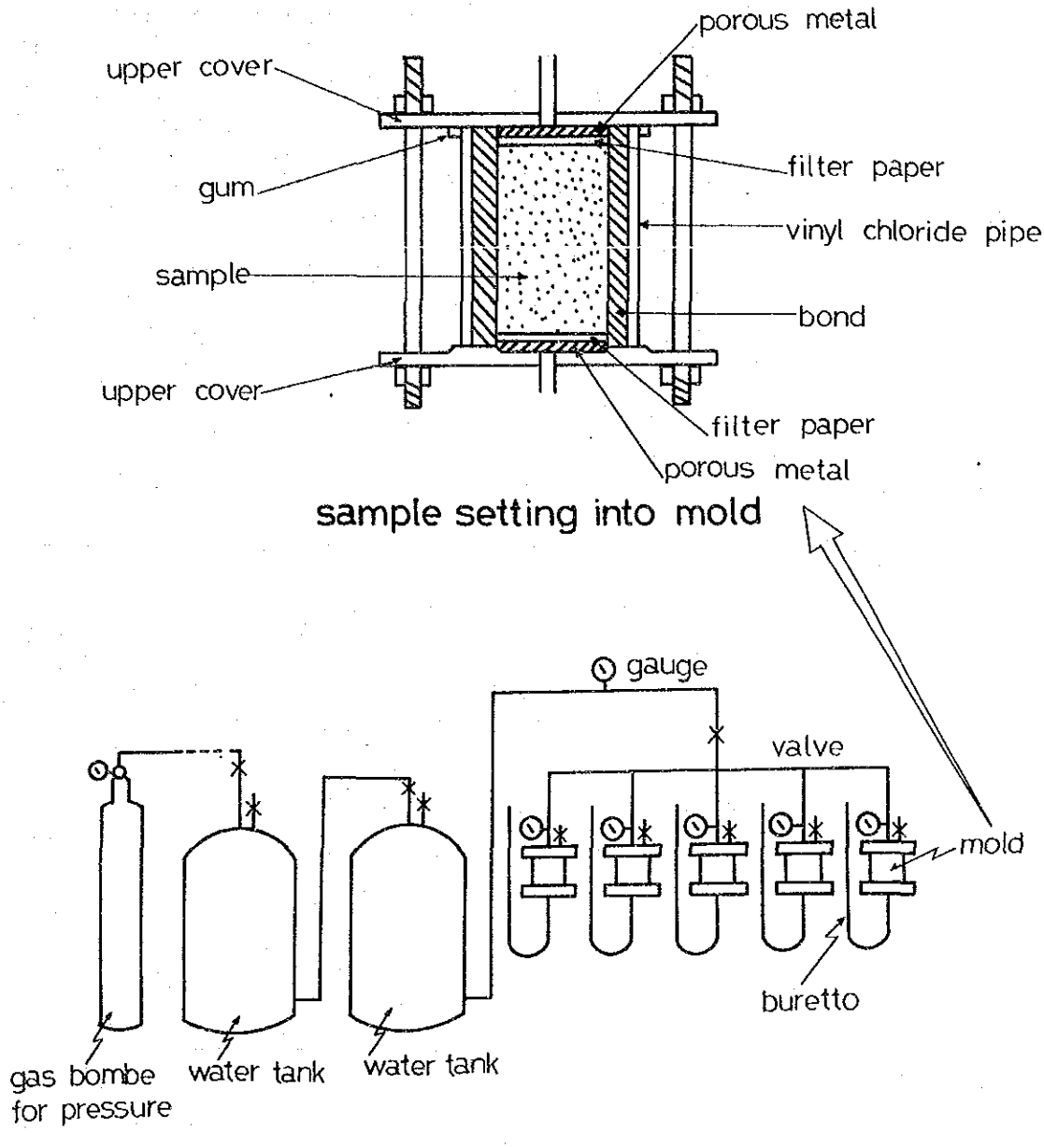

Fig. III. 2-15 Appratus for Core Permeability Test

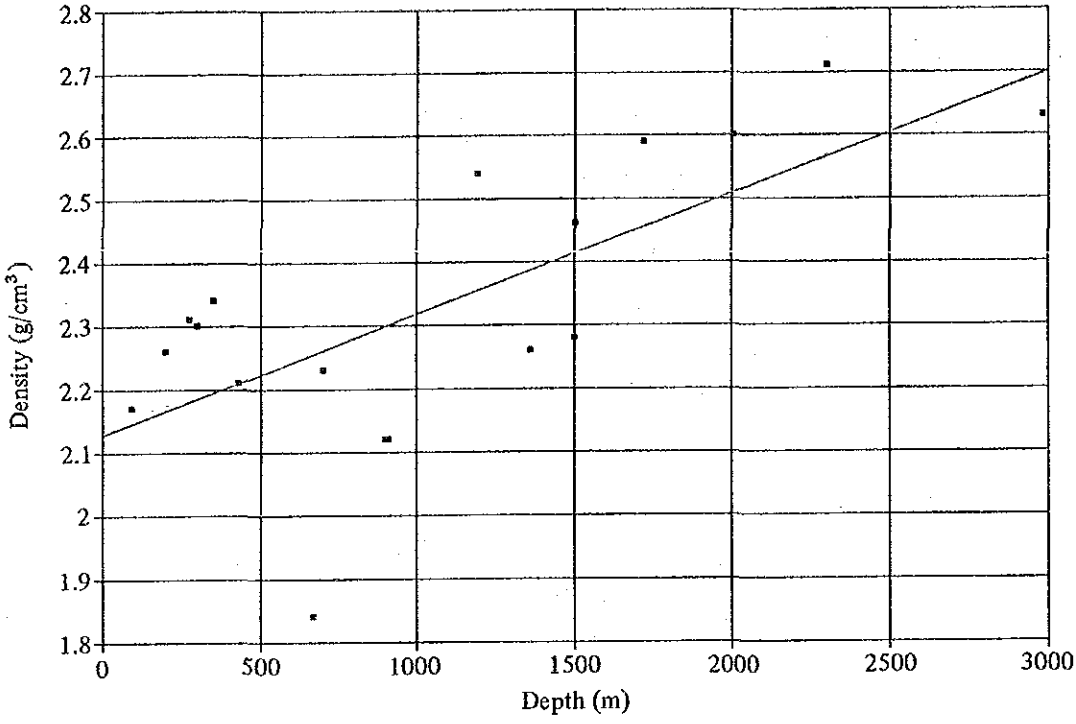

Fig. III. 2-16 Relation between Density and Depth

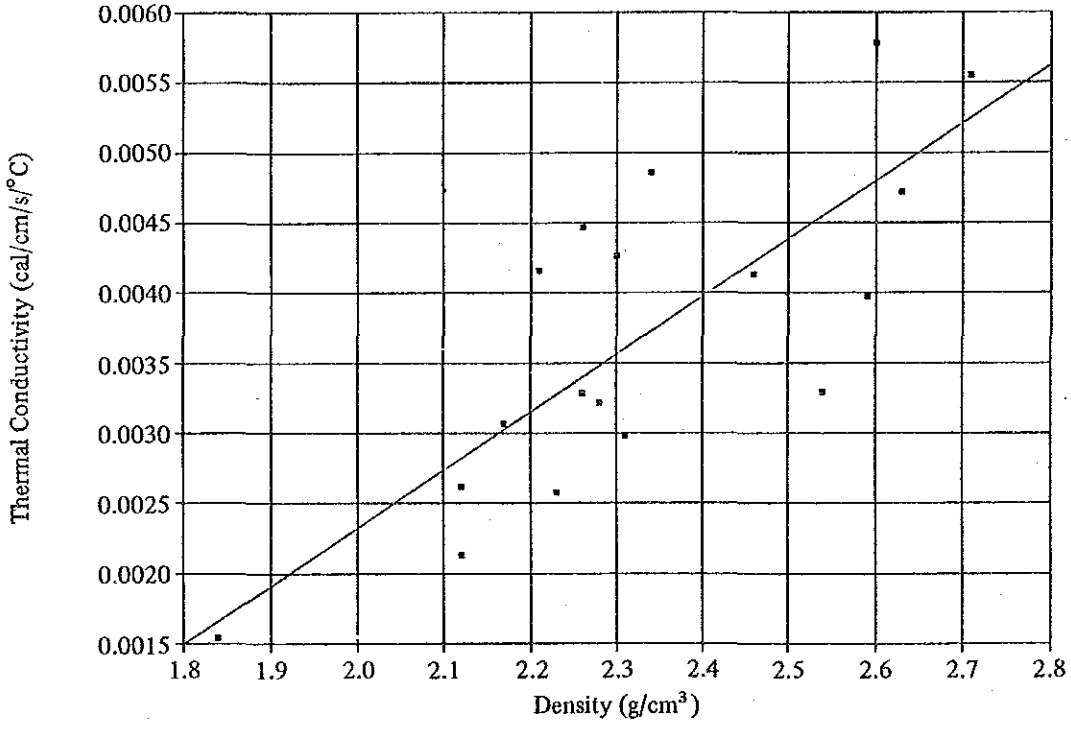

Fig. III. 2-17 Relation between Thermal Conductivity and Density

2.4 Selection of the best fitted model by history match

(1) Production and re-injection history

Production and re-injection histories in each well are ambiguous because the flow rate of wells has not been measured at regular intervals. Therefore, the production history is estimated by the wellhead pressure history using an occasional measurement of production rate at a fixed wellhead pressure.

PR-2 well is used for a re-injection at one time. The re-injection history is also unknown in detail, so that the history is calculated from an accumulated injection rate as an average rate (Fig. III.2-19). The re-injection temperature is reckoned to be 78°C (Fig. III.2-20).

The production and re-injection histories in each well are, thus, shown in Figs. III.2-21 to III.2-27.

(2) Data for history match

Observation values that could be compared with calculation values in this simulation are as follows:

- reservoir pressure by static logging
- fluid temperature by chemical thermometer

① Reservoir pressure: The pressure logging at the static condition has been carried out at an enough recovery time after the completion of drilling. Therefore, we can decide the pressure value at the middle depth of the layer including the main feed point in each well. The observation values of the reservoir pressure are shown in Table III.2-7.

② Fluid temperature: The fluid temperature is defined as a hot water temperature before flashing. If the flashing point exists inside the borehole, fluid temperature is judged from the downhole temperature logging. However, the fluids flash outside the borehole (i.e. in the formation) in this area. Therefore, the chemical thermometer is acceptable as the fluid temperature because this is calculated by the chemical analysis measured at regular intervals. The chemical thermometer has been proposed by some investigators such as *White (1965), Ellis (1970), Truesdell (1976) and Fournier and Truesdell (1973, 1974).* The Na/K thermometer by Fournier and Truesdell (1973) is suitable in this field with the exception of PR-2. The Na-K-Ca thermometer is appropriate for PR-2. The history of chemical thermometer in each well is indicated in Tables III.2-8 to III.2-13.

(3) Results of history match

We have completed a history match of about the first 7 years (2,589 days) of production at La Primavera field. The starting day was on the 20th, May in 1981, whereas the end was on the 30th, June in 1988. The time step ranges from 1 day to 30 days in dependence on the computational condition.

Figs. III.2-28 to III.2-40 show the comparison (match) between the pressure drawdown and temperature calculated in the simulation and the pressure drawdown and temperature measured in selected seven wells of PR-1, 2, 5, 8, 9, 12 and 13.

The history match of pressure and temperature shows good agreement with the measured values as a whole. As to PR-9, the feed points are located in both layers 3 and 4. The history

match of pressure is, therefore, carried out in both layers, while the temperature is only matched for the layer 4 which reflects the main fluid temperature.

Figs. III.2-41 ~ III.2-51 delineate the calculated areal distribution of pressure and temperature after about 7 years (2,589 days) for each layer. Moreover, the fracture permeabilities in the best fitted model by history match are shown in Figs. III.2-52 to III.2-61 for each layer. In this history match, the coincidence between the measured and calculated values is mainly obtained from the adjustment of fracture permeabilities.

(4) Discussion on the results of history match

① In the history match, an amendment of fracture permeability mainly leads to be a satisfactory accordance of the measured value with the calculated value in fluid temperature and reservoir pressure. The reasons why we change fracture permeability are as follows:

1) Fluids flash in the formation under the producing condition in this area. This means poor permeability around the wellbore which is consistent with poor kh value of PR-1, 8, 12 and 13.

2) Water front is important parameter in case of the flashing in the formation.
In La Primavera area, water front is distributed in the vicinity of wellbore. This fact indicates poor permeability of the reservoir and poor water supply into the reservoir.

From the above reasons, we tried to decrease the fracture permeability in the blocks including productive feed points, resulting in good history match.

② As far as PR-2 is concerned, another procedure is adopted to match the measured chemical temperature with the calculated temperature. The procedure is to decrease the fluid temperature by the infiltration of shallow cold water. The reason why we accept the procedure is as follows:

When the permeability becomes low to generate flashing in the formation, the formation pressure becomes extremely higher than that of the measured value in the case of re-injection.

However, we can not obtain good history match by this method, because small capacity of fractures does not draw the cold water.

③ Fluid temperature by the Na/K chemical thermometer of PR-5 decreased abruptly at a month elapsed since production is started, namely 243°C to 207°C. This phenomenon is interpreted to be the infiltration of shallow cold water along the fault observed in the surface. Therefore, we tried the same procedure as the case of PR-2.

In conclusion, we can obtain good history match by a combination method of the infiltration of cold water and the decrease of fracture permeability.

④ Although the history match terminates on the 30th, June in 1988 and the production of PR-13 does not carried out, the static pressure of PR-13 for layer 3 shows a decrease of about 13 kg/cm^2 compared with initial static pressure. The phenomenon is ascribed to the influence of PR-8 which is situated in the same layer of PR-13.

⑤ An accumulated production rate is smaller than the capacity of computational area. Therefore, the boundary effect is small for the calculation of history match. To confirm the boundary condition, it is necessary to carry out the history match with voluminous

production rate.

However, the history match is a reliable estimate because it includes a match of no flow condition that confirms to remain unchanged in pressure and temperature while wells have not produced geothermal fluid.

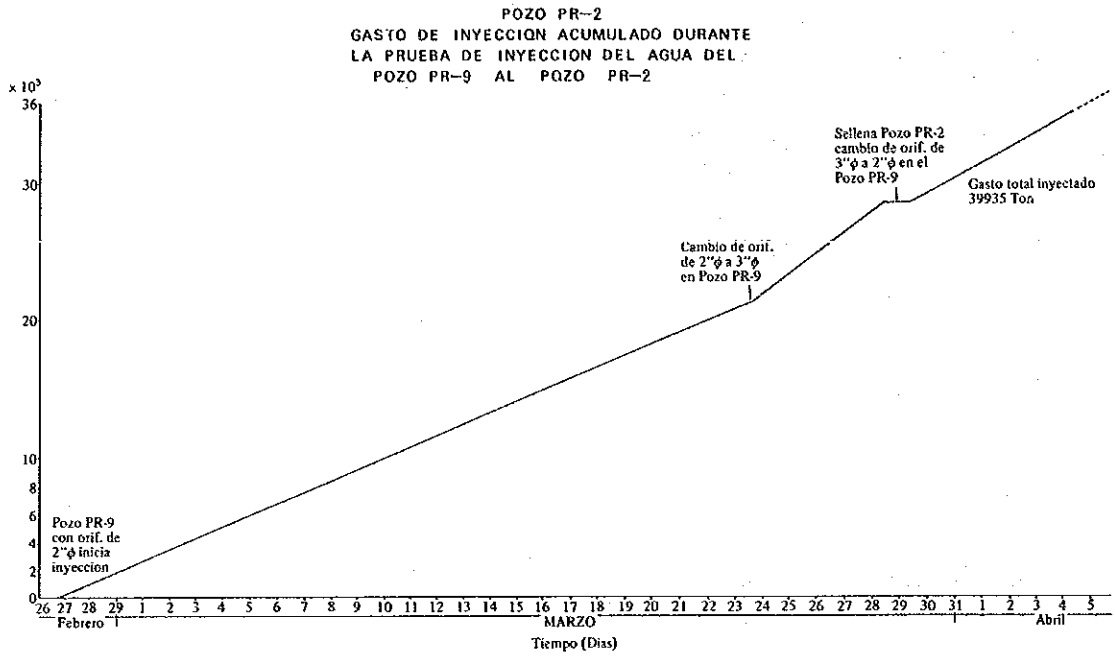

Fig. III. 2-19 Historical Change of the Cumulative Reinjection Flow Amount of PR-2

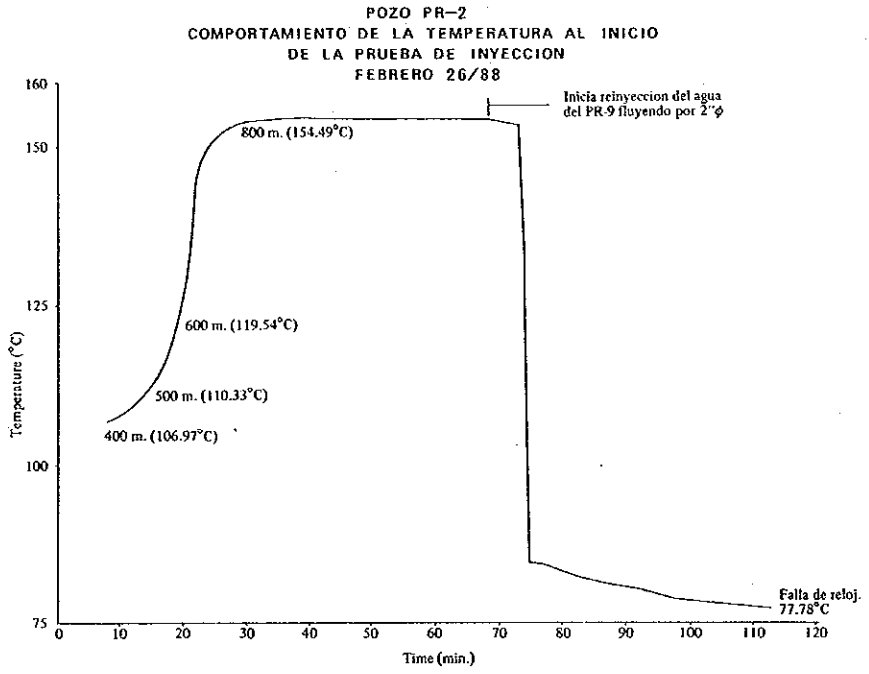

Fig. III. 2-20 Temperature Change of PR-2 due to Reinjection of Water of PR-9

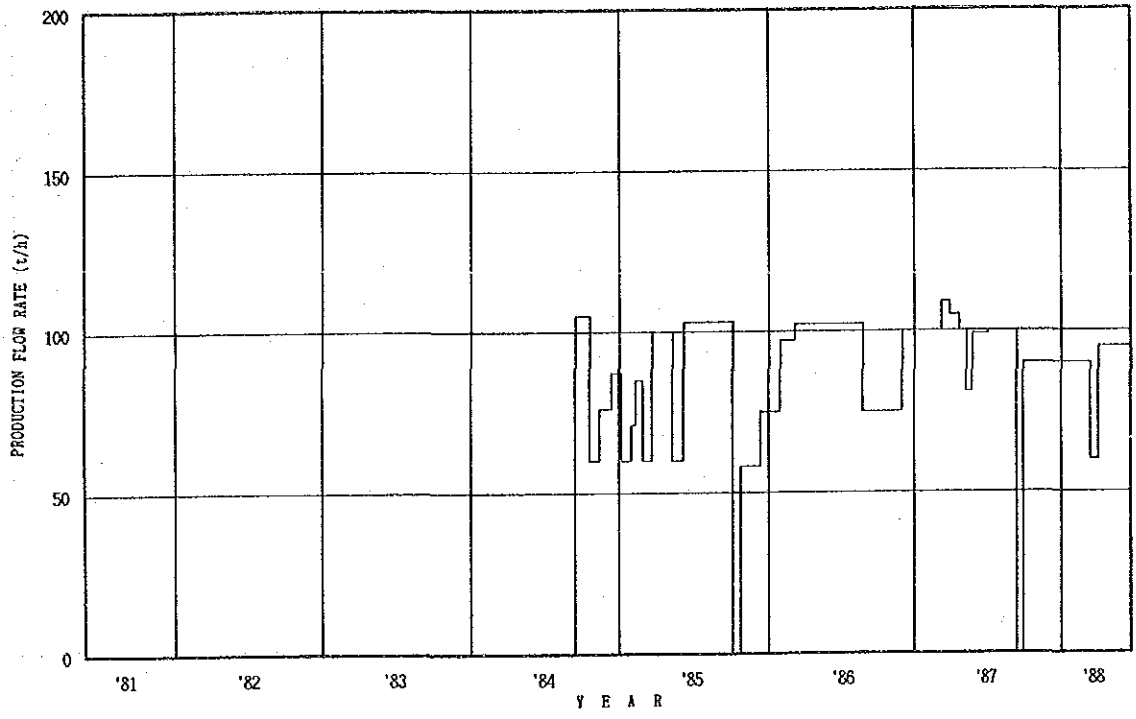

Fig. III. 2-21 Production Flow Rate of PR-1

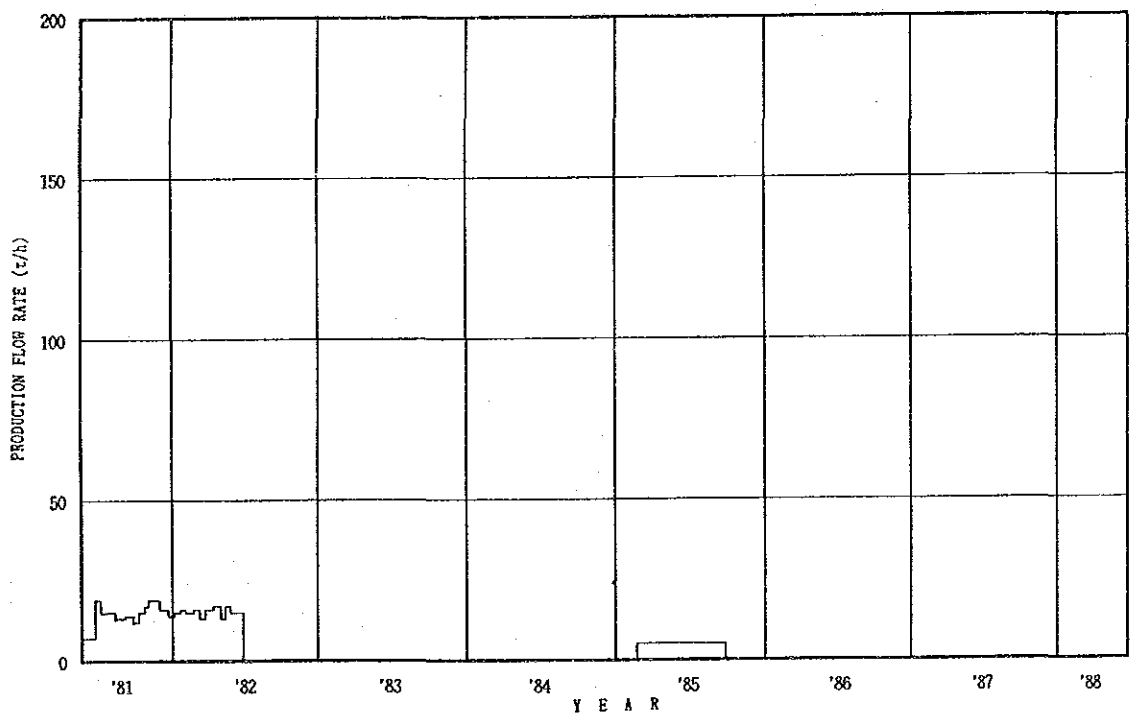

Fig. III. 2-22 Production Flow Rate of PR-2

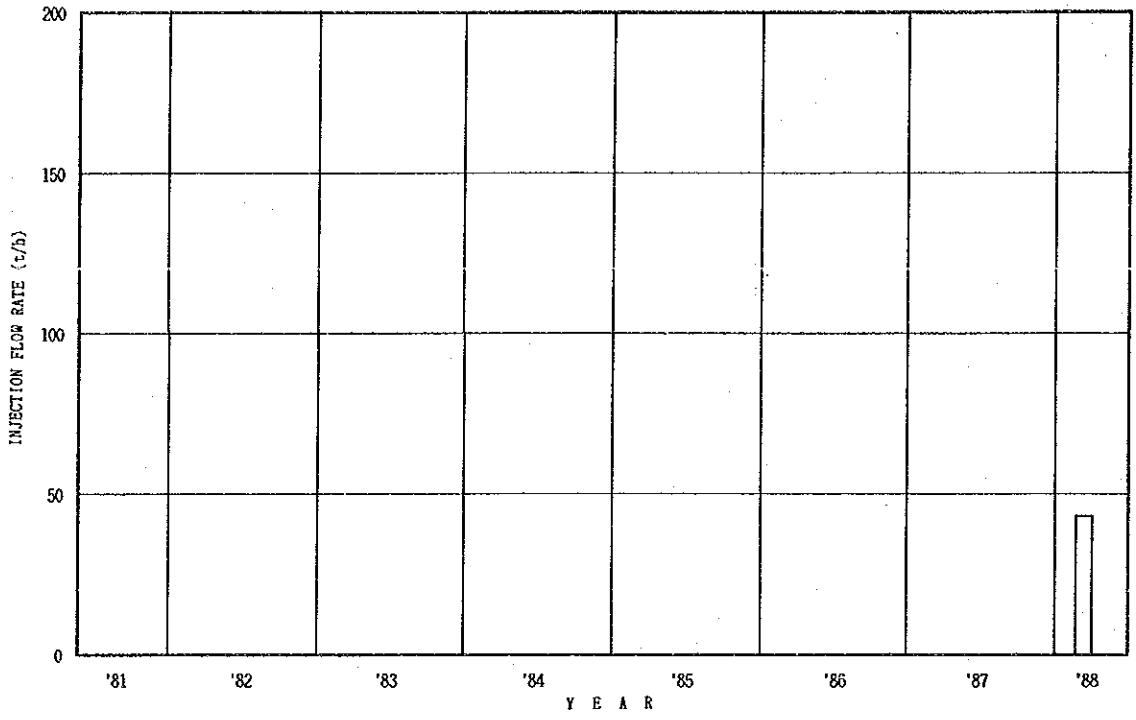

Fig. III. 2-23 Injection Flow Rate of PR-2

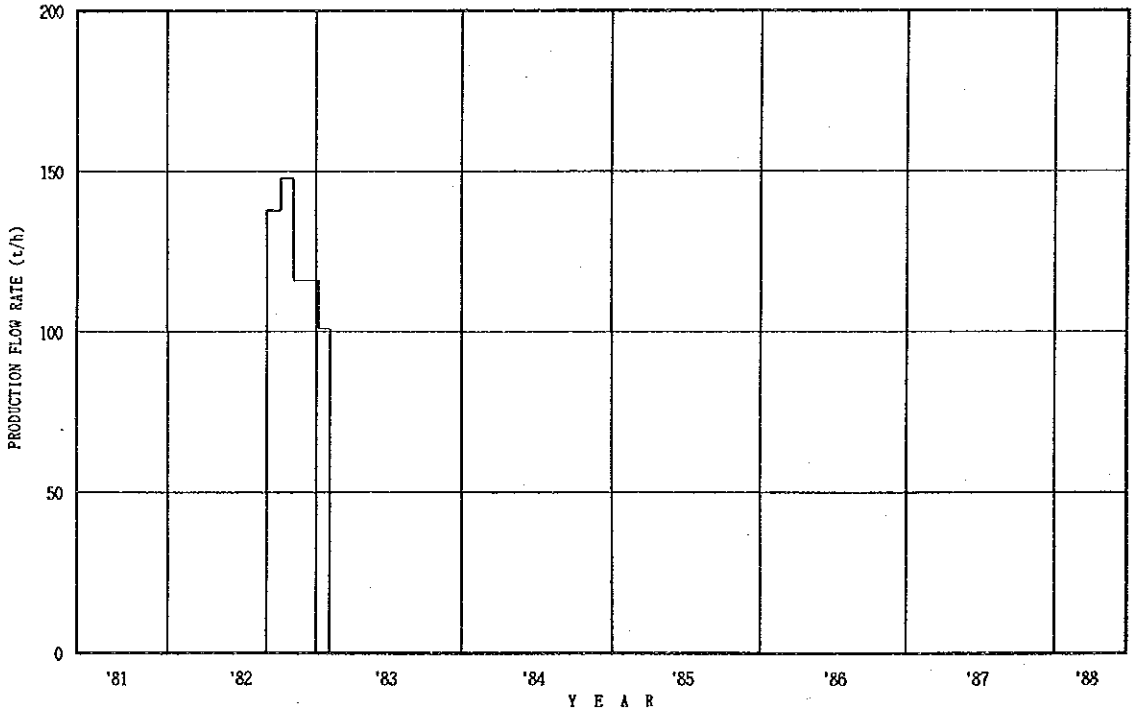

Fig. III. 2-24 Production Flow Rate of PR-5

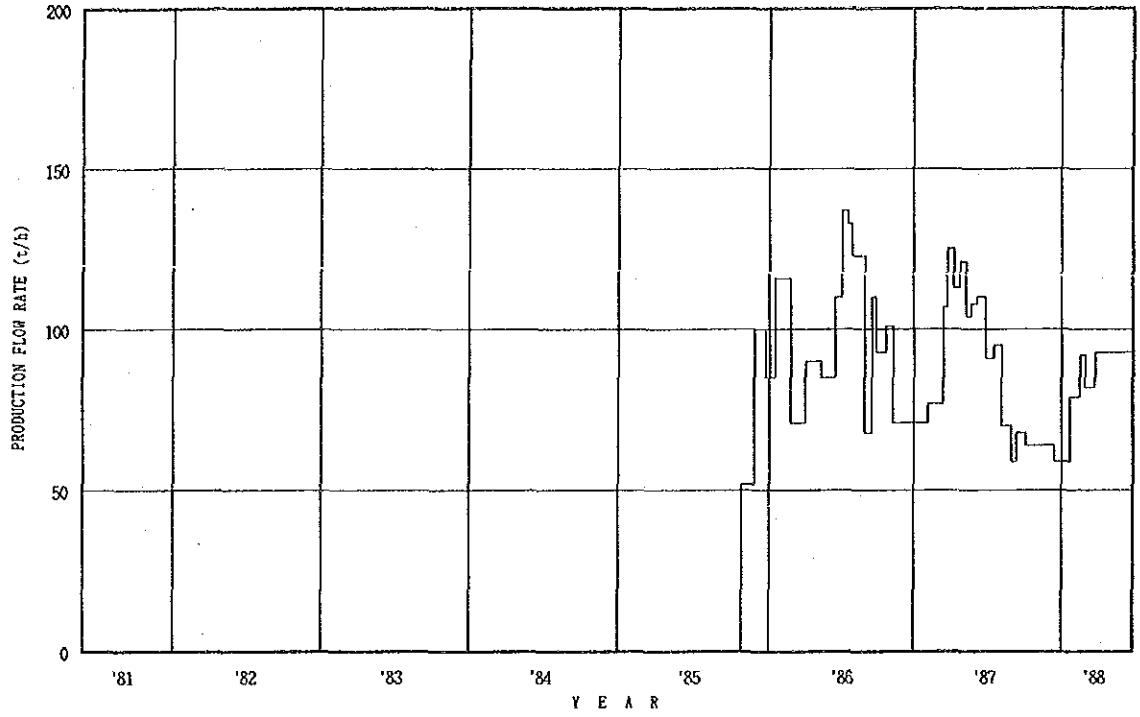

Fig. III. 2-25 Production Flow Rate of PR-8

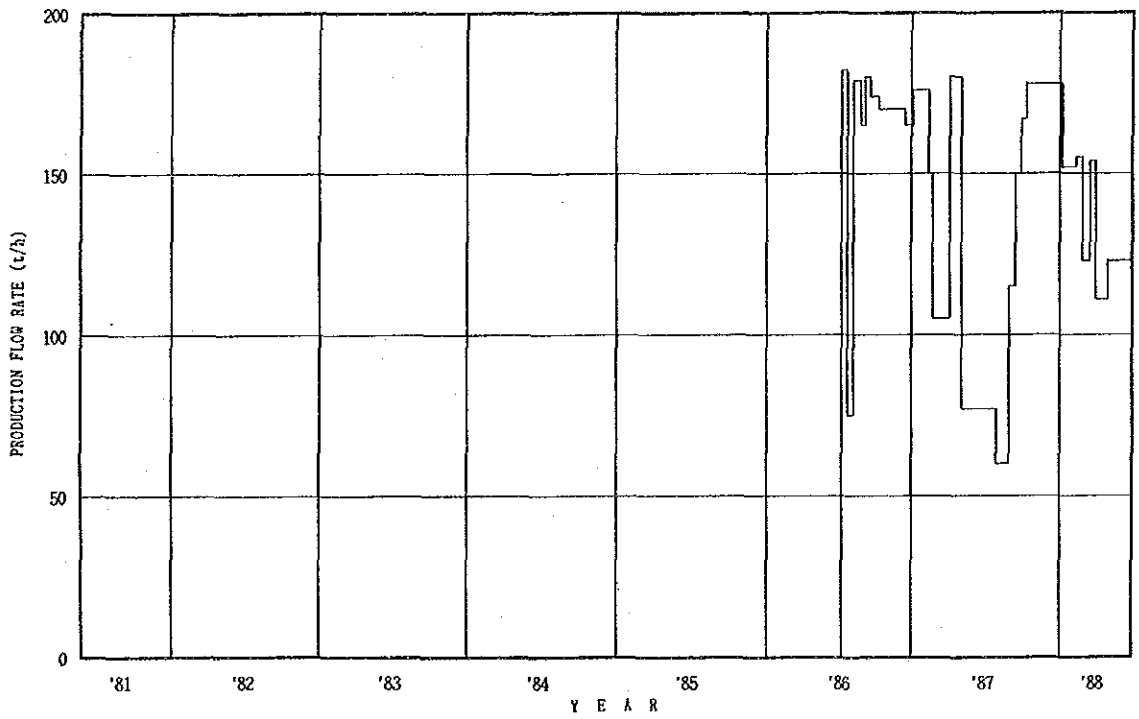

Fig. III. 2-26 Production Flow Rate of PR-9

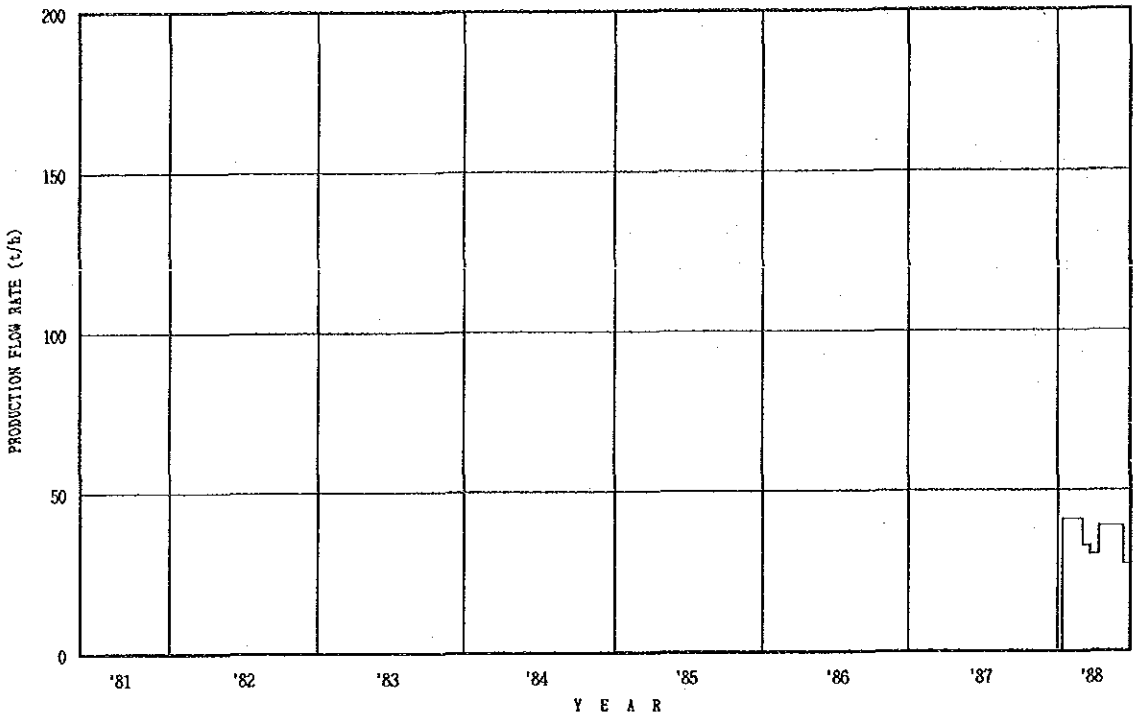

Fig. III. 2-27 Production Flow Rate of PR-12

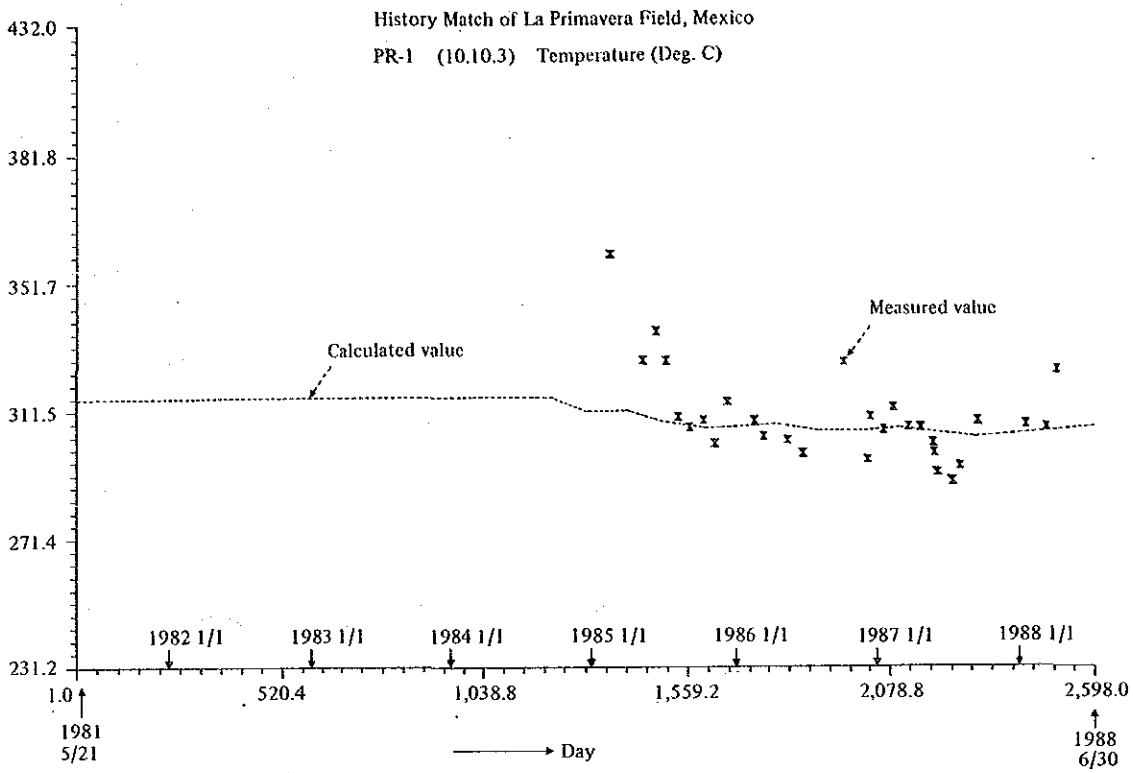

Fig. III. 2-28 Result of History Match of Temperature for PR-1

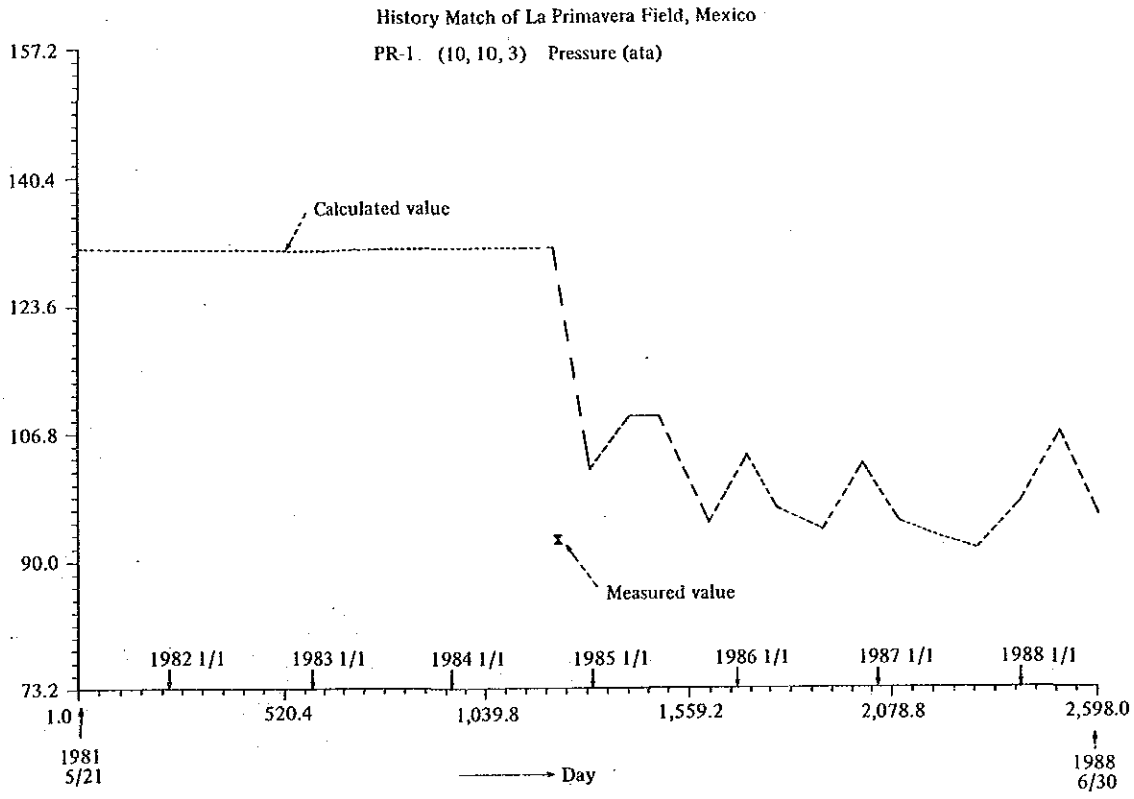

Fig. III. 2-29 Result of History Match of Pressure for PR-1

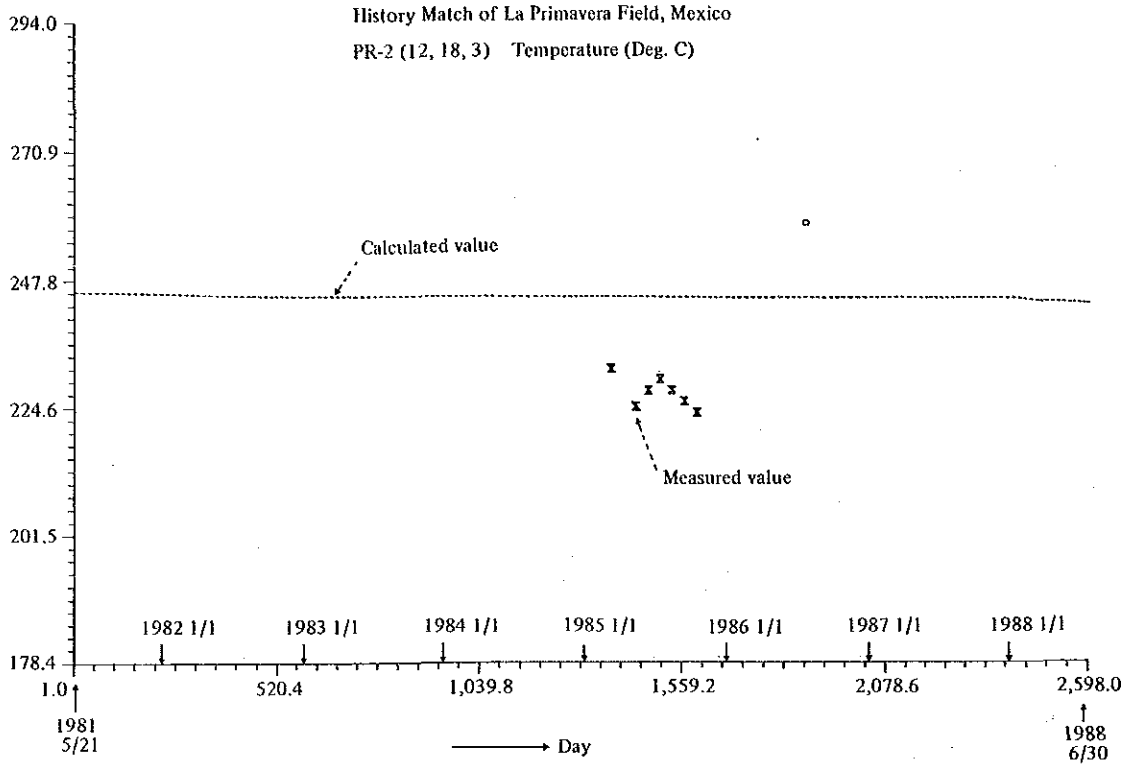

Fig. III. 2-30 Result of History Match of Temperature for PR-2

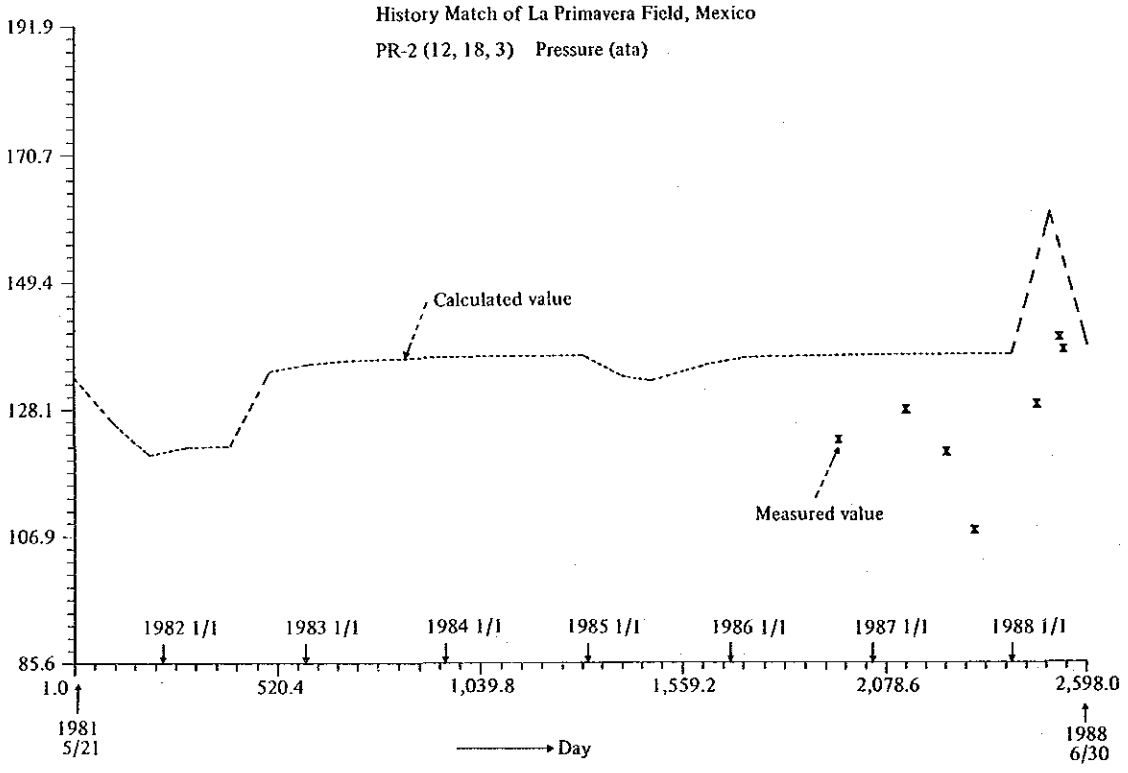

Fig. III. 2-31 Result of History Match of Pressure for PR-2

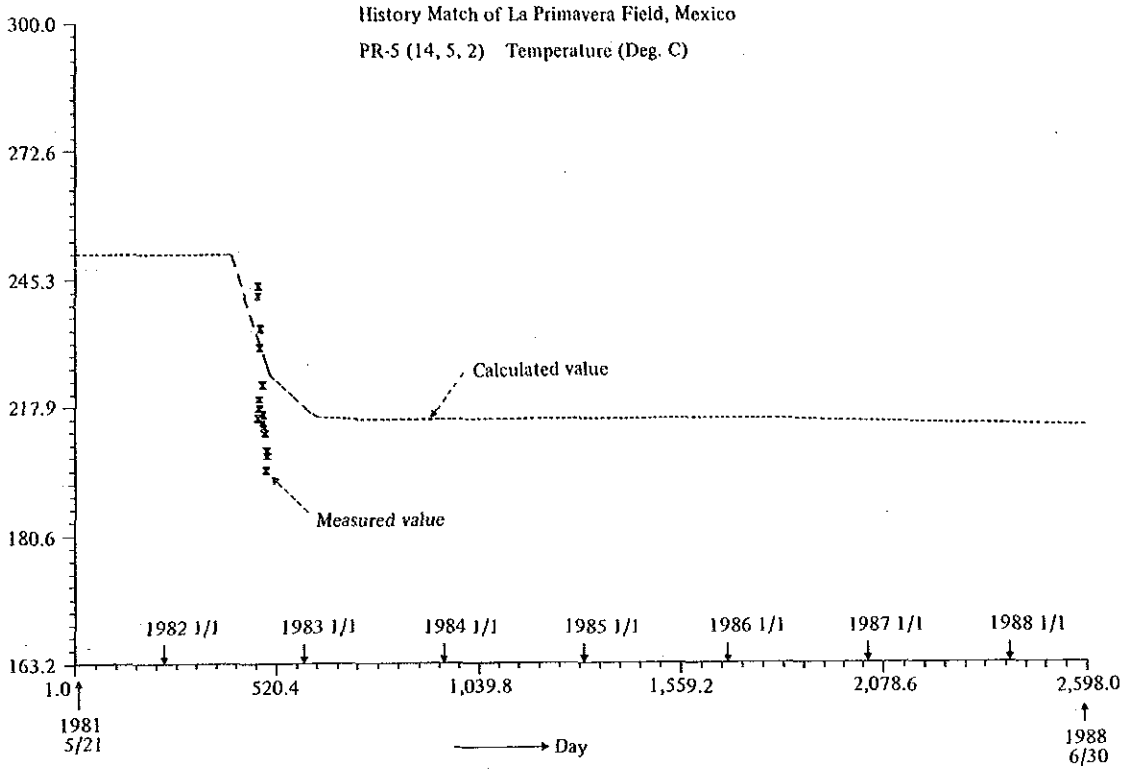

Fig. III. 2-32 Result of History Match of Temperature for PR-5

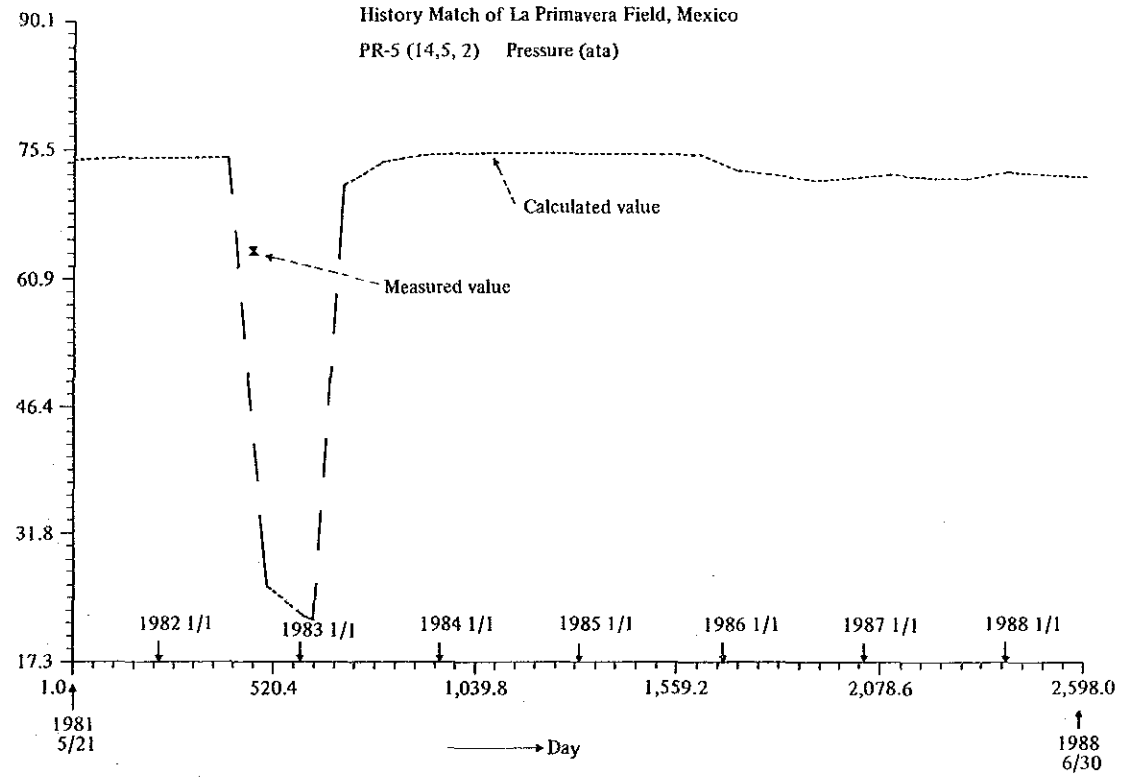

Fig. III. 2-33 Result of History Match of Pressure for PR-5

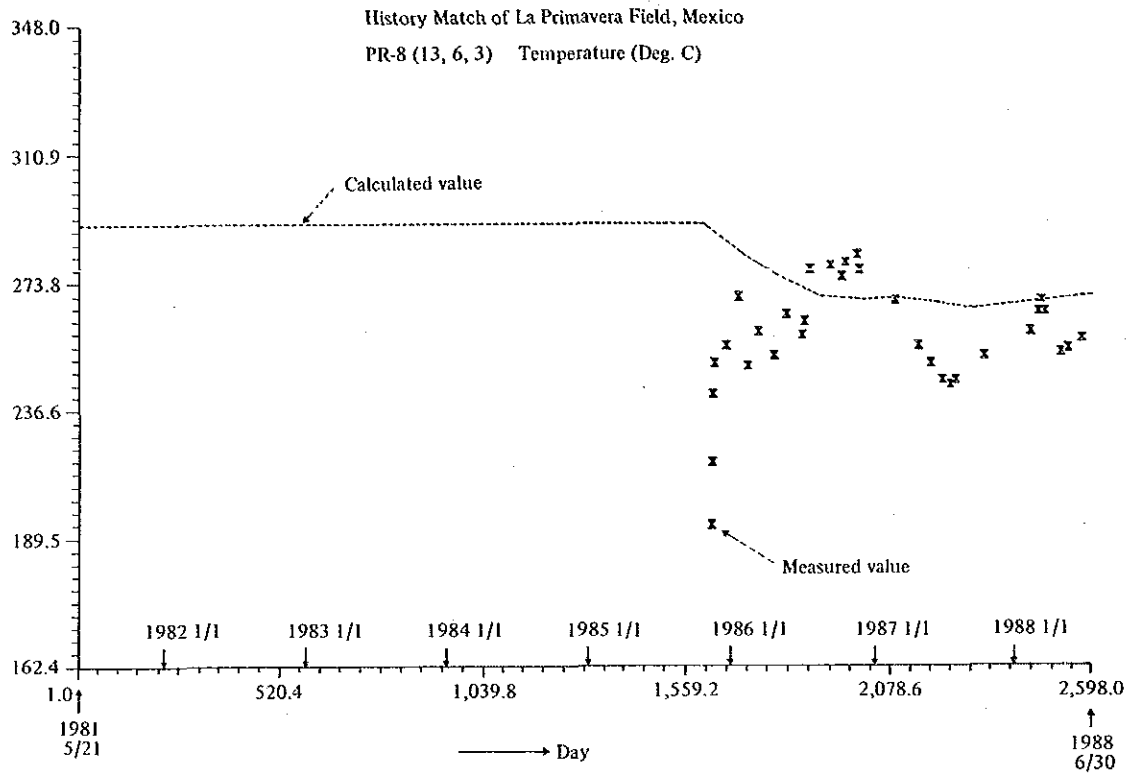

Fig. III. 2-34 Result of History Match of Temperature for PR-8

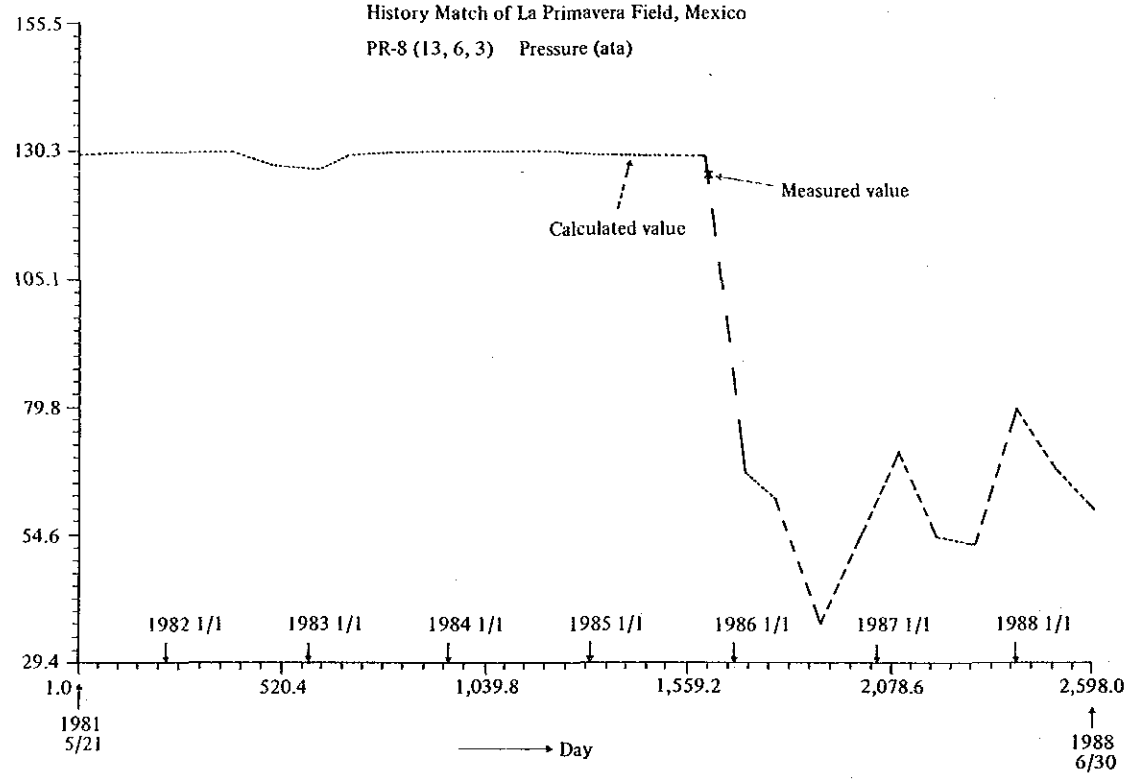

Fig. III. 2-35 Result of History Match of Pressure for PR-8

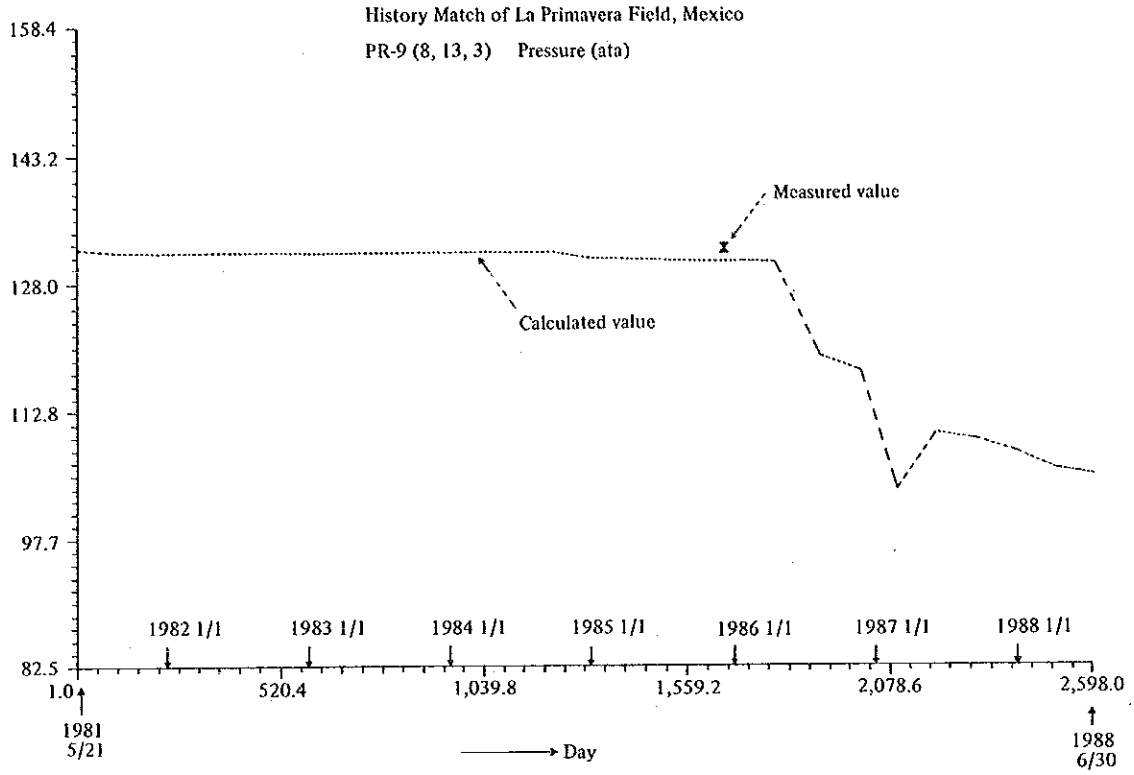

Fig. III. 2-36 Result of History Match of Pressure for PR-9 (Layer 3)

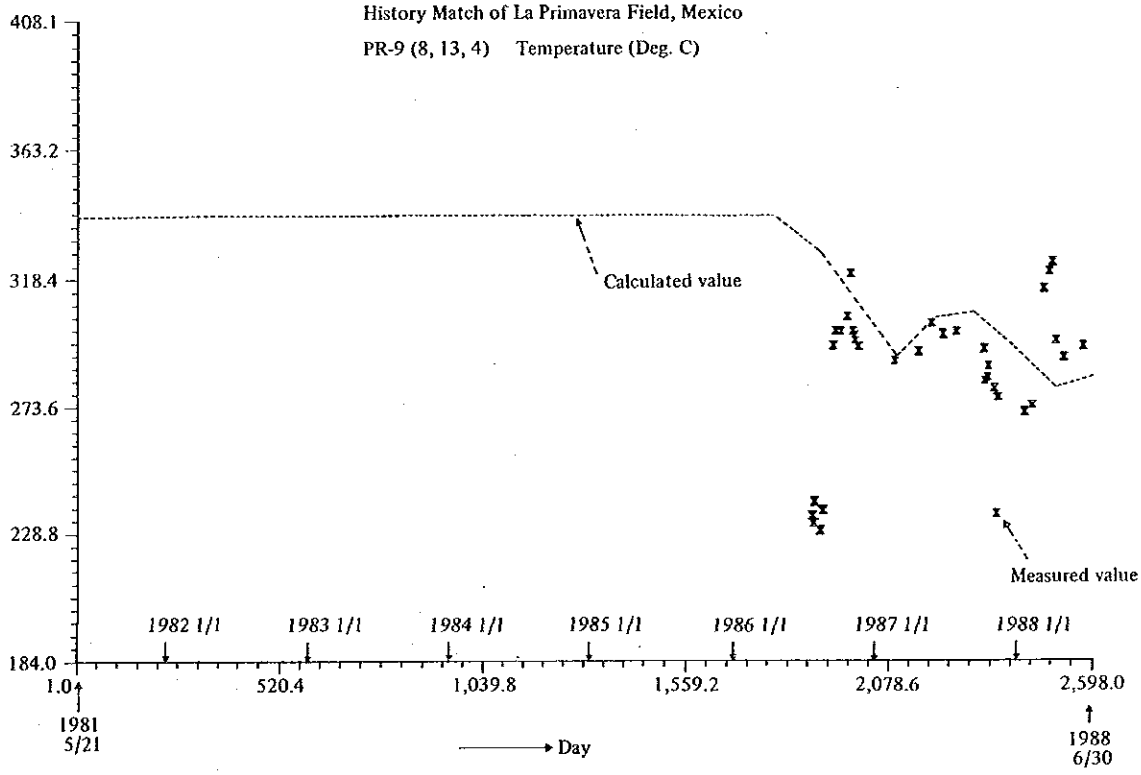

Fig. III. 2-37 Result of History Match of Temperature for PR-9

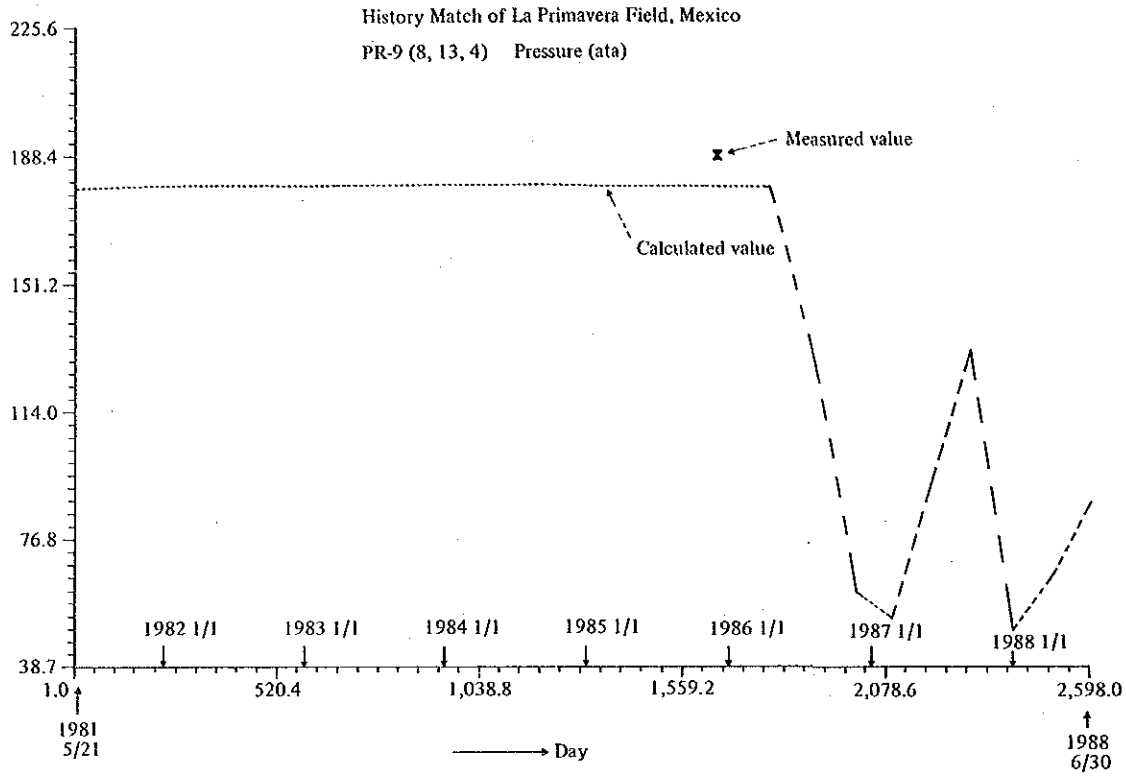

Fig. III. 2-38 Result of History Match of Pressure for PR-9 (Layer 4)

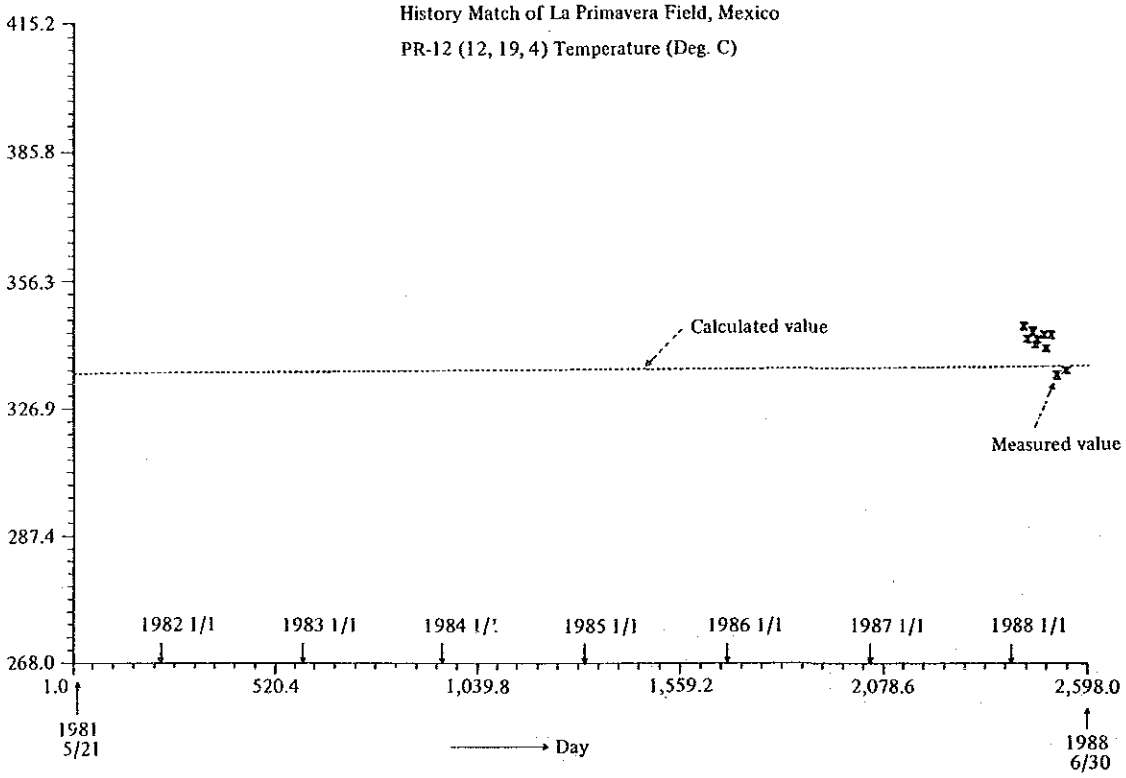

Fig. III. 2-39 Result of History Match of Temperature for PR-12

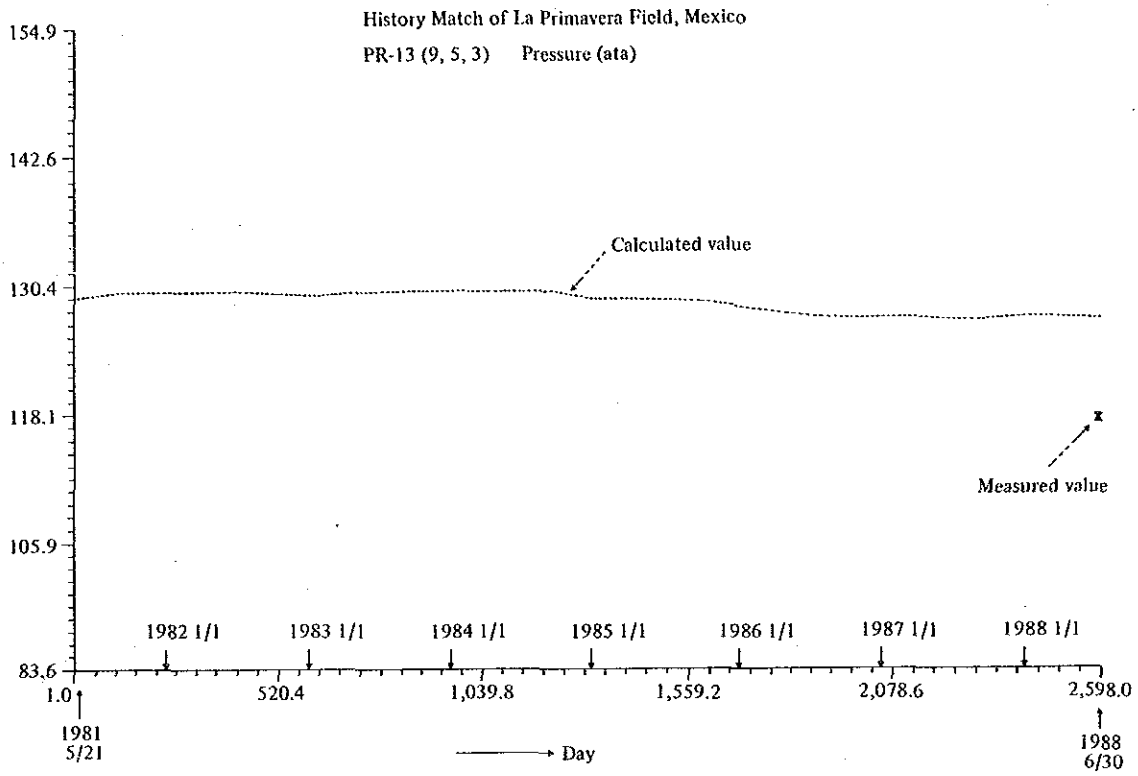

Fig. III. 2-40 Result of History Match of Pressure for PR-13

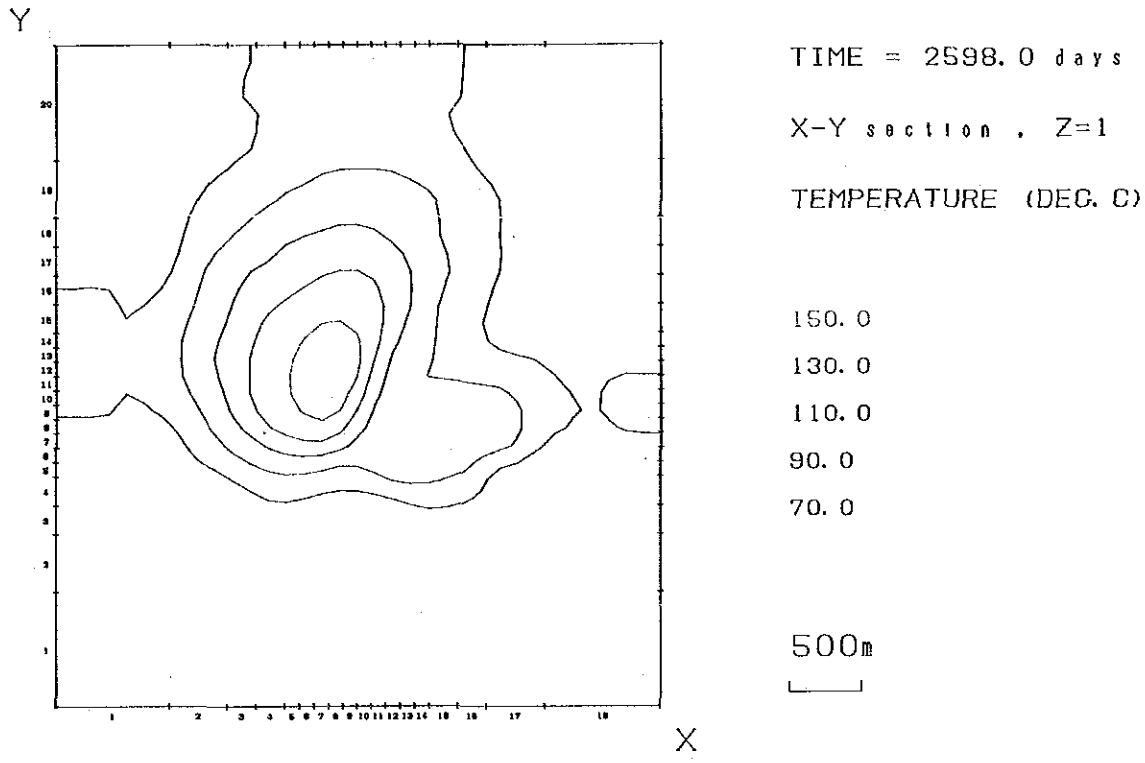

Fig. III. 2-41 Temperature Distribution after 2,598 Days (1988/6/30), Layer 1

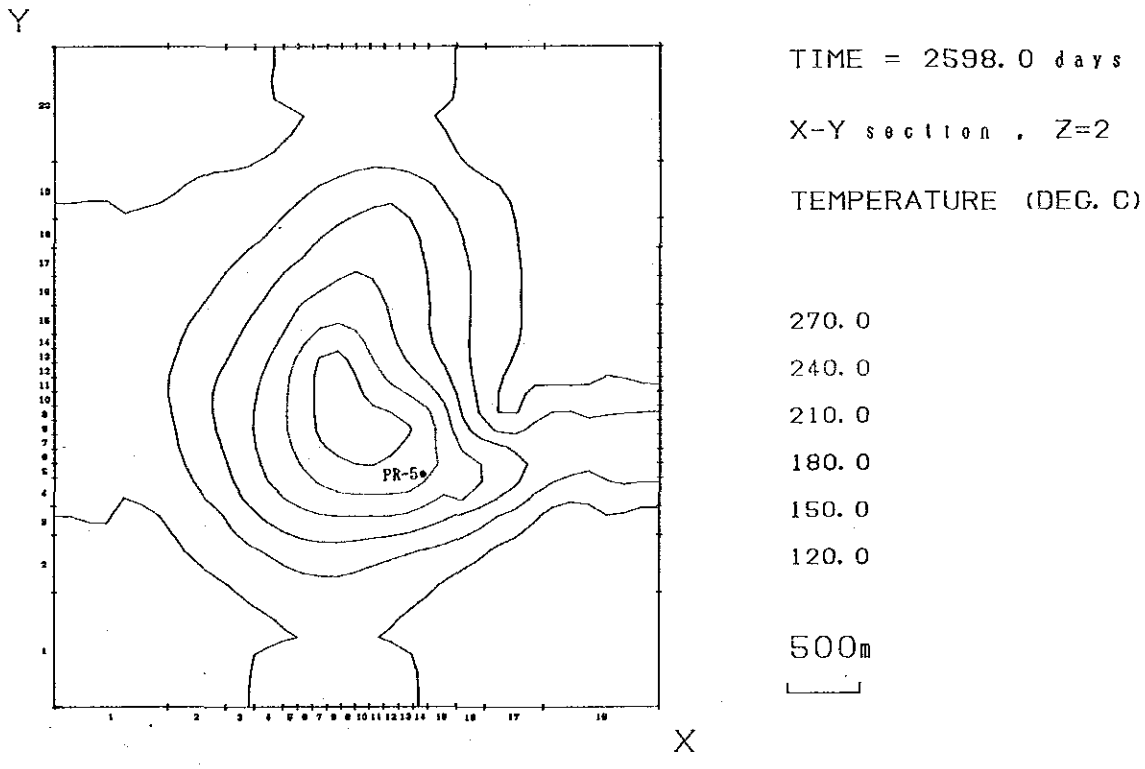

Fig. III. 2-42 Temperature Distribution after 2,598 Days (1988/6/30), Layer 2

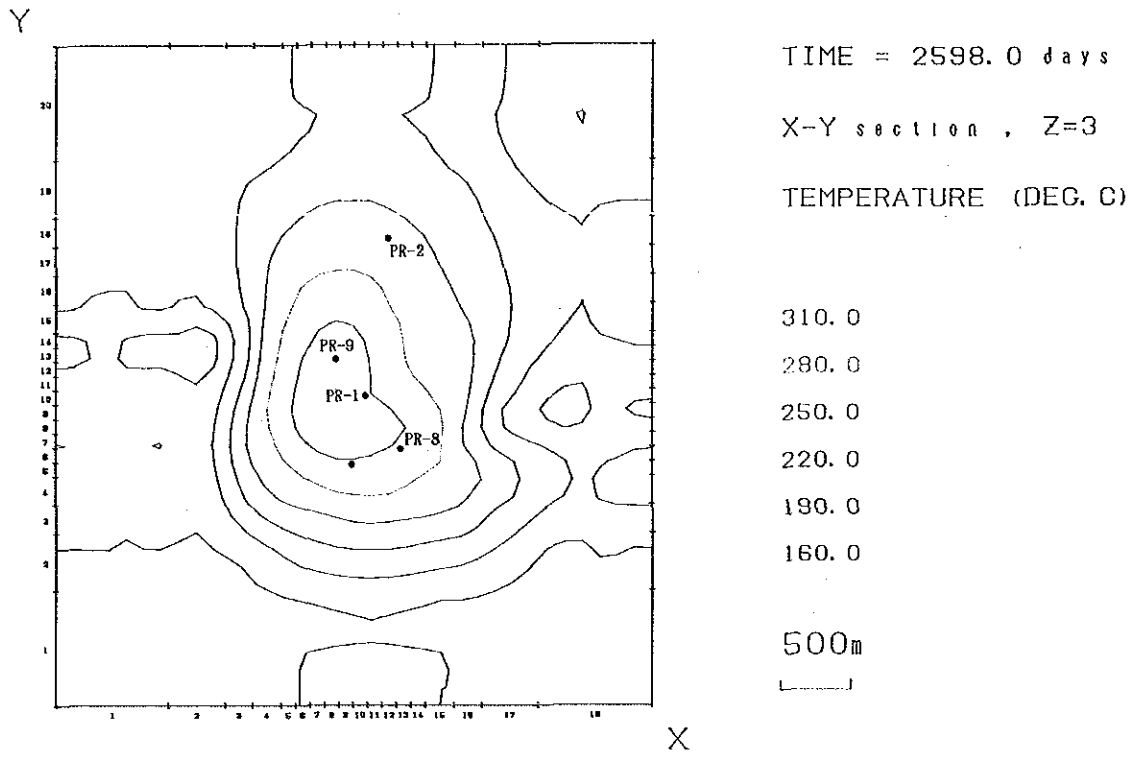

Fig. III. 2-43 Temperature Distribution after 2,598 Days (1988/6/30), Layer 3

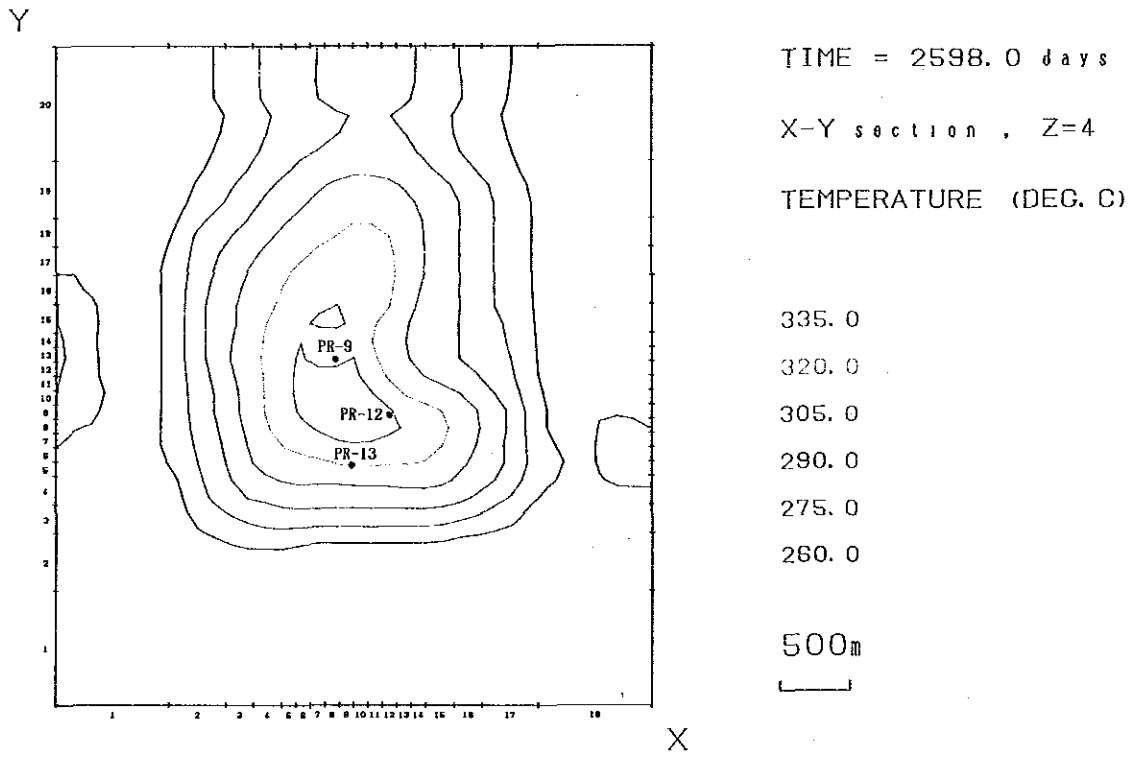

Fig. III. 2-44 Temperature Distribution after 2,598 Days (1988/6/30), Layer 4

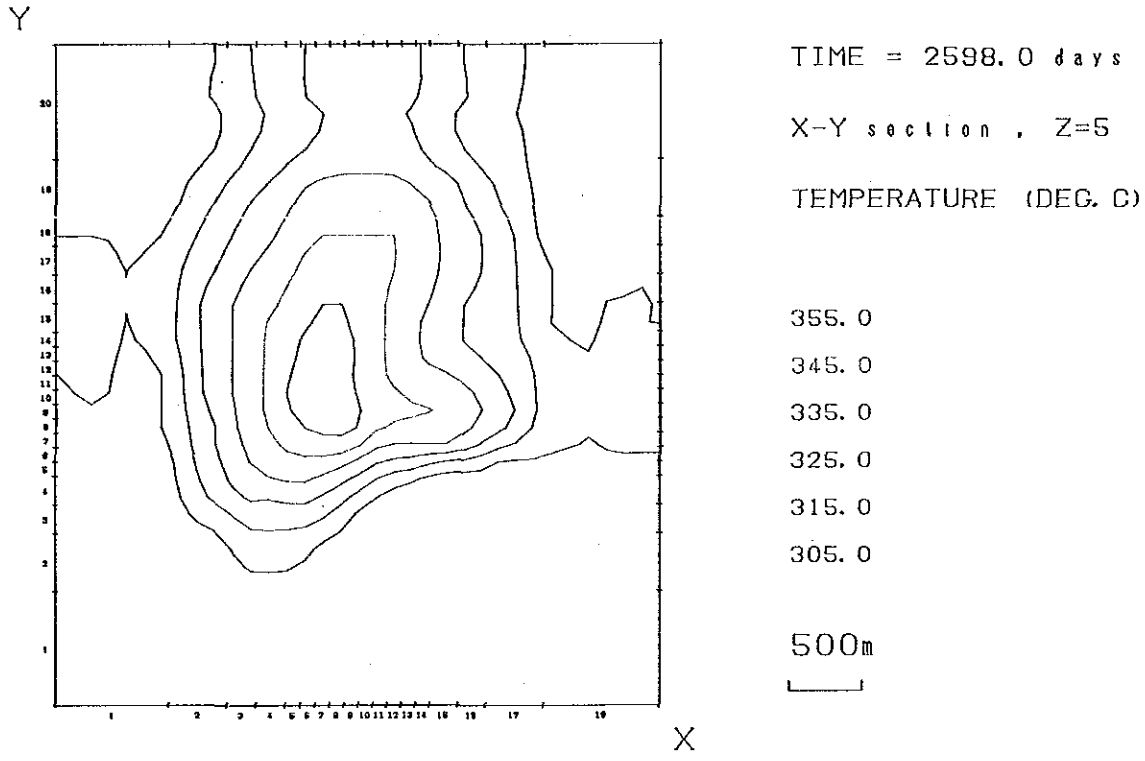

Fig. III. 2-45 Temperature Distribution after 2,598 Days (1988/6/30), Layer 5

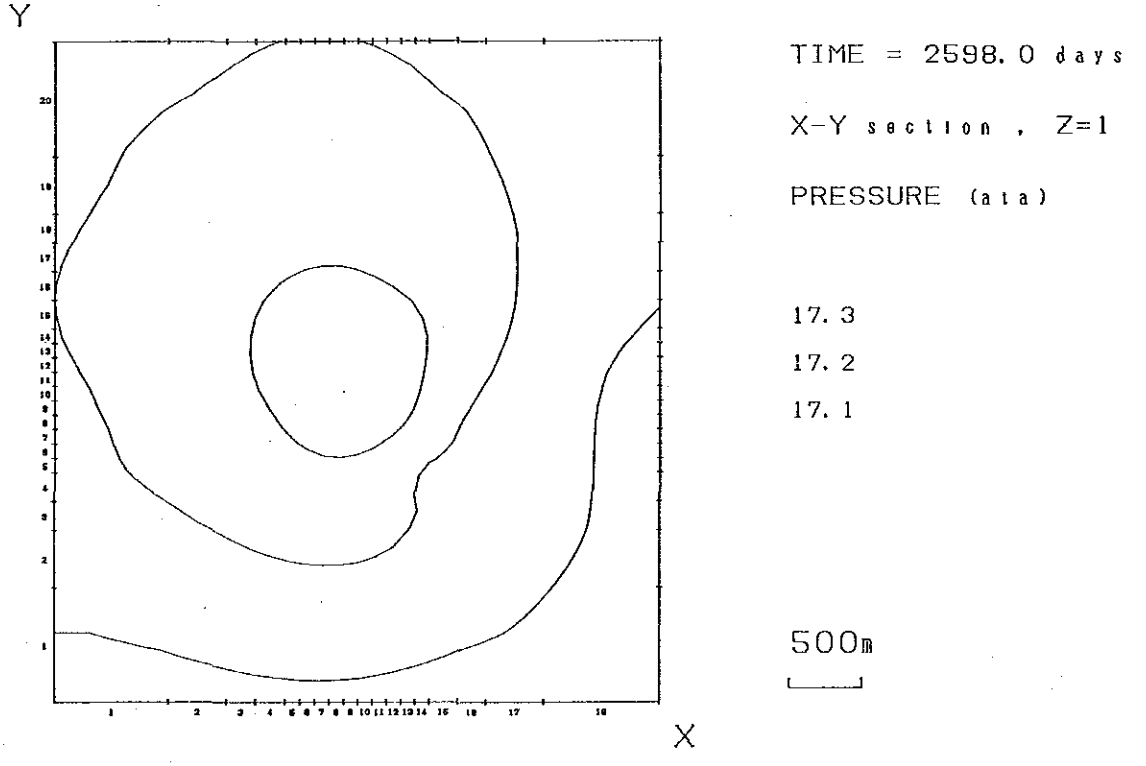

Fig. III. 2-46 Pressure Distribution after 2,598 Days (1988/6/30), Layer 1

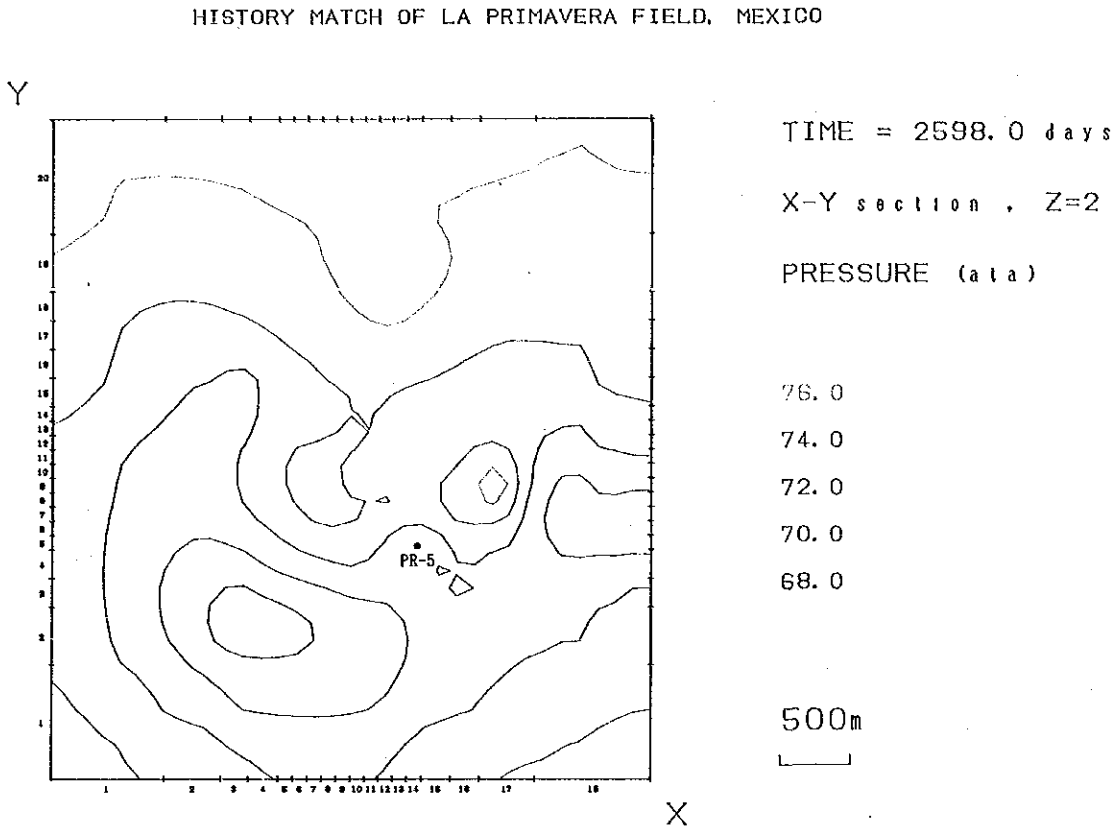

Fig. III. 2-47 Pressure Distribution after 2,598 Days (1988/6/30), Layer 2

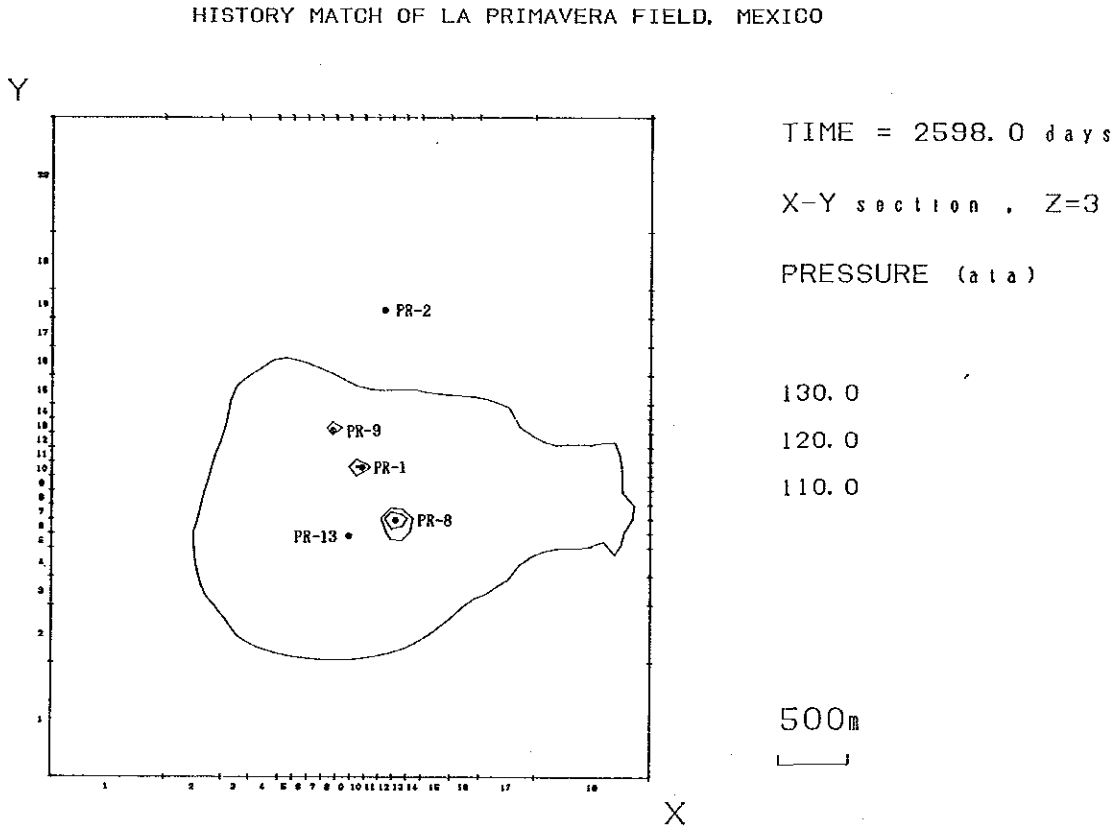

Fig. III. 2-48 Pressure Distribution after 2,598 Days (1988/6/30), Layer 3

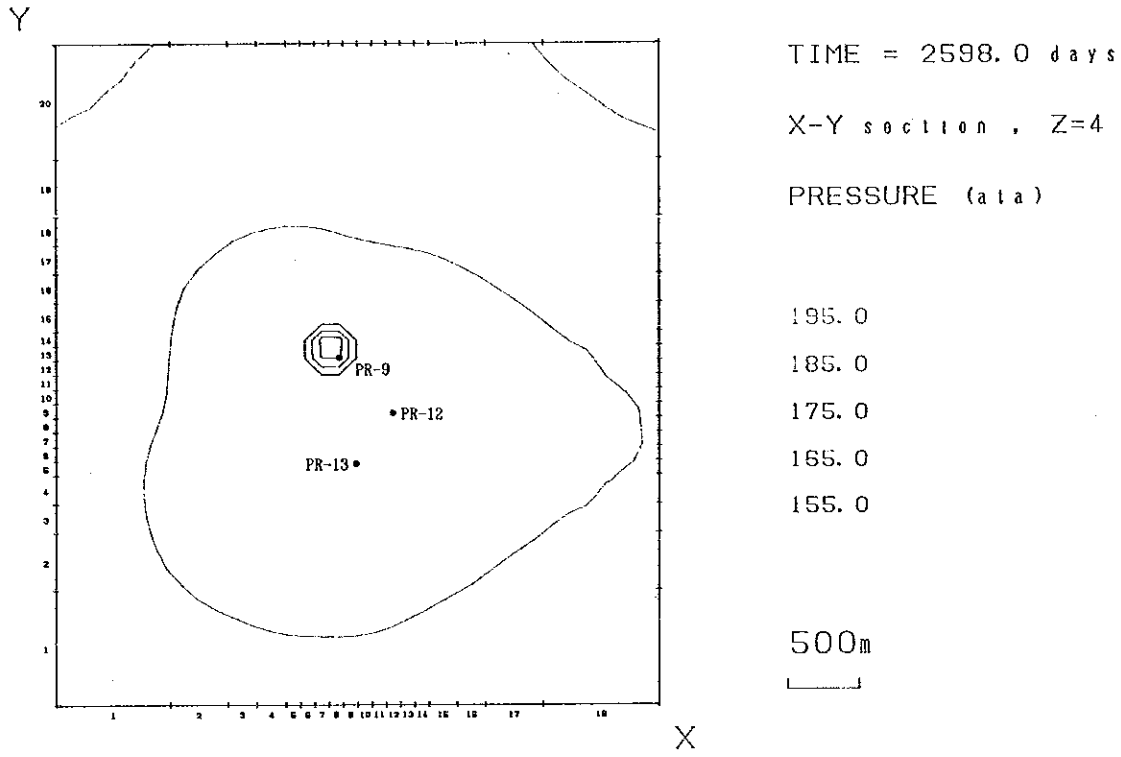

Fig. III. 2-49 Pressure Distribution after 2,598 Days (1988/6/30), Layer 4

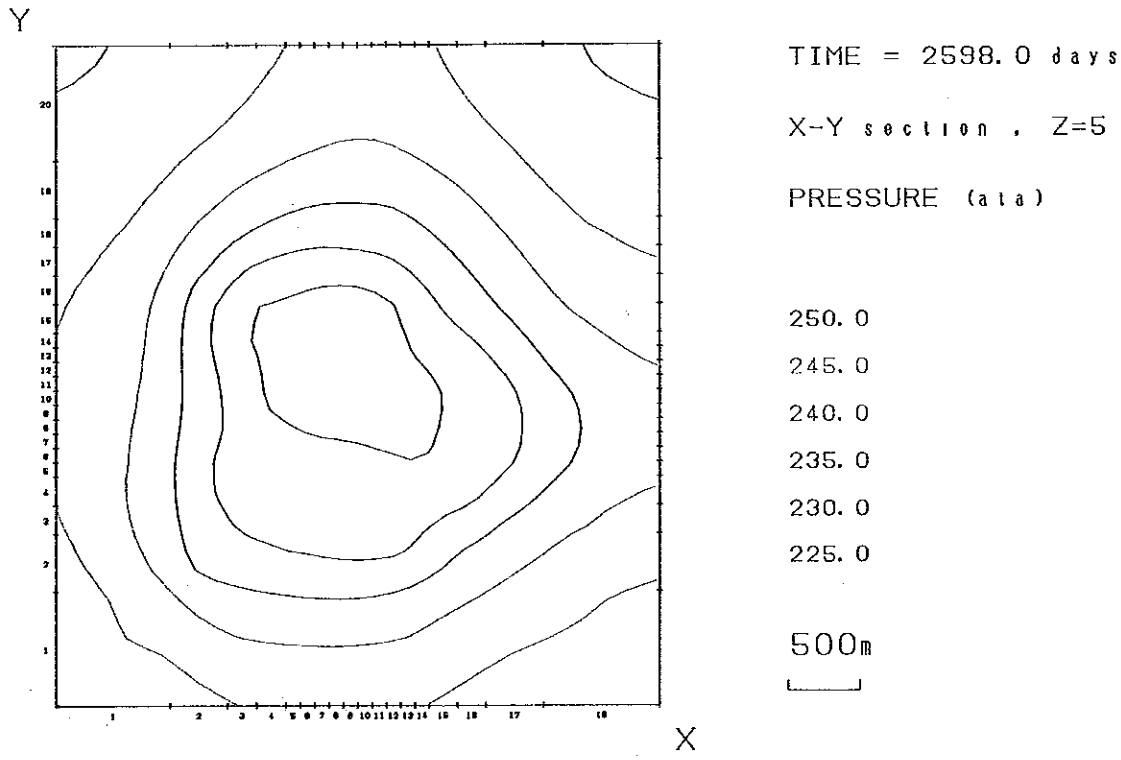

Fig. III. 2-50 Pressure Distribution after 2,598 Days (1988/6/30), Layer 5

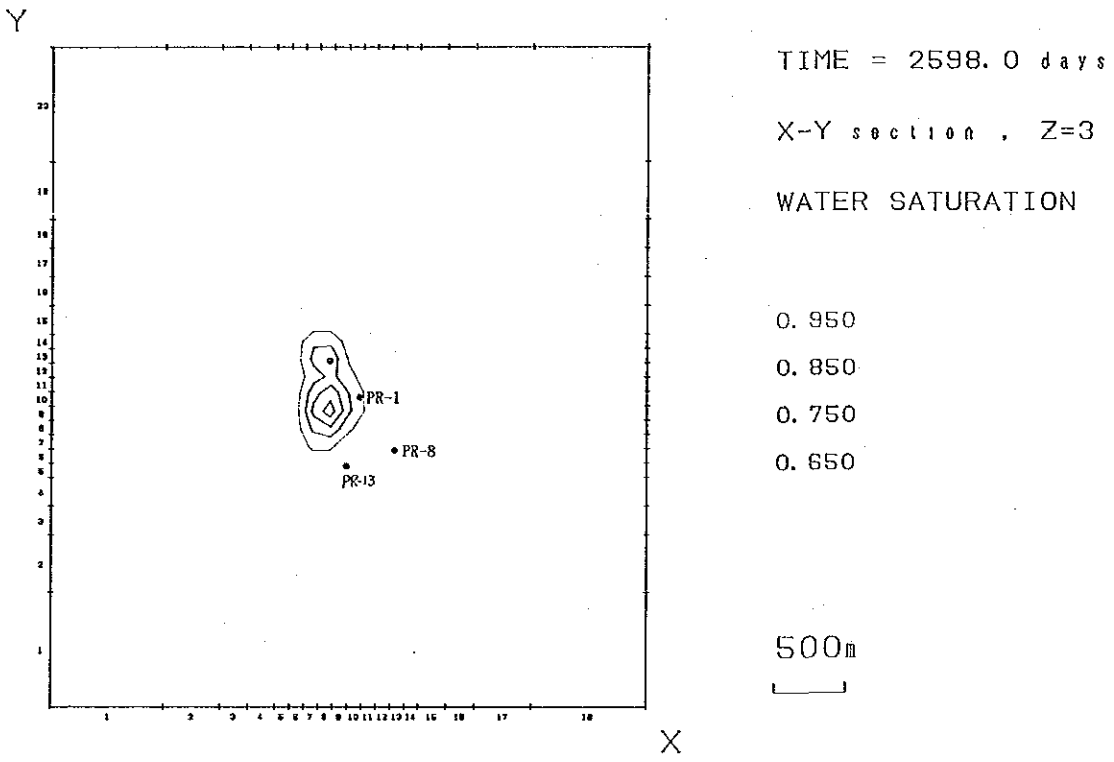

Fig. III. 2-51 Water Saturation after 2,598 Days (1988/6/30)

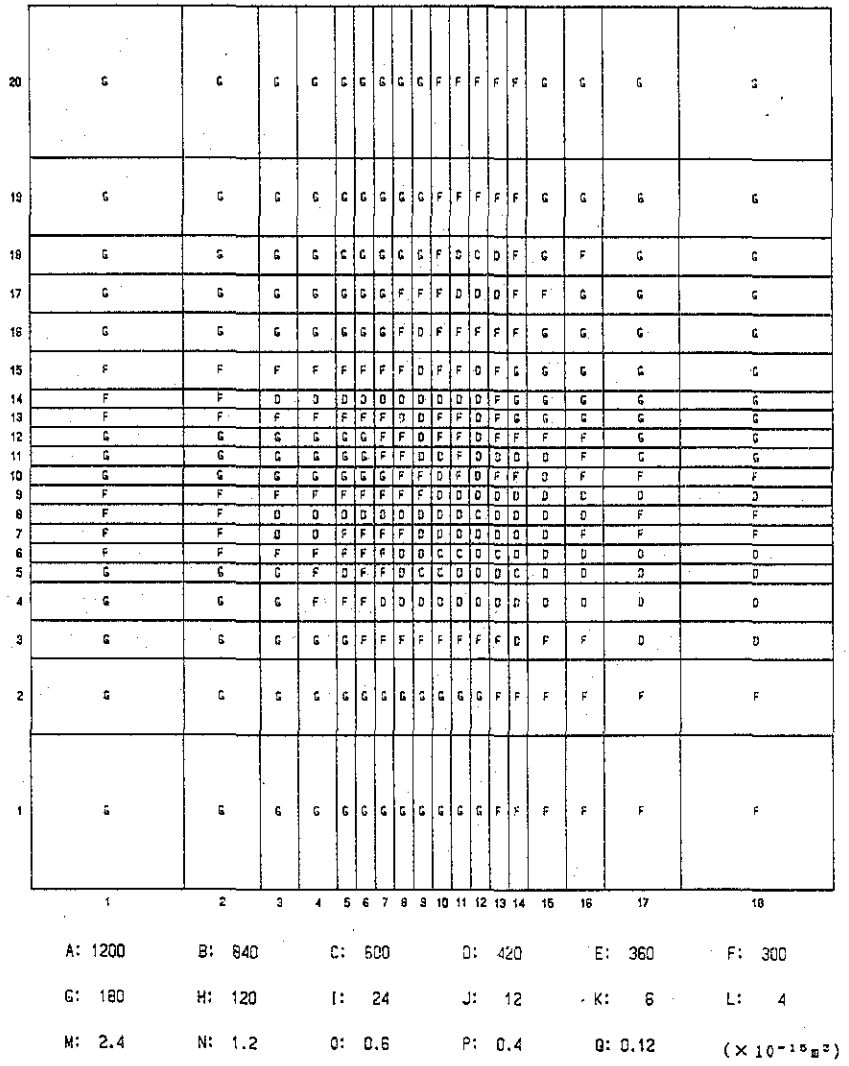

A: 1200 B: 840 C: 600 D: 420 E: 360 F: 300

G: 180 H: 120 I: 24 J: 12 K: 6 L: 4

M: 2.4 N: 1.2 O: 0.6 P: 0.4 Q: 0.12 ($\times 10^{-15}m^2$)

Fig. III. 2-52 Distribution of Horizonal Permeabilities in Layer 1

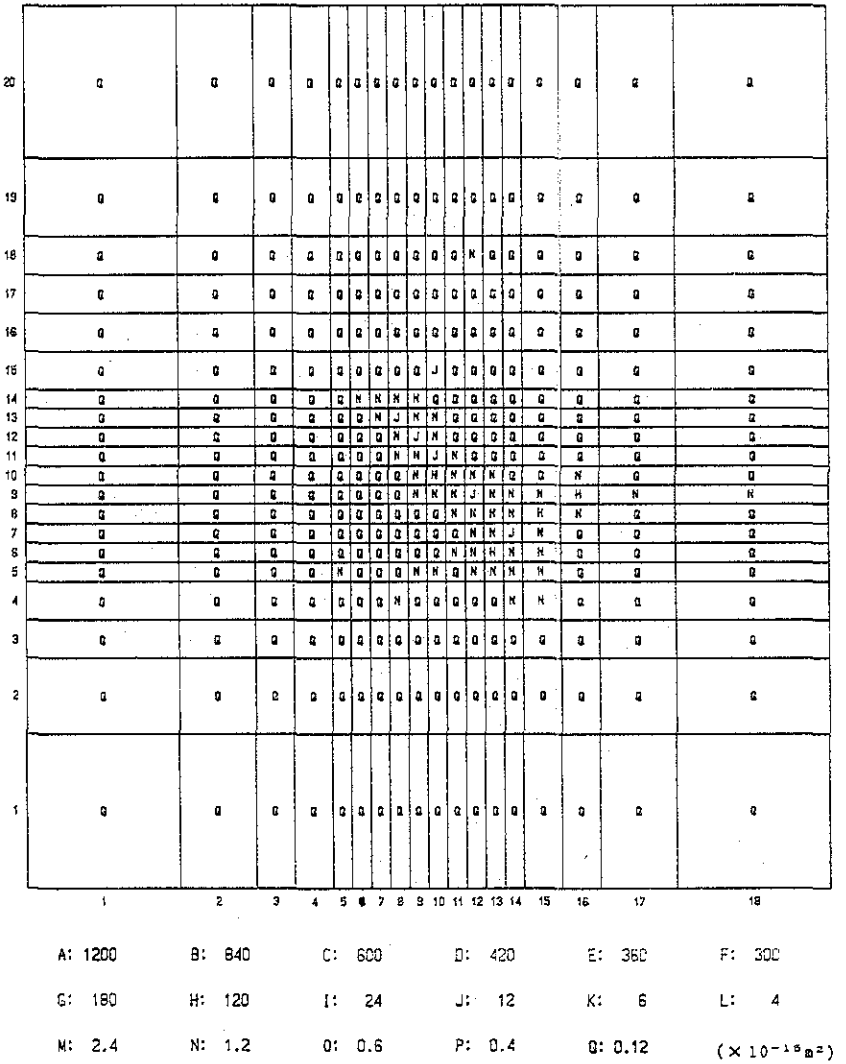

A: 1200 B: 840 C: 600 D: 420 E: 360 F: 300

G: 180 H: 120 I: 24 J: 12 K: 6 L: 4

M: 2.4 N: 1.2 O: 0.6 P: 0.4 Q: 0.12 ($\times 10^{-15}m^2$)

Fig. III. 2-53 Distribution of Horizonal Permeabilities in Layer 2

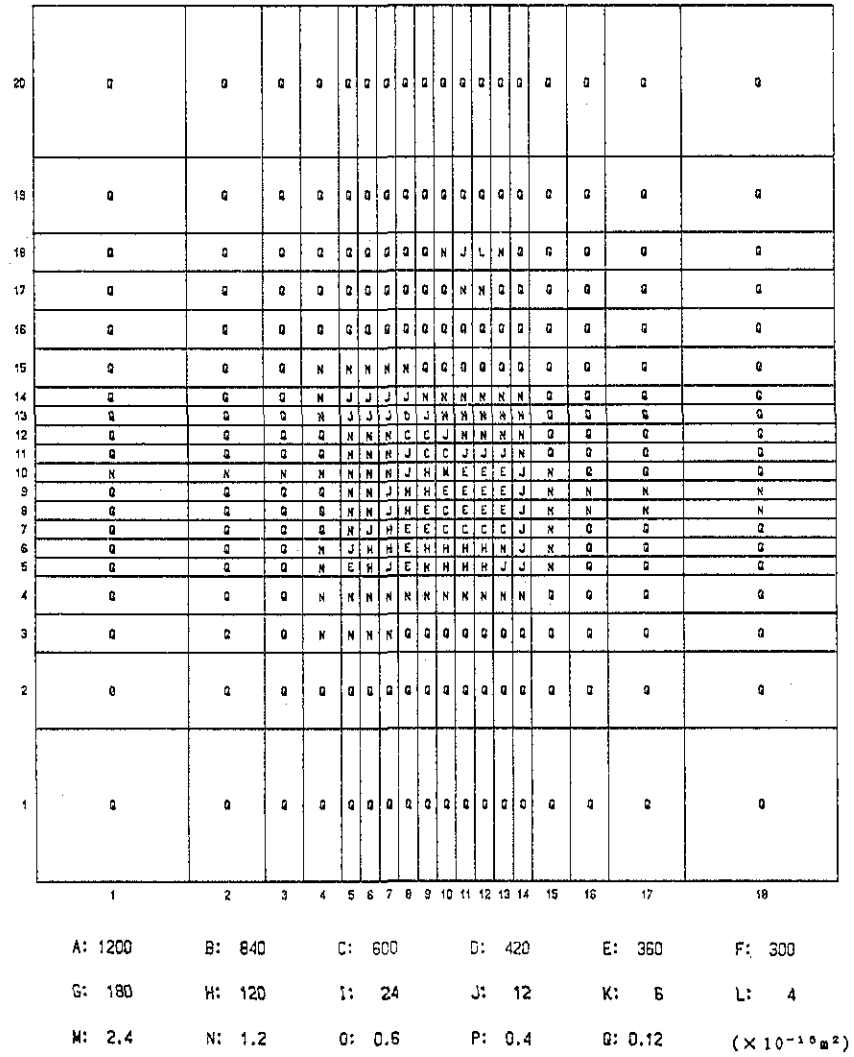

A: 1200 B: 840 C: 600 D: 420 E: 360 F: 300

G: 180 H: 120 I: 24 J: 12 K: 6 L: 4

M: 2.4 N: 1.2 O: 0.6 P: 0.4 Q: 0.12 ($\times 10^{-15}m^2$)

Fig. III. 2-54 Distribution of Horizonal Permeabilities in Layer 3

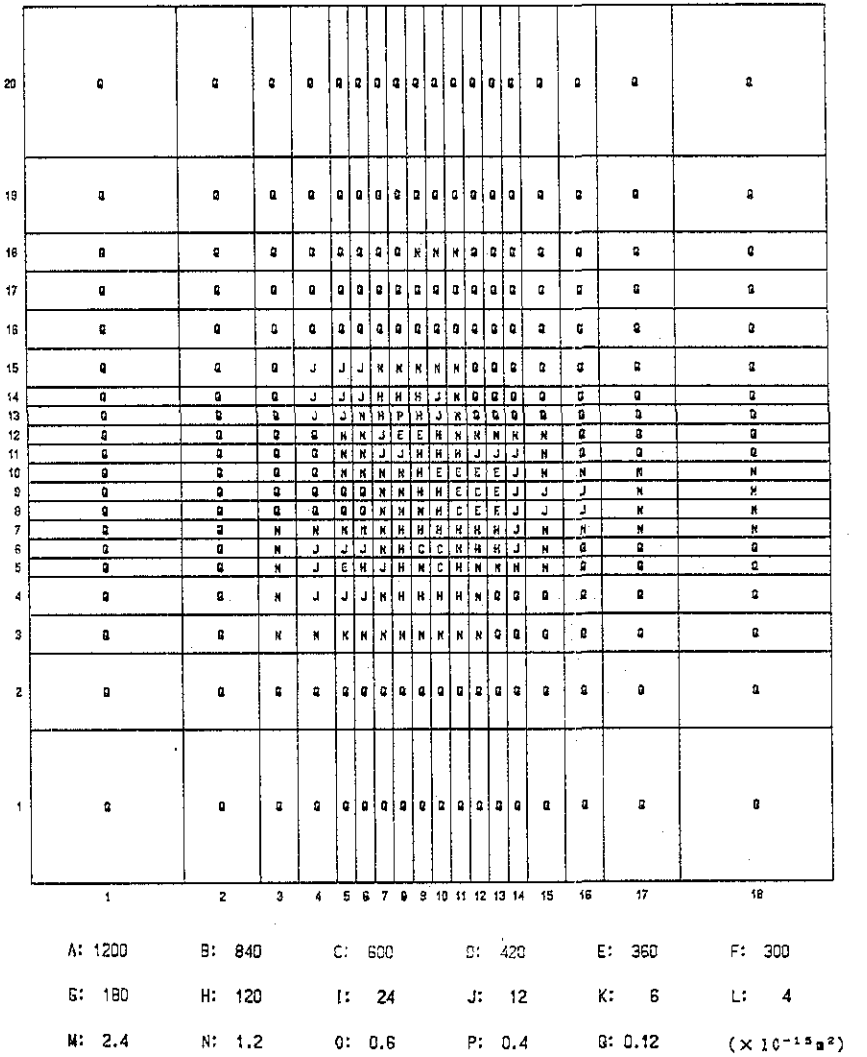

A: 1200 B: 840 C: 600 D: 420 E: 360 F: 300

G: 180 H: 120 I: 24 J: 12 K: 6 L: 4

M: 2.4 N: 1.2 O: 0.6 P: 0.4 Q: 0.12 ($\times 10^{-15}m^2$)

Fig. III. 2-55 Distribution of Horizonal Permeabilities in Layer 4

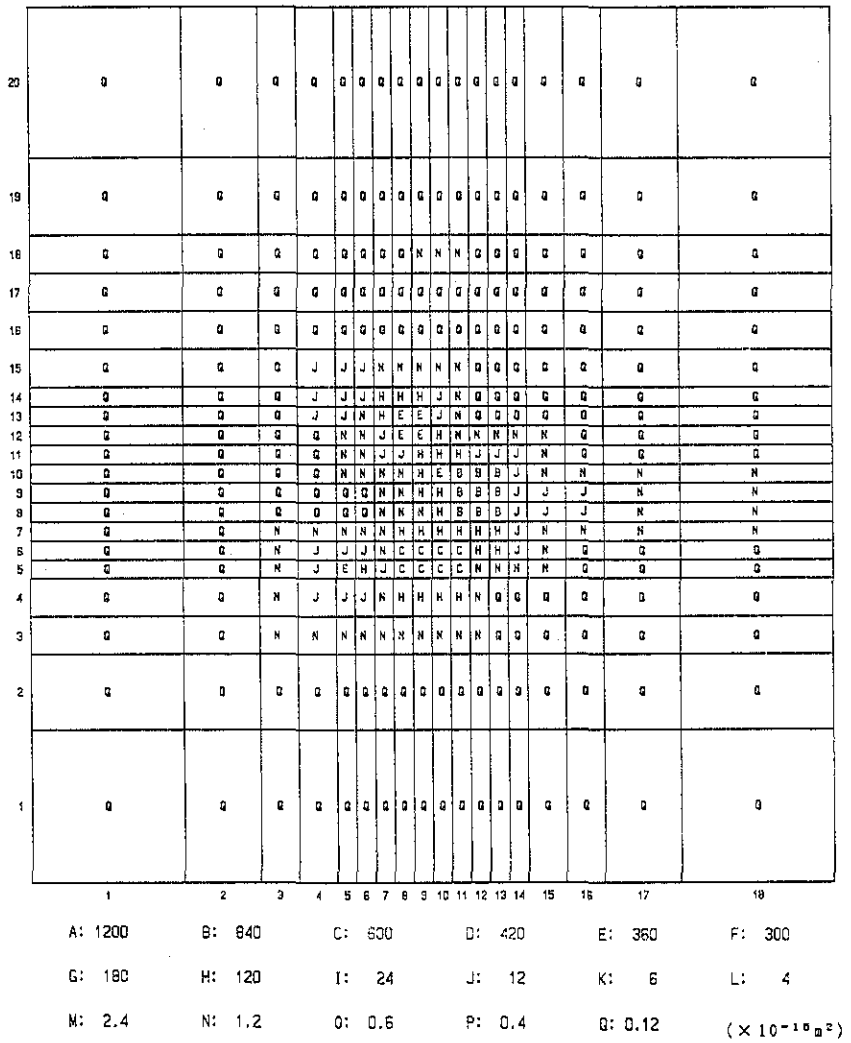

A: 1200 B: 840 C: 600 D: 420 E: 360 F: 300

G: 180 H: 120 I: 24 J: 12 K: 6 L: 4

M: 2.4 N: 1.2 O: 0.6 P: 0.4 Q: 0.12 ($\times 10^{-15}m^2$)

Fig. III. 2-56 Distribution of Horizonal Permeabilities in Layer 5

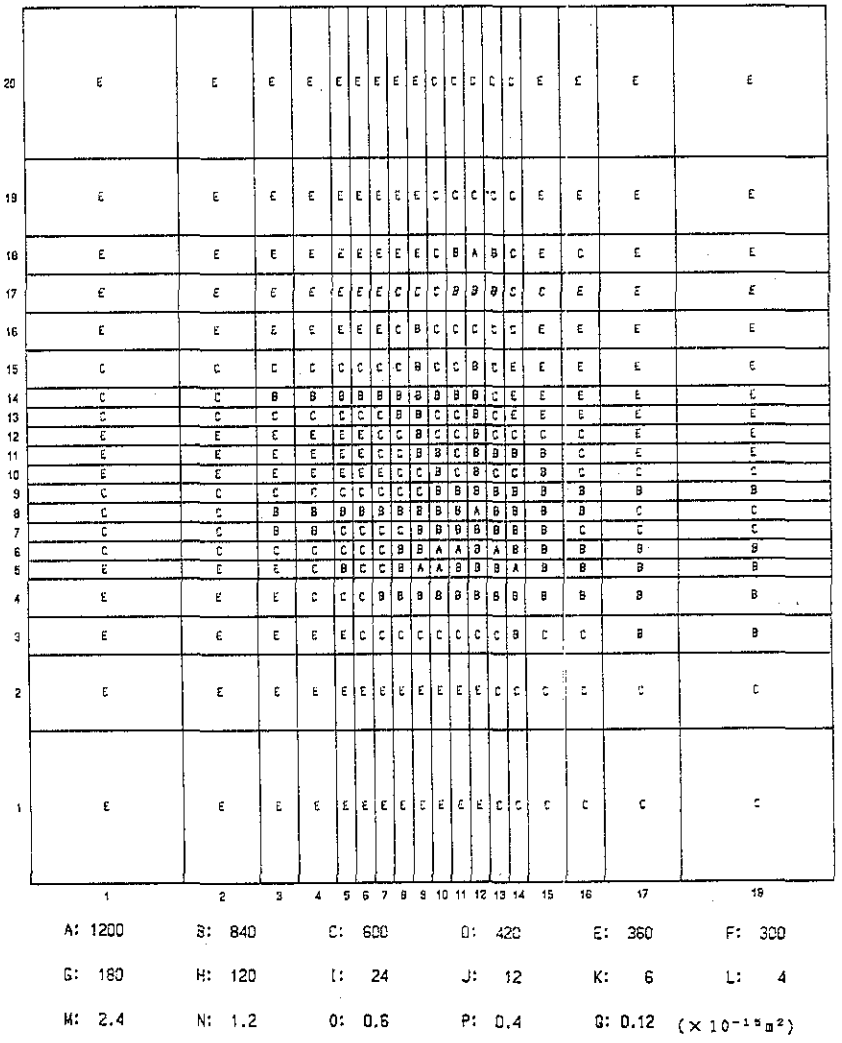

A: 1200 B: 840 C: 600 D: 420 E: 360 F: 300

G: 180 H: 120 I: 24 J: 12 K: 6 L: 4

M: 2.4 N: 1.2 O: 0.6 P: 0.4 Q: 0.12 ($\times 10^{-15}m^2$)

Fig. III. 2-57 Distribution of Vertical Permeabilities in Layer 1

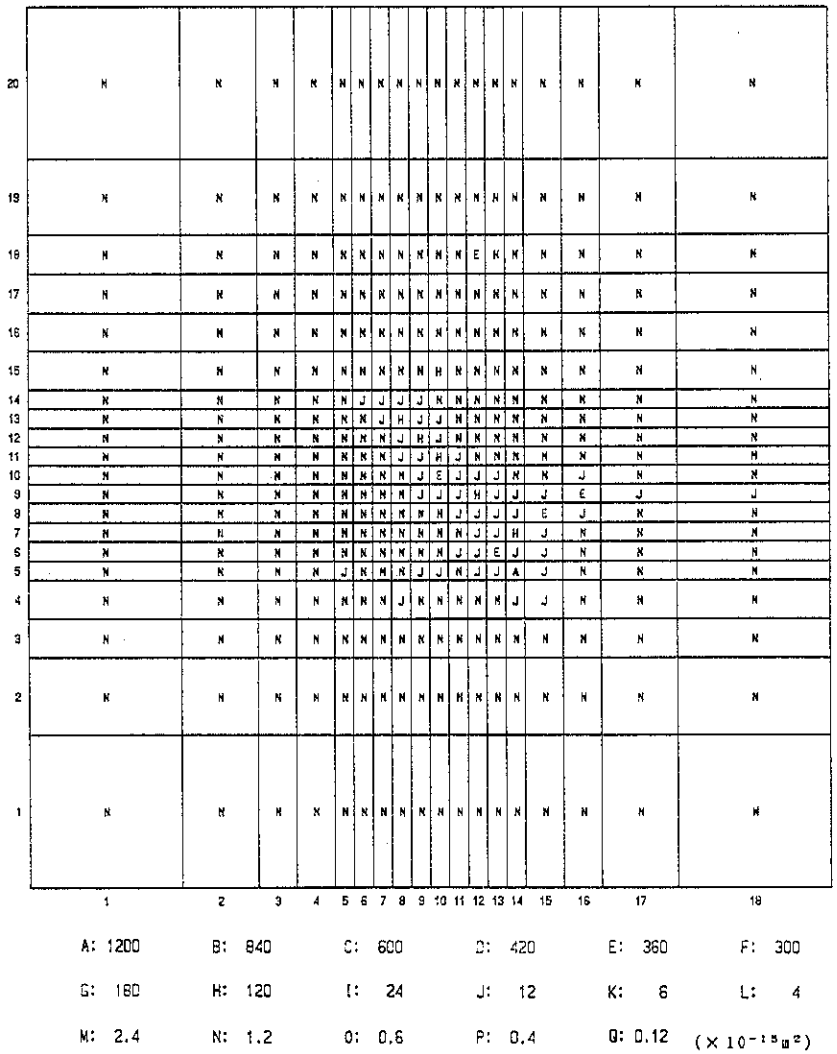

Fig. III. 2-58 Distribution of Vertical Permeabilities in Layer 2

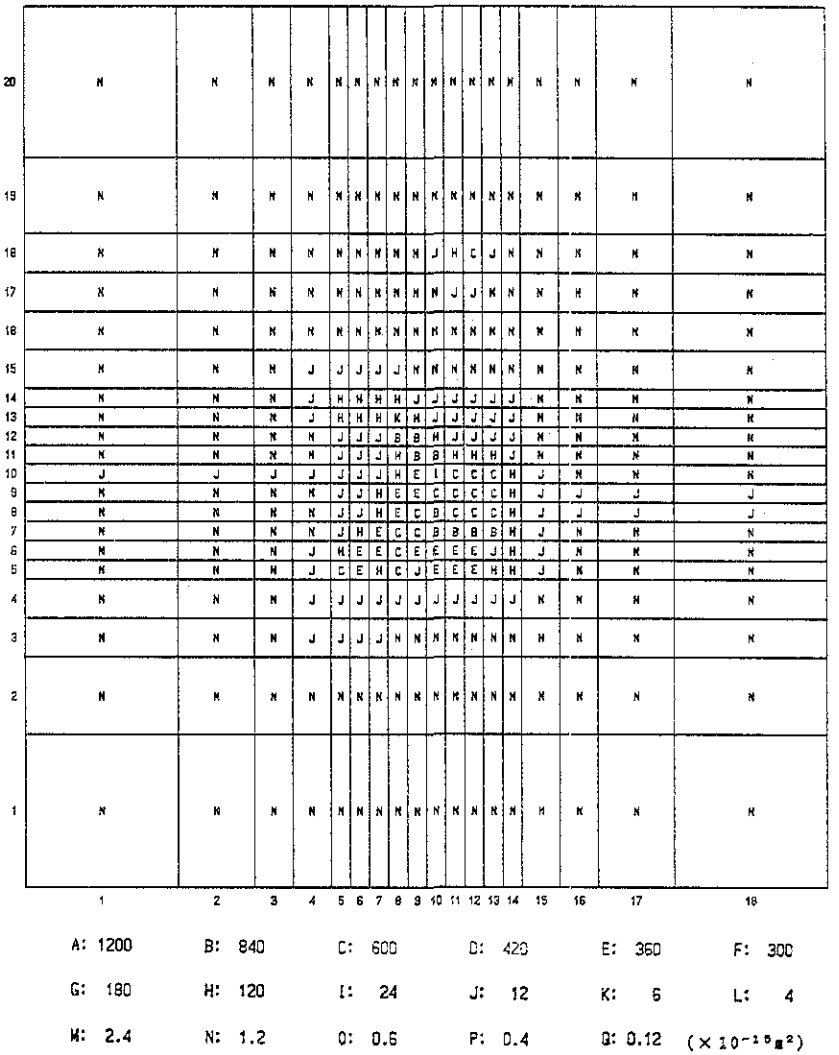

Fig. III. 2-59 Distribution of Vertical Permeabilities in Layer 3

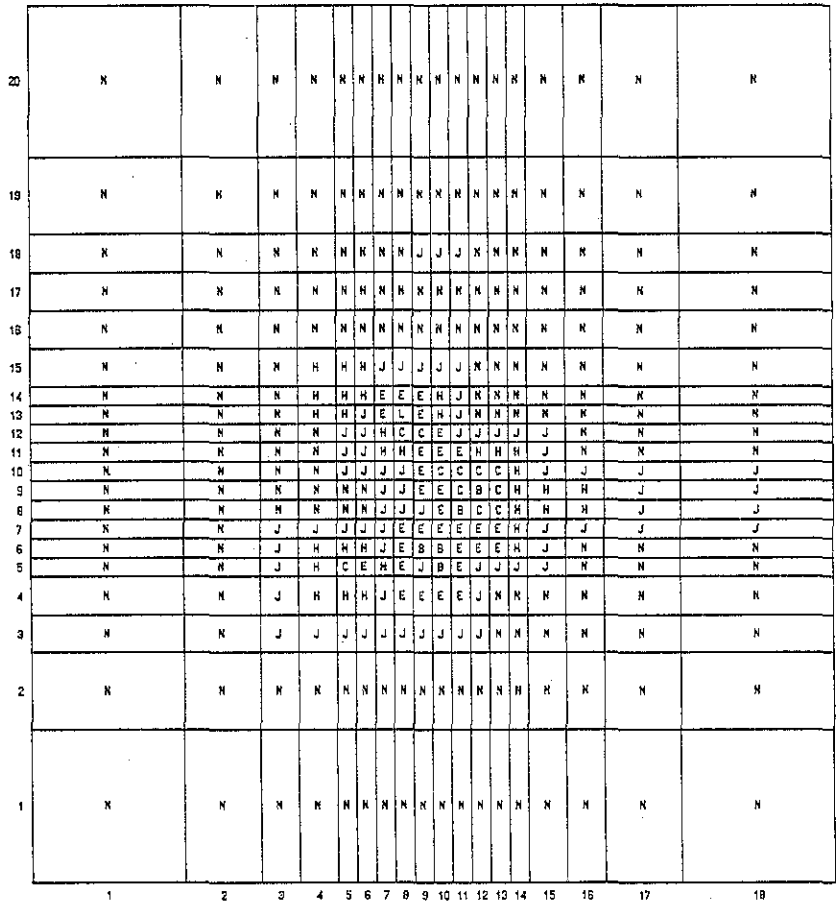

A: 1200 B: 840 C: 600 D: 420 E: 360 F: 300

G: 180 H: 120 I: 24 J: 12 K: 6 L: 4

M: 2.4 N: 1.2 O: 0.6 P: 0.4 Q: 0.12 ($\times 10^{-15}$m^2)

Fig. III. 2-60 Distribution of Vertical Permeabilities in Layer 4

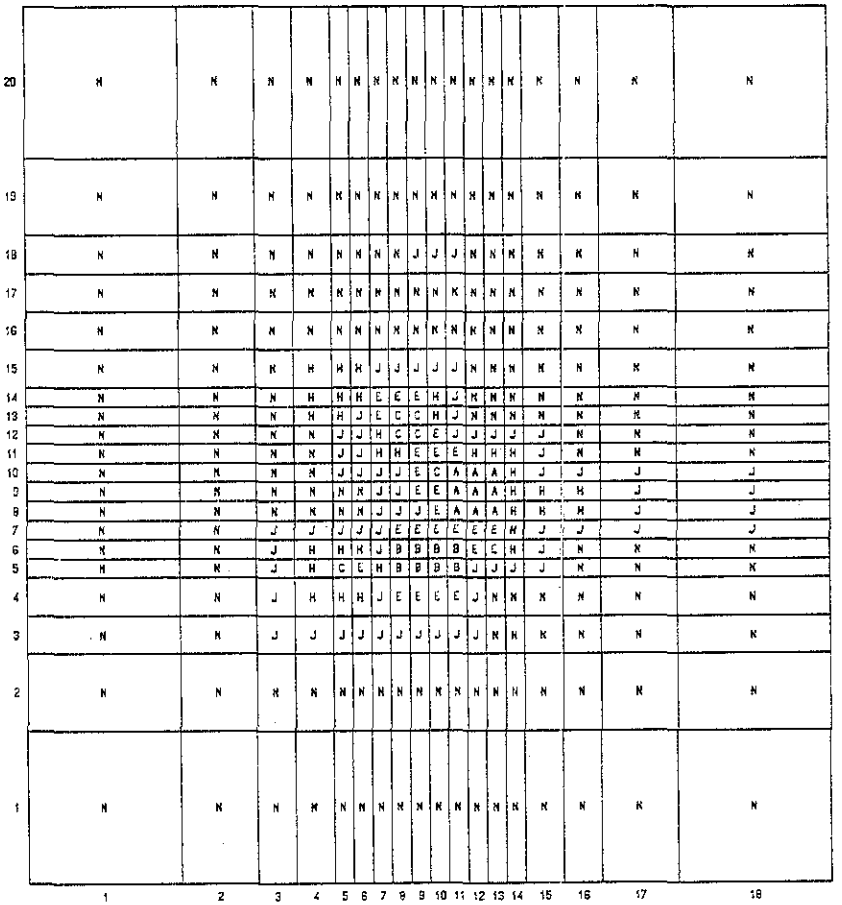

A: 1200 B: 840 C: 600 D: 420 E: 360 F: 300

G: 180 H: 120 I: 24 J: 12 K: 6 L: 4

M: 2.4 N: 1.2 O: 0.6 P: 0.4 Q: 0.12 ($\times 10^{-15}$m^2)

Fig. III. 2-61 Distribution of Vertical Permeabilities in Layer 5

Table III. 2-7 Resevoir Pressure for Match (ata)

Well	Location		Measured Date	Layer				
	I	J		1	2	3	4	5
PR-5	14	5	1982/08/28	–	64	–	–	–
PR-1	10	10	1984/09/28	–	–	93	–	–
PR-8	13	6	1985/10/18	–	–	125	–	–
PR-9	8	13	1985/11/27	–	–	132	188	–
PR-2	12	18	1986/10/03	–	–	122	–	–
PR-2	12	18	1987/03/20	–	–	127	–	–
PR-2	12	18	1987/07/02	–	–	120	–	–
PR-2	12	18	1987/09/12	–	–	107	–	–
PR-2	12	18	1988/02/17	–	–	128	–	–
PR-2	12	18	1988/02/24	–	–	128	–	–
PR-2	12	18	1988/04/19	–	–	139	–	–
PR-2	12	18	1988/04/28	–	–	137	–	–
PR-13	9	5	1988/06/25	–	–	117	–	–

Table III. 2-8 Geothermometers of PR-1

Date	Concentrations (ppm)			Geothermometers (°C)		
	Na	K	Ca	Na/K (W)	Na/K (F)	NaKCa
1985/02/06	782	232	2.4	345	360	318
1985/04/27	760	193	2.4	316	327	304
1985/05/31	751	200	2.4	324	336	307
1985/06/26	764	194	2.2	316	327	305
1985/07/30	770	179	2.2	301	309	298
1985/08/30	768	175	3.2	297	306	290
1985/09/30	760	175	2.6	299	308	294
1985/10/29	764	170	2.2	293	301	294
1985/11/29	758	180	1.4	304	314	306
1986/02/07	751	173	2.1	299	308	297
1986/03/04	745	167	2.2	295	303	294
1986/05/06	749	167	3.6	294	302	286
1986/06/14	733	160	1.2	290	298	299
1986/09/22	730	185	1.6	316	326	308
1986/11/28	718	155	1.4	289	296	296
1986/12/04	710	165	1.4	301	309	302
1987/01/07	725	165	1.6	297	305	299
1987/02/03	720	170	1.6	303	312	302
1987/03/11	733	167	1.8	297	306	297
1987/04/10	730	167	2.4	298	306	293
1987/05/13	723	161	1.8	294	301	295
1987/05/18	731	160	2.6	291	298	289
1987/05/26	750	159	1.8	286	292	292
1987/06/30	744	155	4.0	283	289	279
1987/07/16	729	156	1.6	287	294	293
1987/09/05	730	168	3.0	299	308	291
1988/01/05	742	170	1.6	298	307	300
1988/02/25	745	170	1.5	298	306	301
1988/03/23	705	177	1.9	314	324	304

Table III. 2-9 Geothermometers of PR-2

Date	Concentrations (ppm)			Geothermometers (°C)		
	Na	K	Ca	Na/K (W)	Na/K (F)	NaKCa
1985/02/25	2,577	134	0.6	126	118	231
1985/04/29	2,538	126	0.8	123	115	224
1985/05/31	2,439	127	0.8	127	119	227
1985/06/29	2,489	127	0.6	125	117	229
1985/07/30	2,336	132	1.2	133	126	227
1985/08/30	2,351	129	1.2	131	123	225
1985/09/30	2,380	133	1.6	132	125	223

Table III. 2-10 Geothermometers of PR-5

Date	Concentrations (ppm)			Geothermometers (°C)		
	Na	K	Ca	Na/K (W)	Na/K (F)	NaKCa
1982/09/01	745	117	0	242	243	–
1982/09/02	789	122	0	240	241	–
1982/09/03	777	100	0	216	215	–
1982/09/04	716	95	0	220	219	–
1982/09/06	691	90	0	218	217	–
1982/09/09	726	104	0	230	230	–
1982/09/10	699	103	0	233	234	–
1982/09/11	652	88	0	222	222	–
1982/09/13	642	82	0	215	214	–
1982/09/14	638	86	0	222	222	–
1982/09/15	640	83	0	217	216	–
1982/09/17	632	82	0	217	216	–
1982/09/18	649	82	0	214	213	–
1982/09/21	629	79	0	213	212	–
1982/09/22	620	73	0	206	204	–
1982/09/24	592	72	0	210	208	–
1982/09/27	582	70	0	208	207	–

Table III. 2-11 Geothermometers of PR-8

Date	Concentrations (ppm)			Geothermometers (°C)		
	Na	K	Ca	Na/K (W)	Na/K (F)	NaKCa
1985/10/29	1,078	126	5.2	205	203	242
1985/10/30	972	130	4.4	221	221	251
1985/11/01	890	137	2.6	239	241	266
1985/11/05	854	140	2.8	248	250	269
1985/12/04	842	143	1.2	253	255	282
1986/01/03	824	152	2.8	264	269	277
1986/01/30	834	136	1.1	247	249	280
1986/02/21	856	149	1.4	256	259	283
1986/03/04	848	147	1.6	256	259	280
1986/04/04	851	141	1.8	249	252	275
1986/05/06	849	152	0.8	260	264	292
1986/06/14	849	147	0.8	255	258	290
1986/06/19	851	151	0.6	259	262	296
1986/07/03	826	160	2.0	272	277	286
1986/07/07	826	160	2.0	272	277	286
1986/08/25	819	160	0.7	273	278	301
1986/09/22	810	155	1.4	270	275	289
1986/10/01	815	160	1.2	274	279	293
1986/10/09	840	165	1.2	274	279	294
1986/10/30	831	165	1.2	276	281	295
1986/11/06	826	160	1.2	272	277	293
1987/02/09	816	150	0.8	264	268	294
1987/04/10	809	137	1.0	252	255	283
1987/05/13	848	139	0.8	248	250	285
1987/06/12	857	136	0.9	243	245	281
1987/07/04	823	130	0.8	243	244	281
1987/07/16	805	128	0.8	244	245	281
1987/09/28	812	135	2.6	250	252	269
1988/01/27	795	138	1.1	256	259	284
1988/02/18	783	141	1.0	261	265	288
1988/02/22	776	143	0.8	264	268	292
1988/02/27	773	141	0.9	263	267	290
1988/03/04	775	140	1.0	261	265	288
1988/04/14	803	134	1.0	250	253	282
1988/05/02	810	136	1.2	251	254	280
1988/06/02	808	139	1.0	254	257	285

Table III. 2-12 Geothermometers of PR-9

Date	Concentrations (ppm)			Geothermometers (°C)		
	Na	K	Ca	Na/K (W)	Na/K (F)	NaKCa
1986/07/11	1,350	200	109.0	234	235	229
1986/07/14	824	120	19.0	232	232	236
1986/07/15	720	105	11.0	232	233	239
1986/07/17	716	110	6.0	239	240	250
1986/07/21	717	105	4.4	233	233	250
1986/07/31	701	100	3.4	229	230	251
1986/08/07	701	105	3.6	236	237	254
1986/09/01	650	140	1.7	288	295	290
1986/09/09	655	145	2.2	293	300	289
1986/09/22	635	140	1.8	292	300	290
1986/10/09	660	150	2.0	297	305	293
1986/10/20	630	155	1.2	310	320	305
1986/10/24	655	145	1.2	293	300	297
1986/10/27	683	150	3.0	291	299	285
1986/10/30	689	150	1.8	290	297	292
1986/11/06	675	145	1.8	288	295	290
1987/02/09	670	140	1.0	283	290	290
1987/04/10	676	144	2.0	286	293	288
1987/05/13	678	152	5.2	295	303	279
1987/06/12	687	151	2.4	291	299	288
1987/07/16	643	142	0.4	292	300	313
1987/09/24	646	138	2.6	287	294	283
1987/09/28	659	132	3.2	277	283	276
1987/10/03	658	133	2.8	278	284	278
1987/10/06	661	137	3.8	282	288	276
1987/10/20	655	129	1.5	274	280	284
1987/10/26	849	127	1.5	235	236	269
1987/10/31	650	126	2.0	272	277	279
1988/01/05	691	130	1.8	267	272	280
1988/01/28	676	129	1.8	270	274	280
1988/02/25	673	161	1.0	306	315	308
1988/03/11	659	163	0.9	311	321	312
1988/03/18	659	165	0.9	313	324	313
1988/03/26	667	145	1.1	290	297	298
1988/04/15	666	140	0.9	284	291	298
1988/06/02	665	143	1.0	288	295	298

Table III. 2-13 Geothermometers of PR-12

Date	Concentrations (ppm)			Geothermometers (°C)		
	Na	K	Ca	Na/K (W)	Na/K (F)	NaKCa
1988/01/21	810	226	3.6	333	346	308
1988/01/28	740	203	4.8	330	343	299
1988/02/04	756	208	3.6	330	343	305
1988/02/11	772	214	3.2	332	345	308
1988/02/17	766	209	3.4	329	342	305
1988/02/25	748	206	4.6	331	343	301
1988/03/11	741	205	3.0	331	344	307
1988/03/18	706	192	3.2	328	341	303
1988/03/26	752	208	3.0	331	344	308
1988/04/14	810	214	3.3	323	335	304
1988/05/02	776	206	3.0	324	336	305
1988/06/17	723	200	2.2	331	344	311
1988/06/20	731	206	2.6	335	348	310
1988/06/27	756	210	2.6	332	345	310
1988/07/05	757	203	2.6	326	338	307
1988/07/11	733	200	2.6	329	342	308

2.5 Performance predictions

(1) Prediction method

From the history match, we obtained a model that can be used to predict the response of the reservoir and individual wells to various exploitation schemes. The ultimate objective of any future prediction is to estimate the generating capacity of the resource based on various developing assumptions. There are currently 7 wells available for us at the La Primavera field. The following four cases were to be studied as shown in Table III.2-14.

Case 1 : 50 MW power production with 29 future wells
Case 2 : 50 MW with 17 future wells
Case 3 : 75 MW with 29 future wells
Case 4 : 100 MW with 29 future wells

When we extend the history match calculation for the prediction, many makeup wells should be added to the existing wells. The locations and the tentative efficiency of makeup wells are based upon the geothermal reservoir structure as previously stated in Chapter III.-1.2. That is to say, the makeup wells are arranged within productive zones at intervals of more than 200 m (Fig. III.2-2). Although the real efficiency of the existing wells are shown in Table III.2-15, the tentative efficiency of makeup wells was decided as given in an example below.

In case 1,

We calculated for a period of 20 years with 500t/h using 7 existing wells and 29 future wells. In this case, the efficiency of each well is allocated in proportion to the rank of productivity shown in Table III.2-16. The rank of productivity is decided by the geological situation (presence or absence of fractures et.), the low resistivity by MT method and the temperature in the location of each well. According to the rank, a total flow rate of each case is divided into each well by proportional allotment.
Table III.2-17 shows a tentative efficiency of each well in four cases with real calculation.

Additional assumptions for the prediction were as follows:

① Wells continue producing at the fixed flow rate of steam at the wellhead pressure of 6.5 ata for a period of 20 year (9,903 days) from on the 1st, July in 1988 to the 30th, June in 2008.
② The electrical efficiency was assumed to be 10 t/h/1 MW.
③ Hot water with steam did not re-inject but discharges into the land surface.

The decision of the generating capacity depends upon the values of pressure and water saturation on the 30th, June in 2008, namely after the calculation of 20 years for each cases.

(2) Calculational results

The calculated areal distribution of pressure and water saturation in fractures after 20 years is shown in Figs. III.2-62 to III.2-77 for layers 3 and 4 who make up the main reservoir in this

area. In every case, the values of pressure and water saturation decreased around the center of the calculation area where the production wells were concentrated. The values can maintain the fixed wellhead pressure and do not make any super-heated regions in every blocks (grids).

In case 4 (1,000 t/h, —100 MW), however, the decreasing rates of pressure and water saturation were very much larger than those of other cases. This fact suggests that the recharge of fluid flow from the surrounding areas is limited.

We brought a grid of PR-9 into focus because the pressure and water saturation in the grid showed the most decrease in all cases as given in Figs. III.2-78 and III.2-79. These figures indicate that the pressure tends to keep about 68 ata for a period of 20 years and the water saturation is also about 35% constantly in case 3 (750 t/h, 75 MW).

From the above mentioned facts of cases 3 and 4, it is concluded that a feasible 75 MW is a reliable estimate of the generating capacity in a stable condition for this reservoir.

Table III. 2-14 Cases for Reservoir Predictions

(1) Well head pressure is set to be 6.5 ata.
(2) Reservoir behaviors are simulated for twenty years.

	Output Power (MWe)	Steam Production Rate (t/h)	Number of Production Wells	Number of Existing Wells	Number of Future Wells
Case 1	50	500	36	7	29
Case 2	50	500	24	7	17
Case 3	75	750	36	7	29
Case 4	100	1,000	36	7	29

Table III. 2-15 Well Efficiency in the La Primavera Area

* Temperaturas estabilizadas.

Pozo No.	Profundidad de Isotermas (°C = MT)					Intervalo Productor	Produccion a Separacion al	Presion de aire	Prof. Total
	100°C	150°C	200°C	250°C	300°C		Vapor	Agua	
1	500	660	770	1,280	1,800	1,440 – 1,818	63	55.4	1,822
2	610	975	1,300	1,630	1,900	1,567 – 1,995	8	4	2,000
4							Cerrado		668
5	350	630	840	1,070		874 – 1,213	Cerrado		1,215
8	680	940	1,190	1,700		1,423 – 1,850	48	75	1,861
9	450	730	1,270	1,380	1,845	1,735 – 2,161	80	117.7	2,986
10	675	1,240	1,750	1,920	2,271	1,798 – 2,143	Calentamiento		2,271
12	550	675	825	1,330	1,750	1,877 – 2,293	26.13	30.3	2,303
11	450	660	860	1,300	1,800	1,800 – 2,150	Calentamiento		2,157

Table III. 2-16 Summary of Tentative Production Wells

Well		Location			Rank of Productivity	Notes
		I	J	K		
Existing wells	PR-1	10	10	3	1	
	PR-8	13	6	3	1	
	PR-9	8	13	3～4	1	
	PR-10	16	9	4	2	
	PR-11	5	5	3	1	
	PR-12	12	9	4	2	
	PR-13	9	5	3～4	2	
Future wells	PR-31	10	8	3	2	
	PR-32	11	6	3	3	
	PR-33	8	9	3	4	
	PR-34	8	7	3	3	
	PR-35	7	5	3	4	Used for case 1～4
	PR-36	6	14	3	5	
	PR-41	11	4	4	4	
	PR-42	4	15	4	5	
	PR-43	4	13	4	5	
	PR-44	12	11	4	5	
	PR-45	14	11	4	5	
	PR-46	14	9	4	5	
	PR-51	5	9	3	6	
	PR-52	6	7	3	5	
	PR-54	12	13	3	6	
	PR-55	14	13	3	6	
	PR-56	14	4	3	6	
Future wells	PR-61	15	7	4	6	
	PR-62	10	13	4	5	
	PR-63	8	15	4	6	
	PR-64	8	11	4	5	
	PR-65	7	3	4	6	
	PR-66	5	11	4	6	Used for case 1, 3, 4
	PR-81	17	7	4	6	
	PR-82	11	15	4	6	
	PR-83	9	3	4	6	
	PR-84	3	7	4	6	
	PR-85	3	5	4	6	
	PR-86	3	3	4	6	

Rank of Productivity	1	2	3	4	5	6
Proportion of Steam Production (%)	100	70	50	30	20	10

Table III. 2-17 Tentative Efficiency of each Well in Four Cases

Well	Case 1	Case 2	Case 3	Case 4
PR- 1	44	48	65	66
8	44	44	44	45
9	44	48	65	94
10	29	33	46	66
11	44	48	65	94
12	29	33	46	66
13	29	33	46	28
PR-31	29	33	46	66
32	22	24	33	47
33	12	14	20	28
34	22	24	33	47
35	12	14	20	28
36	8	10	13	19
PR-41	12	14	20	28
42	8	10	13	19
43	8	10	13	19
44	8	10	13	19
45	8	10	13	19
46	8	10	13	19
PR-51	4	5	6	9
52	8	10	13	19
54	4	5	6	9
55	4	5	6	9
56	4	5	6	9
PR-61	4		6	9
62	8		13	19
63	4		6	9
64	8		13	19
65	4		6	9
66	4		6	9
PR-81	4		6	9
82	4		6	9
83	4		6	9
84	4		6	9
85	4		6	9
86	4		6	9
Total	500	500	750	1,000

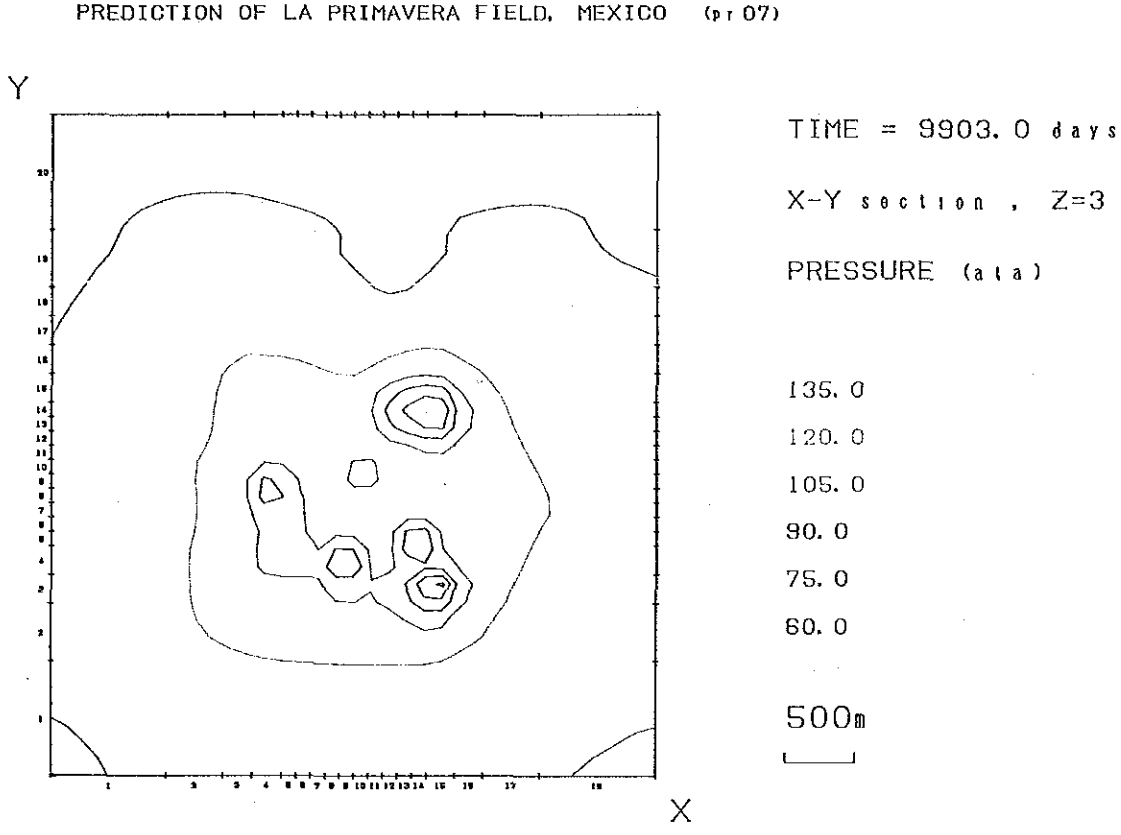

Fig. III. 2-62 Prediction of Pressure after 9,903 Days, Layer 3 (case l)

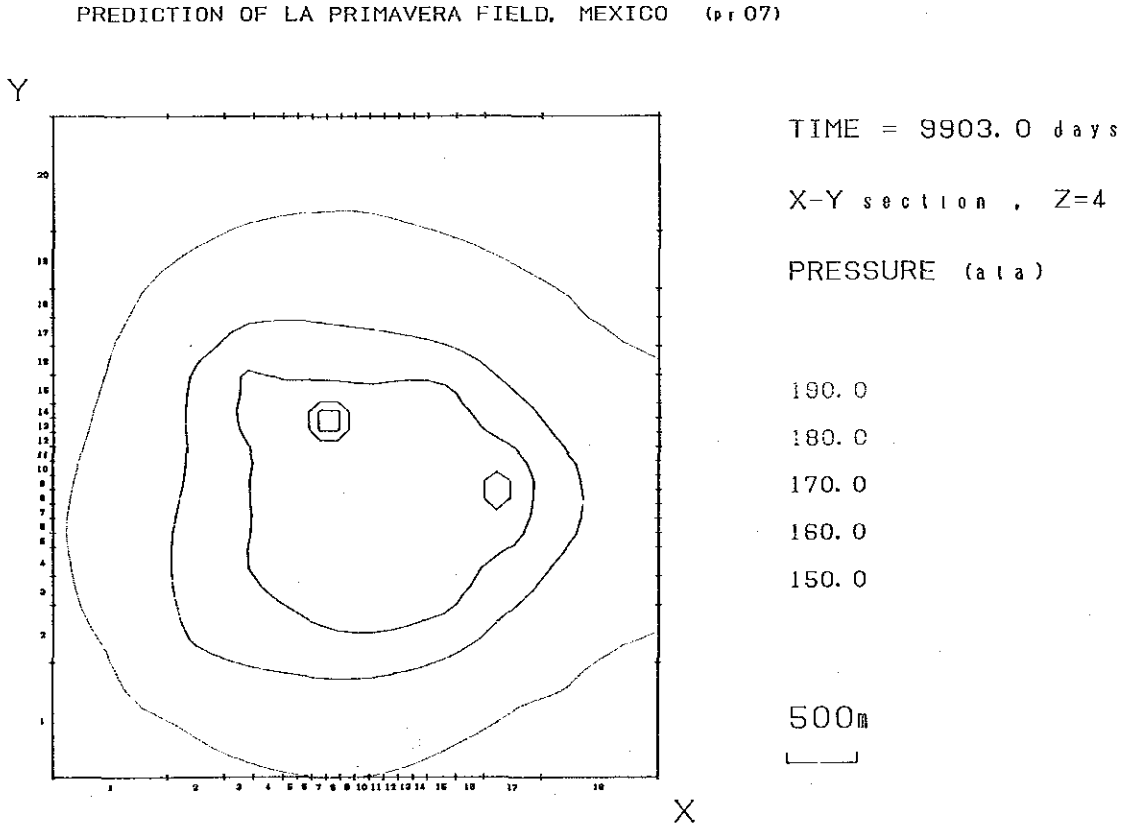

Fig. III. 2-63 Prediction of Pressure after 9,903 Days, Layer 4 (case 1)

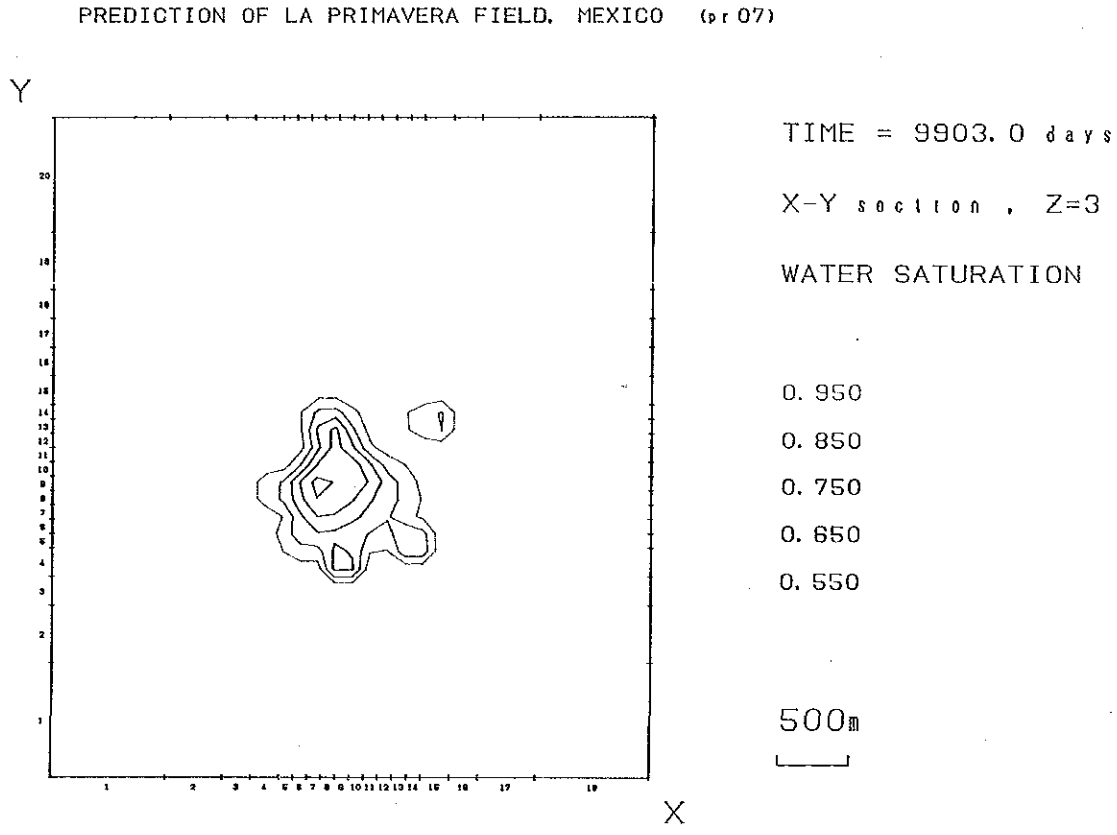

Fig. III. 2-64 Prediction of Water Saturation after 9,903 Days, Layer 3 (case 1)

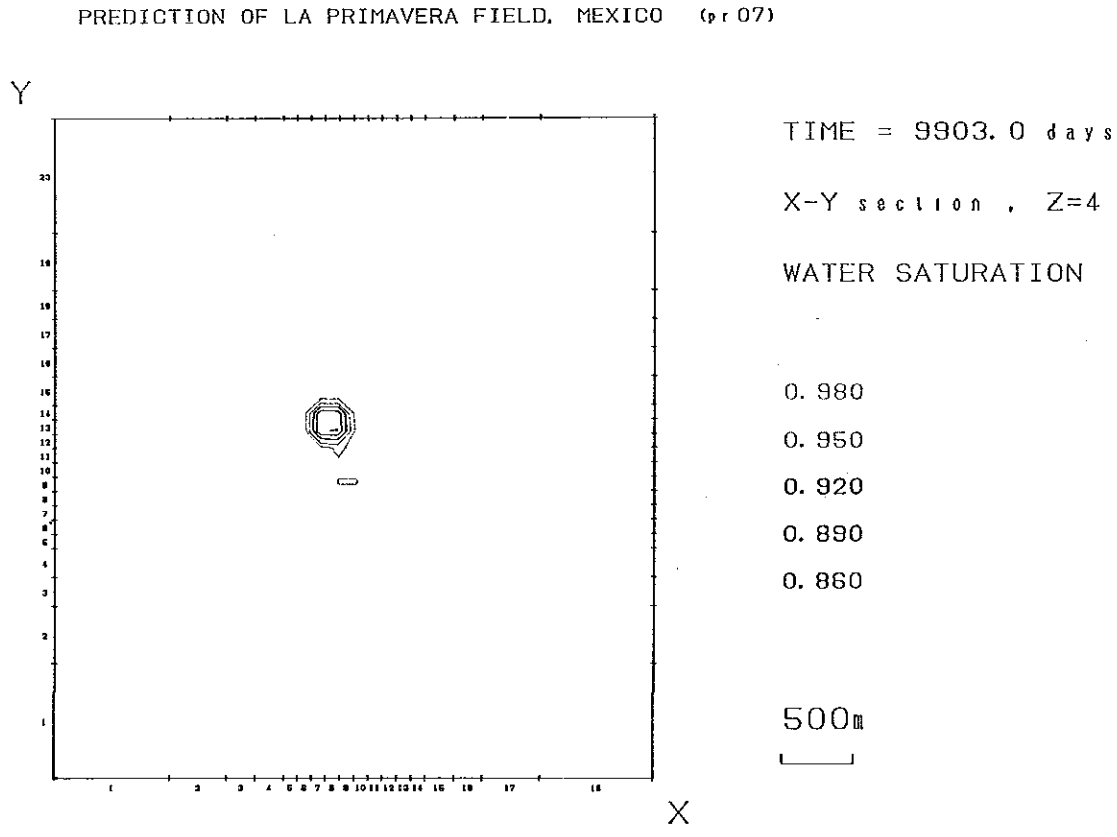

Fig. III. 2-65 Prediction of Water Saturation after 9,903 Days, Layer 4 (case 1)

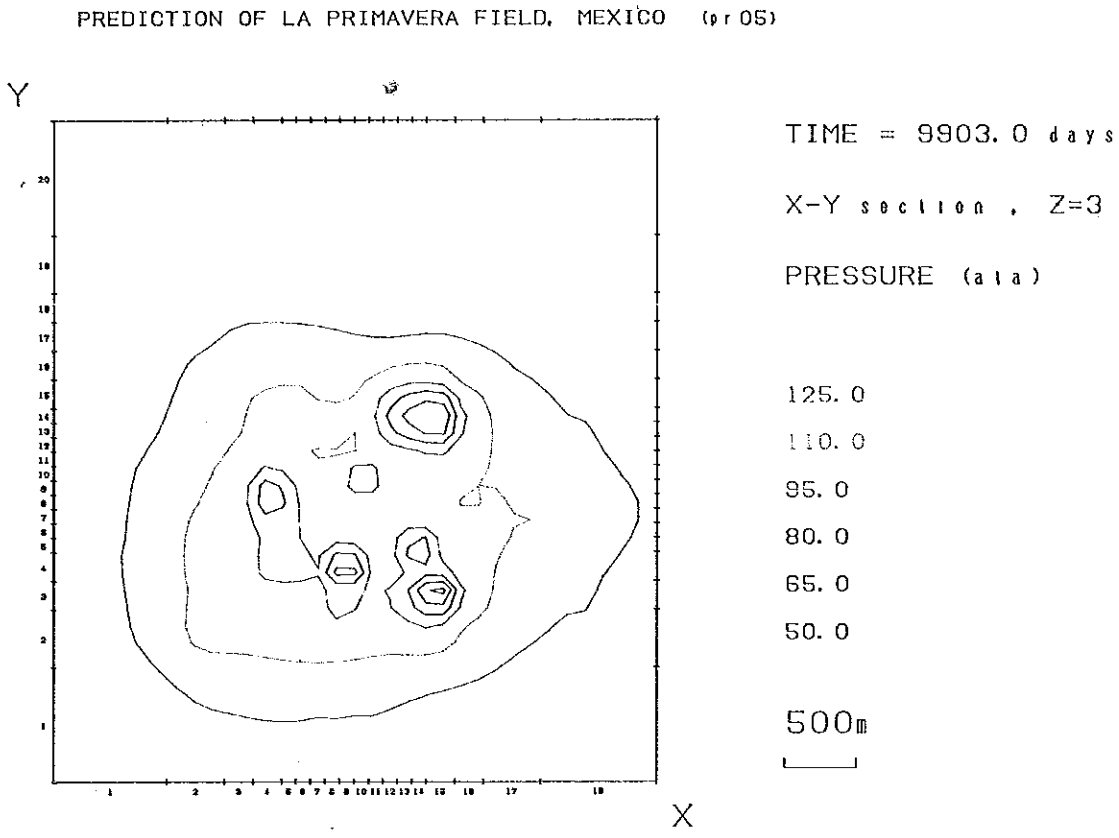

Fig. III. 2-66 Prediction of Pressure after 9,903 Days, Layer 3 (case 2)

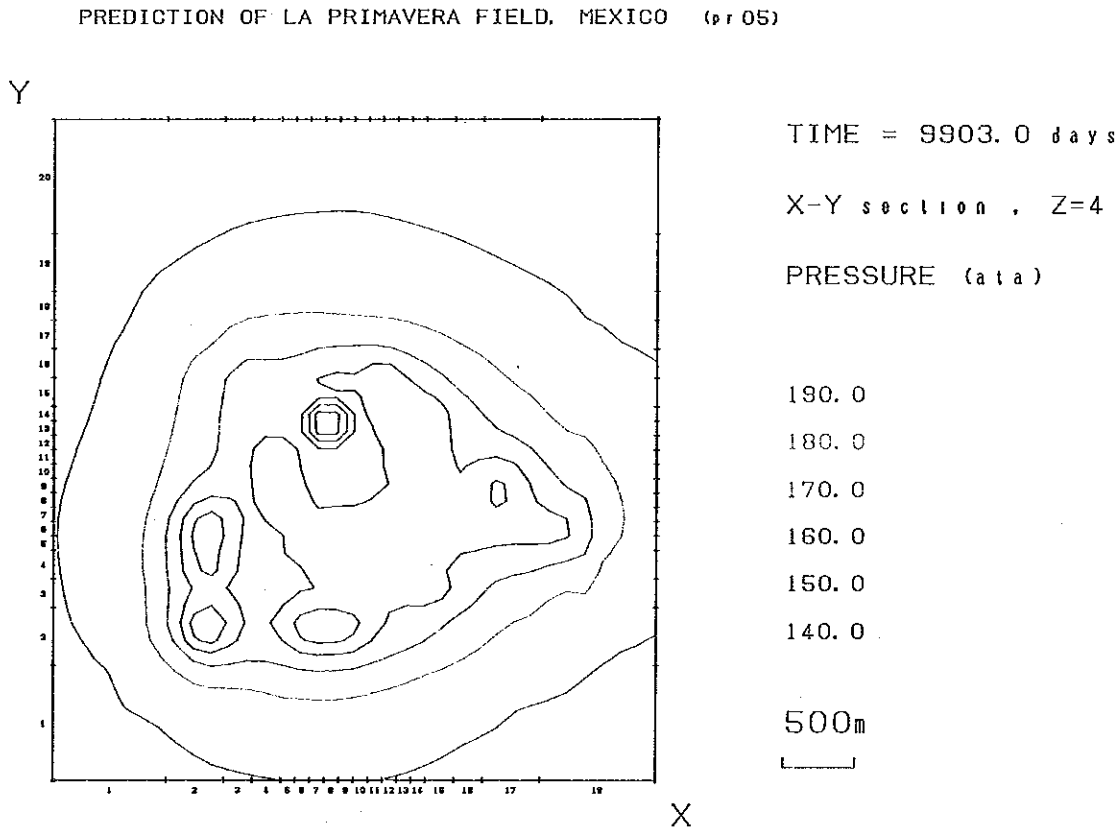

Fig. III. 2-67 Prediction of Pressure after 9,903 Days, Layer 4 (case 2)

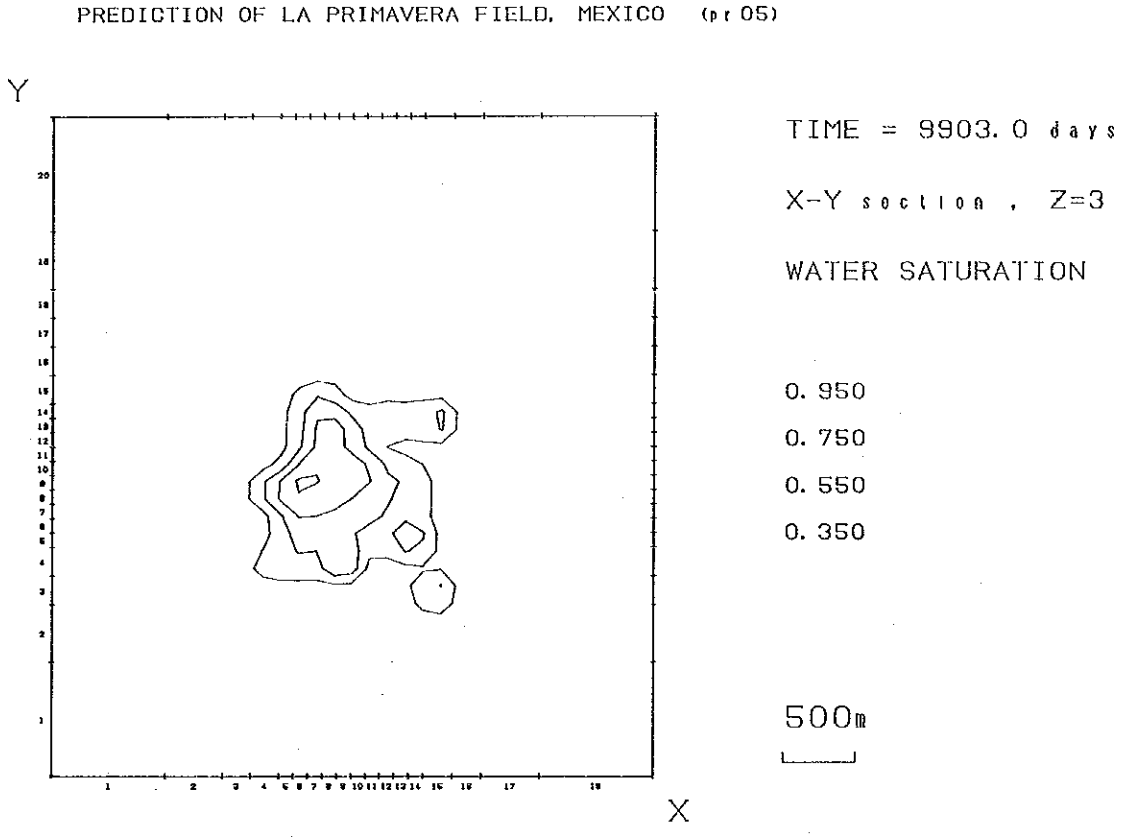

Fig. III. 2-68 Prediction of Water Saturation after 9,903 Days, Layer 3 (case 2)

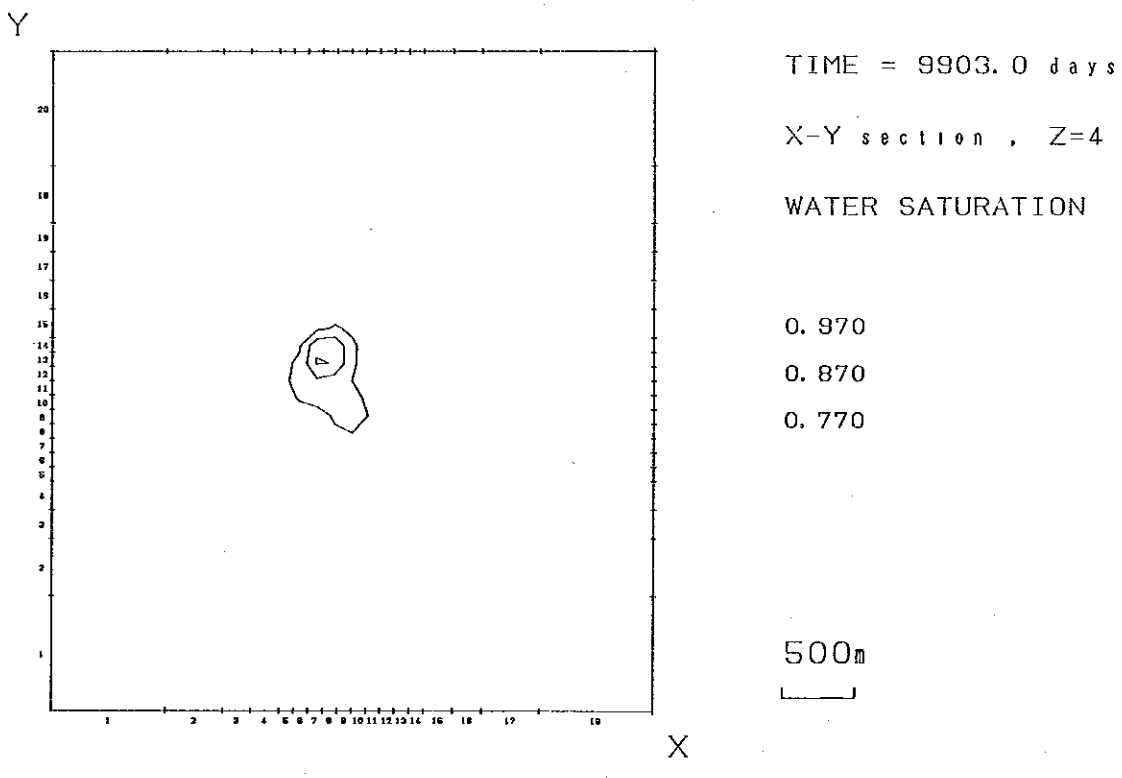

Fig. III. 2-69 Prediction of Water Saturation after 9,903 Days, Layer 4 (case 2)

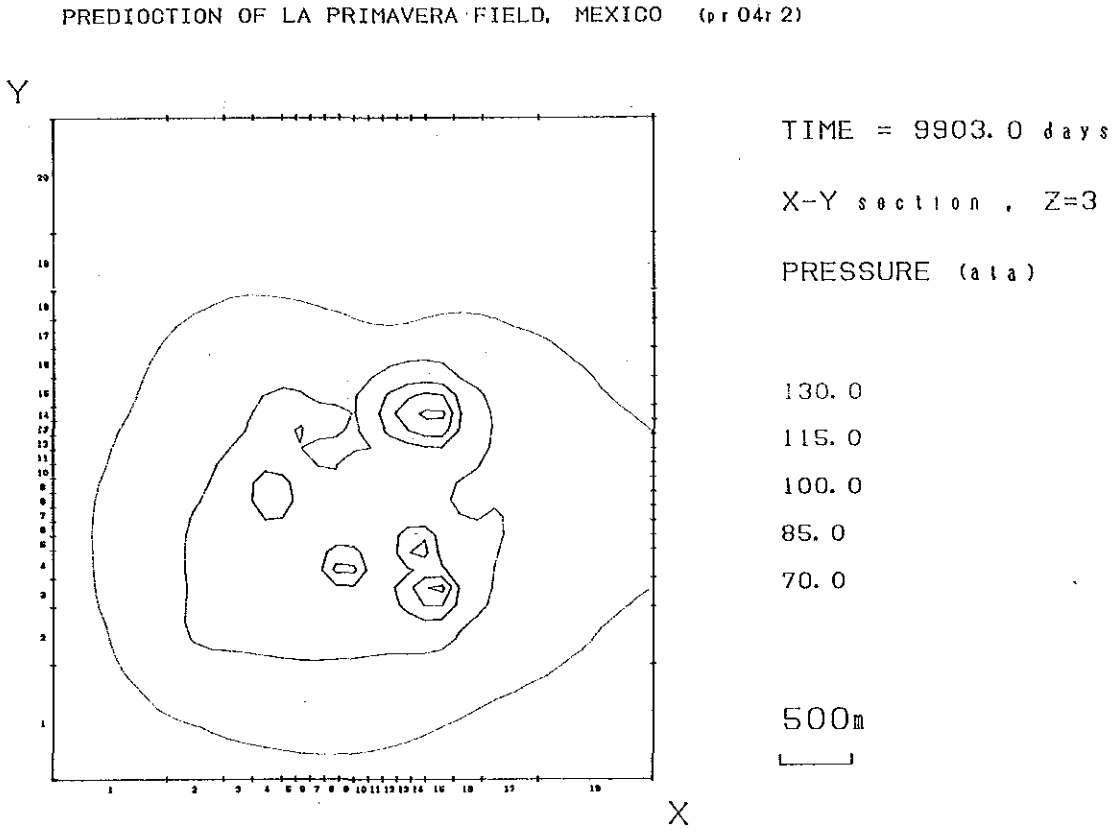

Fig. III. 2-70 Prediction of Pressure after 9,903 Days, Layer 3 (case 3)

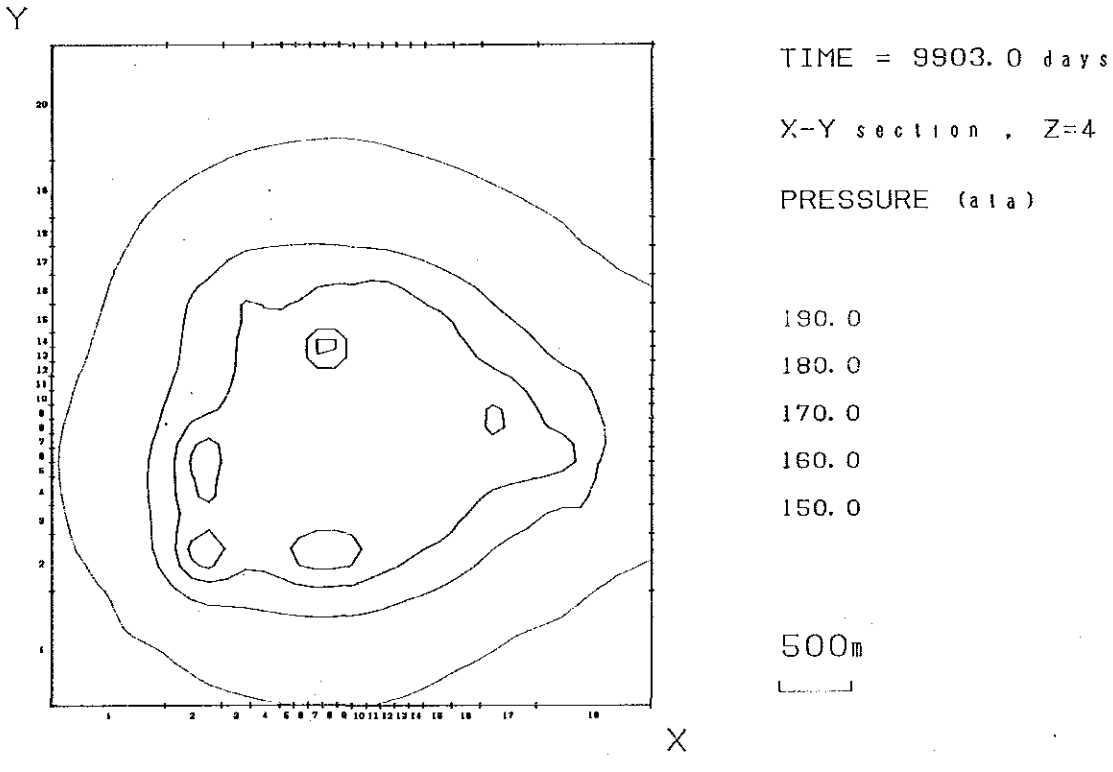

Fig. III. 2-71 Prediction of Pressure after 9,903 Days, layer 4 (case 3)

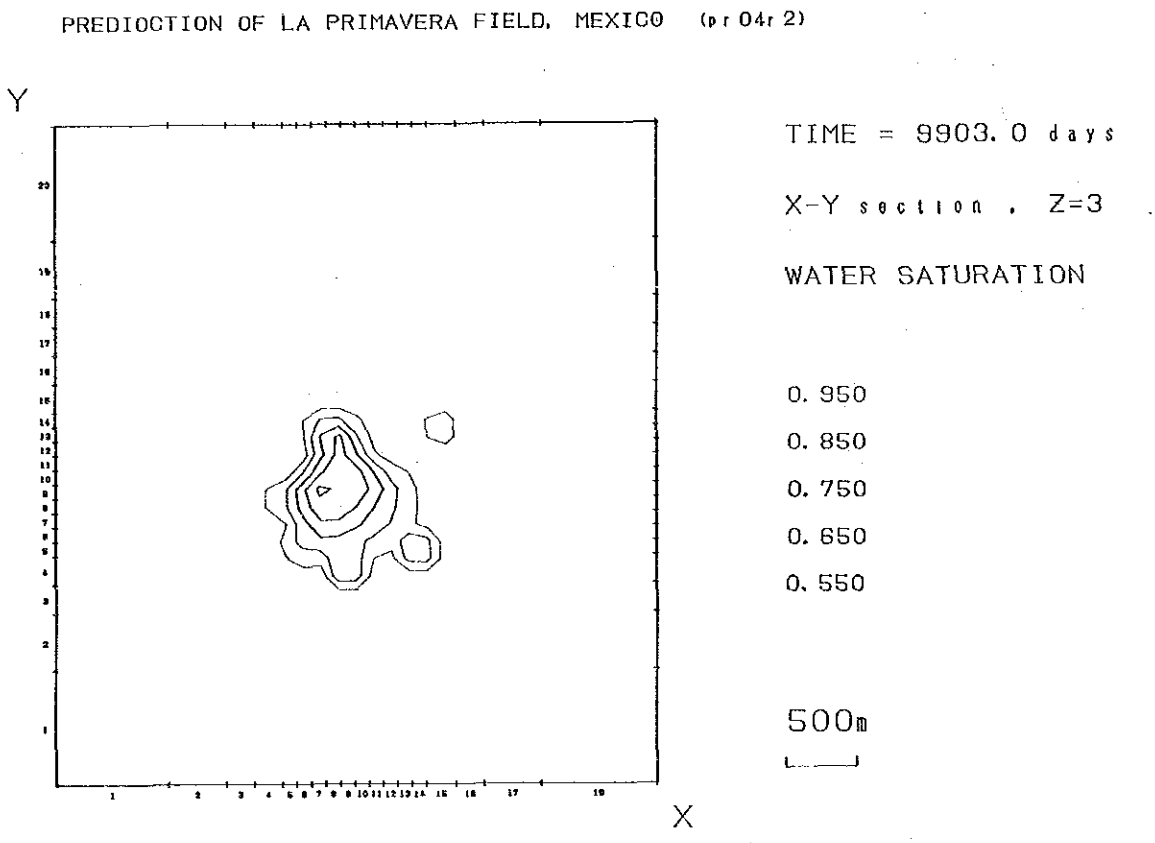

Fig. III. 2-72 Prediction of Water Saturation after 9,903 Days, Layer 3 (case 3)

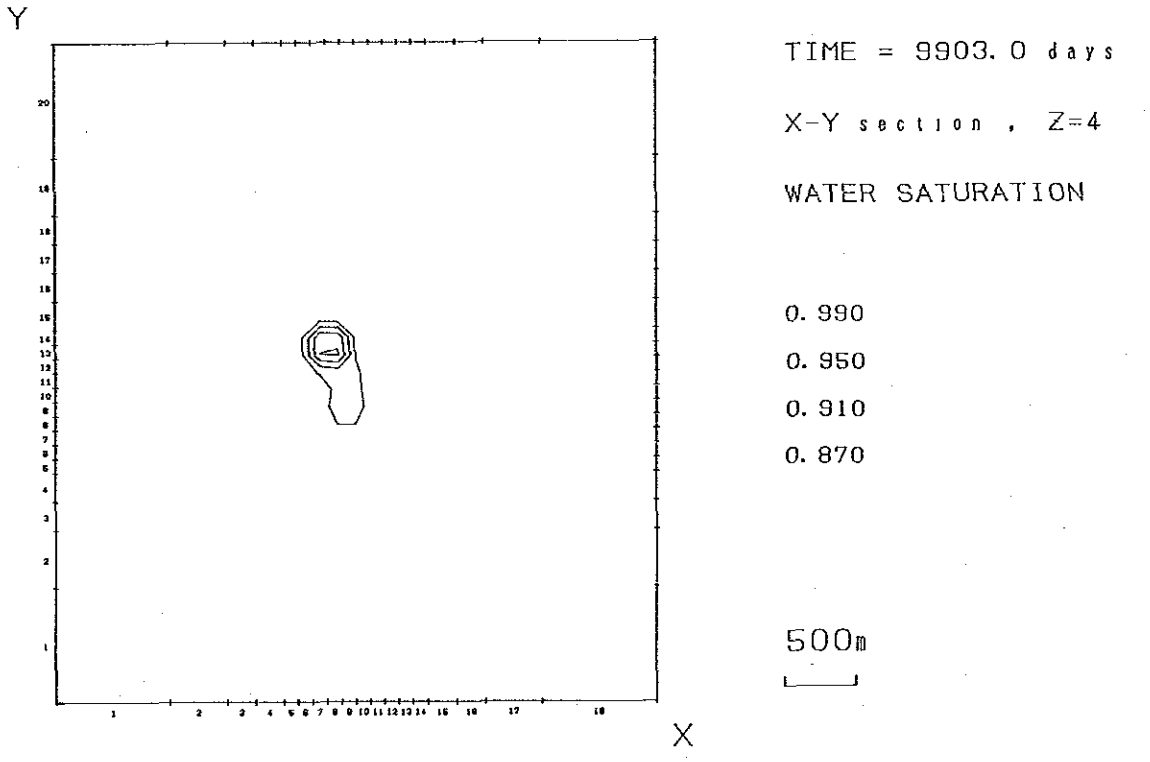

Fig. III. 2-73 Prediction of Water Saturation after 9,903 Days, Layer 4 (case 3)

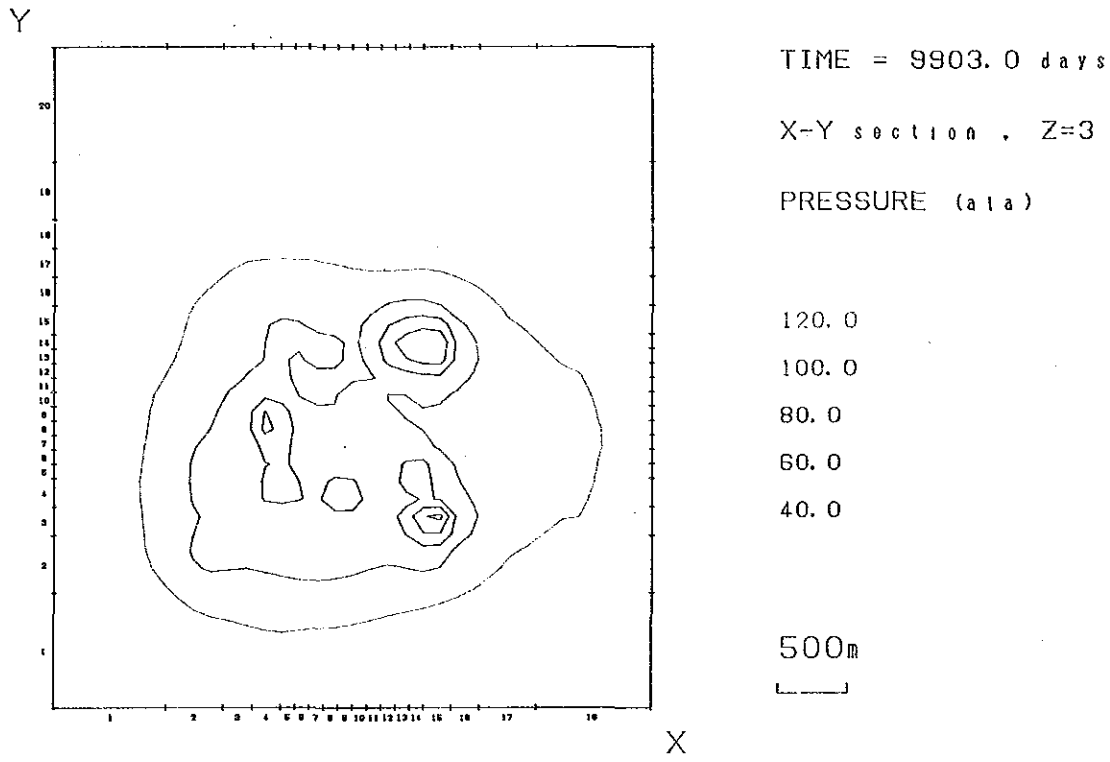

Fig. III. 2-74 Prediction of Pressure after 9,903 Days, Layer 3 (case 4)

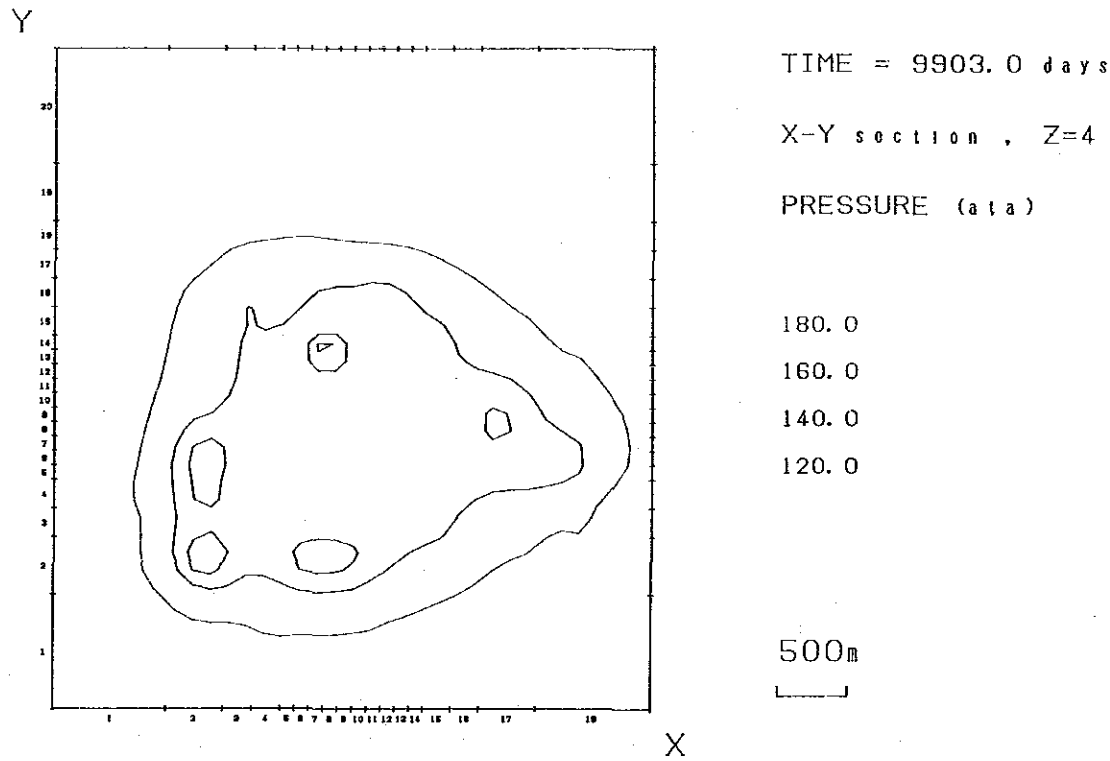

Fig. III. 2-75 Prediction of Pressure after 9,903 Days, Layer 4 (case 4)

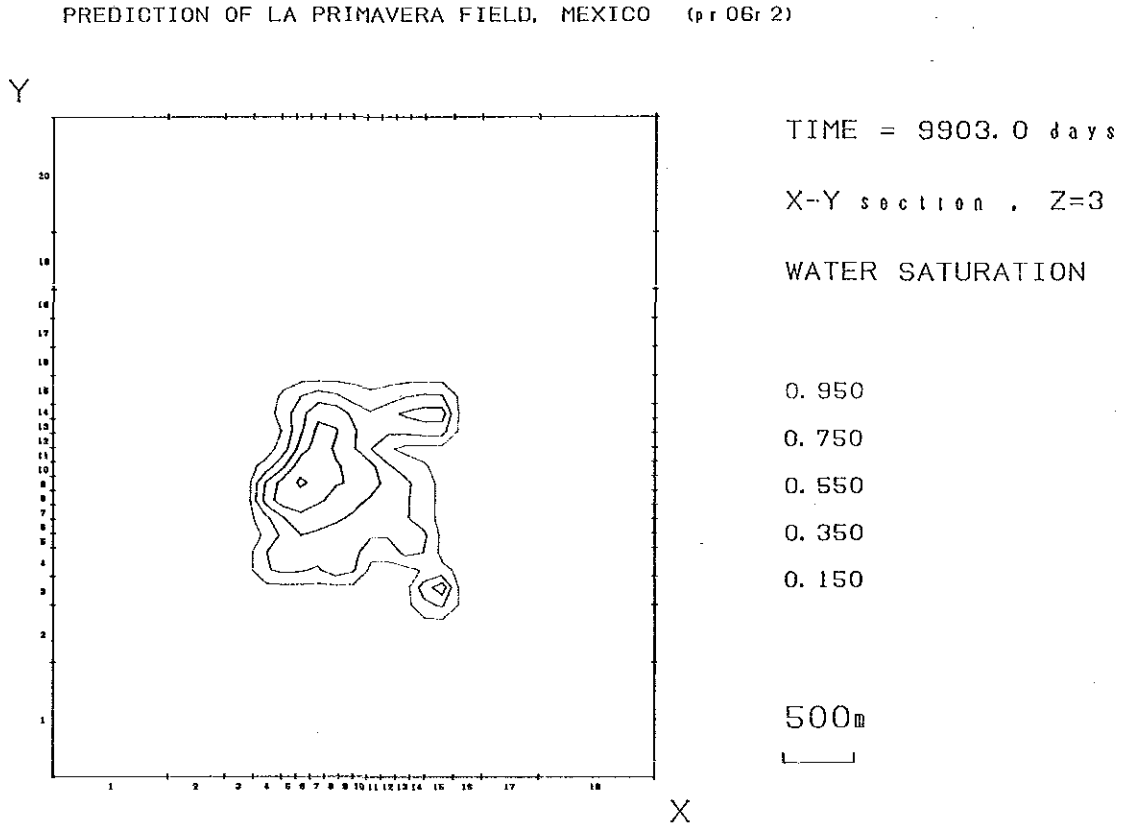

Fig. III. 2-76 Prediction of Water Saturation after 9,903 Days, Layer 3 (case 4)

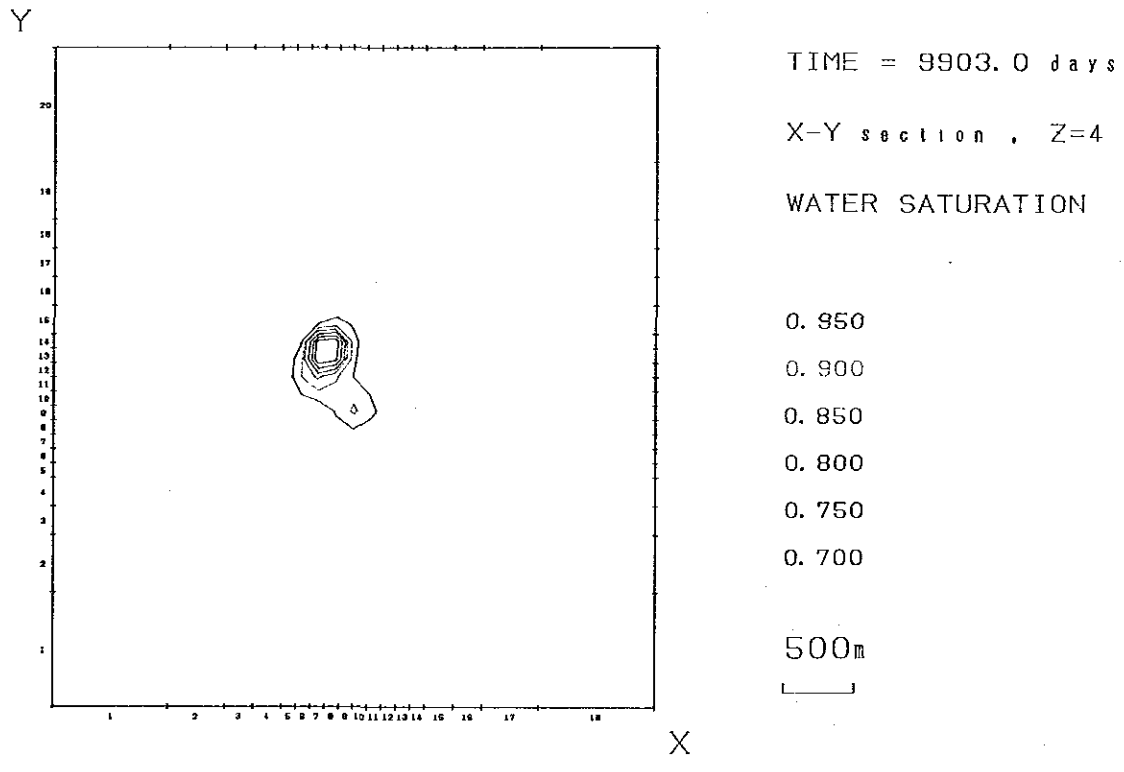

Fig. III. 2-77 Prediction of Water Saturation after 9,903 Days, Layer 4 (case 4)

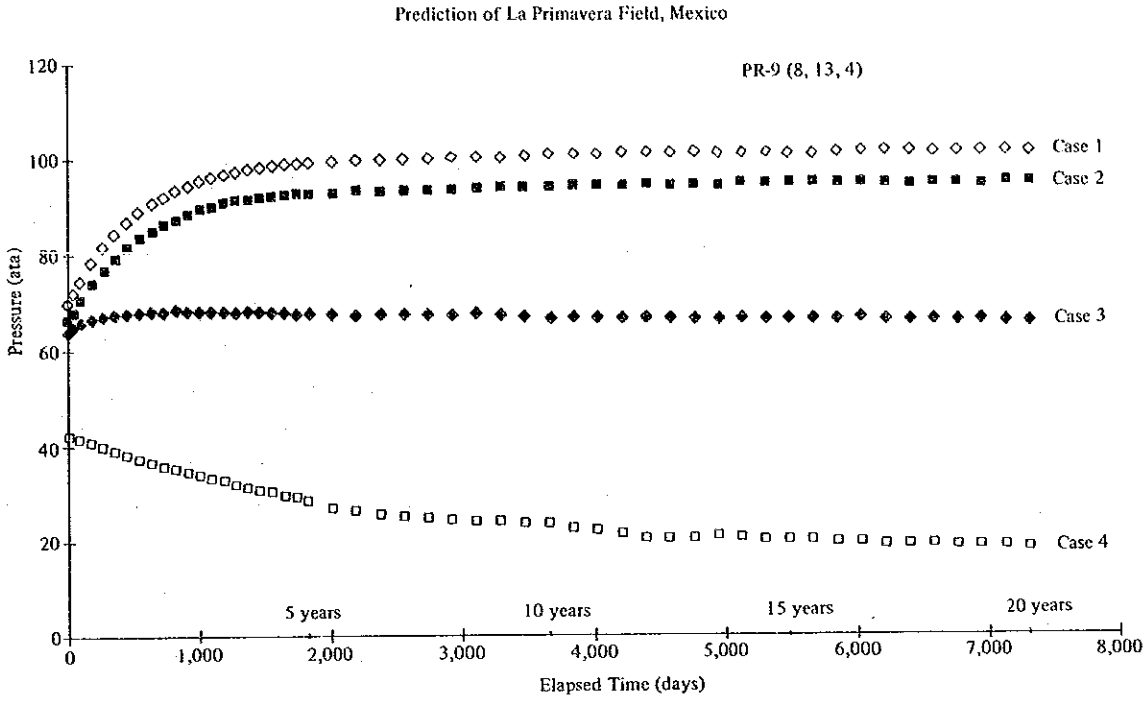

Fig. III. 2-78 Prediction of Reservoir Pressure near PR-9

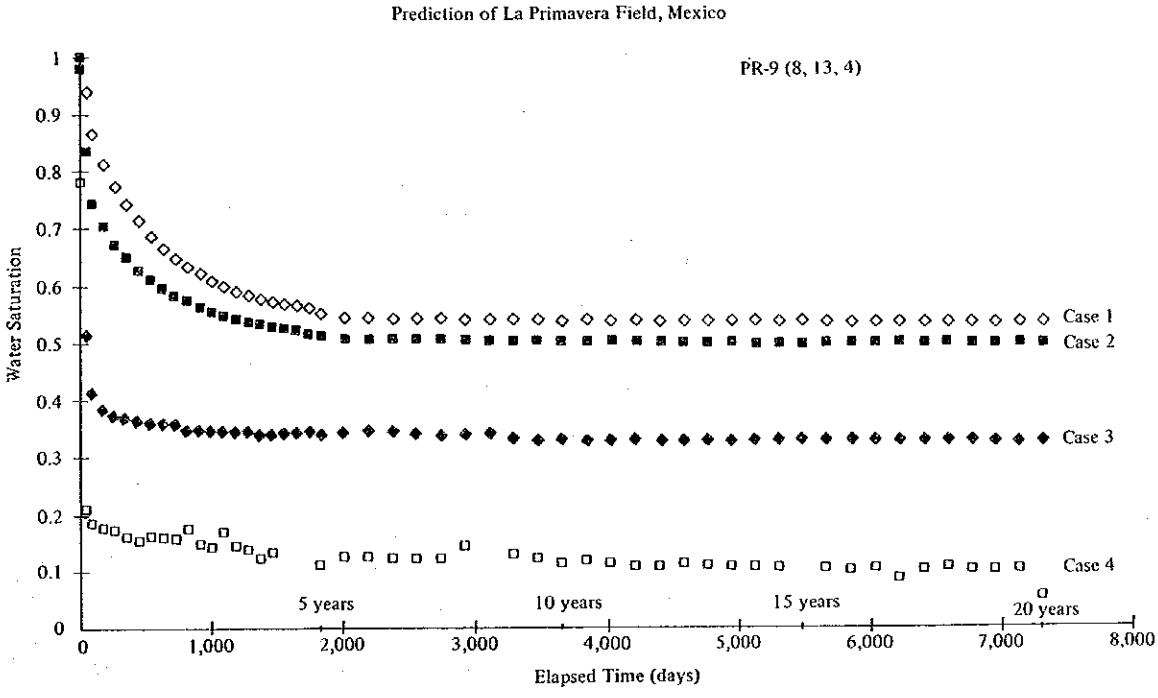

Fig. III. 2-79 Prediction of Water Saturation near PR-9

3. Work plan of generating plants

3.1 Possible power generation

The 75 MW power production is strictly a feasible generation. When we make a work plan of generating stations, the following studies are required to decide how generating capacity is reasonable:

① The efficiencies of five production wells such as PR-1, 8, 9, 12 and 13 were already shown in Figs. II.3-5 and II.3-23 and Table III.2-15. To plan generating plants, it is necessary to add the efficiencies of PR-10 and PR-11 of which well tests have not yet been carried out. Then, we anticipate the efficiency of PR-10 and PR-11 by the preparation of Table III.3-1. Table III.3-1 indicates that the output of steam at a fixed wellhead pressure is roughly proportional to the fluid temperature at the main feed point because the value of kh is approximately 10^{-13} (m^3) showing a narrow dispersion. Therefore, if we measure the fluid temperature, the output of steam can be estimated. Since we have no data of the fluid temperature of PR-10 and PR-11, an attempt is made to estimate the output of these wells based on the assumption that the fluid temperature is equivalent to the static temperature. Consequently, we can expect a steam output of about 40 t/h from each of these wells.

The total of the steam output is about 265 t/h at the wellhead pressure of 8 ata under present conditions. The output makes a total of 26 MW power generation possible. If an additional steam of about 235 t/h could be obtained in future, a 50 MW power generation will be possible. If an additional 485 t/h is obtained, a 75 MW is possible.

② As shown in Fig. III.2-2 and Table III.2-14, the possible number of drilling as production wells can be estimated at about 30 on the basis of the distributions of subsurface temperature, pressure and permeabilities. However, a given question occurs as to how many wells are necessary to obtain the steam output of 235 t/h or 485 t/h. Because the number of production wells controls the cost of a geothermal power plant, a feasibility study including economical analysis is required before making the decision of the generating capacity of geothermal power plant.

Table III. 3-1 Well Data in the La Primavera Area

Well	kh (m^3)	Static Temp. at main feed point	Fluid Temp. at main feed point	Chemical thermometer	Vapor at wellhead (8 ata / 7 atg)
PR-1	7.6×10^{-13}	304 ~ 305°C	299°C	300°C	40 t/h
PR-8	2.1×10^{-13}	More than 270°C	231°C	280°C	19 t/h
PR-9		345°C			61 t/h
PR-10		295°C			
PR-11		275°C			
PR-12	2.7×10^{-13}	Approx. 330°C	220°C	320 ~ 330°C	26 t/h
PR-13	$2.6 \sim 3.3 \times 10^{-13}$	Approx. 280°C	276°C	Approx. 280°C	40 t/h

3.2 Proposal for the work plan of next stage

As mentioned above, problems remain to be solved in order to decide the generating capacity of the power plant. Therefore, we propose the fulfillment of the feasibility study about development and construction of geothermal power plant as given below.

① The best method to catch reliably the future behavior of the reservoir is to produce continuously and simultaneously all steam of the existing seven wells for a period of about 1 year or more. However, steam production without utilization makes a loss economically.

② Instead of such steam production without utilization, we recommend the feasibility study and the fulfillment of the wellhead generation like that which has already been carried out in Los Azufres. For instance, if the wellhead generation is adopted under present conditions by using the existing wells, a total of 15 MW generation by 3 units (a 5 MW per 1 unit) is possible, made up as follows:

PR-9 : 1 unit
PR-1 + PR-12 : 1 unit
PR-11 + PR-13 : 1 unit

Where, the electrical efficiency is 5 MW/60t/h.

PR-10 will not be able to be used for wellhead generation because of collapse, and PR-8 is a spare well. This method is very effective for not only the gathering of data about the reservoir behavior but also the utilization of production wells until the full-scale power plant will be completed to construct.

③ It is necessary to study the viable economy for a 50 MW or 75 MW geothermal power plant. In the study, the number of production wells is a key parameter in the achivement of commercial profit.

④ It is better drill an additional two or three exploration wells with reference to the distributions of pressure, temperature and permeabilities in the best fitted model by the history match. The objective of drilling is to confirm the confidence of the best model and to predict the steam output per a well within the computed area.

The following conclusions are reached for the necessary work procedures of the next stage:

- The fulfillment of the long production tests, the wellhead generation, the economical analysis and the drilling of exploration wells.
- The integrate analysis using the above mentioned investigations
- The decision of the generating capacity of geothermal power plant in this area.

Moreover, the following considerations are added:

- The re-injection of hot water should be accepted because the limitation of steam output is controlled by the decrease of pressure and water saturation in the reservoir.
- The uplift and the up-flow zones are situated in the vicinity of PR-12.
- The formation temperature has arisen to the west of PR-9 where the NW or WNW trending faults develop in the reservoir.